UNIVERSITY OF MESSINA

DEPARTMENT OF ENGINEERING

DOCTORAL PROGRAM IN “CHEMISTRY AND ENGINEERING OF MATERIALS AND CONSTRUCTIONS ”

Two-dimensional Molybdenum disulfide electrochemical-based sensors for biomedical applications

Doctoral thesis of :

Rayhane Zribi

Tutor:

Prof. Giovanni Neri

Ph.D. Coordinator:

Prof. Edoardo Proverbio

Doctoral course 2019-2022 - XXXV Cycle (SSD-CHIM_07)

Abstract

The era of 2D materials started in 2004, exactly with the discovery of graphene by the group of Andre Geim and Konstantin Novoselov. They were awarded the Nobel Prize in 2010 for isolating the atomic layer of graphene from graphite, demonstrating the unique properties of this material. In addition to graphene, 2D nanomaterials, comprising individual nanosheets or layered multi-sheet planar materials, have been among the most intriguing nanomaterials of the last ten years. These thin 2D nanomaterials have special characteristics and properties that differentiate them from bulk ones. Among these 2D materials, we find transition metals dichalcogenides (TMDs), which this thesis deals with, thanks to their crucial properties such as the indirect-to-direct bandgap conversion going from bulk to monolayer, large surface-to-volume area, high carrier mobility, etc...

This Ph.D. project deals with the most famous 2D-TMDs, molybdenum disulfide (MoS_2). Recently, this material has been used in different research applications, particularly chemical sensors, which haven't stopped growing due to the real necessity to replace the costly techniques used at the moment. This thesis work was done in collaboration between CNR-IPCF Messina and the University of Messina, in which materials synthesis and characterization were done at CNR-IPCF Messina while sensors' development was done at the University of Messina.

Herein, MoS_2 has been exfoliated using the Liquid Phase Exfoliation (LPE) technique first and then with Liquid Cascade Centrifugation (LCC). The obtained materials were characterized using microscopic techniques such as scanning electron microscopy and atomic force microscopy and spectroscopic techniques such as UV-Visible spectroscopy, Raman spectroscopy, and Dynamic Light scattering. The 2D property of the as-prepared materials was confirmed from all these characterizations, and all the basic parameters like concentration, size, and thickness were computed.

The materials prepared via LPE were then used to modify different commercial screen-printed electrodes, gold, and carbon, used for the simultaneous and selective determination of Tyrosine, Dopamine, and Riboflavin. Using the same material together with gold nanoparticles, an electrochemical sensor was developed for Folic Acid determination.

On the other hand, the materials obtained via LCC were then used to study the electrochemical and sensing properties of 2D-MoS_2 nanosheets using different biomolecules for comparison.

Riassunto

L'era dei materiali 2D è iniziata nel 2004, esattamente con la scoperta del grafene da parte del gruppo di Andre Geim e Konstantin Novoselov. Hanno ricevuto il Premio Nobel nel 2010 per l'isolamento dello strato atomico di grafene dalla grafite, dimostrando le proprietà uniche di questo materiale. Oltre al grafene, i nanomateriali 2D, comprendenti singoli nanosheet o materiali planari multistrato stratificati, sono stati tra i nanomateriali più intriganti degli ultimi dieci anni. Questi sottili nanomateriali 2D hanno caratteristiche e proprietà speciali che li rendono diversi da quelli sfusi. Tra questi materiali 2D, troviamo i dichalcogenuri dei metalli di transizione (TMD), a cui siamo interessati in questa tesi, grazie alle loro proprietà cruciali come la conversione bandgap indiretta-diretta che passa da massa a monostrato, grande superficie a volume area, elevata mobilità del vettore, ecc...

Questo progetto di dottorato si occupa del più famoso 2D-TMD che è il disolfuro di molibdeno (MoS_2). Recentemente questo materiale è stato utilizzato in diverse applicazioni di ricerca, ed in particolare nel campo dei sensori chimici, che non ha smesso di crescere per la reale necessità di sostituire le costose tecniche attualmente utilizzate. Questo lavoro di tesi è stato svolto in collaborazione tra CNR-IPCF Messina e Università di Messina, in cui la sintesi e la caratterizzazione dei materiali è stata effettuata presso CNR-IPCF Messina mentre lo sviluppo del sensore è stato svolto presso l'Università di Messina.

Qui, MoS_2 è stato esfoliato utilizzando prima la tecnica di esfoliazione in fase liquida (LPE) e successivamente con centrifugazione a cascata liquida (LCC). I materiali ottenuti sono stati caratterizzati utilizzando tecniche microscopiche come la microscopia elettronica a scansione e la microscopia a forza atomica e tecniche spettroscopiche come la spettroscopia UV-visibile, la spettroscopia Raman e la diffusione dinamica della luce. Da tutta questa caratterizzazione, è stata confermata la proprietà 2D dei materiali preparati e sono stati calcolati tutti i parametri di base come concentrazione, dimensione e spessore.

I materiali preparati tramite LPE sono stati poi utilizzati per modificare diversi elettrodi serigrafati commerciali, oro e carbonio, che sono stati utilizzati per la determinazione simultanea e selettiva di Tirosina, Dopamina e Riboflavina. Utilizzando lo stesso materiale insieme a nanoparticelle d'oro, è stato sviluppato un sensore elettrochimico per la determinazione dell'acido folico.

D'altra parte, i materiali ottenuti tramite LCC sono stati poi utilizzati per studiare le proprietà elettrochimiche e di rilevamento dei nanosheet 2D-MoS_2 utilizzando diverse biomolecole per il confronto.

Motivation

In the medical field, the old conventional analytical instruments are used less than before due to different factors such as the high test cost, no longer practical, and meeting almost none of the important criteria that facilitate the examination. Therefore, the development of new techniques allowing the detection and monitoring of chemical species in the human body are highly requested and constantly focused on improving its efficiency, namely decreasing the cost of the test and the waiting time, preventing serious complications, being as much non-invasive as possible to reduce the post-traumatic effect and at the same time they should guarantee the same performance and reliability as the conventional and well-assessed techniques.

For this reason, new diagnostic techniques monitor patients' state of health and sometimes prevent them from serious diseases. These techniques are usually used to detect species in the urine, sweat, exhaled air, and blood. For example, in 1970, German engineer Anton H. Clemens discovered the first glucometer, “Ames Reflectance Meter” used in American hospitals. A moving needle indicates the blood glucose after about a minute. This great discovery came after revealing the first oxygen electrode in 1956 by Clark, followed by the development of the first enzymatic glucose electrode by Clark and Lyons in 1962 using Glucose oxidase as an enzyme.

Since that, great interest has been directed towards the development of chemical sensors, i.e. devices capable of detecting the presence of a specific substance in a given environment, generating a signal providing qualitative or quantitative information relative to the target analyte.

In recent decades, a huge number of devices have been developed using different kinds of materials for the detection of different biomolecules. The chemical sensors can be classified according to their transduction mechanism so that we can find capacitive, gravimetric, resistive, and electrochemical sensors, etc. The latter is one of the best-known and most widely used sensors in the field of medical biology.

As mentioned earlier, different types of materials have been used to improve the electrochemical sensors, and over the past two decades, researchers have focused on the exploitation of 2D materials to boost the performances of chemical and electrochemical sensors because of their interesting chemical-physical properties. This attention came after the discovery of graphene in 2004, which is considered revolutionary material due to its outstanding properties. A few years later, other 2D materials arose in the field, such as Transition Metal Dichalcogenides, the perfect graphene alternative. Among them, we find the Molybdenum Disulfide, which was extensively exploited and investigated in this thesis.

Acknowledgments

First, I want to thank ALLAH for all the will and courage he gave me to complete this doctoral work. He has been and will always be next to me and by my side to succeed in achieving my goals and dreams.

I would like to acknowledge and express my deepest thanks and gratitude to

Prof. Giovanni Neri, my dear supervisor, for his enthusiasm, encouragement, scientific advice, accessibility to answer my questions whenever they arose, and stewardship throughout my Ph.D. thesis. Thank you for believing in me and my capacities and always encouraging me. Thank you for being the most amazing mentor during my Ph.D. and the best pillar during the hardest moments I went through.

A special thanks also to **Dr. Pietro Giuseppe Gucciardi** and **Dr. Antonino Foti,** with whom I worked closely at the National Research Council (CNR-IPCF Messina), as well as all the researchers inside this amazing institute, Maria Grazia, Antonella, Onofrio, David… for the support and encouragement they provide during this challenging life step.

We built up this team and started working together since my master's thesis and during these years they were the greatest supervisors for both career advancement and personal attitude. Their guidance and advice carried me through all the stages of my Ph.D. life and I will always be thankful for them. I couldn't have imagined having better mentors. This thesis owes them a lot!

Also, I would like to thank **Prof. Claudia Espro** and **Prof. Daniela Iannazzo** for all their help, support, and friendship.

I warmly thank **Prof. Jonathan Claussen** and **Prof. Carmen Gomes,** who welcomed me to their laboratories at Iowa State University, in the United States of America, for a 6-month internship that exceeded my expectations and taught me a lot. Thanks to all the lab group and a special one to Zachary Johnson, "best lab partner", with whom I worked closely, for all the great work and support.

I also want to thank **Prof. Yvan Bonnassieux,** who accepted me for a 3-month internship in his laboratory of Physics of Interface and Thin Films (LPICM)-CNRS at école Polytechnique- Paris in France, in which I worked closely with **Prof. Aleix Guell** and **Prof. Razvigor Ossikovski**. This experience was so beneficial for my career.

Special thanks to **Prof. Ramzi Maalej,** who made my doctoral thesis more exciting than I ever thought, and thanks to him, I realized how much I can accept challenges.

Also, I would like to thank **Prof. Nouha Ghorbel** from the University of Sfax for being the best professor who taught me in my bachelor's and helped me a lot even after that.

To **Prof. Wissem Cheikhrouhou**: I will be forever grateful for all your support.

I would like to express my sincere thanks to my lab group "LabSensori" past and present members **Gianluca, Consuelo, Sanaz**… my dear colleagues, and my second family, with whom I learned, worked, and laughed a lot, as well as the best Erasmus students ever **Ratiba, Khaoula,** and **Sarra** for all the special moments we had and a special one for my forever favorite friends and colleagues **Angelo**, **Viviana,** and **Simona.**

For my best friends **Sami, Rihab, Estelle, Abir, Emna, and Mimi,** thank you for all your support and all you have done for me… I LOVE YOU!

Rayhane Zribi

الى جدي العزيز المرحوم محمد

الذي رحل ليعيش تحت الأرض بسلام تام... رحل وترك خلفه غصة فقد ومرارة شوق، ومكان يعجز الجميع عن ملأه... رحل عني ولم يرحل مني. ربي أنه ليس معي لكنه في قلبي وفي دعائي... انتقل إلى جوارك لكنه موجود في كل تفاصيل حياتي... اللهم ارحم جدي حبيبي بقدر اشتياقي له واجعله آمن مطمئن في قبره واجعل قبره روضة من رياض الجنة

لروحك النقية التي لا تفارقني أينما ذهبت أهدي أطروحة الدكتوراه

الى عشقي الأبدي و حبي الأول والأخير, الى أبي الغالي سامي

كل الشكر والعرفان لمن لا أحصيه فضلا وتقديرا، لمن شجعني ودعمني إن كنت في أوائل الصفوف أو كنت الأخيرة، أبي الغالي... وإن لم أكن قادرة على منحك من الثناء الوفير ما يليق بك، فأنت في القلب ملكا متوجا وأغلى رفيقا. شكرا لك يا أبي، لن أقول شكرا فقط على ما قدمت ولكن شكرًا لكونك أبي أسعدك الله دهورا و أدام صحتك و أطال عمرك... أحبك وإن كانت كلمة الحب هشة لا تعبر عما يختلج أوصالي.

إلى سيدة حياتي، سلطانتي، وملكتي، أمي الغالية ألفة

فارغة هي حياتي من دونك، تفاصيلي وحدها باهتة إن لم يكللها وجودك، حروفي جوفاء وإحساسي مبتور إن لم تتزين الحياة بوجودك، أنتِ البهجة والفرحة والأمل، أنت لستِ أنتِ فقط! إنما أنت معنى من معاني الرحمة، كسحابة حب أمطرت فملأت الأرض حبورًا، لولا دعمك و دعائك و رضاك لما كنت قادرة على مواصلة مشواري... لكِ كل الشكر يا غالية قلبي.

دمتِ لنا كل شيء...

الى أخي الصغير محمد

يا صديقي ورفيق دربي يا من معه تحلو كل الأوقات وبقربه أشعر بالأمن والأمان ومعه دائما يحلو الكلام. أخي حبيب روحي وأنيس وحدتي وملجأ ذاتي. دمت لي أخا أفتخر به بين الناس، دمت لي سندا وعمودا أتكئ عليه، شكرا لأنك في حياتي شكرا لكونك أخي.

الى كل أفراد عائلتي الحبيبة

رسالة شكر وامتنان أطيّرها لكم لوقوفكم بجانبي دوما، فلوغبتم عن ناظري يوما فأنتم في القلب دوما، أذكر أيام الشّدائد حين لم تفارقوني لحظة واحدة، بل كنتم خيرعون، وسند، وناصح، ما أجمل تلك الأيام بكلّ ما فيها، سعادتي كبيرة بكم، ولن أتخلّى عنكم ما حييت

Thesis Outline

Section I: Chemical Sensors & 2D Materials: State Of Art

This section introduces chemical sensors, particularly the electrochemical sensors and electroanalytical methods used in this thesis. In addition, an overview of the two-dimensional materials' properties and their most popular synthesis methods were illustrated, with a closer look at the Molybdenum disulfide (MoS_2). Finally, the analytes used to develop the electrochemical sensors were introduced.

Section II: Materials & Methods

This section includes the materials used in this thesis, sample preparation steps, and characterization techniques utilized throughout this project. A brief overview of the tools utilized for electrochemical testing is also provided.

Section III: Results & Discussions

This section is divided into two main parts:

- ***Part 1 :*** electrochemical sensors based on 2D materials prepared via Liquid Phase Exfoliation.
- ***Part 2 :*** electrochemical sensors based on 2D materials prepared via Liquid Cascade Centrifugation.

Section IV: Side Works

This section presents an overview of side works done during the Ph.D. course, which weren't considered in the main plan of this thesis project.

Section V: General Conclusions

The major conclusions and recommendations for potential future studies are presented in this section.

Table of Contents

List of Abreviations

AC: alternating current

AFM: Atomic force microscopy

ALD: atomic layer deposition

BN: boron nitride

c: concentration

CBM : conduction band minimum

CC : carbon cloth

CE: counter electrode

CV: cyclic voltammetry

CVD : chemical vapor deposition

DA: dopamine

DLS: Dynamic light scattering

DPV : differential pulse voltammetry

E: young’ modulus

EIS: electrochemical impedence spectroscpy

E_s: potential step

FA: folic acid

H_2: hydrogen

HER: hydrogen evolution reaction

LCC: liquid cascade centrifugation

LPE: liquid phase exfoliation

LSV: linear sweep voltammetry

ME: mechanical exfoliation

MoO_3: molybdenum oxide

MoO_x: molybdenum oxide

MoS_2: molybdenum disulfide

MXene: metal carbide/nitride

O_2: oxygen

OER: oxygen evolution reaction

PBS: phosphate buffer saline

PLD: pulsed laser deposition

RE: reference electrode

RF: riboflavin

S: sensitivity

SC: sodium cholate

SEM-EDS: Scanning Electron Microscopy- Energy Dispersive X-ray Spectroscopy

SPE: screen-printed electrode

SWV: square wave voltammetry

TMDs: transition metal dichalcogenides

Tyr: tyrosine

UA: uric acid

UV-Vis: UV-Visible spectroscopy

VBM: valence band maximum

WE: working electrode

<L>: lateral size

<N>: thickness

Γ: strain

ε: extinction coefficient

σ: stress

υ: scan rate

Section I

Chemical Sensors & 2D Materials: State of the Art

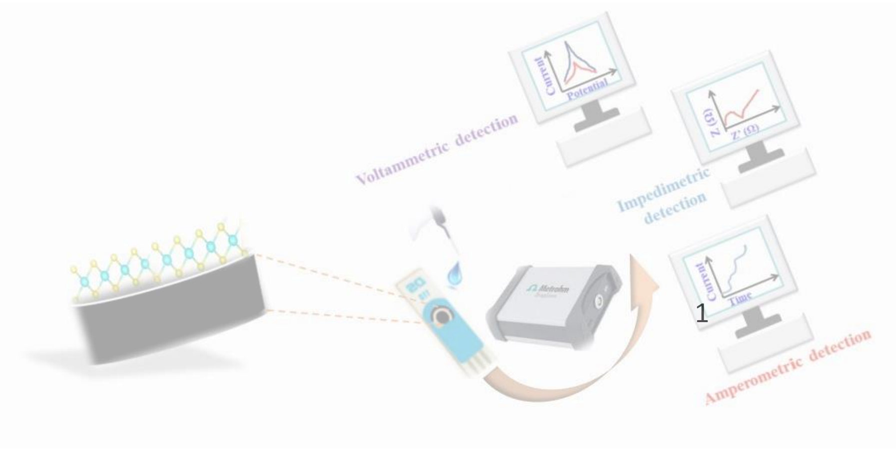

I. Chemical sensors

As a general definition, a chemical sensor is an autonomous analysis device capable to identify the presence of a specific substance, generating a signal that provides qualitative and/or quantitative information relative to the analyzed species [1].

It is usually able to transform the interaction occurring between the sensor and the analyte species into a measurable signal. Indeed, as showed in Fig.I.1, the sensor is generally composed by a receptor consisting of a sensitive and selective layer that allows the recognition of the target analytes taking advantage of specific reactions, and by a transducer system that transforms the chemical interaction into an analytically useful electric signal [2]. Often, the two functions are intimately linked.

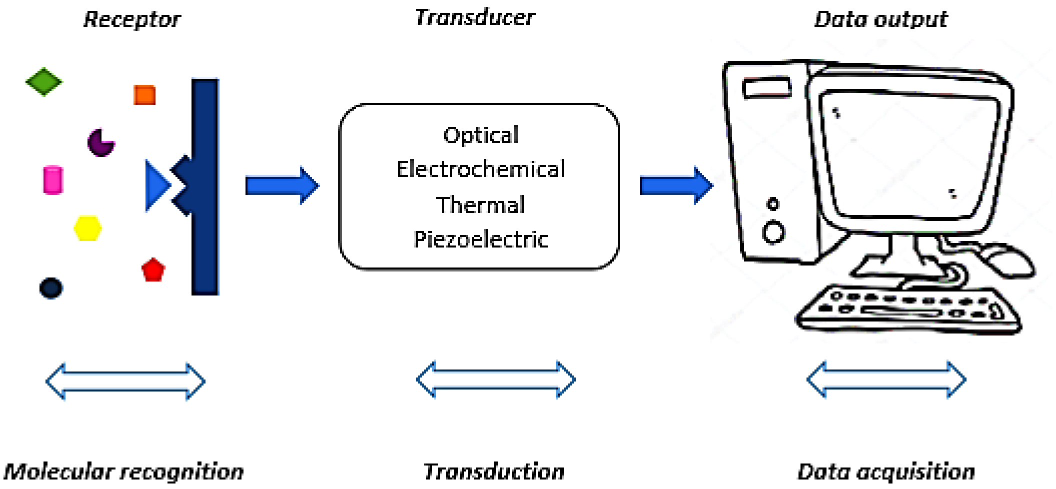

Figure I. 1. Schematic diagrams of a chemical sensor.

The receptors of the analytical sensor can be classified according to their operating principles, taking into consideration the type of interaction occurring. This interaction can be, on one hand, physical when noticing a change in optical, electrical, temperature, or mass properties. On the second hand, it can be chemical when the receptor and the target analyte interact chemically in a way generating by that the analytical signal.

I.1. Chemical sensors' type

Chemical sensors can be classified into two groups depending on the working principle or the target molecule. These two groups are illustrated in schema I.1 below.

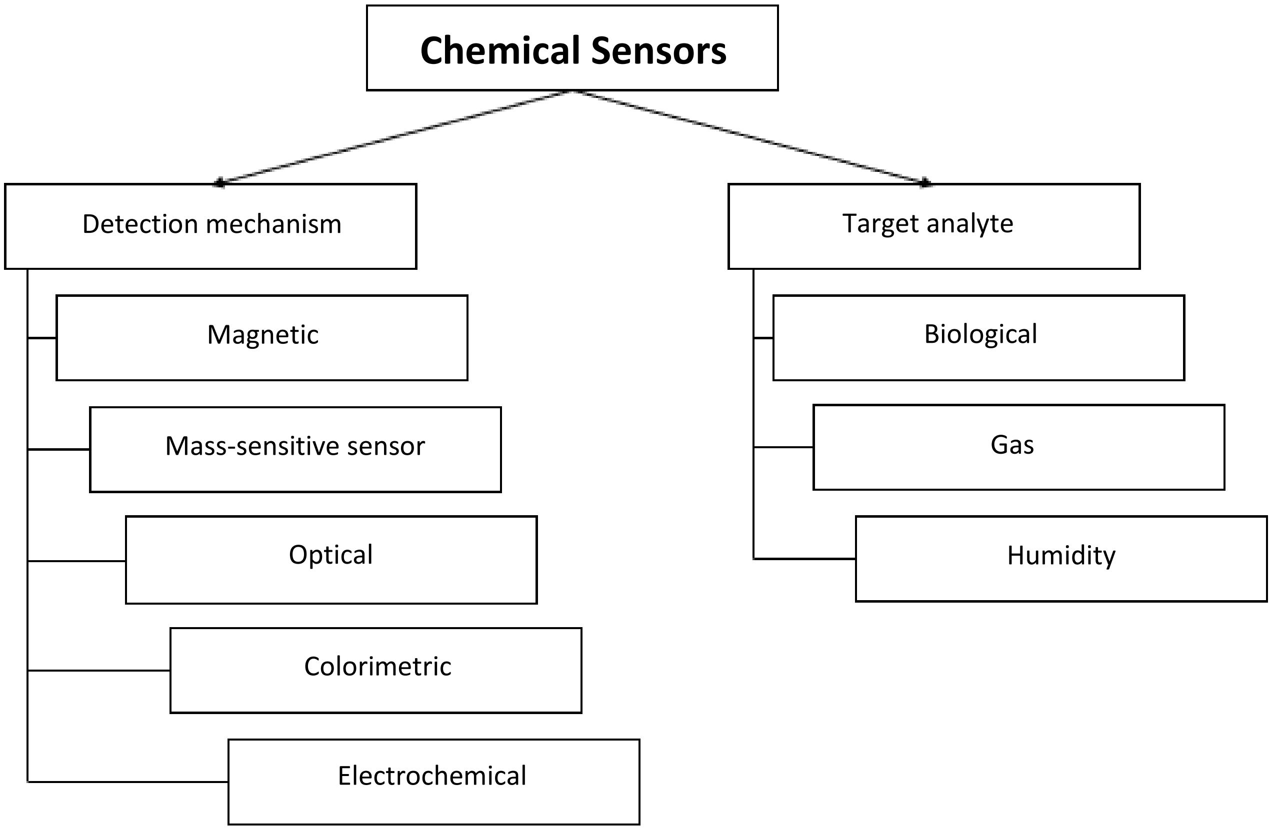

Schema I. 1. Chemical sensors' type.

I.2. Electrochemistry and electrochemical sensors

Electrochemistry is the field of chemistry that connects chemistry and electricity [3]. It illustrates the chemical reaction that happens together with the change of electrical energy. Electrochemical sensors are the type of sensors widely used in this area of chemistry [4, 5]. Their working principle consists of transforming the electrochemical interaction between the analyte and the sensor in an electrical signal [3]. They are currently the subject of many research and development in the field of biology [6], medicine [7] , industry [2], environmental [8], and agricultural analyses [9], and they also represent the most developed chemical sensor. Such devices occupy a leading position among the currently available sensors which are already at the commercial stage.

These sensors have the advantage of allowing rapid and selective analysis. Thus, it is possible to carry out a continuous analysis of a product or to follow the physiological state and the health situation of a patient. Furthermore, these sensors can be miniaturized and implanted in the human body for a continuous survey in some cases.

The operating principle of electrochemical sensors is based on the variations of the current or the variation of the electrical properties. These reactions occur generally on the surface of the working electrode of an electrochemical sensor. The electrochemical cells can be composed of two electrodes (the working electrode and the reference electrode) or of three electrodes (the working electrode, the counter-electrode, and a reference electrode).

Electrochemical sensors are classified according to their mode of transduction so we find potentiometric, conductimetric, and amperometric sensors [2, 10]:

- *Potentiometric sensor:* it is based on zero current measuring the difference of potential between the working electrode and the reference electrode. The sensor undergoes potential variations by bringing the material into contact with the species present in the solution. This type of sensor doesn't consume material and doesn't disturb the analyzed environment.

- *Conductimetric sensor:* it is a sensor that measures the ability of a solution to conduct current between two electrodes. In this case, the sensor's response depends on the conduction properties of the studied medium in which it is placed. Generally, it does not modify the environment analysis.

- *Amperometric sensor:* it is a sensor that determines the current caused by the consumption of electroactive species, by oxidation or reduction, present in the solution. The experimental setups are defined in a way that the activity of the electroactive species is proportional to the current. Depending on the models, the material consumed at the measurement electrode is restored or not at the counter electrode. This sensor generally disturbs the analyzed environment.

I.3. Two electrodes and three electrodes electrochemical cell

Speaking about electrochemical sensors, two types of cells can be distinguished as illustrated in Fig.I.2. The first one, which is the simplest one, consists of two main electrodes: the principle one is called the working electrode (WE) which represents the site of the electrochemical reaction. It is composed of a sensitive layer that interacts with the species present in solution. The second one is called a reference electrode (RE), having a constant potential. This type of cell is used in case of static methods when there is no current circulation. The second electrochemical cell, in addition to the mentioned electrodes above, is composed of a third electrode called counter electrode (CE). This cell is used for the dynamic methods when the current circulates in the system. Here, the current flows between the working and the counter electrodes and the reference electrode help in the determination of the potential of the working electrode [11].

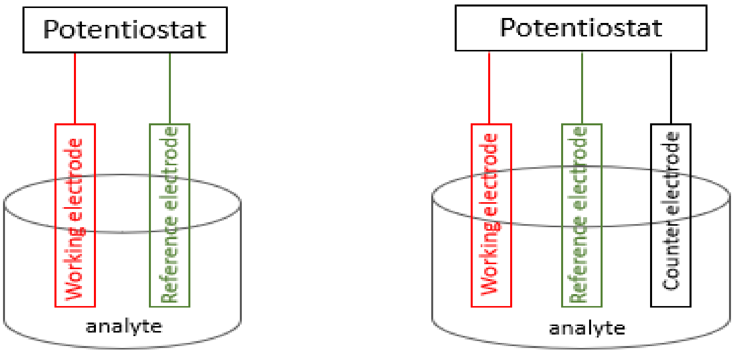

Figure I. 2. Two-electrode (left) and three-electrode (right) electrochemical cells.

One of the most well know commercial three-electrode cell is the screen-printed electrode SPC from DropSens. Generally, commercial devices with three Screen Printed Electrodes (SPE) equipped with a working electrode, an auxiliary electrode and a pseudo-reference electrode, as illustrated in Fig.I.3, are used to manufacture most commun sensors.

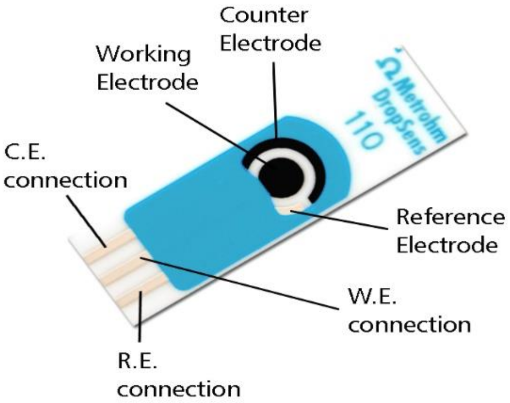

Figure I. 3. Three-electrode Screen-Printed Electrode from DropSens.

The working and counter electrodes can be made from different materials; it can be carbon, gold or platinum. Regarding the gold electrodes, two types can be distinguished: screen printed electrodes with high (AT) and low (BT) temperature curing inks which have different properties. The main difference between these two kinds of electrodes is that, the surface of gold AT type is smooth while the surface of gold BT type is a very porous [12].

I.4. Characteristic parameters

To obtain a reliable chemical sensor, the device must meet specific parameters related to its performance and manufacturing method. The absence of one or more characteristics can be a problem and the sensor can be commercialized only when the problem is solved. For a better comprehension of these features, a definition will be given in the following [4] :

- *Accuracy:* An instrument’s accuracy is defined by the ability of the device in providing a value as near as possible of the real value. It defines the difference in % that can be obtained between the real value and the value obtained in sensor’s output.

- *Sensitivity:* the sensor's sensitivity is defined as its ability in detecting the smallest value's variation of the analyzed analyte. Mathematically, the sensitivity (S) can be expressed as the ratio between the variation of the empirical value R and the variation of the real value E (Eq.I.1)

$$S = \frac{\mathrm{dR}}{\mathrm{dE}} \tag{I.1}$$

  It also represents the slope of the tangent to the calibration curve of the device and it is constant in the case of a linear sensor.

- *Linearity:* the linearity of an instrument is the relation between the output and input signal. The more the trend of this relation approaches a straight line the more the system is said to be "linear".

- *Selectivity:* A chemical sensor is assumed to respond only to the target species of interest. It is the characteristic of chemical sensors that poses the most difficulties during its development. In fact, few are the applications in which the analyzed chemical species are isolated, and generally the examined medium is a complex matrix and other species are present. Their presence can in some cases give a false response so close to the response of the target which gives rise to interference phenomena.

- *Response and recovery time:* the response time of a sensor characterizes the time gap between the moment when the sensor undergoes a change and the time when 90% of the maximum amplitude of the output signal, corresponds to the response of the variation of the target analyte concentration. Recovery time, by analogy with response time, is also defined so that the sensor signal completes 90% of its return path when it is no longer exposed to the analyte species.

- *Stability and reproducibility:* they are the essential properties of a sensor. Stability is defined as the ability of the sensor in providing the same output signal several times during its lifetime when it is exposed to the same concentration of a specific analyte. While reproducibility represents the ability to reproduce the sensor having the same characteristics and performances.

- *Detection limit:* this is a very important feature and generally the lower the limit the better is. But nowadays, we admit that this value must simply meet the application's requirements.

II. Electrochemical methods

The electrochemical methods are analytical techniques used in the study of chemical systems and have been applied for detecting biomolecules in solutions [3]. Generally, these techniques measure the potential, the charge, or the current to determine the analyte's concentration or characterize its chemical reactivity. Taking into consideration the type of the applied electrical signal, we can classify these analyzing techniques into four categories [13]:

- *Potentiostatic method* in which a controlled potential is applied and the current signal is collected.
- *Galvanostatic method*, which is the inverse of the potentiostatic method. The current is applied, and the potential is measured.
- *Potentiometric method* in which the current is zero and the potential is collected.
- *Impedance method*, also called *Electrochemical Impedance Spectroscopy*, in which a specific potential is applied, and the impedance is computed.

In this thesis, potentiostatic methods were used for the electrochemical tests, while electrochemical impedance spectroscopy was used as an electrochemical characterization of the sensor.

A general classification divides the potentiostatic methods into three main subgroups:

- Step potential method (chronoamperometry).
- Scanning potential methods (Linear Sweep Voltammetry LSV and Cyclic Voltammetry CV).
- Pulse potential methods (Differential Pulse Voltammetry DPV and Square Wave Voltammetry SWV).

II.1. Step potential method: Chronoamperometry

Chronoamperometry is an electrochemical technique in which a certain potential is applied to the working electrode, and the current is monitored as a function of time. The oxidation or the reduction of the electroactive species (Eq.I.2) in the chemical reaction takes place exactly when the potential steps from an initial value in which no reaction is occurring to a value that promotes the reaction that has a diffusion nature (Fig.I.4.a).

$$O + ne \longleftrightarrow R \qquad (I.2)$$

To better understand the current-time relationship, the concentration-time function presented in Fig.I.4.b. can be used. This latter relationship presents a concentration gradient so close to the surface of the working electrode. At the beginning of a potential step E_s, the diffusion layer is thin and the concentration gradient is sharp. Over time, the diffusion layer's thickness increases leading to a decrease in the concentration gradient and an exponential diminution of the current (Fig.I.4.c).

The process described is expressed by means of the Cottrell relation (Eq.I.3):

$$i(t) = nFAC^* \sqrt{\frac{D}{\pi\, t}} \qquad (I.3)$$

i = current

n = number of transferred electrons

F = faraday constant

A = electrode surface area

C* = concentration of the analyte

D = diffusion constant

t = time

Therefore, at a given instant time t, the faradic current will depend proportionally on the concentration of the analyte species in the solution. In most cases, the diffusion coefficient (D) of the species can be determined by plotting the i-$t^{-1/2}$ curve and from equation I.3 the area of the electrode can be computed [4, 14].

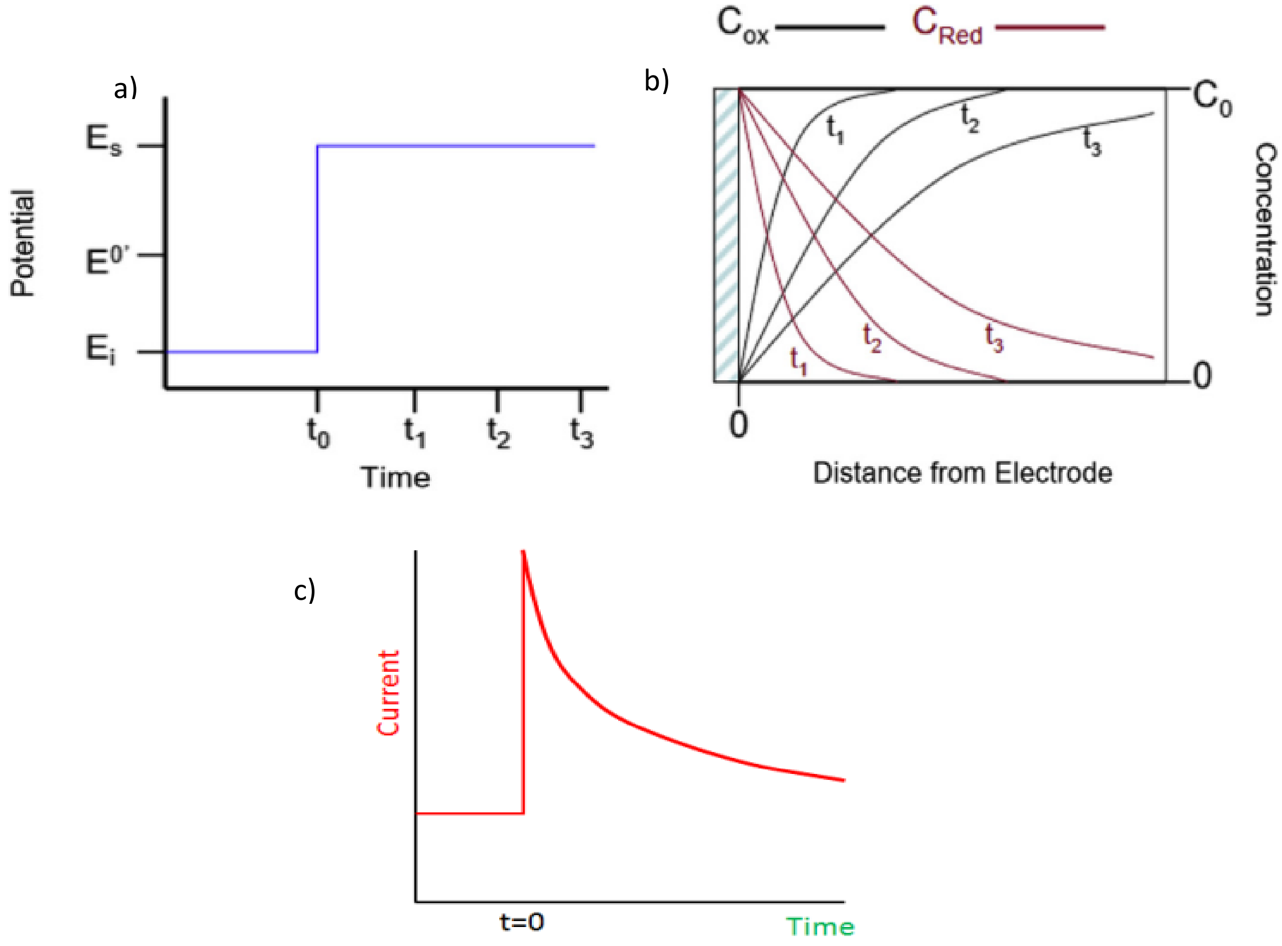

Figure I. 4. a) Potential-time diagram, b) concentration-time relationship and c) current-time response to the step potential.

II.2. Scanning potential methods

II.2.a. Linear Sweep Voltammetry

Considering the way in which the potential is varying over time, this technique is named Linear Sweep Voltammetry (LSV). The potential varies linearly over time (Fig.I.5.a) between an initial value, in which the species in solution are stable, up to a value higher than its discharge value at a suitable scan rate υ [15, 16]. The potential varies according to the following equation (I.4):

$$E(t)=E_i - \upsilon.t \tag{I.4}$$

The scan rate will affect the shape of the i-E characteristic which can be exploited to extract a variety of information about the electrochemical process. Initially, when the potential is very distant from the discharge potential of the electroactive species, no faradic current is recorded. But reaching a value close to the discharge potential, the redox process is activated and the faradic current starts to flow. The obtained i-E curve will have a sigmoidal shape as shown in Fig.I.5.b.

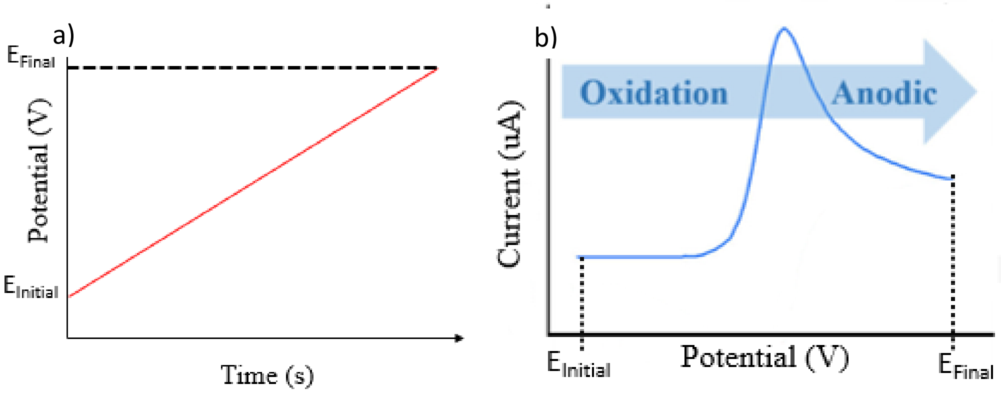

Figure I. 5. a) Potential-time diagram, b) Current-potential response to the potential variation.

II.2.b. Cyclic Voltammetry

Cyclic voltammetry (CV) is one of the most used techniques to acquire qualitative information about the nature of the electrochemical reaction. The peculiarity of this technique lies in the fact that it provides a large number of information while ensuring simplicity of execution and interpretation of the results. Cyclic voltammetry is often used as a preliminary electrochemical investigation, in fact, it offers a rapid identification and localization of redox processes related to the electroactive species of interest [15, 17].

In the previous paragraph, the potential is made to vary in a linear and monotonous way between two potential values. However, in most voltametric analyses, it is preferred to vary the potential according to a triangular wave as shown in Fig.I.6.a. In this way, during the same analysis, it is possible to record the trend of the current cyclically while the potential is varied between a lower value to a higher one (anodic current) and vice versa (cathodic current). The i-E characteristic resulting from this analysis has the same characteristics as the LSV but in this case, it is possible to observe the presence of oxidative and reductive processes affecting the analyte species (Fig.I.6.b) [18].

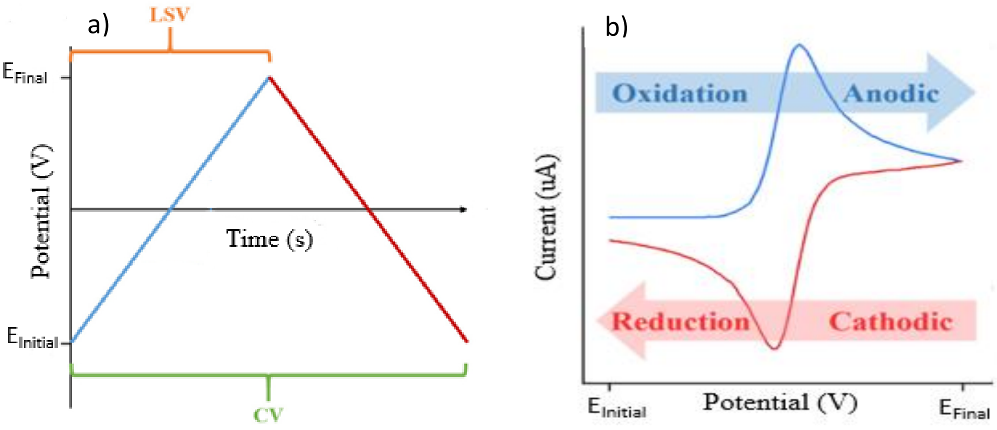

Figure I. 6. a) Potential-time diagram, b) Current-potential cycle.

In this method, a lot of key factors such as the potential range, the scanning direction, the scan rate, and the number of cycles can be changed and providing by that useful information about the mechanism of the electrode process which can be obtained after analyzing their effect on the resulting voltammograms.

II.3. Pulse potential methods

II.3.a. Differential Pulse Voltammetry

Although the cyclic voltammetry method is the most used technique and possesses unique capabilities in the qualitative study of the electrochemical process, sometimes, it has not been very successful in the quantitative study. Differential pulse voltammetry (DPV) allows to limit the capacitive current, caused by the accumulation of the ions in front of the working electrode, by improving its sensitivity and detection limits compared to the common linear scan voltammetry. The typical form of the potential in a certain time interval in the case of differential pulse voltammetry is shown in Fig.I.7.a. This can be thought of as the combination of a linear increase in potential to which pulses of equal intensity are superimposed. The current is sampled twice during each pulse. The first sampling is done an instant before the application of the pulse (i_1 in Fig.I.7.a) and the second just before the end of the pulse (i_2 in Fig.I.7.a). The difference between those two currents Δi is the final reported current obtained in the below voltammogram Fig.I.7.b [5, 19, 20].

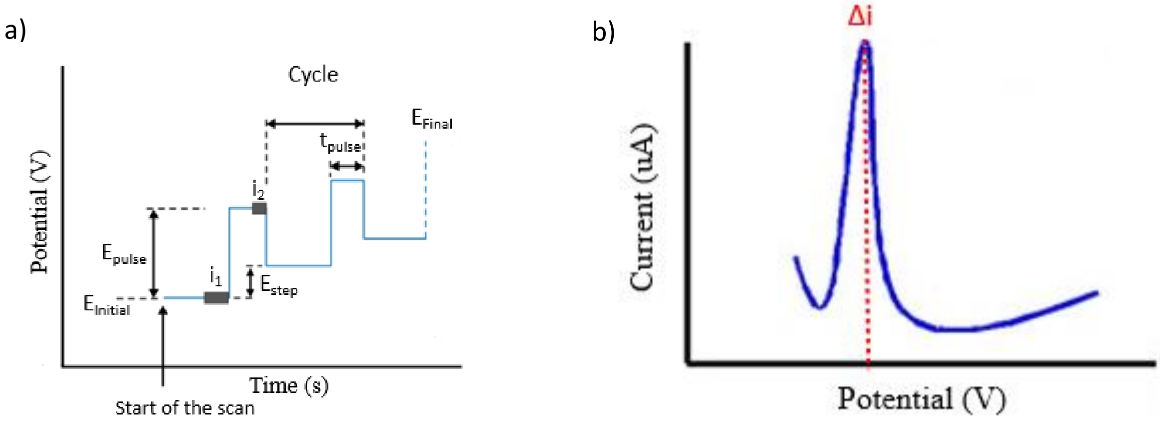

Figure I. 7. a) Potential-time diagram, b) Differential Pulse Voltammetry voltammogram.

II.3.b. Square Wave Voltammetry

This method was invented by Ramaley and Krause [3]. Square wave voltammetry (SWV) combines the advantages of the various potential pulse methods, in fact, it is able to reduce the effects of capacitive currents and guarantee high sensitivity and a low detection limit in a very short execution time.

The typical waveform for the potential in the case of square wave voltammetry is shown in Fig.I.8.a. In this method, the potential pulses are applied successively and without a time gap in a way that there is no time to the working electrode to recover the diffusion layer [21, 22]. Therefore, this characteristic represents the main difference between the DPV and SWV.

The main variables of the SWV are the pulse amplitude ΔE, the pulse width t_p, and the potential step ΔE_S. The pulse width can also be expressed as a function of time, $f=1/2t_p$.

As shown in Fig.I.8.a, the amplitude of the pulse is large, so that its inversion causes the reverse reaction. In other words, since the forward pulse value causes oxidation of the species, the reverse pulse introduces their reduction. The forward current is recorded at the end of the first pulse whose direction agrees with the potential step, the reverse current is instead recorded at the end of the second pulse which has the opposite direction. This means that, in the square wave voltammetry method, the current is sampled twice per each potential cycle.

Figure I.8.b shows the sampled currents variation over time while in Fig.I.7.c, ΔE presents the deduction of the forward currents from the reverse currents and the curve in red in Fig.I.8.c represents the final obtained SWV voltammogram similar to the final DPV voltammogram [21].

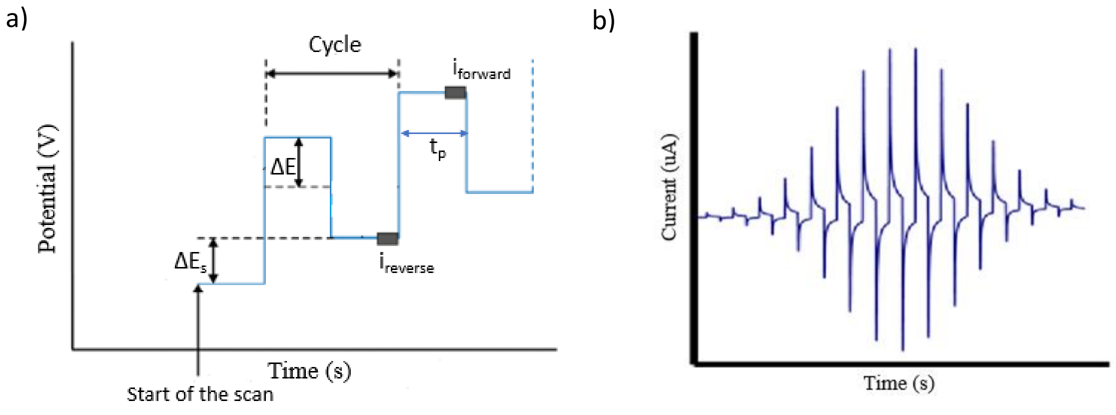

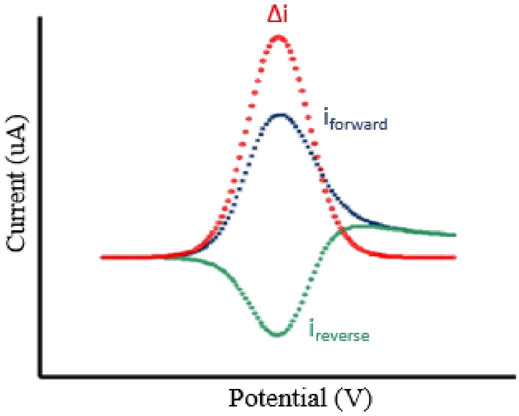

Figure I. 8. a) Potential-time diagram, b) variation of the current over time in the course of the square wave voltammetry, c) typical square wave voltammogram.

III. Two-dimensional materials

Since the early discovery of the chemical sensors, described above in the previous paragraphs, several materials have been used for their development and optimization. Depending on the size of the material, we find the nanodots (0D), nanowires (1D), nanosheets (2D), and bulk crystals (3D). This thesis will focus on the two-dimensional (2D) material and more precisely on transition metals dichalcogenide (TMDs).

III.1. Graphene history and overview of other two-dimensional materials

The era of 2D materials started in 2004, exactly with the discovery of graphene by Andre Geim and Konstantin Novoselov. They were awarded the Nobel Prize in 2010 after demonstrating the peculiar physical properties of this 2D material named graphene, isolated from graphite. Historically, graphene didn't really start at that time. It was first discovered theoretically by Wallace in 1947 and experimentally by Bohem and his group in 1962 who introduced the term graphene for the first time in 1986 [23, 24]. It is composed of a single layer of sp^2 hybridized carbon "C" atoms linked with strong covalent bonds forming a honeycomb structure as shown in Fig.I.9 [25].

The extensive honeycomb network of the graphene is the cornerstone of other important allotropes: once stacked it forms 3D graphite, once rolled it forms 1D nanotubes, and once wrapped it forms 0D fullerenes [25].

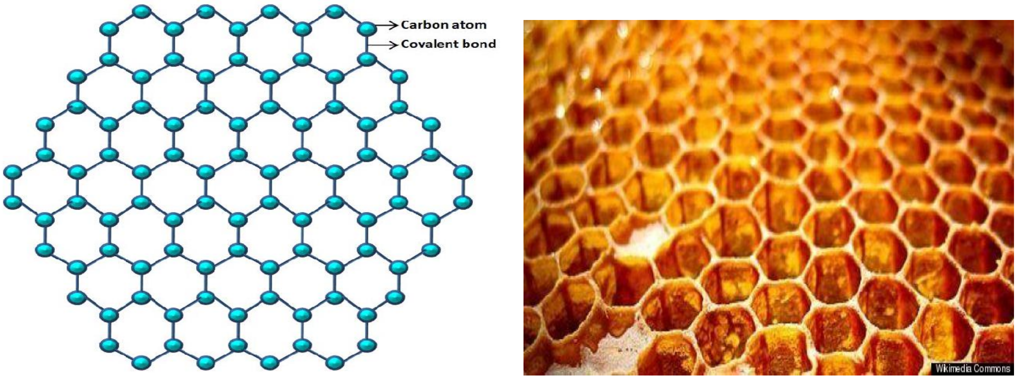

Figure I. 9. Graphene honeycomb structure.

Owning very important properties such high thermal and electrical conductivity at room temperature, strength and large specific surface area benefit graphene results extremely appealing in several research fields [25-27]. However, being a gapless material, graphene cannot be employed for some applications and especially for nanoelectronics applications [28]. Unlike Graphene, other two-dimensional materials can be suitable to overcome this problem.

In addition to graphene, 2D nanomaterials, including individual nanosheets or layered multi-sheet planar materials, have been considered among the most intriguing nanomaterials of the last ten years. These thin 2D nanomaterials have special characteristics and properties that make them different from bulk ones [29-31]. 2D nanomaterials have single or multiple layers with strong in-plane and weak out-plane bonding as atomically ordered networks. In this type of material, the electrons move freely in the 2D plane; while their motion in out of plane direction is limited. These materials are a nanostructures with number of layers ranging from about 10 down to 1 single layer (monolayer). Multi-layered material with considerable thickness will be classified as three-dimension (3D) materials.

In this family, the 2D materials are classified into different subgroups as discussed below:

Firstly, we find the graphene like materials and the best representative of this group is the graphite like *Boron Nitride (BN)*. It was first considered as a synthetic compoud driving from the the chemical reaction between boric oxide and potassium cyanide [32] before they discover the first natural analog of cubic boron nitride [33]. This material is also called “white graphene” due to its similar structure to graphene. In this case, the nitrogen and boron atoms are linked together via covalent bonds while the layers stacking is ruled by Van Der Waals bonds forming the 3D crystals. This material possesses a strong chemical corrosion resistance, a good thermal conductivity, a wide band gap and a high-temperature resistance [34]. Generally, Boron Nitrides exist in three different crystalline structures: graphite-like hexagonal BN (h-BN), diamond- like cubic BN (c-BN), and wurtzite BN (w-BN) but h-BN is the most stable phase under standard conditions [35].

Secondly, we find *Xenes* group. It represents the materials whose main component is only one element, such as borophene, silicene, germanene, stanene, phosphorene (also called black phosphorus), arsenene, antimonene, bismuthene, and tellurene [36]. Xenes have drawn a lot of interest because of their important properties, including their high specific surface area, thin thickness, rapid carrier mobility, adjustable layer-dependent band gaps, and in-plane anisotropy [37].

In addition to the above mentioned groups, we find *MXenes*. Usually, these materials are obtained by selective etching of the A layers from the MAX phase which are ternary carbides or nitrides having the following general formula $M_{n+1}AX_n$: M represents the transition metal, A is a group IIIA or IVA element, X is Carbides C and/or Nitrides N [38]. This subgroup presents good electrical conductivity, thermal stability, and elevated surface area [31].

Also, we find the Transition Metal Dichalcogenides (TMDs) group. This subclass of 2D materials has drawn attention throughout the past few decades. These two-dimensional (2D) compounds are made of transition metals of group 4–10 (such as tungsten, molybdenum, and nickel) and chalcogen elements (such as sulfur, selenium, and tellurium). In general, transition metal compounds in groups 4–7 have layered structures, whereas those in groups 8–10 have non-layered structures (one exception is

$PtSe_2$). They have gained significant attention in recent years due to their unique physical and chemical properties, which make them promising for a wide range of applications, including electronics [39], supercapacitors [40], catalysis [41], and sensors [42, 43]. Due to their easily tunable properties, TMDs have attracted the greatest attention in the sector of electrochemical sensors.

III.2. Two-dimensional (2D) materials structures

Two-dimensional materials can be found in different shapes and morphologies [32] (Fig.I.10.) such as (a) Nano island structure [44], (b) branched nanostructures [45], (c) nanoplates [46], (d) nanosheets [47], (e) nanowalls [48], and (f) nanodisk [49].

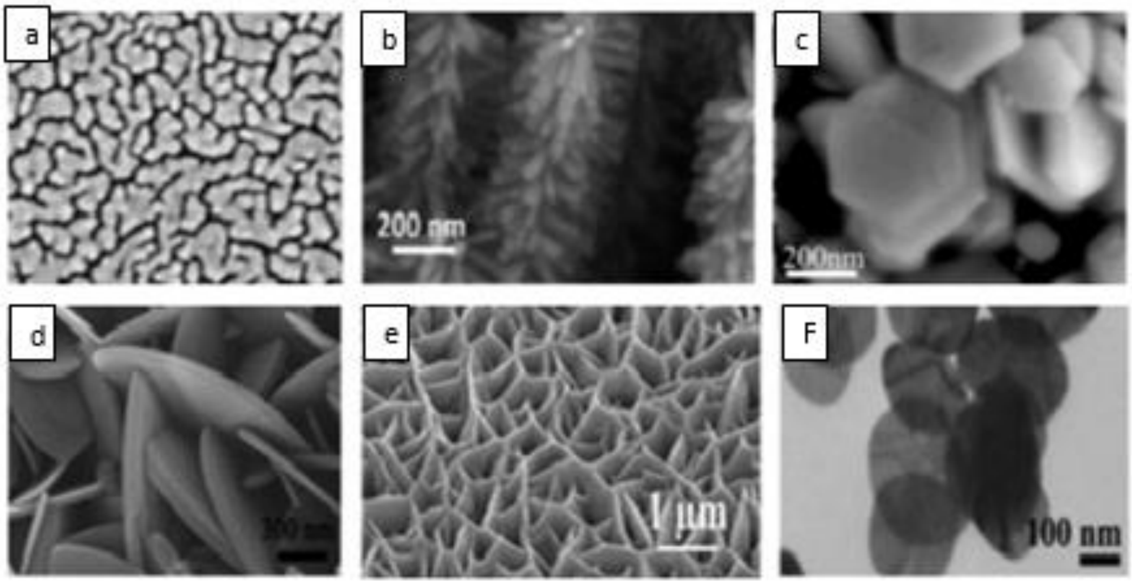

Figure I. 10. Different 2D materials structures: (a) Nano Island structure, (b) branched nanostructures, (c) nanoplates, (d) nanosheets, (e) nanowalls, and (f) nanodisks [32]..

III.3. General properties of two-dimensional materials

2D materials occupy the attention of researchers in different fields because of their extraordinary properties. Here are presented some of the most famous properties.

First, they are optically transparent. Also, 2D materials exhibit unique properties due to their ultra-thin nature, typically consisting of a single layer or a few layers of atoms arranged in a planar structure. They have a thickness of just one or a few atomic layers, typically ranging from a few angstroms to a few nanometers. Due to their thinness, they have a high surface area compared to their volume. This high surface-to-volume ratio can lead to enhanced surface interactions and enables unique surface-dependent properties. They can also lead to quantum confinement effects, where the electronic and optical properties of the material are influenced by the size and shape of the material at the nanoscale. In addition to that, 2D materials are inherently flexible and can be bent, stretched, and twisted without losing their structural integrity. This property makes them suitable for flexible electronics and wearable devices. Despite being atomically thin, some 2D materials can exhibit remarkable mechanical strength and stiffness. Graphene, for example, has an incredibly high tensile strength and Young's modulus. Several 2D materials present excellent electrical conductivity, making them highly suitable for electronic and optoelectronic applications and possess high thermal conductivity due to the strong covalent bonding between atoms in the plane. This property makes them promising for thermal management applications. The exposed surface of 2D materials can exhibit high reactivity due to the absence of bulk atoms. This reactivity can be harnessed for various catalytic and sensing applications. Some 2D materials, such as transition metal dichalcogenides (TMDs), exhibit layer-dependent properties. The bandgap of 2D transition metal disulfides (TMDs) (ranging between 1-2 eV) changes with the number of layers, allowing for tunable electronic properties.

In addition, under ambient conditions, 2D materials show important stability in contrast with 3D materials which give rise to strong interaction with ambient gases [50]. Also, the two-dimensional electron confinement of ultra-thin 2D nanomaterials makes it possible to obtain very convincing electrical properties compared to other nanomaterials [29].

III.4. Different synthesis methods of two-dimensional materials

Several synthetic methods have been reported in the literature for the preparation of two-dimensional materials. One of the requirements for creating dependable electrochemical sensors and utilizing their commercial applications is the manufacturing of high-quality, scalable, and cost-effective layered nanomaterials. The techniques used to create few layered nanosheets can typically be split into two categories: “bottom-up” and “top-down.” Both chemical and physical techniques have been developed for “bottom-up” growth [31]. Below is a quick definition of the most popular preparation methods.

III.4.a. Bottom-up techniques

❖ Pulsed Laser Deposition

Pulsed Laser Deposition (PLD) works as follows: a target, that is put near the substrate, is vaporized within the vacuum chamber using a high-power laser (Fig.I.11). Therefore, since it is quick, inexpensive, and extremely dependable, this approach was used in the synthesis of various 2D Mo-based materials. Despite all these benefits, PLD-deposited layers of materials have high defect rates and inconsistent coverage, making them poorly suited for the development of large-scale films [51].

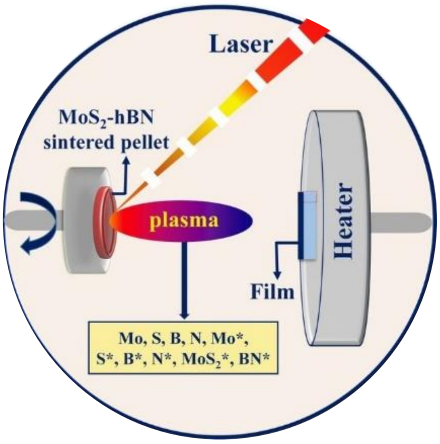

Figure I. 11. Pulsed Laser Deposition process.

❖ Spray pyrolysis

This procedure consists in vaporizing a solution containing the reactive precursors and after that spraying it onto the substrate using a nebulizer. Then, the substrate is kept at a high temperature, which enables the precursor reactions to begin on the substrate surface and result in the formation of a film. The procedure may be carried out in a reaction chamber with a vacuum or in the air (Fig.I.12). The sprayer parameters, furnace, and substrate temperature are controlled in this approach to determine the metrology parameters of the deposited film [52].

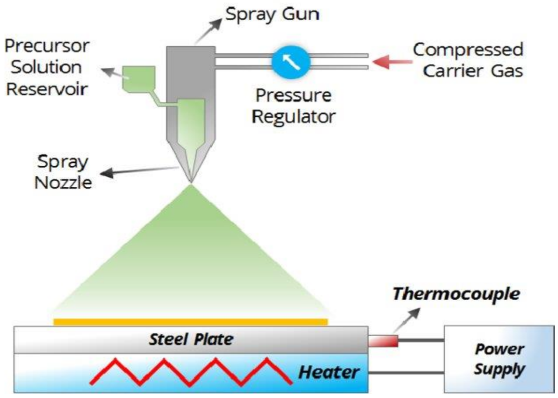

Figure I. 12. Spray pyrolysis principle.

❖ Chemical Vapor Deposition

Chemical vapor deposition (CVD) is a process by which a solid material is deposited by a gas/vapor phase from a chemical process that reacts and /or decomposes on the surface of the heated substrate (Fig.I.13). Currently, this technique is one of the best for graphene prepration on large areas. Varying the experimental conditions, the substrate, its temperature, the composition of the of reaction gas, the flow of gas, or its pressure, different materials can be grown in composition and morphology. The ability to achieve rapid growth rates, deposit materials that are difficult to evaporate, and produce epitaxial layers, makes this approach particularly valuable even if it is not ideal for the large-scale production of 2D materials or for a mixture of materials. Additionally, it exhibits excellent repeatability. Despite these intriguing benefits, CVD equipment is complex, necessitating frequently high temperatures as well as some utilization of hazardous and corrosive gases [53].

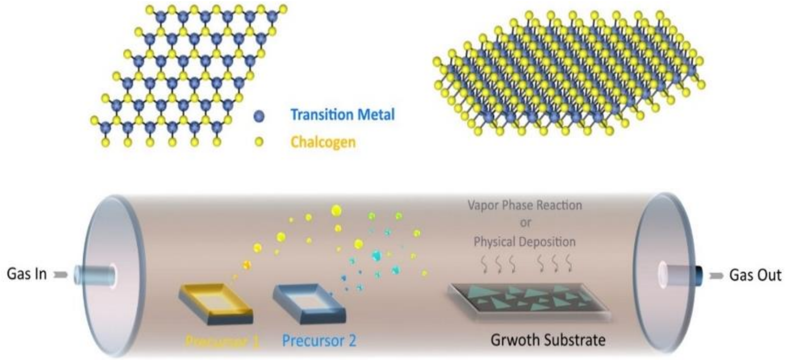

Figure I. 13. Chemical Vapor Deposition process

- ❖ Atomic Layer Deposition

Atomic Layer Deposition (ALD) is based on the exploitation of chemical reactions that take place between reagents in a gas phase. The successive reactions of the reactant precursors on a substrate's surface result in the formation of a thin layer. This technique is also utilized to create a controlled thickness of 2D layered materials (Fig.I.14). High-quality films, conformity, and low-temperature processing are the main benefits of this method. However, it also has several drawbacks, including the long time for the chemical processes to develop and the waste of material [54].

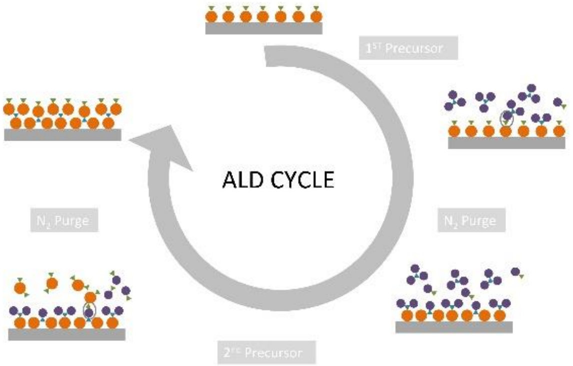

Figure I. 14. Atomic Layer Deposition process.

III.4.b. Top-down techniques

- Chemical etching and chemical intercalation

MXenes are mostly obtained using chemical etching or intercalation technique. These compounds are made using layered ternary carbides and nitrides, often known as MAX, in one or more atomic layers. The single A layers, which are mostly made of aluminum, are etched to produce MXenes using hydrofluoric acid (HF) or other chemical etching solutions [31]. In the case of chemical intercalation, Small-radius cations, such as K^+, Li^+, Na^+, Cu^{2+}, intercalate into the space between bulk crystals to help in separating the layers of the bulk from each other (Fig.I.15). This intercalation increases the interspacing, causing the weakening of the Van der Waals neighboring layers of bulk crystals leading at the end to a full separation of the layers [55].

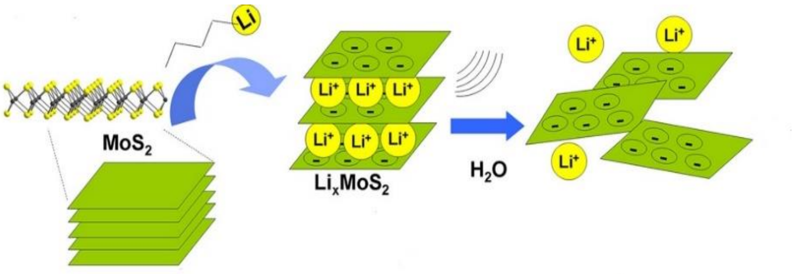

Figure I. 15. Chemical intercalation using Lithium ions.

- Mechanical exfoliation

The simplest and least expensive approach is the mechanical exfoliation (ME), sometimes referred as the scotch tape method. It was successfully developed in 2004 by Geim and Novosclov when they isolated for the first time graphene [23]. Since then, this process has grown in popularity and is the least harmful when compared to other two-dimensional materials preparation methods. With the use of adhesive tape, this mechanical process simply peels off one or few layer from the bulk crystal (Fig.I.16), which naturally has numerous layers linked with Van der Waals bonds [56].

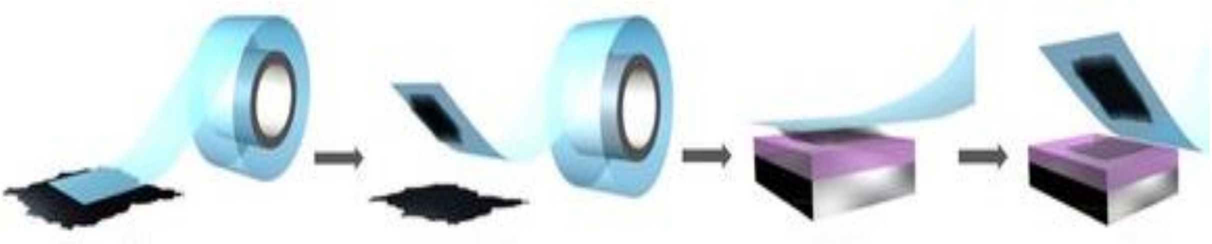

Figure I. 16. Mechanical exfoliation technique

- Liquid Phase Exfoliation

With an excellent balance between quality and cost, liquid-phase exfoliation (LPE) is the primary method for developing two-dimensional materials. Both the academic and industrial sectors have extensively used LPE. Simply, as illustrated in Fig.I.17, this method produce 2D nanosheets by ultrasonication of a bulk material previously dissolved in a liquid media [57]. In most cases, the force produced by ultrasound, the nature of the liquid media, and the speed of centrifugation, which is used to better separate the bigger flakes from the smaller ones, have been widely considered the main causes of the fragmentation and exfoliation of the bulk material into nanosheets [58].

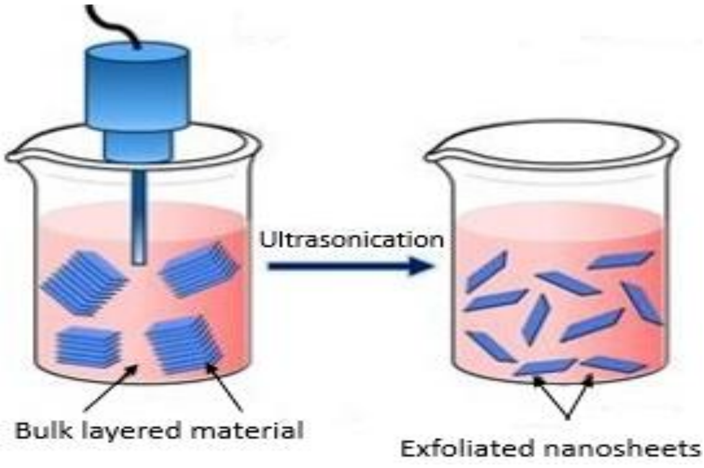

Figure I. 17. Liquid Phase Exfoliation mechanism.

III.5. Applications of two-dimensional materials

As already discussed above, the outstanding electronic, optical, and mechanical properties of 2D materials have gained significant attention in many application fields. Here are some of their potential applications:

- *Electronics:* 2D materials such as graphene, transition metal dichalcogenides (TMDs), and black phosphorus have high electron mobility, which enables fast switching of devices. Graphene has been used to make transistors, while TMDs have been used to make photodetectors and memory devices [59].
- *Optoelectronics:* TMDs are semiconductors with direct bandgaps, which makes them attractive for optoelectronic devices such as LEDs and photovoltaic cells [59].
- *Energy storage:* 2D materials such as graphene and transition metal dichalcogenides (TMDs) have been explored for their potential in energy storage applications such as batteries and supercapacitors. They have high surface area and high conductivity, which can improve the energy storage capacity of these devices in addition to their ability to adsorb ions [60].
- *Catalysis:* 2D materials have high catalytic activity due to their unique electronic and chemical properties. They can be used as catalysts in a wide range of reactions, including water splitting, hydrogen evolution, and carbon dioxide reduction [61].
- *Sensing:* 2D materials have high sensitivity to their environment, which makes them promising candidates for sensing applications. They have been used to make gas sensors, biosensors, and chemical sensors [29, 62].
- *Biomedical applications:* 2D materials have also been explored for their potential use in biomedical applications. Graphene and TMDs have been investigated for their potential use as drug delivery vehicles, while black phosphorus has been explored for its antibacterial properties [63].

- *Wearable electronics:* Due to their flexibility, TMDs have been explored for use in wearable electronics. They have the potential to make lightweight, flexible, and stretchable electronic devices [39].

Overall, 2D materials have a wide range of potential applications in electronics, optoelectronics, energy storage, catalysis, sensing, and biomedical applications. Their unique properties and versatility make them promising candidates for a wide range of technological applications [52, 54, 61, 62, 64].

IV. Transition Metals Dichalcogenides and introduction to Molybdenum disulfide MoS_2

As previously mentioned, two-dimensional materials are becoming a leading class of materials for making contemporary electronic devices and 2D layered transition metal dichalcogenides play a role of particular importance. Figure I.18. shows the possible layered and non-layered structures of TMDs materials and we can find over 40 different types of transition metals dichalcogenides with MX_2 as a stoichiometry.

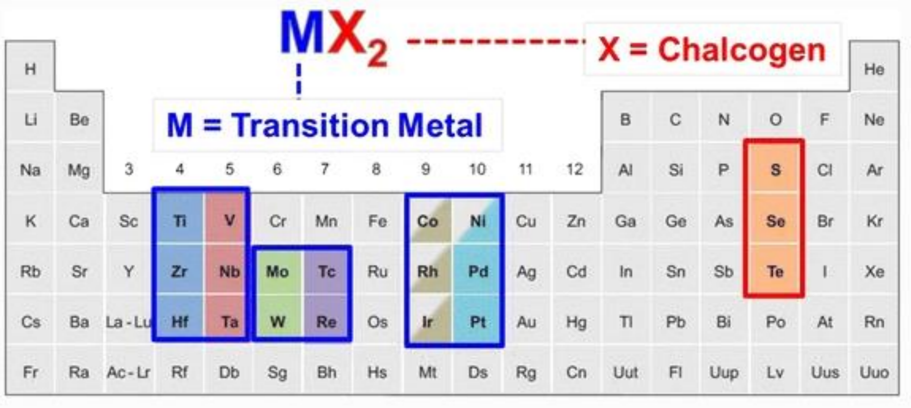

Figure I. 18. Periodic table.

In the bulk TMDs, layers of Metal atoms are arranged in a hexagonal network sandwiched between two layers of chalcogen [61]. The intralayer is kept by a strong covalent bond while the interlayers are assembled by Van der Waals interactions that can be easily separated. However, despite the fact that this family of 2D materials have a similar structure to the other 2D subclasses, in terms of electrical conductivity they present a wide range, in fact they span from insulators like HfS_2 to semiconductors like MoS_2 and semi-metals like WTe arriving to true metals like NbS_2 [65].

Among this 2D TMDs, Molybdenum disulfide (MoS_2) is the most known [53, 66]. Researchers are putting a lot of effort in the study of 2D MoS_2, especially because of its capabilities and adaptability for a variety of applications. Being an inorganic compound composed of molybdenum Mo and sulfur S, MoS_2 exists in the nature in the form of molybdenite, a crystalline mineral or jordisite.

IV.1. Molybdenum disulfide MoS_2 poly-types

The 2D-MoS_2 (TMDCs) exists in three possible poly-types, which are 1T, 2H and 3R (Fig.I.19). Digits represent the number of layers in the crystallographic unit cell, while letters display the symmetry so that H = hexagonal structure, R = rhombohedral structure and T = tetragonal structure.

- *1H-MoS_2 structure*

1H-MoS_2 structure is the first 2D material artificially created and considered as a stable structure. It is a semiconductor with a band gap around 1.9 eV. It represents one repetition of the layer having hexagonal symmetry and Mo atom are sandwiched between two trigonal atomic layers of S atoms (Fig.I.19.a).

- *1T-MoS_2 structure*

The 1T-MoS_2 structure is a new metastable metallic modification of molybdenum disulfide (Fig.I.19.b). It represents one repetition of the layer having tetragonal symmetry with octahedrally coordinated Mo and S atoms.

- *2H-MoS_2 structure*

Concerning the 2H-MoS_2 structure (Fig.I.19.c), it is a semiconductor with a band gap ranging between 1.2 eV and 1.3 eV. It represents two repetitions of the layer having hexagonal symmetry and the coordination between Mo and S is trigonal prismatic.

- *3R-MoS_2 structure*

Finally, the 3R-MoS_2 structure (Fig.I.19.d) has regular layered structures with trigonal prismatic coordination of Mo atoms by the S atoms, similarly to 2H polytope. Rhombohedral symmetry is present in 3R-MoS_2, which has three layers stacked along the c-axis and considered as a metastable structure [61, 65, 67, 68] .

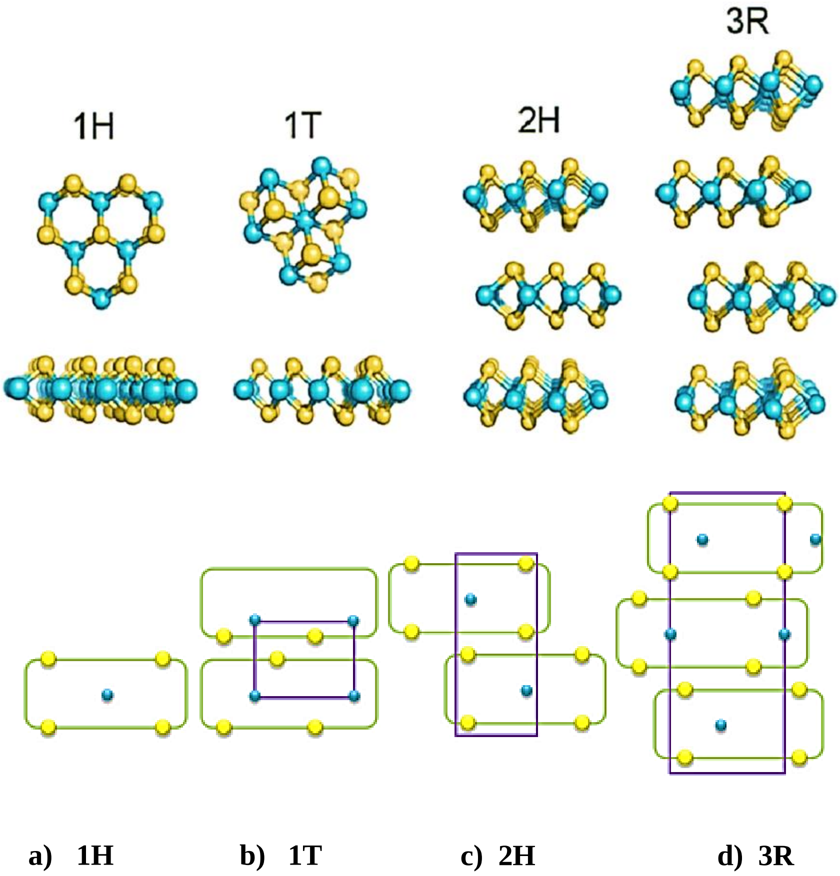

a) 1H **b) 1T** **c) 2H** **d) 3R**

Figure I. 19. Schematic drawing of common MoS_2 poly-types.

IV.2. Molybdenum disulfide MoS_2 properties

- *Electronic band structure of MoS_2*

Understanding the electrical process in various electronic devices requires knowledge of electronic band structure. It is known that the graphene electronic band diagram displays a zero-band gap and linear energy dispersion around the K point. Since graphene has a gapless electrical band structure, it can’t be used in many applications. Here, one of the most fascinating properties of the MoS_2 is its electronic band structure. Figure I.20, depicts the electronic band structure of bulk and monolayer MoS_2. For bulk MoS_2, an indirect band gap of 1.2 eV is created by the valence band maximum (VBM) positioned at the Γ point and the conduction band minimum (CBM) situated halfway in the Γ- K direction.

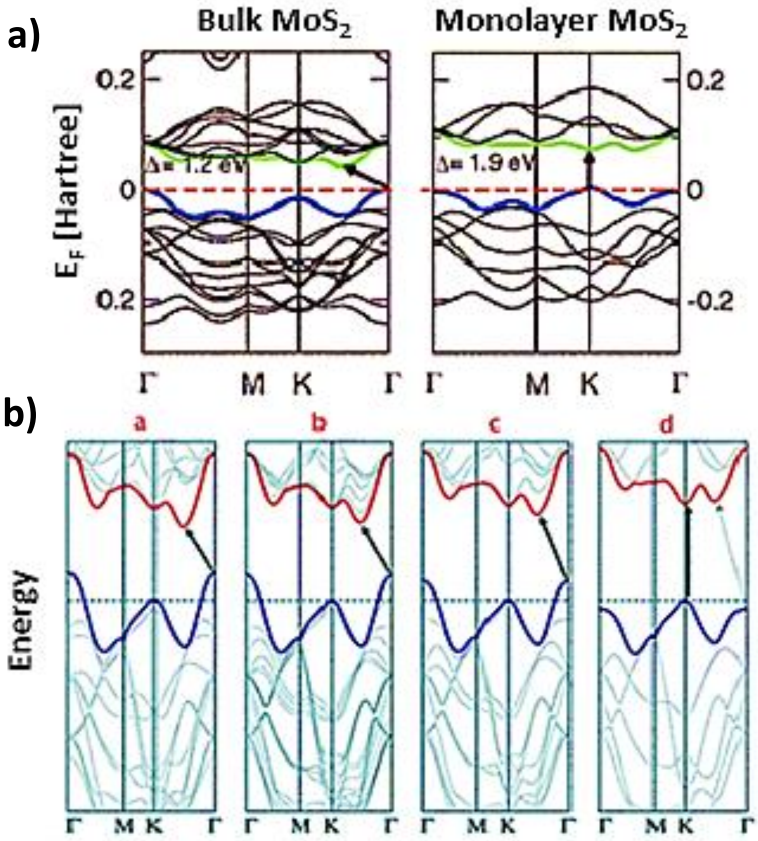

Figure I. 20. a) Band structure of bulk and monolayer MoS_2, b) transition from bulk to monolayer MoS_2: (a)bulk MoS_2, (b) quadrilayer MoS_2, (c) bilayer MoS_2, and (d) monolayer MoS_2 [69].

Looking to the monolayer band structure of MoS_2, together the conduction band, situated between Γ and K point, and the valance band, positioned at the Γ point, changes in a way that expands the indirect excitonic transition and establishes a straight K-K band transition giving rise to a direct band gap of around 1.9 eV. Comparing the different band structures of MoS_2, it is noted that the direct excitonic bands at K Brillouin point remain unchangeable going from bulk to monolayer [53].

- *Mechanical properties of* MoS_2

Molybdenum disulfide (MoS_2) is a two-dimensional material with unique mechanical properties. Its first key mechanical property is Young's modulus which is expressed in Pascal (Pa) as it defined the ratio between strain (Γ) and stress (σ) following the equation (I.5.):

$$E = \frac{\sigma}{\Gamma} \tag{I.5}$$

The Young's modulus of MoS_2 is in the range of 270-290 GPa, that changes according to the number of layers, which is comparable to that of steel [64]. This makes it a suitable material for applications where stiffness is required.

- *Optical properties of* MoS_2

When excited with light, 2D-MoS_2 emits light in the visible range. The photoluminescence spectrum of MoS_2 exhibits a peak at around 1.85 eV, which corresponds to the bandgap energy. The peak position can shift depending on the number of layers and the presence of defects [70]. Also, some other properties can be directly extracted from the UV-Vis spectrum of the MoS_2 such as nanosheets concentration, lateral size, and the thickness which refers to the number of layers [71, 72].

IV.3. Molybdenum disulfide based heterostructures

After the discovery of this revolutionary transition metal dichalcogenide, several materials have been used in combination with molybdenum disulfide studying by that the changes introduced in its properties. Due to their enormous surface area and ease of functionalization with other functional groups, MoS_2 nanosheets are attractive building blocks for the creation of nanohybrids together with graphene, Nobel metal nanoparticles and metal oxides. Herein, we will limit ourselves presenting only some of the most famous combinations. Firstly, molybdenum disulfide has been widely used together with graphene, graphene oxide, and reduced graphene oxide [73]. Due to the ultrathin structure of graphene, the integration of graphene-based materials offers a number of benefits, including enhanced conductivity, electron transfer rate, and/or higher surface-to-volume ratio. A further advantage of this exceptional substance is its capacity to be functionalized with heteroatoms, other molecules, or functional groups. The amount of oxygen functional groups in a material has a significant impact on its electrical and chemical characteristics [74-76]. Secondly, a lot of studies have been reported the combination 2D-MoS_2/Nobel metals studying the properties of these nanohybrid structures. Moreover, nanohybrid demonstrated strong electrocatalytic activity for the oxidation of different biological molecules such as glucose [77] and other food safety application such as the detection of nitrite in food and drink industry [78]. It is reported that it exhibits better electrocatalytic ability than pure Nobel metal and pure 2D-MoS_2 [78, 79]. In addition to graphene-based materials and Nobel metals nanohybrids, molybdenum oxide together with molybdenum disulfide form a fascinated heterostructure for multiple applications [80]. In fact, in the last few years, molybdenum oxide (MoO_x) nanomaterials have been proposed for many applications thanks to their physical, electrical, and chemical properties. Different molybdenum oxides are among the most versatile electronic oxides and also find applications in catalysis, sensors, biosystems, and so on [31]. These compounds present various stoichiometries, ranging from full stoichiometric MoO_3 as well as MoO_{3-x}, where $2 < x < 3$, and eventually semi-metallic MoO_2. One of the main differences between these two types of MoO_x is the bandgap, in which MoO_3 has the wider one which is about 3.2 eV. Usually, MoO_3 is found in three different crystalline structures: orthorhombic, monoclinic, and hexagonal phases, whereas MoO_2 crystalizes in the monoclinic structure. MoO_3 nanosheets have unique outer-d valence electrons which can be exchanged in electrochemical reactions. However, as the degree of reduction increases, the lattice may collapse and the layered structure is lost [31, 81]. Taking into consideration all these crucial properties, the heterostructure sulfide/oxide seems to be very successful [82]. These systems have been reported to improve the electrical properties, enhancing the supercapacitor performance, the storage properties and hydrogen evolution. Hybrid MoO_3/MoS_2 composites reveal more satisfying electrochemical properties than pure MoO_3 and MoS_2 [80].

V. Biomedical analytes

As mentioned in the previous paragraphs, 2D materials and especially transition metals dichalcogenides were widely used in the field of sensing due to their crucial properties. This material has been widely used for the development of several biosensors [83]. In this thesis work, Molybdenum disulfide MoS_2 based electrochemical sensors were developed for the investigation of amino acid, such as tyrosine, neurotransmitters, like dopamine, vitamins, including riboflavin and folic acid, and body waste product like uric acid.

V.1. Tyrosine

Tyrosine (Tyr, 4-hydroxyphenylalanine, Fig.I.21) is an aromatic amino acid. The normal range for tyrosine concentration in the blood plasma is typically around 38-100 μmol/L [84]. It's worth noting that these values are approximate and can vary between different sources and laboratories. It is a fundamental component of proteins and is essential for creating and preserving a favorable nitrogen balance in the human body. Additionally, it is a precursor amino acid for significant neurotransmitters in the central nervous system such as dopamine, which are crucial for humans and help in regulating brain functioning as well as the production of the thyroid hormones. Therefore, it serves as a biomarker for the early identification of certain brain disorders [85]. Furthermore, it helps in maintaining a healthy skin since it is involved in the production of melanin, the pigment that gives skin its color [86]. Some studies have suggested that tyrosine supplements may help to protect the skin from UV damage and it was proved that low level of Tyr could cause albinism whereas, a high level induces Parkinson's disease, depression, and mood disorders [85, 87].

Also, Tyr has been shown to improve cognitive performance, particularly in situations that are mentally demanding or stressful by helping people to improve their attention, focus, and working memory and it has a potential in reducing the effects of stress and anxiety. It may help to improve mood and reduce the physical symptoms of stress, such as elevated heart rate and blood pressure and in this case, it may help to reduce the perception of fatigue during exercise, which can allow individuals to enhance their exercise performance. Food rich in Tyr, including cheese, egg, and yogurt, are indeed used in tyrosine-deficient individuals' diets.

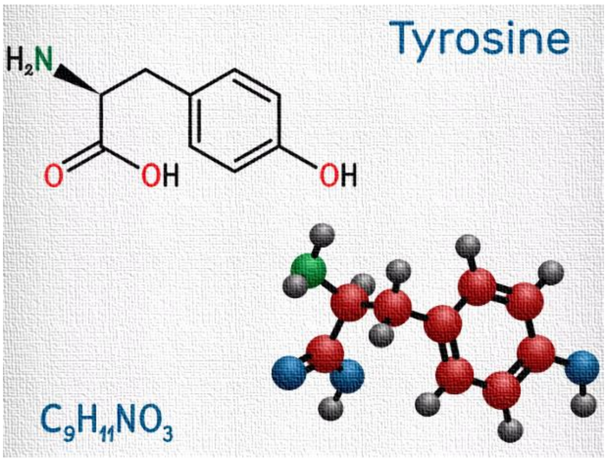

Figure I. 21. Chemical formula, 3D conformer, and molecular structure of Tyrosine.

V.2. Dopamine

Dopamine (DA) is a primary neurotransmitter [88], which is a chemical messenger in the brain that transmits signals between neurons. It is primarily synthesized from Tyr through a series of enzymatic reactions. It is a catecholamine, a type of organic compound that contains a catechol and an amine group (Fig.I.22). Dopamine is synthesized in the brain and is involved in many functions. First, DA is often associated with the brain's reward system, and is involved in the experience of pleasure. It is released in response to pleasurable stimuli such as exercising and drugs, providing people a sense of fulfillment that drives them to addiction. In fact, schizophrenia and high dopamine levels in the brain are related and that’s why specific medications are administrated to treat and control hallucinations caused by the increase of DA in the body [88]. Also, it plays a role in regulating mood disorders. Parkinson's disease results in the death of dopamine-producing neurons in the brain. That’s why, patients can take DA supplements as well as inhibitors of the enzymes that break down dopamine to make up for their lack of it [85]. Additionally, it is also involved in motivation and goal-directed behavior and helps to facilitate the processing of information in the brain and the formation of memories. DA levels in the human body can vary depending on different factors, and there isn't a fixed concentration that can be universally stated.

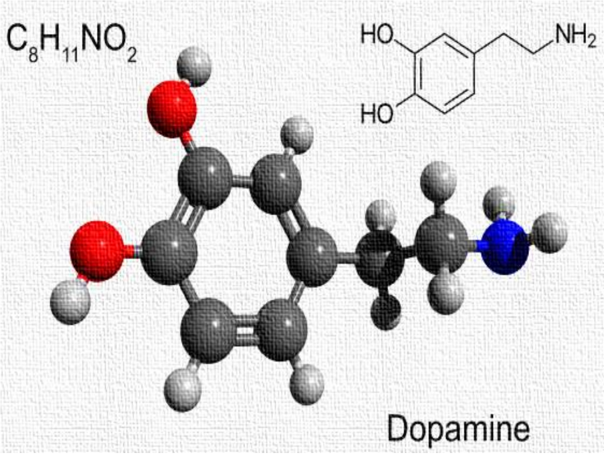

Figure I. 22. Chemical formula, 3D conformer, and molecular structure of Dopamine.

V.3. Riboflavin

Riboflavin (RF), also known as vitamin B2 (Fig.I.23), is a water-soluble vitamin that plays an important role in the body's metabolism [89]. It is one of the essential B-complex vitamins, which means that it cannot be produced by the body and must be obtained through the diet. The normal range for plasma riboflavin levels is typically considered to be around 6.2-39 nmol/L [90]. Riboflavin is involved in several metabolic pathways, including the conversion of carbohydrates into energy, so that it allows to maximize the energy available to the body and aids in muscle recovery, and the metabolism of fats and proteins [89]. It is also important for the maintenance of healthy skin, eyes, the nervous system and it supports proper thyroidal and suprarenal gland function, promoting hormone at their ideal levels. In addition to that, its anti-aging effects, its antioxidant properties enable the detoxification of the liver. Additionally, redox reactions, which involve the transfer of electrons, provide the bulk of the energy generated within the body. Flavoenzymes, which are coenzymes generated from riboflavin, take part in redox reactions in this process. For instance, Flavin Adenine Dinucleotide (FAD) is a component of the electron transport (respiratory) chain, which is essential for the creation of energy [91, 92].

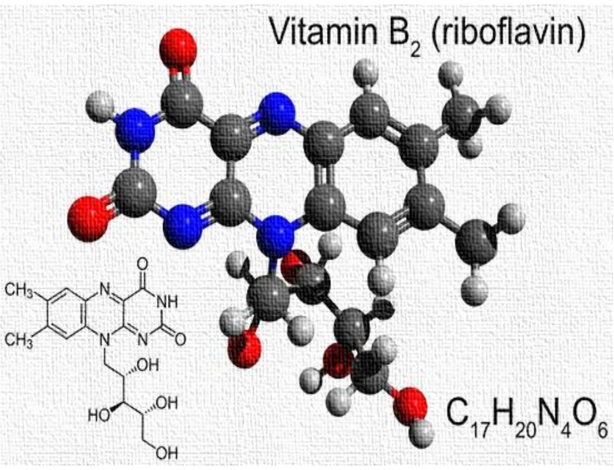

Figure I. 23. Chemical formula, 3D conformer, and molecular structure of Riboflavin.

V.4. Folic acid

Folic acid, also known as folate or vitamin B9 (FA, Fig.I.24), is a water-soluble vitamin that is important for many bodily functions, including the production of red blood cells and DNA synthesis. The normal range for serum or plasma folic acid levels is typically considered to be around 0.23-1 μmol/L [93]. It is essential for the proper growth and development of the body, especially during pregnancy. Folate is found naturally in many foods, such as leafy green vegetables, fruits, and beans. It can also be found in fortified foods, such as breads and cereals. However, it can be difficult to get enough folic acid through diet alone, which is why many people take folic acid supplements. In fact, it is particularly important for women who are pregnant or planning to become pregnant, as it can help prevent birth defects in the baby's brain and spine. As any other type of vitamin, high doses of folic acid can mask symptoms of vitamin B12 deficiency, which can lead to nerve damage if left untreated [94].

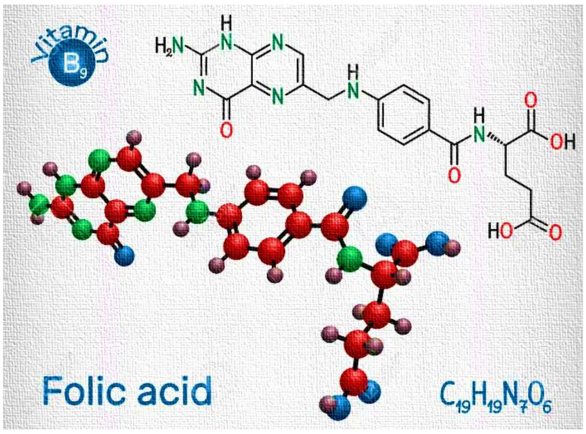

Figure I. 24. Chemical formula, 3D conformer, and molecular structure of Folic Acid.

V.5. Uric Acid

Uric acid (UA, Fig.I.25) is a natural waste product produced by the breakdown of purines, which are substances found in many foods and in the body's own cells. Normally, it is dissolved in the blood and excreted by the kidneys in the form of urine. The normal range for uric acid levels in the blood can vary slightly between different sources and laboratories, but it is generally considered to be around 310-630 µmol/L for men and 230-530 µmol/L for women [95]. However, when the body produces too much uric acid or the kidneys are unable to eliminate it effectively, it can build up in the blood and lead to kidney stones, chronic kidney disease, and may also be a risk factor for cardiovascular issues, as well as for insulin resistance and type 2 diabetes. In this work, UA was essentially used in the selective test as it is the most famous interferent biomolecule in the electrochemical studies [96].

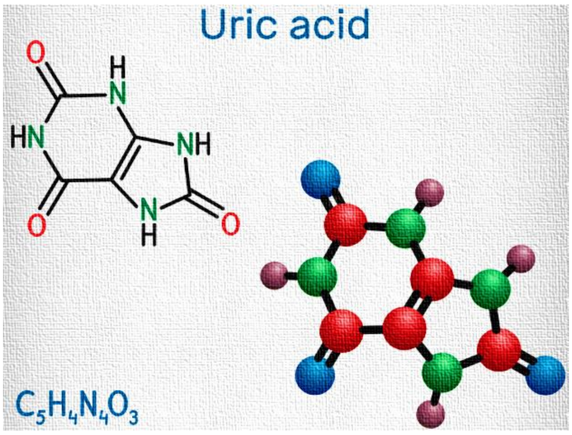

Figure I. 25. Chemical formula, 3D conformer, and molecular structure of Uric Acid.

References

1. Hulanicki, A., S. Glab, and F. Ingman, *Chemical sensors: definitions and classification.* Pure and applied chemistry, 1991. **63**(9): p. 1247-1250.
2. Baranwal, J., et al. *Electrochemical Sensors and Their Applications: A Review*. Chemosensors, 2022. **10**, DOI: 10.3390/chemosensors10090363.
3. Bard, A.J. and L.R. Faulkner, *Fundamentals and applications.* Electrochemical methods, 2001. **2**(482): p. 580-632.
4. Ensafi, A.A., *Chapter 1 - An introduction to sensors and biosensors*, in *Electrochemical Biosensors*, A.A. Ensafi, Editor. 2019, Elsevier. p. 1-10.
5. Simões, F.R. and M.G. Xavier. *6 – Electrochemical Sensors*. 2017.
6. Maduraiveeran, G., M. Sasidharan, and V. Ganesan, *Electrochemical sensor and biosensor platforms based on advanced nanomaterials for biological and biomedical applications.* Biosensors and Bioelectronics, 2018. **103**: p. 113-129.
7. Gan, T. and S. Hu, *Electrochemical sensors based on graphene materials.* Microchimica Acta, 2011. **175**(1): p. 1-19.
8. Moro, G., K. De Wael, and L.M. Moretto, *Challenges in the electrochemical (bio)sensing of nonelectroactive food and environmental contaminants.* Current Opinion in Electrochemistry, 2019. **16**: p. 57-65.
9. Smart, A., et al., *Screen-printed carbon based biosensors and their applications in agri-food safety.* TrAC Trends in Analytical Chemistry, 2020. **127**: p. 115898.
10. Bakker, E. and M. Telting-Diaz, *Electrochemical Sensors.* Analytical Chemistry, 2002. **74**(12): p. 2781-2800.
11. Rouessac Francis, R.A., *Chemical Analysis: Modern Instrumentation Methods and Techniques*. 2nd ed.
12. *DropSens*. Available from: https://www.dropsens.com/en/screen_printed_electrodes_pag.html.
13. Vogiazi, V., et al., *A Comprehensive Review: Development of Electrochemical Biosensors for Detection of Cyanotoxins in Freshwater.* ACS Sensors, 2019. **4**(5): p. 1151-1173.

14. Inzelt, G., *Chronoamperometry, Chronocoulometry, and Chronopotentiometry*, in *Encyclopedia of Applied Electrochemistry*, G. Kreysa, K.-i. Ota, and R.F. Savinell, Editors. 2014, Springer New York: New York, NY. p. 207-214.
15. *Linear Sweep and Cyclic Voltametry: The Principles*. Available from: https://www.ceb.cam.ac.uk/research/groups/rg-eme/Edu/linear-sweep-and-cyclic-voltametry-the-principles.
16. *chemical dictionary*. Available from: https://www.chemicool.com/definition/linear_sweep_voltammetry.html.
17. Rezaei, B. and N. Irannejad, *Chapter 2 - Electrochemical detection techniques in biosensor applications*, in *Electrochemical Biosensors*, A.A. Ensafi, Editor. 2019, Elsevier. p. 11-43.
18. Kim, T., et al., *Applications of voltammetry in lithium ion battery research.* Journal of Electrochemical Science and Technology, 2020. **11**(1): p. 14-25.
19. Aqmar, N., et al. *Embedded 32-bit differential pulse voltammetry (DPV) technique for 3-electrode cell sensing*. in *IOP Conference Series: Materials Science and Engineering*. 2018. IOP Publishing.
20. *knowledge base*. Available from: https://www.palmsens.com/knowledgebase-article/differential-pulse-voltammetry-dpv/.
21. Mirceski, V., et al., *Square-wave voltammetry: a review on the recent progress.* Electroanalysis, 2013. **25**(11): p. 2411-2422.
22. Christopher M. A. Brett, A.M.O.B., *Electrochemistry: Principles, methods, and applications*. Oxford University Press. 427.
23. Geim, A.K., *Graphene prehistory.* Physica Scripta, 2012. **2012**(T146): p. 014003.
24. Katesnelson, M.I., in *graphene. Encyclopedia Britannica*. 2016.
25. Allen, M.J., V.C. Tung, and R.B. Kaner, *Honeycomb carbon: a review of graphene.* Chemical reviews, 2010. **110**(1): p. 132-145.
26. Choi, W., et al., *Synthesis of graphene and its applications: a review.* Critical Reviews in Solid State and Materials Sciences, 2010. **35**(1): p. 52-71.
27. Chung, C., et al., *Biomedical applications of graphene and graphene oxide.* Accounts of chemical research, 2013. **46**(10): p. 2211-2224.

28. Sahu, S. and G. Rout, *Band gap opening in graphene: a short theoretical study.* International Nano Letters, 2017. **7**: p. 81-89.
29. Neri, G., *Thin 2D: The new dimensionality in gas sensing.* Chemosensors, 2017. **5**(3): p. 21.
30. Cao, X., et al., *Engineering two-dimensional layered nanomaterials for wearable biomedical sensors and power devices.* Materials Chemistry Frontiers, 2018. **2**(11): p. 1944-1986.
31. Zribi, R. and G. Neri, *Mo-based layered nanostructures for the electrochemical sensing of biomolecules.* Sensors, 2020. **20**(18): p. 5404.
32. Gupta, A., T. Sakthivel, and S. Seal, *Recent development in 2D materials beyond graphene.* Progress in Materials Science, 2015. **73**: p. 44-126.
33. Dobrzhinetskaya, L.F., et al., *Qingsongite, natural cubic boron nitride: The first boron mineral from the Earth's mantle.* 2014. **99**(4): p. 764-772.
34. Ouyang, J., et al., *2D materials-based nanomedicine: From discovery to applications.* Advanced Drug Delivery Reviews, 2022. **185**: p. 114268.
35. Weng, Q., et al., *Functionalized hexagonal boron nitride nanomaterials: emerging properties and applications.* Chemical Society Reviews, 2016. **45**(14): p. 3989-4012.
36. Tao, W., et al., *Emerging two-dimensional monoelemental materials (Xenes) for biomedical applications.* Chemical Society Reviews, 2019. **48**(11): p. 2891-2912.
37. Wang, T., et al., *Xenes as an emerging 2D monoelemental family: Fundamental electrochemistry and energy applications.* Advanced Functional Materials, 2020. **30**(36): p. 2002885.
38. Zhan, X., et al., *MXene and MXene-based composites: synthesis, properties and environment-related applications.* Nanoscale Horizons, 2020. **5**(2): p. 235-258.
39. Jiang, D., et al., *Flexible electronics based on 2D transition metal dichalcogenides.* Journal of Materials Chemistry A, 2022. **10**(1): p. 89-121.
40. Ali, M., et al., *2D-TMDs based electrode material for supercapacitor applications.* International Journal of Energy Research, 2022.

41. Zhang, J., et al., *Discovering superior basal plane active two-dimensional catalysts for hydrogen evolution.* Materials Today, 2019. **25**: p. 28-34.
42. Tajik, S., et al., *Transition metal dichalcogenides: Synthesis and use in the development of electrochemical sensors and biosensors.* Biosensors and Bioelectronics, 2022. **216**: p. 114674.
43. Wang, Z., et al., *An overview on room-temperature chemiresistor gas sensors based on 2D materials: Research status and challenge.* Composites Part B: Engineering, 2023. **248**: p. 110378.
44. Karakouz, T., et al., *Morphology and refractive index sensitivity of gold island films.* Chemistry of Materials, 2009. **21**(24): p. 5875-5885.
45. Kargar, A., et al., *ZnO/CuO heterojunction branched nanowires for photoelectrochemical hydrogen generation.* Acs Nano, 2013. **7**(12): p. 11112-11120.
46. Cheng, L., et al., *High curie temperature Bi1. 85Mn0. 15Te3 nanoplates.* Journal of the American Chemical Society, 2012. **134**(46): p. 18920-18923.
47. Gao, R., et al., *High-yield synthesis of boron nitride nanosheets with strong ultraviolet cathodoluminescence emission.* The Journal of Physical Chemistry C, 2009. **113**(34): p. 15160-15165.
48. Premkumar, T., et al., *Optical and field-emission properties of ZnO nanostructures deposited using high-pressure pulsed laser deposition.* ACS applied materials & interfaces, 2010. **2**(10): p. 2863-2869.
49. Zhang, X., et al., *Synthesis of a highly efficient BiOCl single-crystal nanodisk photocatalyst with exposing {001} facets.* ACS applied materials & interfaces, 2014. **6**(10): p. 7766-7772.
50. Duong, D.L., S.J. Yun, and Y.H. Lee, *van der Waals layered materials: opportunities and challenges.* ACS nano, 2017. **11**(12): p. 11803-11830.
51. Parmar, S., et al., *Coexisting 1T/2H polymorphs, reentrant resistivity behavior, and charge distribution in Mo S 2− hBN 2D/2D composite thin films.* Physical Review Materials, 2019. **3**(7): p. 074007.

52. Park, S.-I., et al., *A review on fabrication processes for electrochromic devices.* International Journal of Precision Engineering and Manufacturing-Green Technology, 2016. **3**: p. 397-421.
53. Venkata Subbaiah, Y., K. Saji, and A. Tiwari, *Atomically thin MoS2: a versatile nongraphene 2D material.* Advanced Functional Materials, 2016. **26**(13): p. 2046-2069.
54. Shen, C., et al., *Atomic Layer Deposition of Metal Oxides and Chalcogenides for High Performance Transistors.* Advanced Science, 2022. **9**(23): p. 2104599.
55. Grayfer, E.D., M.N. Kozlova, and V.E. Fedorov, *Colloidal 2D nanosheets of MoS2 and other transition metal dichalcogenides through liquid-phase exfoliation.* Advances in Colloid and Interface Science, 2017. **245**: p. 40-61.
56. Liu, X., et al., *Thin-film electronics based on all-2D van der Waals heterostructures.* Journal of Information Display, 2021. **22**(4): p. 231-245.
57. Zribi, R., et al., *Exfoliated 2D-MoS2 nanosheets on carbon and gold screen printed electrodes for enzyme-free electrochemical sensing of tyrosine.* Sensors and Actuators B: Chemical, 2020. **303**: p. 127229.
58. Coleman, J.N., et al., *Two-dimensional nanosheets produced by liquid exfoliation of layered materials.* Science, 2011. **331**(6017): p. 568-571.
59. Li, Z., et al., *Intercalation strategy in 2D materials for electronics and optoelectronics.* Small Methods, 2021. **5**(9): p. 2100567.
60. Zhang, X., et al., *2D materials beyond graphene for high-performance energy storage applications.* Advanced Energy Materials, 2016. **6**(23): p. 1600671.
61. He, Z. and W. Que, *Molybdenum disulfide nanomaterials: Structures, properties, synthesis and recent progress on hydrogen evolution reaction.* Applied Materials Today, 2016. **3**: p. 23-56.
62. Jiang, H.-L., et al., *Fabrication and application of arrays related to two-dimensional materials.* Rare Metals, 2022. **41**(1): p. 262-286.
63. Kurapati, R., et al., *Biomedical uses for 2D materials beyond graphene: current advances and challenges ahead.* Advanced Materials, 2016. **28**(29): p. 6052-6074.

64. Zhang, R. and R. Cheung, *Mechanical properties and applications of two-dimensional materials.* Two-dimensional Materials-Synthesis, Characterization and Potential Applications. Rijeka, Crotia: InTech, 2016: p. 219-246.
65. Wilson, J.A. and A.D. Yoffe, *The transition metal dichalcogenides discussion and interpretation of the observed optical, electrical and structural properties.* Advances in Physics, 1969. **18**(73): p. 193-335.
66. Li, X. and H. Zhu, *Two-dimensional MoS2: Properties, preparation, and applications.* Journal of Materiomics, 2015. **1**(1): p. 33-44.
67. Benavente, E., et al., *Intercalation chemistry of molybdenum disulfide.* Coordination Chemistry Reviews, 2002. **224**(1): p. 87-109.
68. Tian, X., et al., *Recent advances in MoS2-based nanomaterial sensors for room-temperature gas detection: a review.* Sensors & Diagnostics, 2023.
69. Splendiani, A., et al., *Emerging Photoluminescence in Monolayer MoS2.* Nano Letters, 2010. **10**(4): p. 1271-1275.
70. McCreary, K.M., et al., *A-and B-exciton photoluminescence intensity ratio as a measure of sample quality for transition metal dichalcogenide monolayers.* Apl Materials, 2018. **6**(11): p. 111106.
71. Backes, C., et al., *Edge and confinement effects allow in situ measurement of size and thickness of liquid-exfoliated nanosheets.* Nature Communications, 2014. **5**(1): p. 4576.
72. Zribi, R., et al., *Electrochemical and sensing properties of 2D-MoS2 nanosheets produced via liquid cascade centrifugation.* Electrochimica Acta, 2022. **436**: p. 141433.
73. Kudr, J., V. Adam, and O. Zitka, *Fabrication of Graphene/Molybdenum Disulfide Composites and Their Usage as Actuators for Electrochemical Sensors and Biosensors.* Molecules, 2019. **24**(18): p. 3374.
74. Zhou, M., Y. Zhai, and S. Dong, *Electrochemical Sensing and Biosensing Platform Based on Chemically Reduced Graphene Oxide.* Analytical Chemistry, 2009. **81**(14): p. 5603-5613.

75. Hirsch, A. and F. Hauke, *Post-Graphene 2D Chemistry: The Emerging Field of Molybdenum Disulfide and Black Phosphorus Functionalization.* Angewandte Chemie International Edition, 2018. **57**(16): p. 4338-4354.
76. Kumar, N.A., et al., *Graphene and molybdenum disulfide hybrids: synthesis and applications.* Materials Today, 2015. **18**(5): p. 286-298.
77. Li, X. and X. Du, *Molybdenum disulfide nanosheets supported Au-Pd bimetallic nanoparticles for non-enzymatic electrochemical sensing of hydrogen peroxide and glucose.* Sensors and Actuators B: Chemical, 2017. **239**: p. 536-543.
78. Han, Y., et al., *Sensitive electrochemical sensor for nitrite ions based on rose-like AuNPs/MoS2/graphene composite.* Biosensors and Bioelectronics, 2019. **142**: p. 111529.
79. Su, S., et al., *MoS2–Au@Pt nanohybrids as a sensing platform for electrochemical nonenzymatic glucose detection.* New Journal of Chemistry, 2018. **42**(9): p. 6750-6755.
80. Zhao, S., et al., *Core–Sheath Structured MoO3@MoS2 Composite for High-Performance Lithium-Ion Battery Anodes.* Energy & Fuels, 2020. **34**(9): p. 11498-11507.
81. Zribi, R., et al., *Fabrication of a novel electrochemical sensor based on carbon cloth matrix functionalized with MoO3 and 2D-MoS2 layers for riboflavin determination.* Sensors, 2021. **21**(4): p. 1371.
82. Sari, F.N.I. and J.M. Ting, *MoS2/MoOx-nanostructure-decorated activated carbon cloth for enhanced supercapacitor performance.* ChemSusChem, 2018. **11**(5): p. 897-906.
83. Dalila R, N., et al., *Current and future envision on developing biosensors aided by 2D molybdenum disulfide (MoS2) productions.* Biosensors and Bioelectronics, 2019. **132**: p. 248-264.
84. *Health matters*. Available from: https://healthmatters.io/understand-blood-test-results/tyrosine-plasma.
85. An, M. and Y. Gao, *Urinary Biomarkers of Brain Diseases.* Genomics, Proteomics & Bioinformatics, 2015. **13**(6): p. 345-354.

86. Rzepka, Z., et al., *From tyrosine to melanin: Signaling pathways and factors regulating melanogenesis.* Postepy higieny i medycyny doswiadczalnej (Online), 2016. **70**: p. 695-708.
87. Leibowitz, M., M. Dogliotti, and G. Hart, *Schizophrenia and albinism.* Dermatology, 1978. **156**(6): p. 367-370.
88. Iversen, S.D. and L.L. Iversen, *Dopamine: 50 years in perspective.* Trends in Neurosciences, 2007. **30**(5): p. 188-193.
89. Powers, H.J., *Riboflavin (vitamin B-2) and health.* The American Journal of Clinical Nutrition, 2003. **77**(6): p. 1352-1360.
90. *health matterss*. Available from: https://healthmatters.io/understand-blood-test-results/vitamin-b2-riboflavin-plasma.
91. Kennedy, D.O., *B vitamins and the brain: mechanisms, dose and efficacy—a review*. Nutrients, 2016. **8**(2): p. 68.
92. Pinto, J.T. and J. Zempleni, *Riboflavin.* Advances in Nutrition, 2016. **7**(5): p. 973-975.
93. *World health organization* Available from: https://apps.who.int/iris/bitstream/handle/10665/75584/WHO_NMH_NHD_EPG_12.1_eng.pdf;jsessionid=AF81150CC51F3611AA2FD9828316772A?sequence=1.
94. Eichholzer, M., O. Tönz, and R. Zimmermann, *Folic acid: a public-health challenge.* The Lancet, 2006. **367**(9519): p. 1352-1361.
95. *UCSF Health*. Available from: https://www.ucsfhealth.org/medical-tests/uric-acid----blood-#:~:text=Normal%20values%20range%20between%203.5,deciliter%20(mg%2FdL).
96. Álvarez-Lario, B. and J. Macarrón-Vicente, *Uric acid and evolution.* Rheumatology, 2010. **49**(11): p. 2010-2015.

Section II

Materials

&

Methods

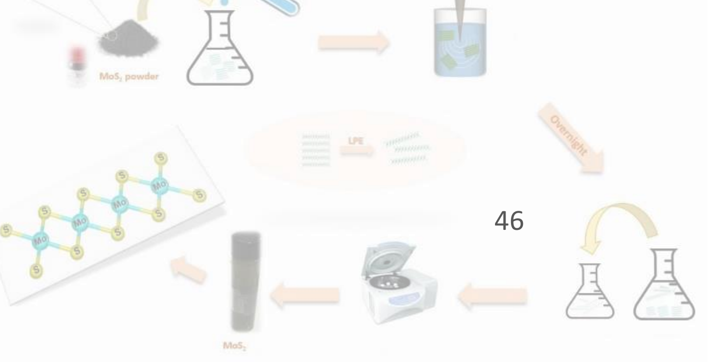

Overview

This section will go further into the preparation process used to synthesize two-dimensional (2D) layered transition metal dichalcogenides (TMDCs) explaining the reason behind choosing these specific methods. After, the synthesis method of α-MoO_3/carbon cloth functionalized with 2D-Molybdenum Disulfide nanosheets will be presented. In addition, a brief definition of the different characterization techniques utilized to analyze the optical and electrical characteristics of the obtained suspensions will be given. Finally, the sensors' preparation method will be illustrated and the electrochemical tests will be mentioned.

I. Pure and nanohybrids molybdenum disulfides nanosheets synthesis

In this thesis work, Molybdenum disulfide nanosheets (2D-MoS_2) were synthesized via Liquid-Phase Exfoliation (LPE) and via Liquid Cascade Centrifugation (LCC).

As discussed in the previous section, LPE represents a powerful and versatile technique that consists in dispersing layered materials in a liquid medium to produce stable colloidal suspensions of nanosheets. This method has several advantages that make it a popular technique for preparing two-dimensional (2D) nanomaterials. First, it is a simple and scalable technique that can produce large quantities of 2D nanomaterials in a short time. Therefore, it emerges as a cost-effective and time-efficient method of producing high-quality nanomaterials. As a consequence, the resulting nanosheets are usually with high crystallinity and low defect density providing a large surface-to-volume ratio, which make them highly reactive and useful for the development of very sensitive electrochemical sensors. Additionally, LPE produces highly versatile nanosheets making it easy to implement them into different composites and devices, e.g. in this case, it provides a suspension that can be easily deposited onto the surface of the electrodes [1-4].

In addition to the LPE advantages, LCC process allows a more efficient separation and isolation of the nanosheets based on their size and density, which can lead to a further improvement of properties and performances of the nanocomposite devices used for the various applications. The idea of repeated centrifugation cycles came after the setting up of new metrological studies for the 2D nanosheets, used for electrochemical sensing applications for the detection of large molecules [5, 6]. Therefore the chemical and structural characterization of 2D nanomaterials needed to be more and more accurate. The efficiency of such procedures and materials has been tested on electrochemical processes such as hydrogen evolution reaction (HER) and oxygen evolution reaction (OER), which involve small molecules, i.e. H_2 and O_2, respectively [6-8].

I.1. Materials and Reagents for 2D-MoS_2 synthesis and sensing tests

Sodium cholate (SC), molybdenum disulfide (MoS_2), Phosphate buffer saline (PBS), L-Tyrosine (Tyr), L-Dopamine (DA), Riboflavin (RF), Folic Acid (FA), Ascorbic Acid (AA), Uric Acid (UA), and Nafion perfluorinated resin solution were purchased from Sigma Aldrich [9].

All of the chemicals required to create MoO_3 were obtained from Hi-Media Specialties and utilized directly without further purification. Carbon Cloth (CC) (Avcarb, formerly BALLARD, USA) was purchased from Vinpro technologies, Hyderabad, India. The Mo metal target that was employed (Sigma Alrich, 2" inch dia. and 3 mm thickness) had a purity of 99.999%).

Tyrosine, dopamine, riboflavin, and uric acid solutions were prepared in PBS at pH 7.4. All analytes solutions were prepared daily before performing electrochemical analyzes. Nafion and PBS, were stable enough to be used for a longer period. Screen-printed electrodes were purchased from Metrohm DropSens.

I.2. Liquid-phase exfoliation of molybdenum disulfide

As illustrated in Figure.II.1, 2D-MoS_2 nanosheets were prepared by liquid phase exfoliation in sodium cholate watery solutions following the procedure detailed in ref [3]. For the first batch “A”, 0.045 mg/mL of SC with 0.15 mg/mL of MoS_2 powder were used, While for the second one “B”, 1.5 mg/mL of SC with 5 mg/mL of MoS_2 were used. Before adding the MoS_2 powder, the solution containing SC was kept for 10 min in bath sonication. Solutions were sonicated by horn sonication (Branson S250) for 30 minutes in an ice bath to reduce detrimental heating effects. The obtained dispersions were allowed to decant overnight in a flask. Then, the day after, the half top part (20 mL, typically) was moved to another vial and centrifuged (ALC 4235, swinging rotor) at 1500 rpm for 15 minutes for batch “A” and then for 90 minutes for batch “B”. The supernatant is rich in few-layer nanosheets and the obtained solution was stable for months. Surfactant, and in this case SC, is fundamental to stabilize the 2D nanosheet solutions. It encapsulates the nanosheets so that electrostatic repulsions can be efficiently exploited (and even tuned) to avoid reaggregation phenomena. The role of the organic solvent is to facilitate the delamination process and to sustain stable dispersions having high concentrations of exfoliated 2D nanosheets and SC is one of the best solvents since it minimizes the surface energy difference with the layered materials [1, 10].

Samples were not prepared all at the same time. During the Ph.D course, first batch called “A” was prepared first. The second one called “B” was synthesized with few optimisation compared to the first one.

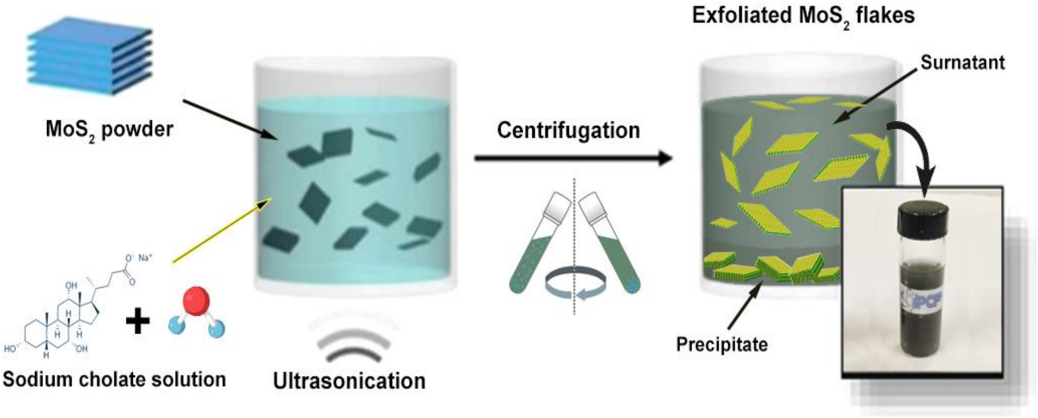

Figure.II.1. Schematic of the procedure for the preparation of exfoliated 2D-MoS_2 nanosheets via LPE for batch "A" and "B"and illustration of the sonifier and centrifugation setups at CNR-IPCF [10] .

I.3. Preparation of the molybdenum disulfide/molybdenum oxide-carbon cloth composite

The 2D-MoS_2-MoO_3CC composite were fabricated as follows: first, pristine carbon cloth substrates were washed for 2 to 3 times with acetone and deionized water under sonication for 2 h, to thoroughly remove organic residues and other impurities. The cleaned carbon cloth substrates, constituted of long nanofibers, were kept in a hot air oven overnight. Afterwards, the dry substrates were placed in a radio-frequency magnetron reactive sputtering (RF) (Huttenger, Germany) in a customized down setup sputtering mode where Ar^+ (99.999%) is used as working gas and O^{-2} (99.999%) as reactive gas in 1:5 ratio. The Mo metal target was fixed in the working pressure of 10^{-2} mbar for depositing a thin layer. A α-MoO_3 thin film (around 350 nm thick) was deposited on carbon cloth substrates at deposition rate of 3 Å/s at 450ºC temperature. The surface contamination on the target material was removed by pre-sputtering the target at 0.01 mbar pressure for 10 min. The RF power was set to 150W, the distance between target and substrate was maintained at 50 mm [11]. Finally, the 2D-MoS_2 suspension (obtained from batch "B") was drop casted onto the bare carbon cloth and carbon cloth dopped with MoO_3 and left to dry at room temperature.

I.4. Liquid cascade centrifugation of molybdenum disulfide

2D-MoS_2 nanosheets were prepared by surfactant-assisted liquid phase exfoliation and cascade centrifugation [5]. Exfoliation of MoS_2 powder (5mg/mL, Fig.II.2.a) was carried out in a SC watery solution (1.5 mg/mL) with a Branson 250 sonifier mounting a flat tip (3/16" diameter) and operating at 50% of power for 30 minutes. Solutions were kept in an ice bath during sonication to reduce detrimental heating effects. The dispersions were allowed to decant overnight. Samples characterized by a surnatant stock containing MoS_2 flakes dispersed in liquid are thus obtained (Fig.II.2.b), with larger crystallites sedimented at the bottom. The surnatant was extracted from the sediment and centrifuged (ALC 4235, swinging rotor) at 1500 rpm for 90 minutes, yielding the "1.5 krpm" sample (Fig.II.2.c). The stock supernatant from the 1.5 krpm centrifugation is then transferred to another vial to be centrifuged at 2 krpm for 90 min, yielding the "2 krpm" sample. The procedure was repeated at 3, 4 and 5 krpm. Fig.II.2.c. shows the images of the solutions, diluted 1:10 v/v, that appear more and more transparent. The sediments produced after each centrifugation step are discarded [5, 7, 12]. The solutions obtained represent batch "C".

Figure.II.2. Schematic of the procedure used to produce small-size enriched 2D-MoS_2 dispersions by liquid phase exfoliation followed by liquid cascade centrifugation. a) Picture of the MoS_2 powder, b) the sample obtained after sonication and decantation, c) images of the solutions obtained after LCC at 1.5, 2, 3, 4, 5 krpm, diluted 1:10 v/v [12].

II. Structural and Electrical characterization techniques

In order to study the morphological properties of the obtained suspensions and for a confirmation of the 2D dimensionality of the material, several characterization techniques have been used that can be classified into three categories:

- Spectroscopic techniques, such as UV-Visible spectroscopy (UV-Vis), Raman spectroscopy, and Dynamic light scattering (DLS).
- Microscopic techniques, such as Scanning Electron Microscopy- Energy Dispersive X-ray Spectroscopy (SEM-EDS) and Atomic Force Microscopy (AFM).
- Electrochemical technique, such as Electrochemical Impedance Spectroscopy (EIS).

II.1. Spectroscopic techniques

II.1.a. UV-Visible spectroscopy

UV-Vis spectroscopy (UV-Vis) is a spectroscopic technique that relies on the interaction of the light radiation and the matter in the spectral range spanning from near ultraviolet to very near-infrared, a domain known as UV-Visible, in which wavelengths are comprised between 200 nm - 800 nm. It provides information about the energy levels and electronic transitions of a molecular system. The absorbance of the material in the near UV and the visible is exploited intensively in quantitative analysis, by application of the Beer-Lambert law following equation (II.1):

$$A = \varepsilon . l . c \qquad \text{(II.1)}$$

Where:

- A is the absorbance,
- ε is the molar attenuation coefficient or absorptivity of the attenuating species,
- l is the optical path length in cm,

- c is the concentration of the absorbing species,

The analyzed sample is crossed by a light radiation (Fig.II.3) and the photons interact with the analytes in solution, bringing the molecules, atoms or ions in an excited state. Thus, part of the incident radiation is absorbed. The transmitted light is then analyzed in order to obtain information on its electronic structure, by comparing the acquired signal with a reference signal where the radiation beam is crossing a solution with no analytes dispersed.

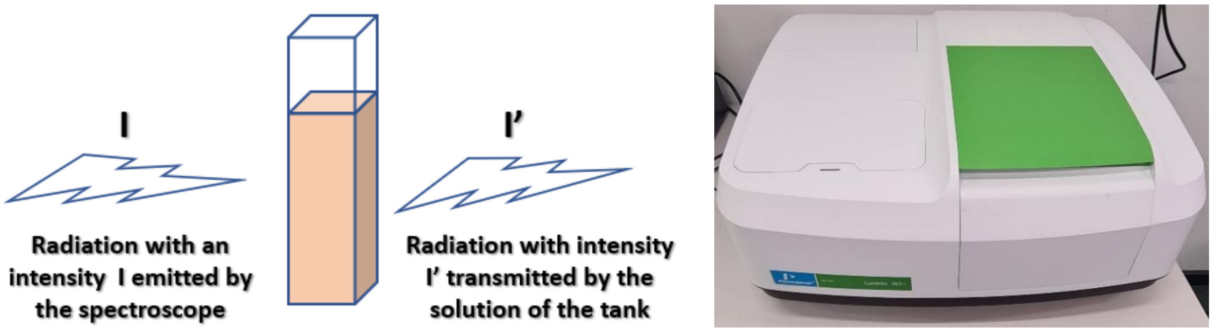

Figure.II.3. Illustration of UV-Vis Principle and the UV-Vis spectrometer at LabSensor.

II.1.b. Raman spectroscopy

Raman spectroscopy is a non-destructive technique and can be used to analyze a wide variety of samples, including solids, liquids, and gases. It can be used to identify unknown compounds, determine the purity of a sample, and study chemical reactions in real-time.

Raman spectroscopy is a technique used to study the vibrational modes of molecules, based on the Raman effect [13]. It can provide detailed information about chemical structure, phase and polymorphy, crystallinity and molecular interactions. The Raman effect occurs when a sample is illuminated with a laser, and the scattered light has an energy slightly different from the one of the incident beam. The monochromatic light source interacting with the electons of the investigated system Bring them to a virtual energy level, when the material re-emits photons, the scattered signal is collected and analyzed by a suitable detector, which is typically a silicon based charge-coupled device (CCD). The recorded radiation has two types of signals as shown in the figure II.4.

below. The first, very majority, corresponds to the Rayleigh scattering: the incident radiation is diffused elastically without change of energy and therefore of wavelength. However, photons, in a very limited number of cases, can exchange energy with the material. The sample absorbs (or gives) energy to the incident photons thus producing Raman Stokes (or anti-Stokes) radiation. The energy variation observed on the photon then provides information about the energy levels of rotation and vibration of the molecule analyzed.

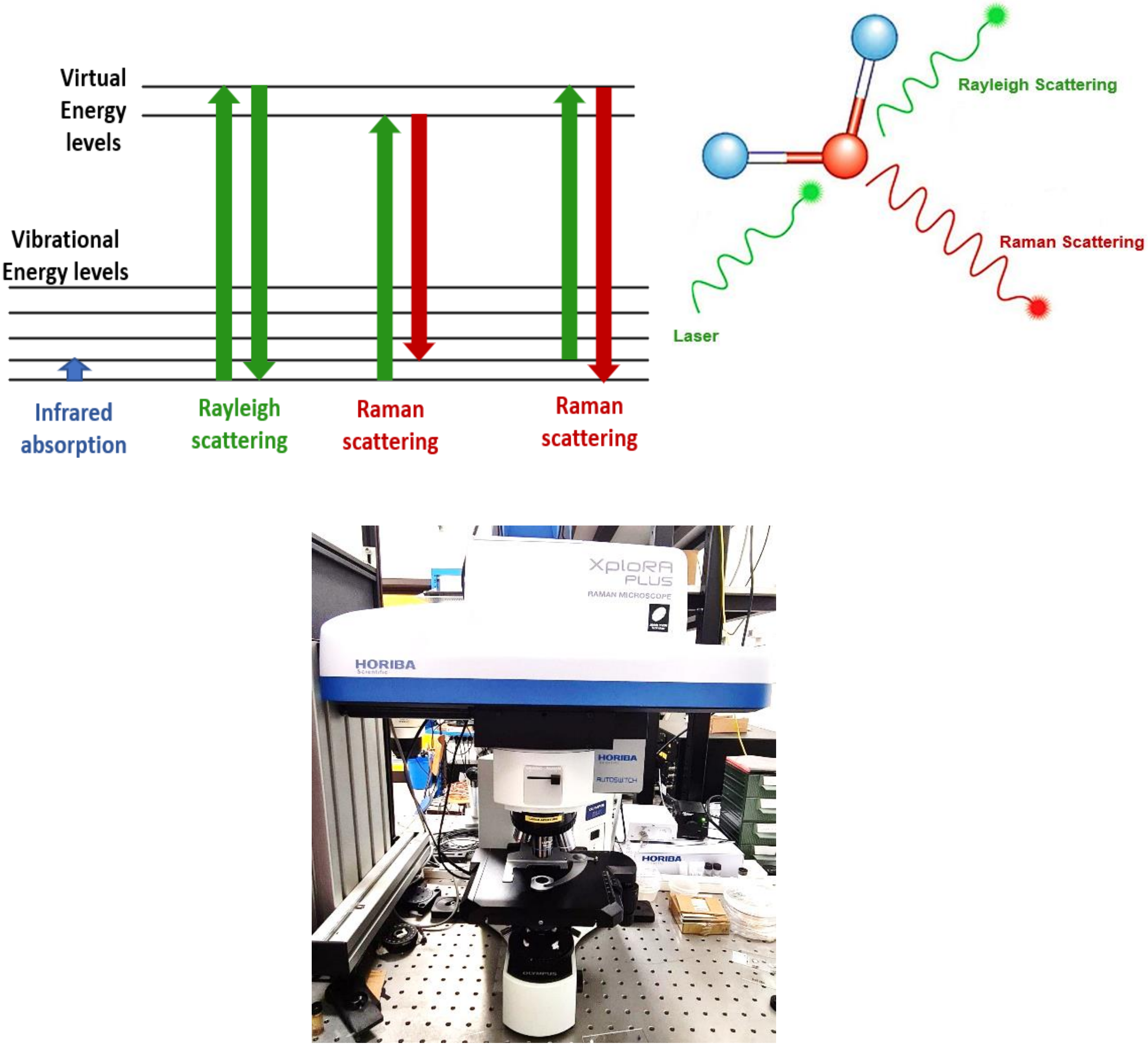

Figure.II.4. Illustration of Raman scattering Principle and Raman spectrometer at IPCF-CNR (XploRa Plus – Horiba Scientific).

.

II.1.c. Dynamic light scattering

Dynamic Light Scattering (DLS) is a non-destructive characterisation technique. It is a useful tool for characterizing the size and size distribution of small particles. This method is based on the analysis of the intensity fluctuations of scattered light by particles undergoing Brownian motion. When a light beam is directed towards a sample, the particles in the solution scatter the light in all directions. The scattered light creates intensity fluctuations, which are collected by a photodetector. The intensity fluctuations are caused by the Brownian motion of the particles, which leads to changes in the scattering angle of the light. By analyzing the intensity fluctuations over time, it is possible to obtain information about the size and size distribution of the particles in the sample (Fig.II.5).

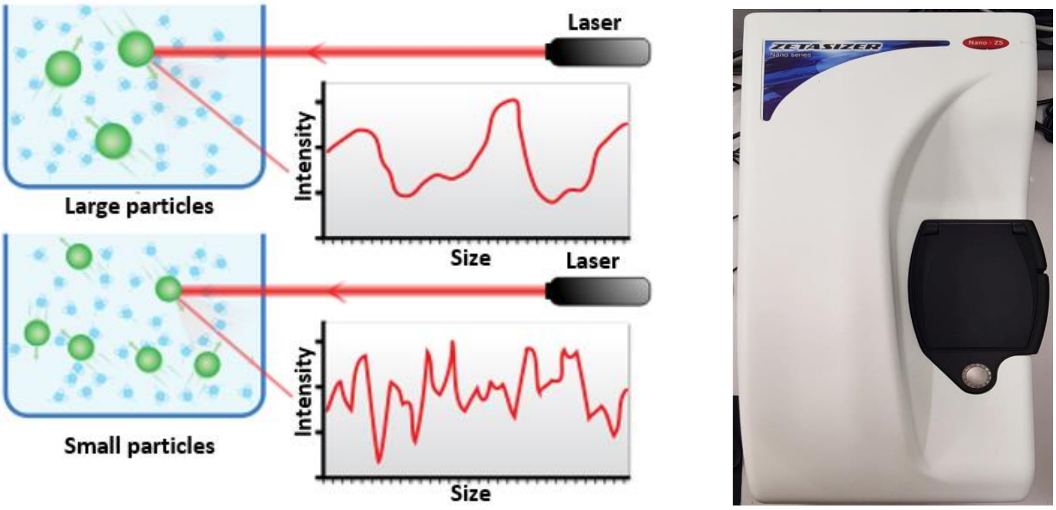

Figure.II.5. Illustration of dynamic light scattering Principle and DLS spectrometer at LabSensor.

II.2. Microscopy techniques

II.2.a. Scanning electron microscopy-Energy Dispersive X-ray Spectroscopy

This technique is a combination of two analytical techniques used in materials science and other fields to study the composition and structure of materials at a very small scale. Scanning electron microscopy (SEM) is a non-destructive technique that provides information about the morphology of the nanomaterials. Here, as illustrated in Fig.II.6, a beam of electrons is focused onto the surface of a sample using series of electromagnetic lenses. The electrons interact with the atoms in the sample, and some of the electrons are scattered or emitted from the surface. These scattered or emitted electrons are then detected by a special detector, and an image is generated based on the pattern of electron emissions. These images come with a resolution of a few nanometers, which is much higher than the resolution of a traditional optical microscope.

In some cases, this technique is coupled with energy-dispersive X-ray spectroscopy (EDX). EDX is an analytical technique used in conjunction with SEM to determine the elemental composition of the sample. As the electron beam strikes the surface of the sample, it causes also the emission of X-rays. EDX detects these X-rays and provides information about the elements present in the sample. The X-ray intensity, and in other words the size of spectrum peaks, is directly proportional to the concentration of the elements in the sample. Also, this technique can provide a mapping of the surface demonstrating the distribution of the existing elements of the studied sample.

By combining the SEM and EDX, images with high resolution with detailed imaging of surface features at the nanoscale level can be generated and elemental composition can also be determined. This makes SEM-EDX a powerful tool for characterizing materials, identifying defects, and analyzing surface features.

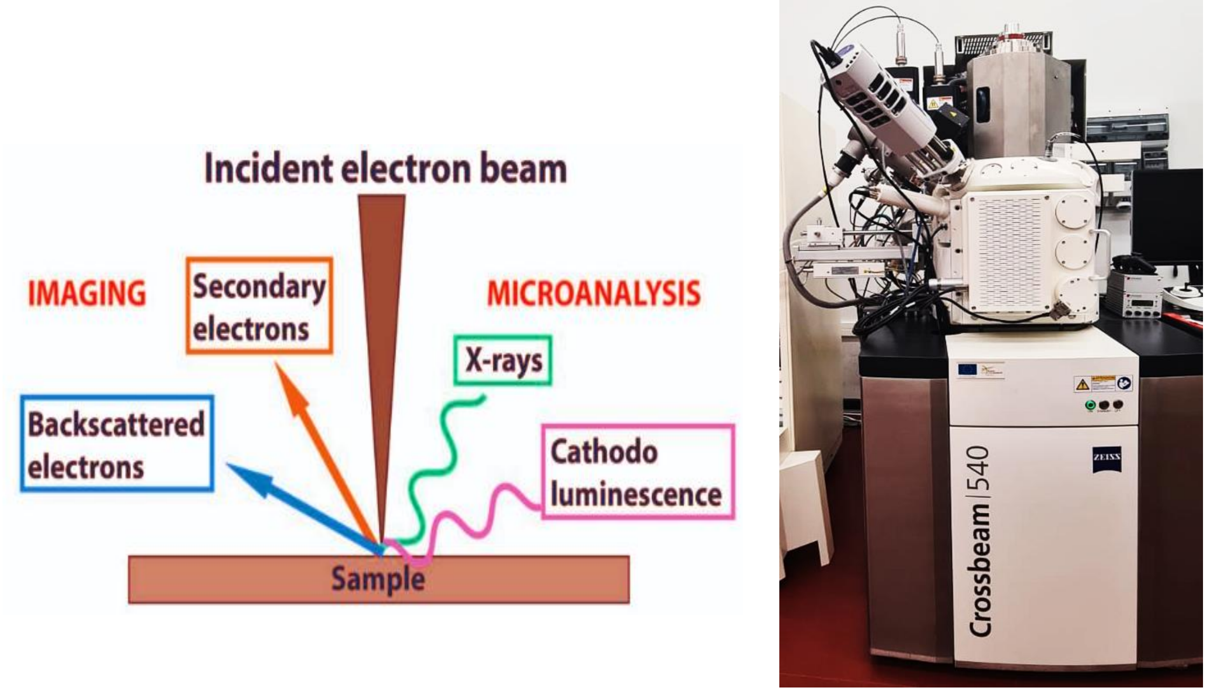

Figure.II.6. Illustration of the electron-matter interaction occurring during SEM analysis and SEM microscope in Engineering departement at University of Messina.

II.2.b. Atomic force microscopy

Atomic force microscopy (AFM) is a microscopic technique that provides high-resolution imaging giving information about the surface morphology. While both SEM and AFM provide high-resolution images, they use different methods to achieve their results.

As shown in Fig.II.7. below, this technique works by using a small probe with a sharp tip (typical tip radius dimensions range from 1 nm to 10 nm) to scan the surface of the sample, and the probe measures the force between the tip and the sample as it moves across the surface. As the tip moves over the surface, the forces between the tip and the sample cause the cantilever to deflect. The deflection of the cantilever is measured by a laser beam that is directed at the back of the cantilever, and the data is used to create an image of the surface of the sample.

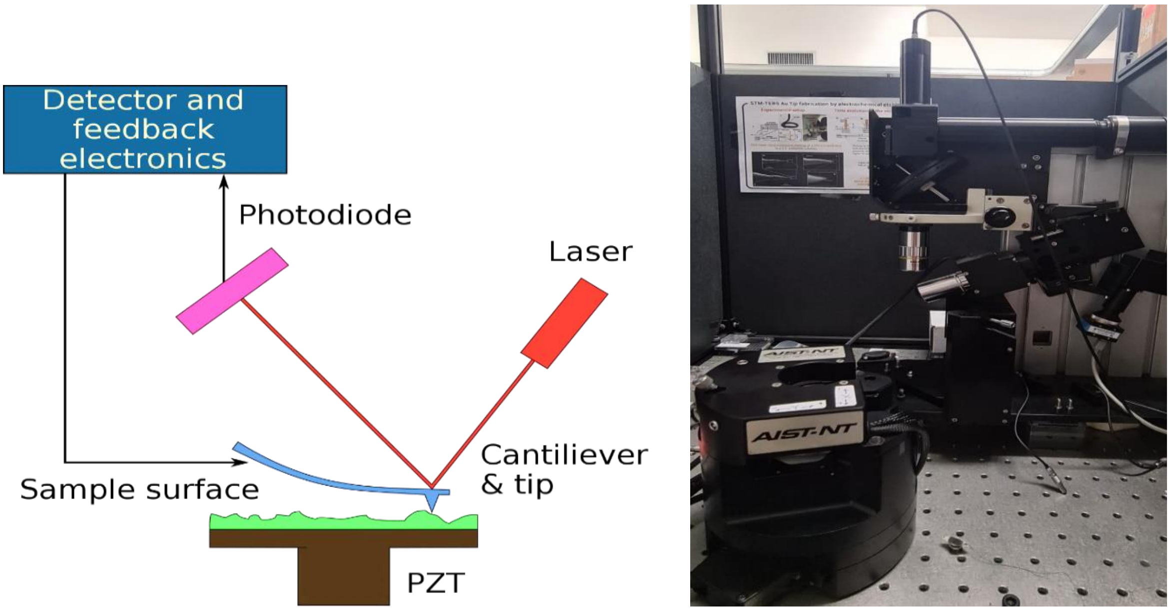

Figure.II.7. Illustration of an Atomic Force Microscope (AFM) contact mode at IPCF-CNR.

SEM typically provides higher resolution images than AFM, because the wavelength of electrons is much shorter than the size of the atoms in the sample. This allows SEM to resolve features on the nanoscale, whereas AFM is typically limited to features that are larger than the tip of the probe.

However, AFM has some advantages over SEM in certain applications. AFM can provide information about the mechanical properties of the sample. In addition, AFM can be used to study samples that are not conductive, whereas SEM requires conductive samples.

II.3. Electrochemical technique: Electrochemical Impedance Spectroscopy

Electrochemical Impedance Spectroscopy (EIS) is a powerful experimental technique used to study the electrical properties of electrochemical systems. It involves the measurement of the complex impedance of a system as a function of frequency. The electrochemical system typically consists of an electrode, an electrolyte, and the interface between them. The EIS technique involves applying an AC voltage to the system and measuring the resulting AC current. By varying the frequency of the AC signal over a range of values, it is possible to obtain information about the electrical impedance of the system. The complex impedance of the system can be represented as a vector in the complex plane, with the real part representing the resistance of the system (or the impedance at zero frequency) and the imaginary part representing the capacitive and inductive components of the impedance.

From the EIS measurement, we obtain a graph called Nyquist plot (Fig.II.8). It is a graphical representation of the frequency response of a system in the complex plane and used to analyze the stability and performance of feedback control systems.

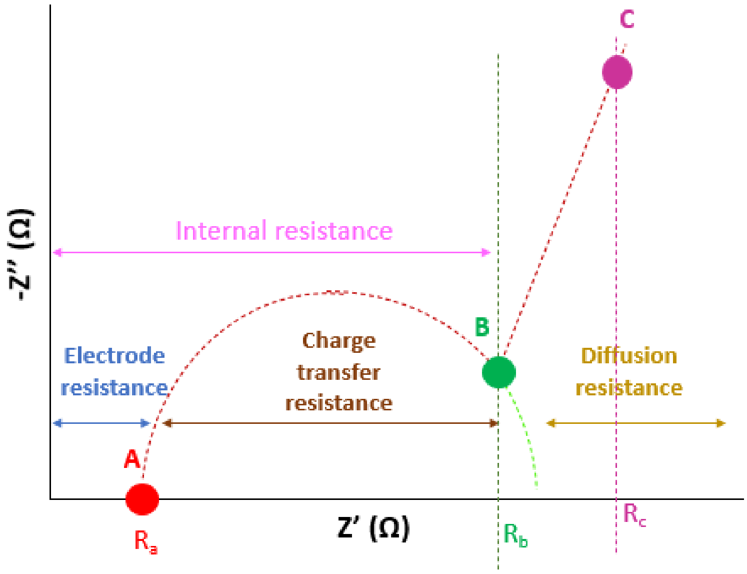

Figure.II.8. Nyquist plot obtained from EIS measurement.

The resistance R_a in Fig.II.8. refers to the electrode resistance. The diameter of the semicircle $R_{ab} = R_b - R_a$ has been attributed to the contact resistance between electrode and current collector, also the so-called charge transfer resistance. The resistance R_b (Fig.II.8), is considered as the internal resistance, which is the sum of the electrode resistance and the charge transfer resistance. The intersection R_c between the BC line and the *Z'* axis, correspond to the overall resistance the electrode. Using electrochemical impedance spectroscopy, it is possible to get important data about electrochemical complex systems. The electrochemical system's components can be represented by the well-known circuit elements where the impedance is well-characterized. Overall, EIS provides an idea about the electrical conductivity of the modified sensor which can give an explanation about how favorable is the electron transfer between the electrode and the electrolyte.

III. Sensors preparation

Screen-printed electrodes (SPEs) were purchased from DropSens, Spain. The SPEs platforms used were: *i)* C110, constituted of a 4 mm diameter carbon working electrode, a silver pseudo-reference electrode and a carbon auxiliary electrode (named SPCE); *ii)* Low (C220AT) and high surface area (C220BT) 4 mm diameter gold electrodes, having a silver pseudo-reference electrode and a gold auxiliary electrode (named SPAuE). Pictures of the bare SPEs platforms and their specifics are reported in the http://dropsens.com/ web site.

To modify the bare SPEs, different volumes of 2D-MoS_2 dispersions, obtained from both LPE and LCC, were directly drop cast onto the surface of working electrodes. The overall volume was deposited by dropping successive volumes of 10 µl each. After each drop, the electrode was permitted to dry before of the successive casting. Moreover, in order to accelerate the process, the sensor was deposited on hot plate at a fixed temperature of 50°C (see Fig.II.9.a.). At the end of the deposition procedure, the sensor was stored at room temperature until further use.

To fabricate the modified SPCE, slices of pristine CC and MoO_3-CC were cut in order to cover entirely the surface of the working electrode of SPCE. Some of these slices were modified by drop casting 2D-MoS_2 suspension (obtained from LPE) and left at room temperature to dry. Then, 6 µL of Nafion solution 5% was dropped on that for enhancing the adhesion on the surface of SPCE and left to dry at room temperature (see Fig.II.9.b.).

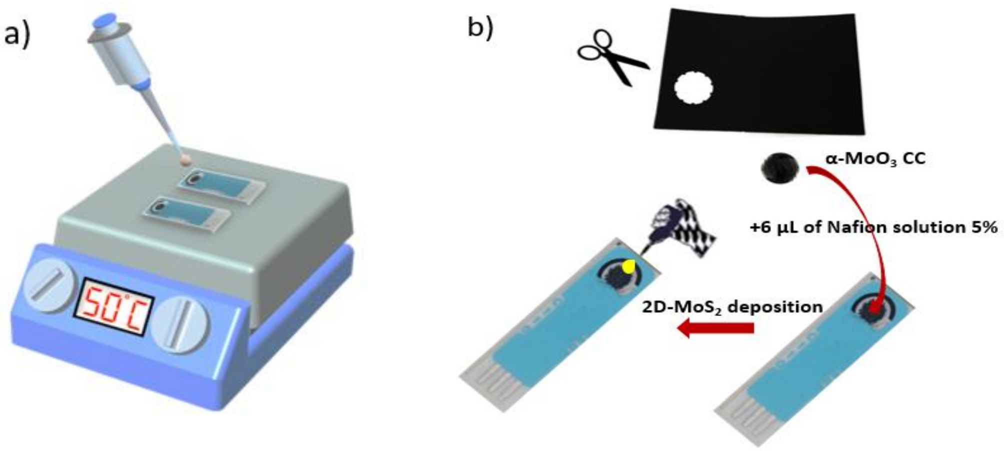

Figure.II.9. a) Fabrication of 2D-MoS$_2$ screen-printed carbon electrode ; b) Fabrication of 2D-MoS$_2$-MoO$_3$CC screen-printed carbon electrode.

IV. Electrochemical measurements

Electrochemical impedance spectroscopy (EIS) was performed by using a potentiostat Galvanostat (Fig.II.10.a). Cyclic voltammetry (CV), Linear Sweep Voltammetry (LSV), Differential Pulse Voltammetry (DPV), Square Wave Voltammetry (SWV), and Chronoamperometry tests were carried out by using a DropSens µStat 400 Potentiostat empowered by Dropview 8400 software for data acquisition (Fig.II.10.b). Tests were performed in aerated 1 M PBS (and in some cases 0.1 M PBS) at pH = 7.4 as electrolyte at scan rate of 50 mV/s in presence of different concentrations of analytes. All experiments were performed at room temperature.

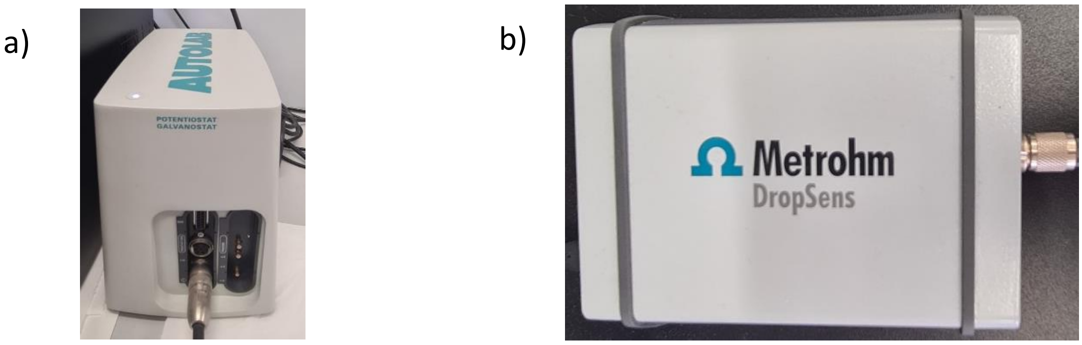

Figure.II. 10. a) DropSens µStat 400 Potentiostat, b) Potentiostat Galvanostat from LabSensor both used in the all electrochemical tests reported in this thesis.

References

1. Zribi, R., et al., *Exfoliated 2D-MoS2 nanosheets on carbon and gold screen printed electrodes for enzyme-free electrochemical sensing of tyrosine.* Sensors and Actuators B: Chemical, 2020. **303**: p. 127229.
2. Coleman, J.N., et al., *Two-dimensional nanosheets produced by liquid exfoliation of layered materials.* Science, 2011. **331**(6017): p. 568-571.
3. Smith, R.J., et al., *Large-scale exfoliation of inorganic layered compounds in aqueous surfactant solutions.* Advanced materials, 2011. **23**(34): p. 3944-3948.
4. Messina, E., et al., *Double-wall nanotubes and graphene nanoplatelets for hybrid conductive adhesives with enhanced thermal and electrical conductivity.* ACS applied materials & interfaces, 2016. **8**(35): p. 23244-23259.
5. Backes, C., et al., *Production of highly monolayer enriched dispersions of liquid-exfoliated nanosheets by liquid cascade centrifugation.* ACS nano, 2016. **10**(1): p. 1589-1601.
6. Kajbafvala, M. and M. Farbod, *Effective size selection of MoS2 nanosheets by a novel liquid cascade centrifugation: Influences of the flakes dimensions on electrochemical and photoelectrochemical applications.* Journal of colloid and interface science, 2018. **527**: p. 159-171.
7. Gholamvand, Z., et al., *Electrochemical applications of two-dimensional nanosheets: the effect of nanosheet length and thickness.* Chemistry of Materials, 2016. **28**(8): p. 2641-2651.
8. Jaramillo, T.F., et al., *Identification of active edge sites for electrochemical H2 evolution from MoS2 nanocatalysts.* science, 2007. **317**(5834): p. 100-102.
9. *Sigma Aldrich*. Available from: https://www.sigmaaldrich.com.
10. Zribi, R., et al., *Simultaneous and selective determination of dopamine and tyrosine in the presence of uric acid with 2D-MoS2 nanosheets modified screen-printed carbon electrodes.* FlatChem, 2020. **24**: p. 100187.
11. Murugesan, D., et al., *α-MoO3 nanostructure on carbon cloth substrate for dopamine detection.* Nanotechnology, 2019. **30**(26): p. 265501.

12. Zribi, R., et al., *Electrochemical and sensing properties of 2D-MoS2 nanosheets produced via liquid cascade centrifugation.* Electrochimica Acta, 2022. **436**: p. 141433.
13. Long, D.A. and D. Long, *The Raman effect: a unified treatment of the theory of Raman scattering by molecules*. Vol. 8. 2002: Wiley Chichester.

Section III

Results

&

Discussions

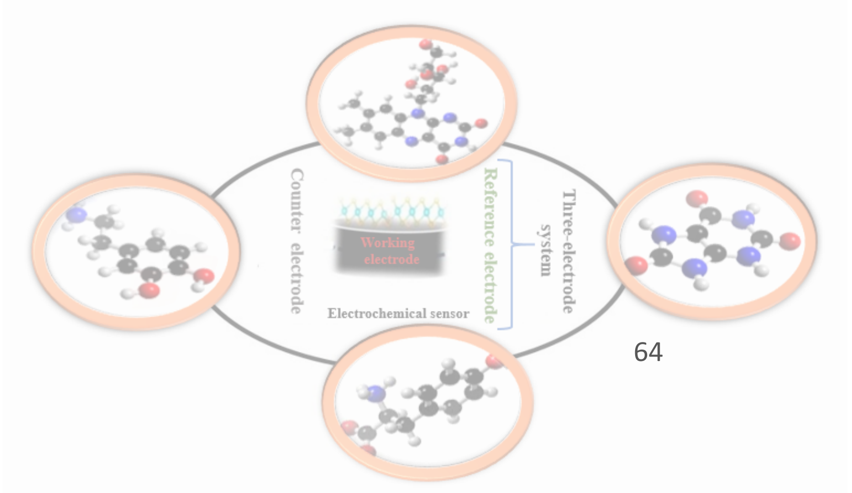

Part 1:

Electrochemical sensors based on 2D-Materials produced via Liquid Phase Exfoliation

Chapter 1

Characterization of samples produced via Liquid Phase Exfoliation

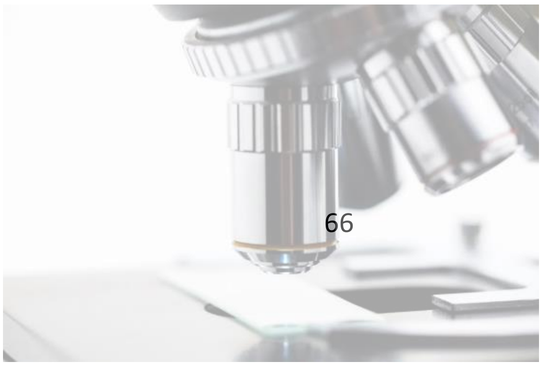

Overview

The results acquired with the as-prepared electrochemical substrates using the sensing layers obtained from LPE as well as the composite derived from this material will be highlighted in this section. Here, the fundamental characterizations that were performed on the samples and sensing substrates will be presented. Batches “A” and “B” present in this chapter refer to the samples produced via liquid phase exfoliation previously detailed in Section II.

I. Characterization and metrology of 2D-Molybdenum disulfide

I.1. Spectroscopic characterization of batches “A” and “B”

1.1.a. UV-Vis spectroscopy

UV-Vis spectroscopy was carried out in the 250 - 900 nm wavelength range (see Fig.III.1.a-b). To reduce the influence of multiple scattering in the measurements and safely apply Beer’s law to estimate concentrations, the samples were diluted 1:10 v/v in SC prior to analysis [1, 2]. Both extinction spectra of the diluted MoS_2 solutions for both batches, show the A- (~ 680 nm) and B- (~ 620 nm) exciton components, together with the C-excitonic band at 400 – 452 nm superposed to a scattering background, consistent to what expected for the 2H polytype of 2D-MoS_2 [3].

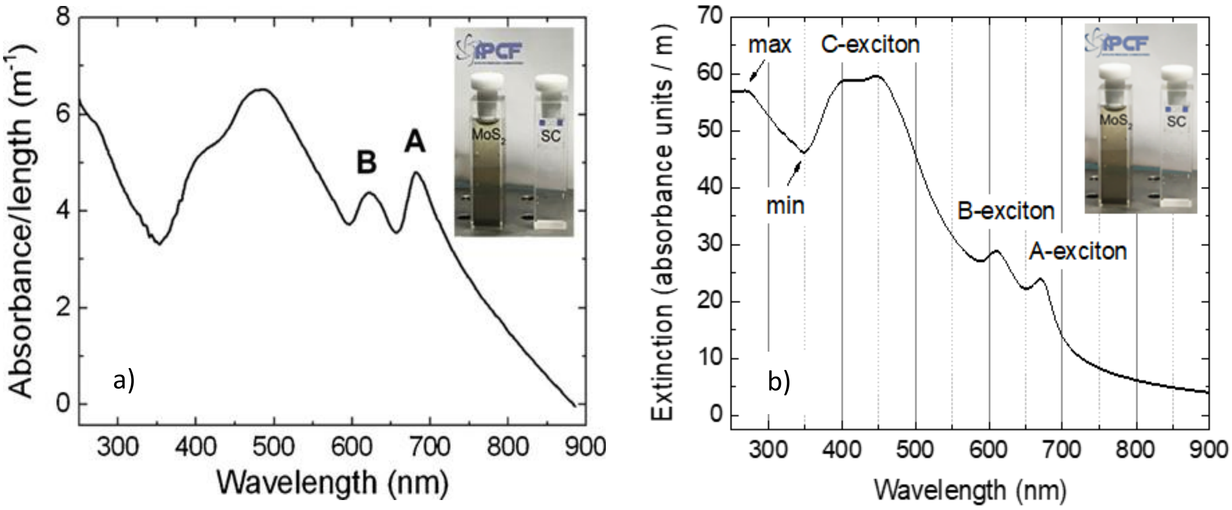

Figure III.1. Extinction spectrum of the MoS_2 dispersion diluted 1:10 v/v: a) batch “A”; b) batch “B”. Inset: picture of the MoS_2 solution compared to the SC solution.

According to the UV-Vis spectra, the size, thickness and the nanosheets concentration in the solutions can be computed following the empirical formulas reported by Backes *et al.* [4] and Varrla *et al.* [5]. The average nanosheets size <L> was calculated from the ratio between the local minimum extinction intensity at 350 nm and B-exciton value Ext_B following the Equation (III.1) :

$$\langle L \rangle\ (\mu m) = \frac{3.5 * ExtB/Ext350 - 0.14}{11.5 - ExtB/Ext350} \qquad (III.1)$$

The nanosheets thickness can be estimated from the position of the A-exciton λ_A (in nm)

$$\langle N \rangle = 2.3 * 10^{36}\ e^{-54888/\lambda_A} \qquad (III.2)$$

Using the value of the extinction coefficient $\varepsilon_{350} = 69\ mL\ mg^{-1}\ cm^{-1}$ of the local minimum at 350 nm we find the concentration c applying Beer's law:

$$c = Ext(350)/\varepsilon_{350} l \qquad (III.3)$$

where l = 1 cm corresponding to the standard quartz cuvette thickness used in our experiments.

In the table III.1. are reported the sample's properties extracted from the UV-Vis spectra of both batch “A” and “B”.

Samples' properties	**Batch “A”**	**Batch “B”**
⟨L⟩	450	170
⟨N⟩	Between 15 and 20	9
c (µg/mL)	0.45	80

Table III.1. Samples' properties extracted from UV-Vis spectra.

I.1.b. Raman spectroscopy

Raman spectroscopy at λ_{ex} = 638 nm and λ_{ex} = 785 nm was carried out first to confirm the nature of the MoS_2 nanosheets, to evaluate the number of layers and also to exclude contaminations and/or distortions of the crystalline matrix. Experiments were carried by focusing the laser beam in the liquid solutions for both batches “A” and “B” and, for comparison, on the pristine powder and also on both gold and carbon electrodes modifed with 2D-MoS_2 dispersion. Measurements on the liquid dispersions were carried out with a laser power of 26 mW (638 nm) and 56 mW (785 nm) (see Fig.III.2.a. and Fig.III.2.b. respectively). On the powder, as well as on the electrodes, laser powers were kept smaller than few hundreds of µW in order to avoid thermal effects that produce shifts of the peaks and changes of the intensity ratios among the bands [6, 7]. Excitation at λ_{ex} = 785 nm is considered as a pre-resonance condition [8] due to the relative proximity to the indirect bandgap transition at 954 nm (1.3 eV) present in bulk MoS_2, this can justify the good signal to noise ratio of the dispersions' spectra.

Spectras for both batches "A" and "B" show the principal one-phonon vibrations E^1_{2g} (in plane) and A^1_g (out of plane), respectively, at 383 and 408 cm^{-1} and no relative shift between the two modes was observed neither in solution nor after deposition on the electrodes between the nanosheets and the powder [6]. These two modes were reported to shift one towards the other when the number of layers ⟨N⟩ decreases below 7 [9, 10]. Therefore, these results confirm the outcome of UV-Vis characterization estimating a large number of average layers per flake for both batches and they are also in agreement with the literature [5, 11]. The nanoflakes spectra are typical of the 2H phase, indicating no modification of the crystal structure upon sonication [12].

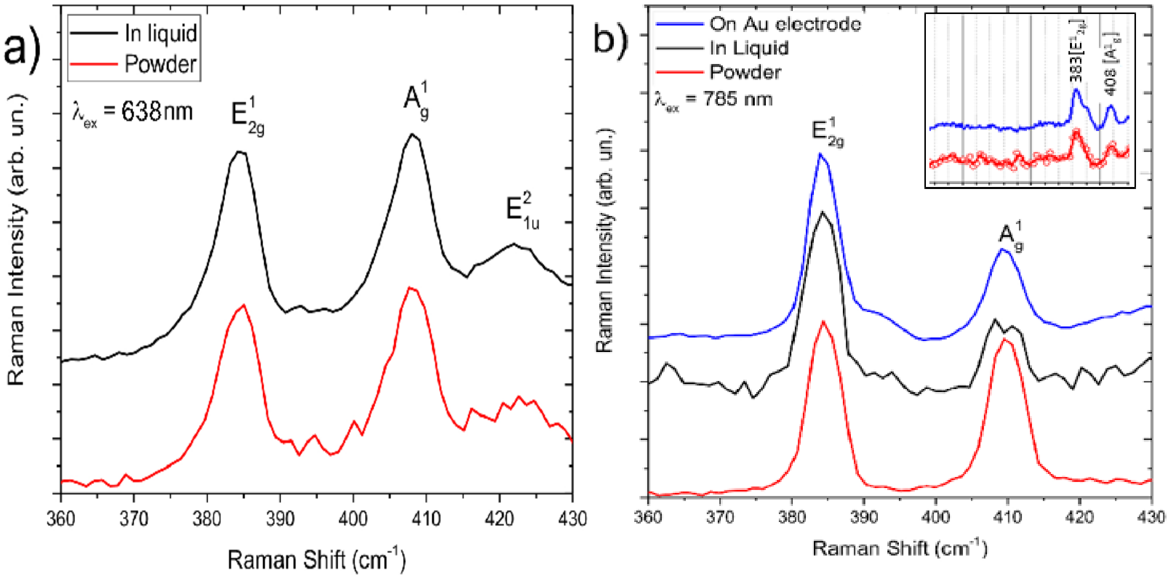

Figure III.2. Raman spectra carried out at a) 638 nm and b) 785 nm on liquid dispersions (batch"A") , on the powder, and on the gold and carbon electrodes after deposition of MoS_2 solution (blue line). The inset (b) represents the raman spectra of batch "B" at 785 nm excitation in which blue line refers to the spectra of the modified carbon electrode and red lines with hollow circles is the 2D-MoS_2 dispersion.

I.2. Microscopic characterization of 2D-Molybdenum disulfide via scanning electron microscopy

SEM measurements were carried out on both carbon and gold electrodes from the two batches “A” and “B”, that were first tested as electrochemical platforms. Images in Fig.III.3. show the bare SPEs and the 2D-MoS_2 layer deposited on the carbon and gold electrodes. The modified electrodes were made using the solutions containing the exfoliated 2D-MoS_2 nanosheets. By using SEM, the surface morphology of the bare electrodes (Fig.III.3.a-b) and the modified 2D-MoS_2/SPAuEs (Fig.III.3.c) and 2D-MoS_2/SPCEs (Fig.III.3.d) was examinated.

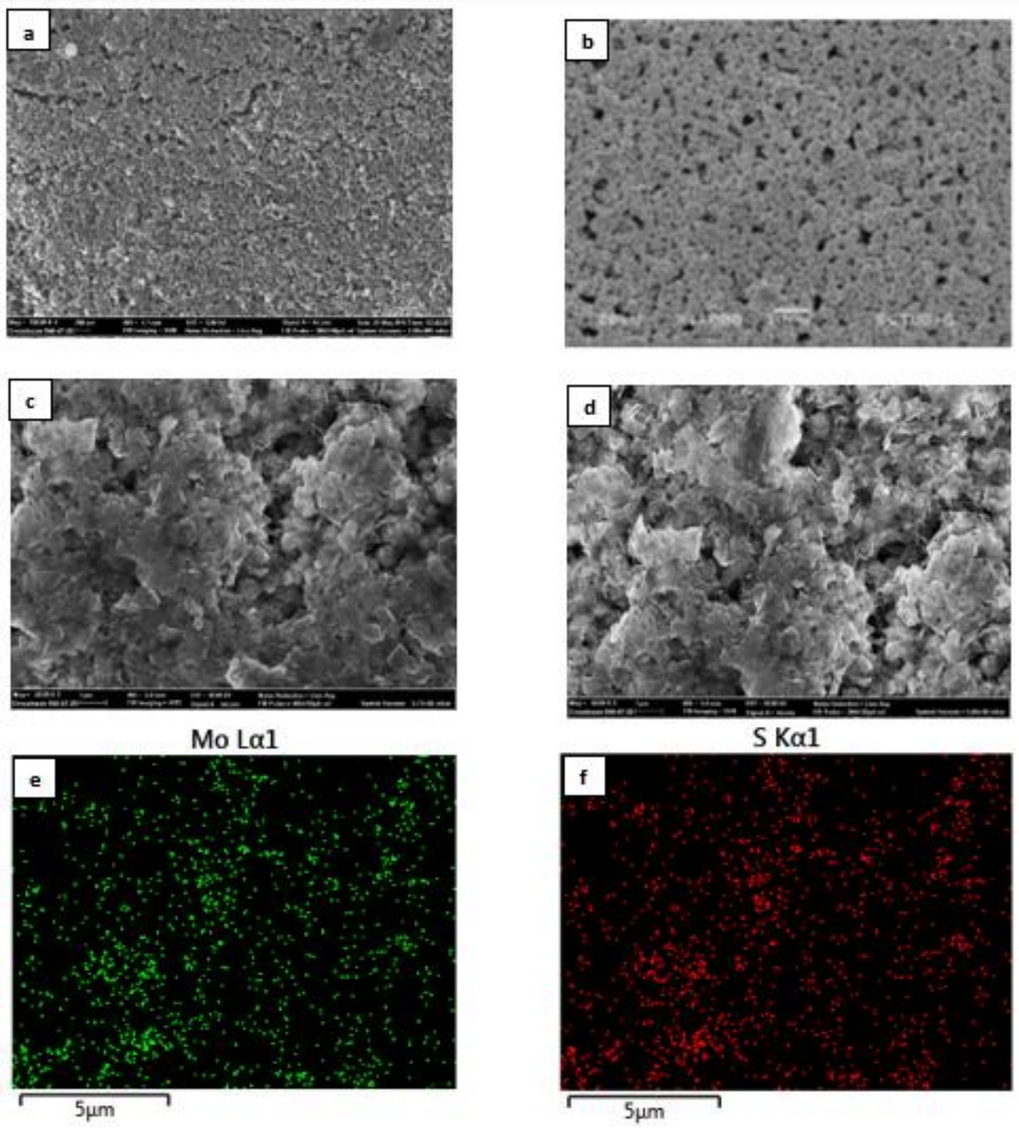

Figure III.3. SEM images showing a) bare SPCE, b) bare SPAuE c) 2D-MoS_2/SPAuE modified electrode d)2D-MoS_2/SPCE modified electrode. e, f) EDX mapping of 2D-MoS_2/SPCE at the sulfur S Kα1 and the molybdenum Mo Lα1 energies.

Nanosheet-like shape of 2D-MoS_2, accumulated across the electrode surface, is highlighted by the SEM analysis of modified electrodes. Mo and S elements make up the nanosheets, with no major impurities, according to energy dispersive X-ray examinations (EDX). Additionally, these two substances seem to be uniformly dispersed across the working electrode's surface.

From this analysis, it is confirmed that the deposited 2D-MoS_2 nanosheets maintain their structures. Furthermore, we can assess that the interaction and assembling on electrode surface does not modify its peculiar characteristics showed in the as-prepared dispersion. Also, to further confirm this fact and investigate the state of 2D-MoS_2 layer deposited on the above SPEs electrodes, Raman analysis were performed and compared with 2D-MoS_2 before deposition. As an example, Raman spectra collected on 2D-MoS_2/SPAuE shown in Fig.III.2.b appears to be similar to the one collected on the 2D-MoS_2 liquid solution, suggesting that no transformation occurs when depositing 2D-MoS_2 on the surface of the working electrode and after drying.

II. Spectroscopic and microscopic characterization of molybdenum disulfide/molybdenum oxid-carbon cloth nanocomposite

II.1. Raman spectroscopy

Raman spectras at λ_{ex}= 638 nm have been acquired first on the bare carbon cloth SPCE “bare CC/SPCE” (Fig.III.4, black line), then on the carbon cloth dopped with molybdenum oxide SPCE “MoO_3-CC/SPCE” (Fig.III.4, blue line) and finally on the carbon cloth dopped with molybdenum oxide and decorated with 2D-MoS_2 nanosheets “MoS_2-MoO_3CC/SPCE” (Fig.III.4, red line).

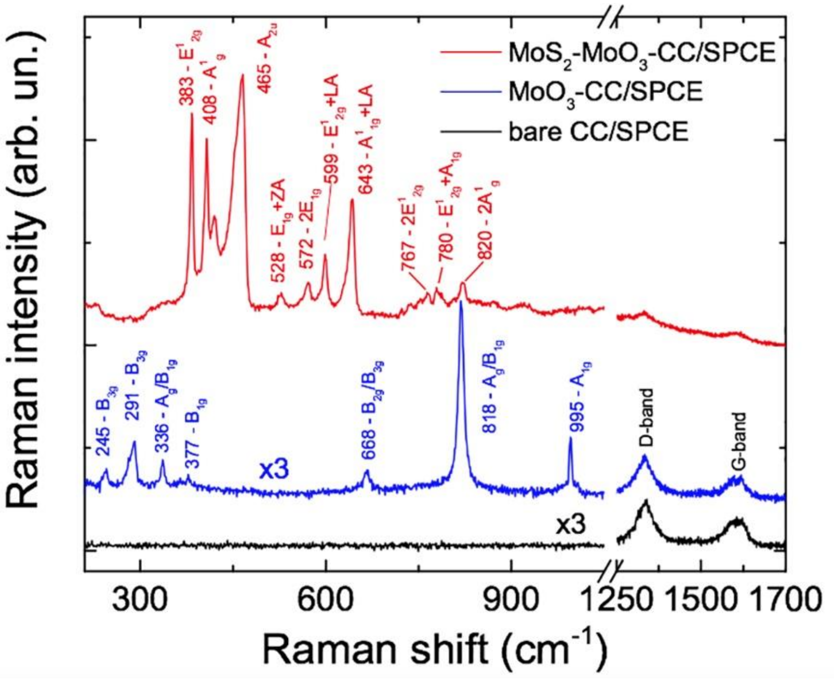

Figure III.4. Raman spectra carried out on the CC/SPCE (black line), MoO$_3$CC/SPCE (blue line) and MoS$_2$-MoO$_3$CC /SPCE (red line). The spectra on CC and MoO$_3$CC were multiplied by a factor 3 to fit the same intensity scale of the MoS$_2$ one. All spectra were offset for clarity.

On the CC/SPCE, only the Raman fingerprint of carbon is detected, namely the D-band peak centered at 1330 cm^{-1} and the G-band around 1600 cm^{-1}. These two bands correspond to the amorphous carbon phase present in the carbon cloth [13]. Concerning the MoO$_3$CC/SPCE (blue line), the superposition of the carbon bands and the MoO$_3$ vibrational modes which are attributed to the α-MoO$_3$ orthorhombic phase was observed [14]. The spectrum of the MoS$_2$-MoO$_3$-CC/SPCE is dominated by the MoS$_2$ signal. At λ_{ex}= 638 nm, the photons are almost resonant with the B-excitonic transition of MoS$_2$, leading to resonant Raman (RR) effects [15, 16]. When the frequency of the incoming light comes close to the specific frequency needed to drive the transfer of an electron from an occupied state to an unoccupied state, the absolute Raman intensity can change by several orders of magnitude. Besides the amplification of first-order transitions, RR scattering also causes the amplification of the second-order Raman processes. These modes exhibit features coming from different crystalline momenta, potentially from the entire Brillouin zone (BZ), with the only constraint of negligible momentum of the phonon pairs involved in the two-phonon process. The strong second order transitions in MoS_2 cover the 500–850 cm^{-1} frequency range. Table III.2 summarizes the Raman modes observed on the sample, their symmetry and transition order.

Sample	Energy (cm^{-1})	Symmetry	Attribution
MoO_3	245	B_{3g}	τ O=Mo=O
MoO_3	291	B_{3g}	ω O=Mo=O
MoO_3	336	A_g/B_{1g}	δ O-Mo-O
MoO_3	377	B_{1g}	δ O=Mo=O (scissoring)
MoO_3	668	B_{2g}/B_{3g}	ν O–Mo–O
MoO_3	818	A_g/B_{1g}	νs O=Mo=O
MoO_3	995	A_g	νasO=Mo=O
CC	1330	A_{1g}	D-band
CC	1605	E_{2g}	G-band
MoS_2	383	$E^1_{2g}(\Gamma)$	First-order
MoS_2	408	$A_{1g}(\Gamma)$	First-order
MoS_2	420	B’	First-order
MoS_2	465	$A_{2u}(\Gamma)$ or 2LA(M)	First or second order
MoS_2	528	$E_{2u}(M) + LA(M)$	Second-order
MoS_2	572	$2E_{1g}(\Gamma)$	Second-order
MoS_2	599	$E^1_{2g}(\Gamma) + LA(M)$	Second-order
MoS_2	643	$A^1_{1g}(M) + LA(M)$	Second-order
MoS_2	767	$2E^1_{2g}(\Gamma)$	Second-order
MoS_2	780	$E^1_{2g} + A_{1g}$	Second-order
MoS_2	820	$2\ A_{1g}(\Gamma)$	Second-order

Table III.2. Peaks frequency, group theory representation and attribution of the modes observed in the Raman spectra of the different samples.

The position of the first-order transitions E^1_{2g} (383 cm^{-1}) and A_{1g} (408 cm^{-1}) is typical of the 2H phase on few layers 2D-MoS_2 [16]. The 466 cm^{-1} peak has been attributed to either an $A_{2u}(\Gamma)$ vibration [8] or to an overtone of a longitudinal acoustic (LA) phonon [6].

II.2. Scanning electron microscopy

A picture of the modified 2D-MoS_2-MoO_3CC/SPCE is reported in Fig.III.5.a. The network morphology of the 2D-MoS_2-MoO_3CC fixed on the working electrode of SPCE is shown in Fig.III.5.b. The large surface of carbon cloth fibers is beneficial for growing the MoO_3 layer and successively to anchoring the 2D-MoS_2 nanosheets.

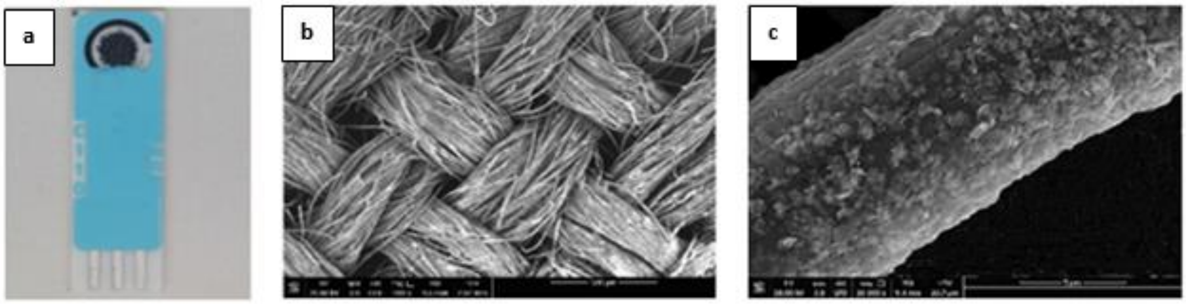

Figure III.5. a) Picture of the modified 2D-MoS_2-MoO_3/SPCE; b) SEM image of the 2D-MoS_2-MoO_3CC network; c) SEM image of the surface of a single 2D-MoS_2-MoO_3CC/SPCE fiber.

This open network structure facilitates the electrolyte ions diffusion during the electrochemical tests. The change of morphology subsequent to the CC surface modification is shown in Fig.III.6.

Unmodified CC fibers present a smooth surface (Fig.III.6.a). In the MoO_3CC, the MoO_3 thin layer covers homogeneously the entire surface of the carbon fibers (Fig.III.6.b). In Fig.III.6.c is shown the two-layers 2D-MoS_2-MoO_3CC composite. The MoS_2 nanosheet particles are clearly seen on the top of underling MoO_3 nanoparticle layer.

There are no remarkable aggregation of MoS_2 sheets on the MoO_3 layer. Furthermore, an increase in the surface roughness is observed, which gives rise to higher active surface area for the modified electrode, and thus enhances its electrochemical activity. The 2D-MoS_2 nanosheets build up an external porous layer covering the MoO_3CC fibers.

EDX elemental mapping analysis (Fig.III.6.d–f) of the MoS_2-MoO_3CC composite-based SPCE confirms the presence and distribution of the main Oxygen, Molybdenum, and Sulfur elements on the electrode’s surface.

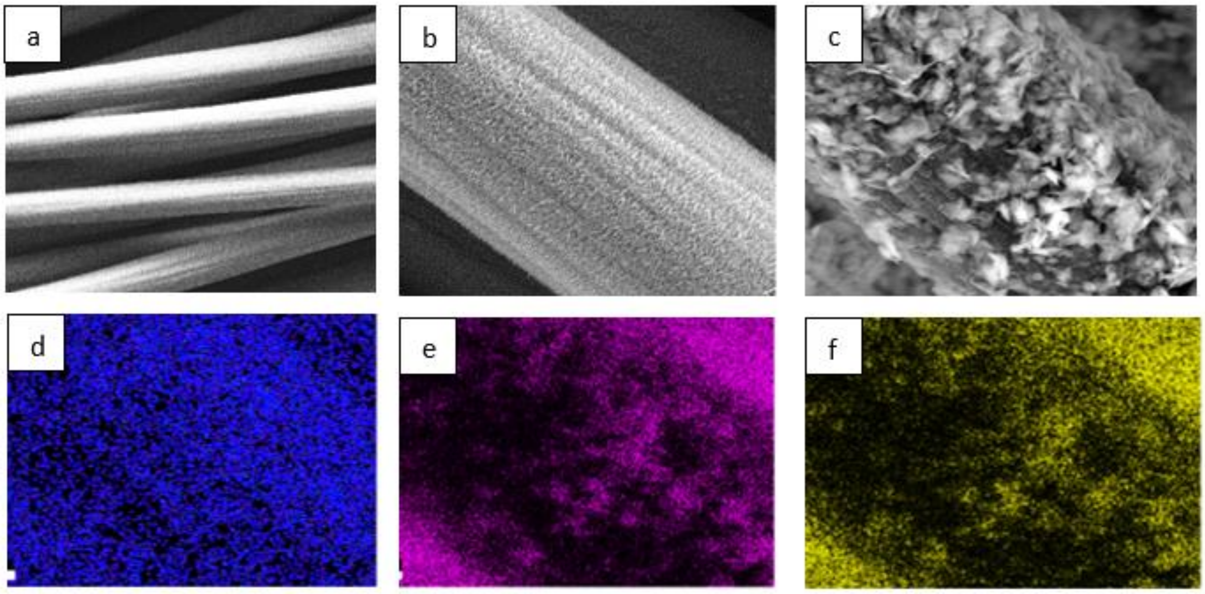

Figure III.6. SEM images of a) CC/SPCE; b) MoO_3-CC/SPCE; c) MoS_2-MoO_3CC/SPCE. (d–f) energy dispersive X-ray (EDX)mapping of the SEM image shown in (c) at the Oxygen, Molybdenum, and Sulfur energies, respectively.

Chapter 2

Electrochemical tests of Batch "A"

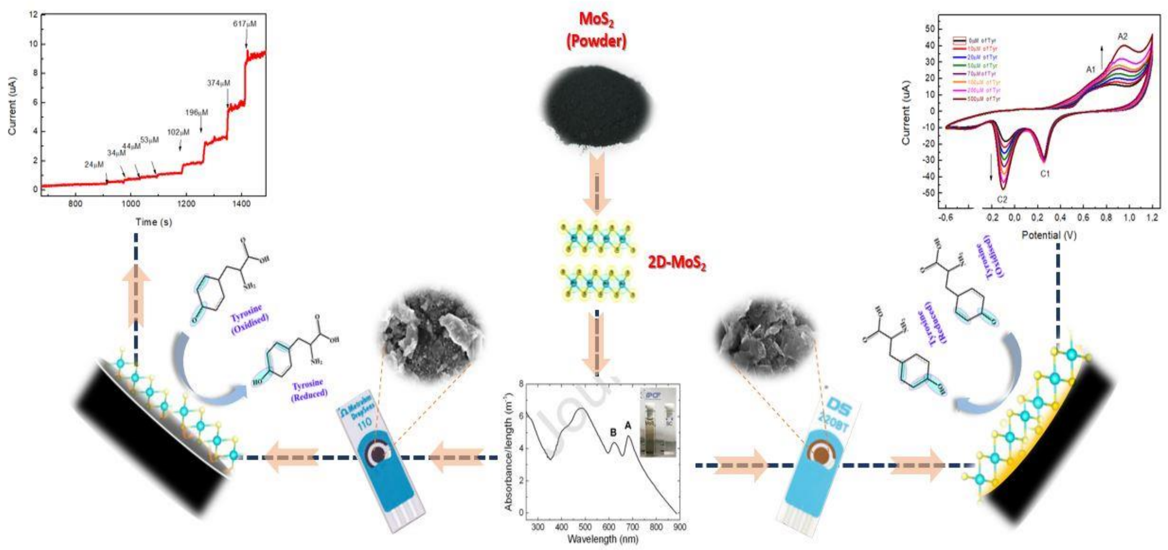

Overview

In this chapter, the electrochemical behaviour of batch”A”, prepared via liquid phase exfoliation will be investigated for the qualitative and quantitative determination of tyrosine. A comparative study will be conducted for this purpose using both carbon and gold screen-printed electrodes. The following paper was published from the research developed in this chapter [Zribi, R.; et al. Sens. Actuators B. 2020, 303, 127229].

I. 2D-Molybdenum disulfide modified gold electrode for Tyrosine detection

I.1. Bare and 2D-MoS_2 modified screen-printed gold electrodes in absence of Tyrosine

The electrochemical behavior of bare gold SPEs and 2D-MoS_2 modified screen-printed gold electrodes was assessed by Cyclic Voltammetry in 0.1 M PBS electrolyte at a scan rate of 50 mV/s. Preliminary tests have shown that the high surface area C220BT gold electrode provided better electrochemical characteristics compared to low surface area C220AT electrode. For this reason, in the following, only data obtained with the C220BT gold electrode will be reported (Fig.III.7). In the potential range between 0 and 0.8 V, no peak was observed on the pristine gold modified electrode. Testing the modified-MoS_2 electrodes, during the first cycle, the appearance of a strong peak at 0.6 V attributed to MoS_2 was noted.

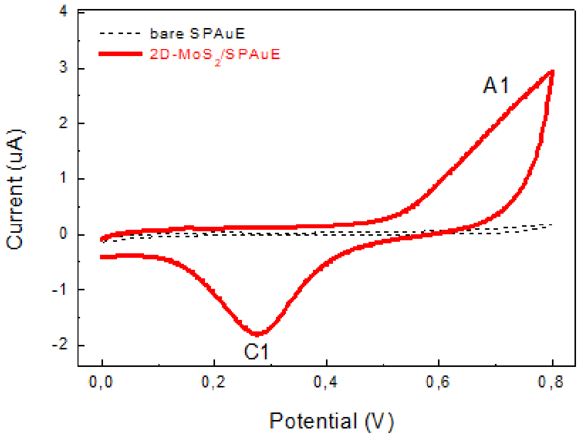

Figure III.7. Electrochemical behavior of bare SPAuEs and 2D-MoS_2/SPAuE in the 0 – 0.8 V potential window. CV was performed in air-saturated 0.1 M PBS electrolyte 50 mV/s.

However, the peak disappears completely after few cycles, in agreement with literature [17]. After this transitory regime, a state characterized by a stable CV cycle is reached (Fig. III.7). The CV cycle evidenced the presence of a peak in anodic direction (A1) around 0.7 V followed, on the reverse scan, by a cathodic peak (C1) centered at about 0.28 V. These peaks were attributed to redox reaction of gold species, formed on the surface of working modified gold electrode at a positive potential higher than 0.5 V. Interestingly, thie peaks couple was observed only on the 2D-MoS_2/SPAuE, suggesting that the presence of 2D-MoS_2 seems essential for its formation.

I.1.a. Evaluation of different MoS_2 nanosheets loading on the electrochemical behavior

The effect of 2D-MoS_2 nanosheets loading deposited on gold SPEs electrodes was investigated. Gold SPEs were modified adding different volumes of the as-prepared 2D-MoS_2 nanosheets suspension (from 50 to 400 µl). Results of the electrochemical investigation with 2D-MoS_2/SPAuE are reported in Fig.III.8.

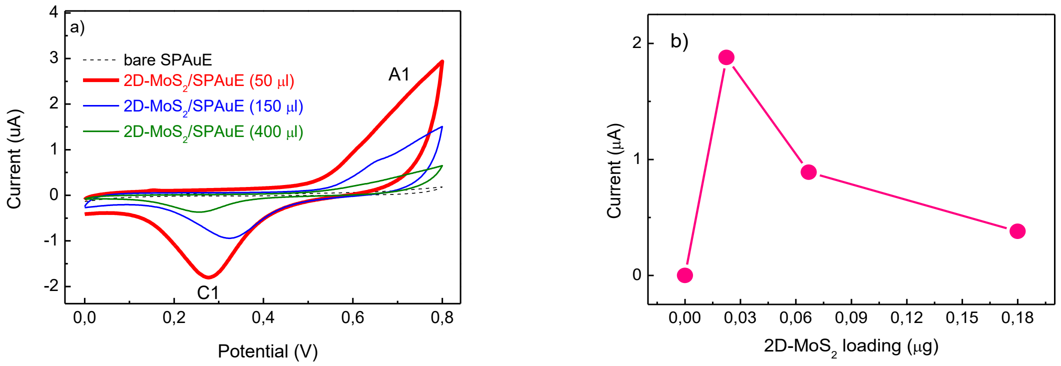

Figure III.8. a) Electrochemical behavior in 0.1 M PBS at a scan rate of 50 mV/s of the 2D-MoS_2/SPAuE in the 0 – 0.8 V potential window. b) Current variation of peak C1 vs. the volume of 2D-MoS_2 nanosheets suspension used for the bare electrodes' modification.

As clearly observed, the intensity of A1 and C1 peaks increases with addition of MoS_2 solution (up to 50 µl) on gold electrode then, for further addition of nanosheets, a large decrease is occurring (see Fig.III.8.a). Plotting the measured C1 peak current (I_p) vs. MoS_2 loading (in µg) (see Fig.III.8.b), appears evident that there is an optimal MoS_2

nanosheets loading on the gold surface leading to the maximization of peak current. To explain this finding, it was supposed that the peaks couple is related to gold species at the interface with 2D-MoS_2 nanosheets. Indeed, a certain coverage of 2D-MoS_2 nanosheets is necessary to create the interface sites but, increasing the coverage, they are gradually blocked by 2D-MoS_2 nanosheets which progressively accumulate on the surface. The interface between the MoS_2 nanosheets and Au seems then to play a peculiar role in the observed enhancement. It could be hypothesized that the charge-transfer efficiency between the MoS_2 nanosheets and the conductive porous structure of the underlying metallic gold electrode SPAuE are factors which influence positively the oxidation-reduction process of surface Au. This is also in agreement with those better electrochemical characteristics found on the high-surface area electrode compared to the low-surface area gold electrode favored by 3D structure of former, which play an important role in both exhibiting more exposed active gold sites for 2D-MoS_2 and preventing 2D-MoS_2 nanosheets from aggregation.

I.1.b. Effect of the potential window

The unmodified and 2D-MoS_2-SPAuE modified gold electrodes was tested in a potential range from -0.6 to 1.2 V. On the unmodified electrode (Fig.III.9), the C1 peak was more intense than the A1 peak. Its intensity was also higher compared to the same peak observed when cycling the electrode in a narrower potential range (0–0.8 V). Thus, this effect seems to be strongly linked to the higher potential used. Other cathodic peaks also appeared at negative potentials, likely due to oxygen reduction on the gold surface. On the 2D-MoS_2/SPAuE modified gold electrode (Fig.III.9), besides the peaks A1 and C1, other relevant peaks, named A2 and C2, were noted at 0.83 V and −0.10 V, respectively. Their intensity increased with the nanosheets loading, suggesting that they come from redox processes involving Molybdenum species. The C2/C1 intensity ratio increased with the MoS_2 loading, which consequently reduced the free gold electrode surface, further confirming the surface coverage by MoS_2 nanosheets.

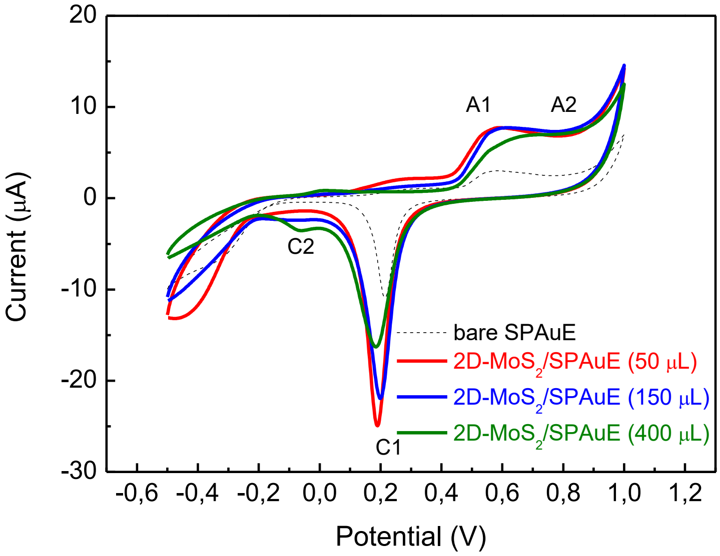

Figure III.9. Electrochemical behavior of bare and modified gold SPE electrodes, in the -0.6-1.2 V potential window. CV was performed in air-saturated 0.1 M PBS at a scan rate of 50 mV/s.

I.2. Bare and 2D-MoS$_2$ modified screen printed gold electrodes in presence of Tyrosine

CV curves of the modified 2D-MoS$_2$/SPAuE gold electrodes at different loadings in presence of Tyr showed interesting features. First, the intensity of all peaks was much higher on the modified electrode (Fig.III.10, red, blue, green lines) than on the unmodified one (Fig.III.10, black dashed line). The peaks A1 and C1 followed the same trend observed in the narrow potential range, while the intensity of the A2 and C2 peaks increased with increasing the 2D-MoS$_2$ loading.

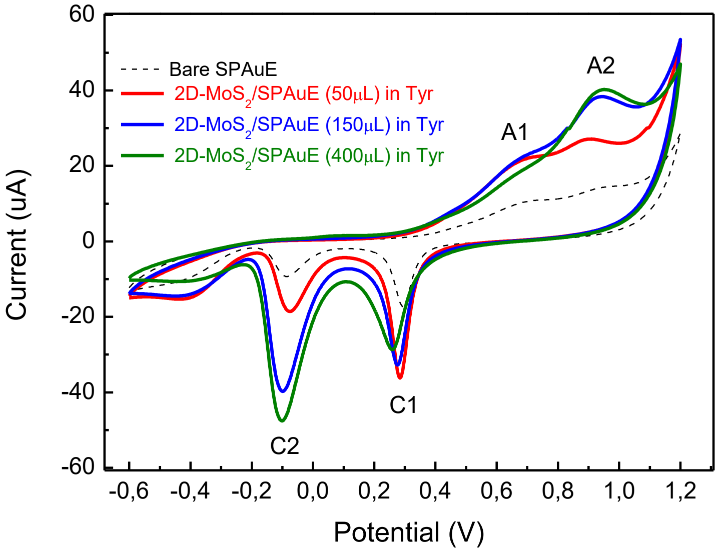

Figure III. 10. CV of 2D-MoS₂/SPAuE, in the -0.6 – 1.2 V potential window, performed in 0.1 M PBS electrolyte and in the presence of 500 μM of tyrosine, at a scan rate of 50 mV/s.

I.2.a. Electroanalytical behavior of gold electrodes in presence of different Tyrosine concentrations

Electroanalytical behavior of gold electrodes in presence of different Tyrosine concentrations was investigated. Here, 2D-MoS_2/SPAuE (400μL) was tested. Voltammetric measurements were performed in the wider potential range (-0.6 - 1.2 V). The A2 and C2 peaks intensity (Fig.III.11.a) increased remarkably with Tyr concentration. The current variation of the C2 peak at different Tyr concentration, is highlighted in Fig.III.11.b. Calibration curves for different loadings of 2D-MoS_2 are displayed in Fig.III.11.c-d. The current enhancement saturated when the loading overcomes 250 μL (Fig.III.11.c., pink and green symbols). The sensor's behavior displays two different linear ranges at low and high concentrations. In the linear range 0 –100 μM, the sensitivity is maximum (≈ 1580 μA mM^{-1} cm^{-2}) considering the cathodic C2 peak variations (Fig.III.11.d.). LOD, computed at a S/N = 3, is 0.5 μM. Sensitivity and LOD values compare well with other previous reports.

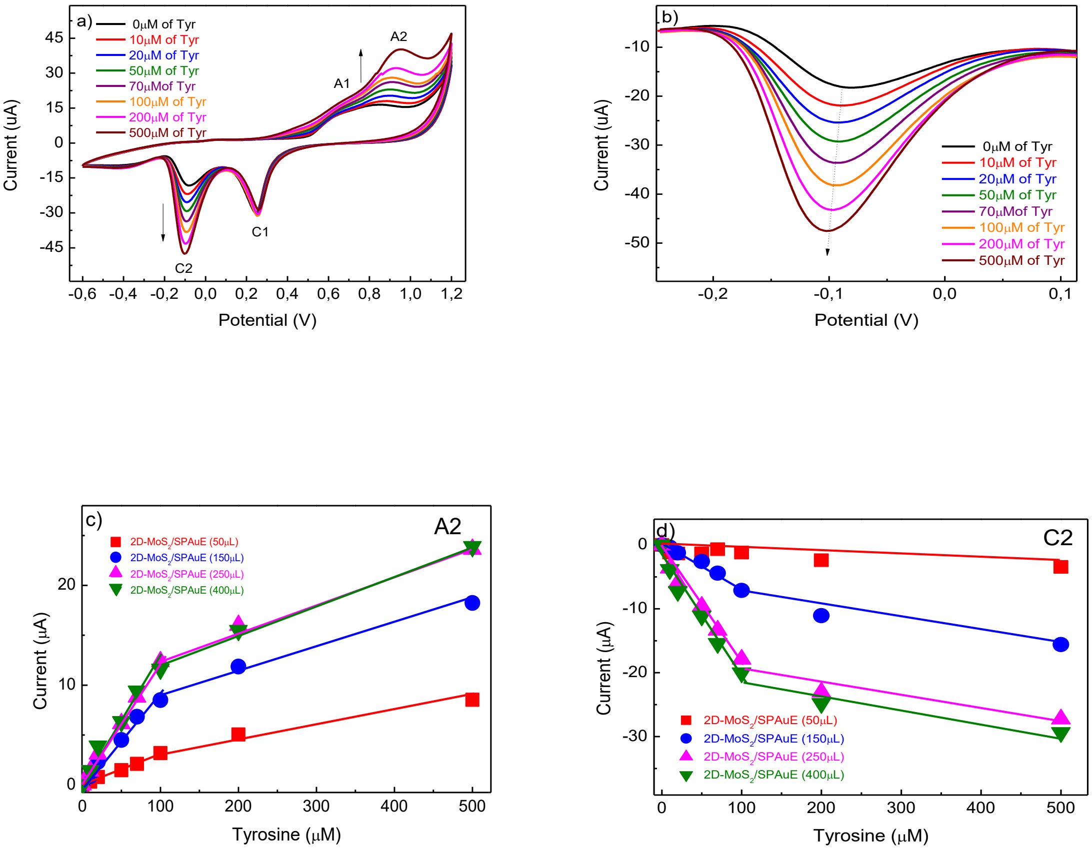

Figure III.11. a) CV of 2D-MoS$_2$/SPAuE (400μL) in 0.1 M PBS electrolyte and in the presence of different concentrations of Tyr, at a scan rate of 50 mV/s. b) Current variations of C1 peak vs. Tyr concentration. c-d) Calibration curves for the voltammetric determination of tyrosine at peak A2 and C2, respectively, with the modified 2D-MoS$_2$/SPAuE electrodes.

I.2.b. Effect of scan rate

Studies were performed while monitoring the current peak as a function of the scan rate (v) in the range of 50 – 400 mV/s . All modified electrodes showed the same behavior that's why only one plot will be presented (see Fig.III.12.a). The peak current increased linearly with the scan rate (see Fig.III.12.b), for all the peaks considered, indicating the occurrence of a surface-controlled process. As the scanning rate increased, the potential peak shifted positively for anodic processes and negatively for cathodic processes, which is typical of irreversible reactions.

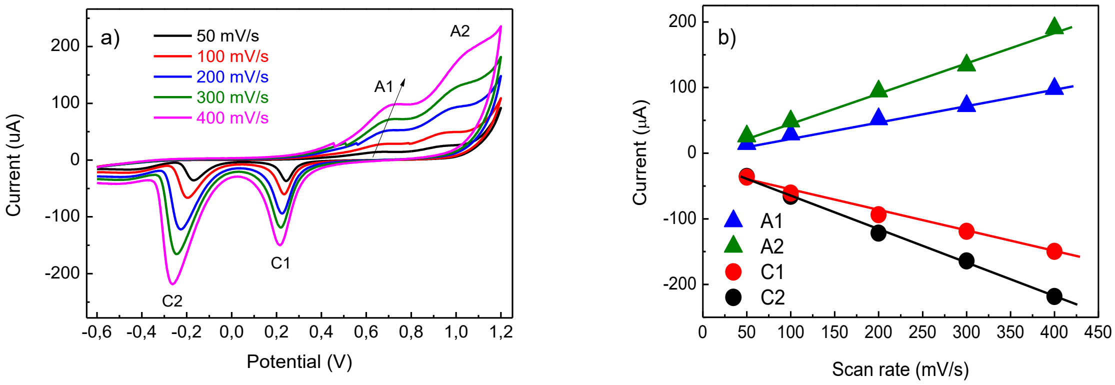

Figure III.12. a) CV of 2D-MoS$_2$/SPAuE, in the -0.6 – 1.2 V potential window, performed in 0.1 M PBS electrolyte and in the presence of 200 µM of tyrosine, at different scan rate b) Plot of the current peak vs scan rates of the different observed peaks.

II. 2D-Molybdenum disulfide modified carbon electrode for Tyrosine detection

II.1. Bare and 2D-MoS$_2$ modified screen-printed carbon electrode in absence of Tyrosine

The electrochemical behavior of unmodified carbon SPEs and 2D-MoS$_2$ modified screen printed electrodes was assessed by CV in 0.1 M PBS electrolyte at a scan rate of 50 mV/s. First, the electrodes were cycled in the potential range between 0 and 0.8 V. In these conditions, no peaks were observed on the unmodified carbon electrodes (Fig.III.13, black dashed line). 2D-MoS$_2$/SPCE exhibited, instead, a larger CV cycle (Fig.III.13, red line), likely due to the higher surface area compared to the bare carbon electrodes. In the anodic direction, a process started to appear at about 0.6 V, likely due to oxygen evolution reaction (OER). No peak was observed, instead, in the cathodic direction.

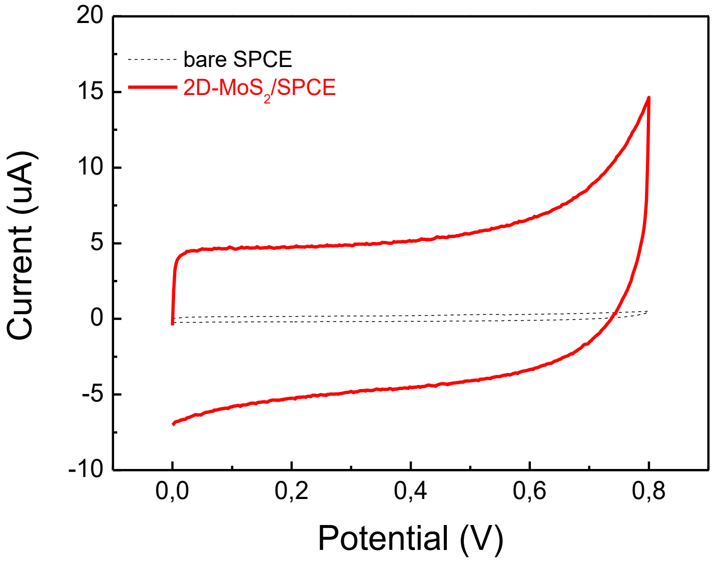

Figure III.13. Electrochemical behavior of bare SPCE and 2D-MoS$_2$/SPCE in the 0 – 0.8 V potential window. CV was performed in air-saturated 0.1 M PBS electrolyte 50 mV/s.

II.1.a. Effect of the potential window

As done in the previous study using gold electrodes, the effect of a wider potential window (−0.6 to 1.2 V) on the electrochemical behavior of the sensor was also evaluated (Fig.III.14). However, except for the rise of the anodic current due to the evolution of oxygen, appearing at a potential more positive than 0.8 V, no peak was noted on the unmodified SPCE and 2D-MoS$_2$/SPCE. Even in presence of tyrosine, no evident enhancement of the oxidation peak for this analyte was observed. This suggests that, for the 2D-MoS$_2$/SPCE, a narrow potential window between 0 and 0.8 V is sufficient for the electroanalytical determination of tyrosine.

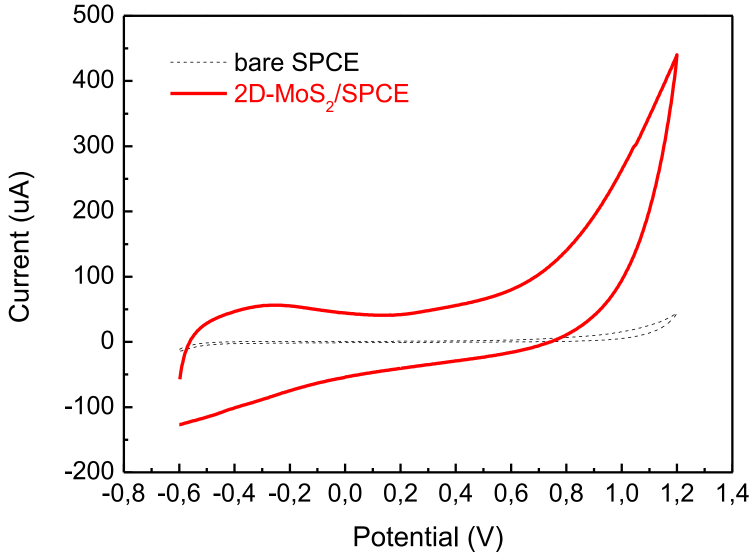

Figure III.14. Electrochemical behavior of the bare and the modified carbon electrode , in the -0.6 - 1.2 V potential window. CV was performed in air-saturated 0.1 M PBS at a scan rate of 50 mV/s.

II.2. Bare and 2D-MoS$_2$ modified screen printed carbon electrode in presence of Tyrosine

Subsequently, the effect of tyrosine addition was investigated. Upon addition of 500 µM of tyrosine, the bare SPCE showed an anodic wave at about 0.7 V, attributed to the irreversible oxidation of Tyr on the carbon nanostructured surface (see Fig.III.15, black line).

On the modified 2D-MoS$_2$/SPCE electrode (see Fig.III.15, red line), the tyrosine oxidation peak was characterized by a higher peak current and a lower potential (0.58 V) whereas no reduction was clearly observed for both bare and modified SPCEs.

The better performances of the modified electrode can be associated with an enhanced electrocatalytic oxidation activity toward tyrosine of the 2D- MoS$_2$ sensing layer which provide more surface area and sufficient electron transfer.

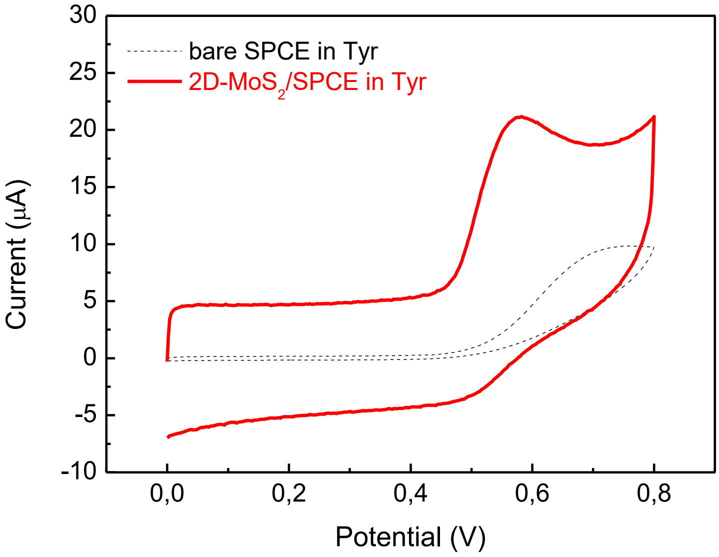

Figure III.15. Electrochemical behavior of the bare and the modified carbon electrode, in the 0 – 0.8 V potential window in presence of 500 µM of Tyr. CV was performed in air-saturated 0.1 M PBS at a scan rate of 50 mV/s.

II.3. Electroanalytical behavior of carbon electrodes in presence of different Tyrosine concentrations

II.3.a. Linear Sweep voltammetry

Since the tyrosine's oxidation is more evident than its reduction, linear sweep voltammetry was used to deeply inverstigate the electrochemical behaviour of the bare and the modified screen printed carbon electrodes as well as the effect of the nanosheets loading on it activity.

- *Effect of 2D-MoS$_2$ loading*

Tyr detection was carried out with carbon electrodes, both unmodified and modified with MoS$_2$. On both carbon electrodes, the irreversible tyrosine oxidation current peak intensity increased with increasing the concentration. The modified electrodes featured, however, a larger signal variation. The calibration curves in Fig.III.16, evidenced the enhancement of the current with the increase of the 2D-MoS_2 loading. This is related to the intrinsic electrocatalytic activity of 2D-MoS_2 [18, 19].

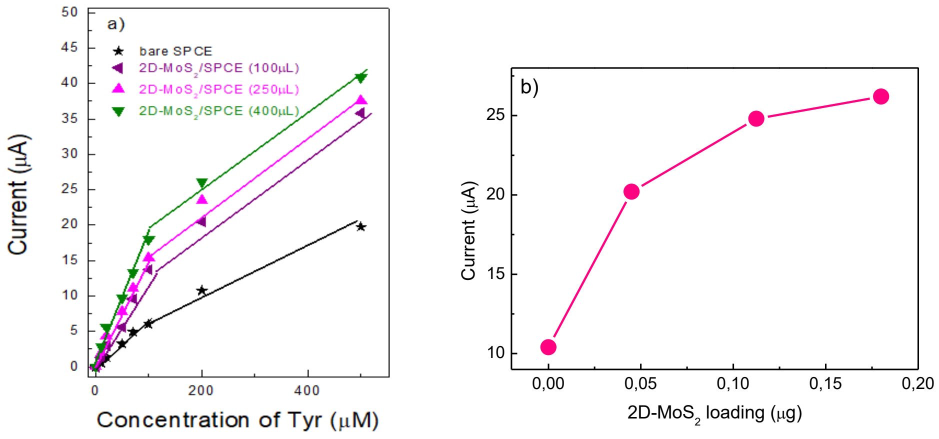

Figure III.16. a) Calibration curves of different modified carbon electrodes for the determination of Tyr, b) Current vs. 2D-MoS_2 nanosheets loading.

❖ *Linear Sweep voltammogram*

From the study done in the previous paragraph, the best modified 2D-MoS_2/SPCE was used for the quantitative study of Tyr using linear sweep voltammetry. In Fig.III.17.a, the LSV of solutions containing different Tyrosine concentrations is reported and in Fig.III.17.b, the corresponding calibration curve is presented.

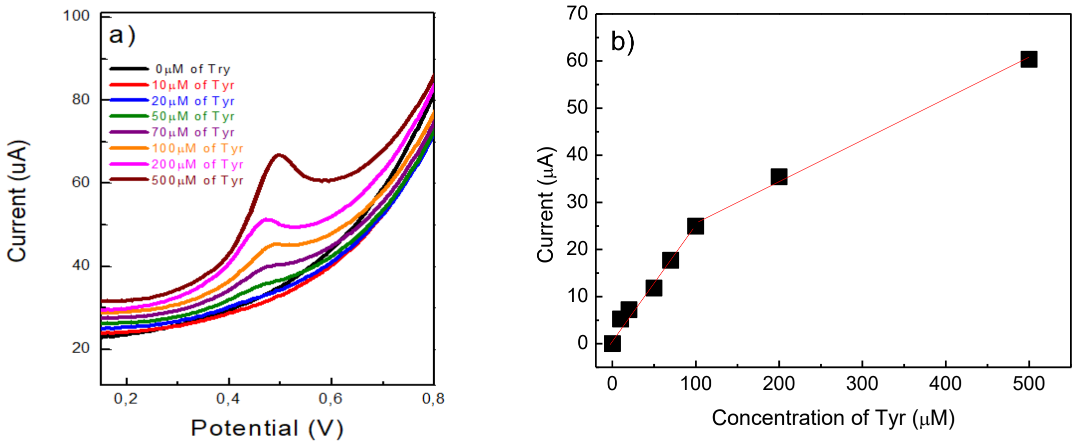

Figure III.17. a) LSV of 2D-MoS_2/ SPCE (400μL) in 0.1 M PBS in presence of different Tyr concentrations at a scan rate of 50 mV/s, b) Calibration curve for the determination of Tyr.

II.3.b. Chronoamperometry

Chronoamperometry was also applied to evaluate the detection capabilities of tyrosine with modified 2D-MoS_2/SPCE electrodes under a constant applied potential (0.6 V vs. Ag/AgCl). Fig.III.18.a displays the current response upon step-wise addition of Tyr. The oxidation current rapidly increased with the Tyr concentration up to 617 µM. The corresponding calibration curve is reported in Fig.III.18.b.

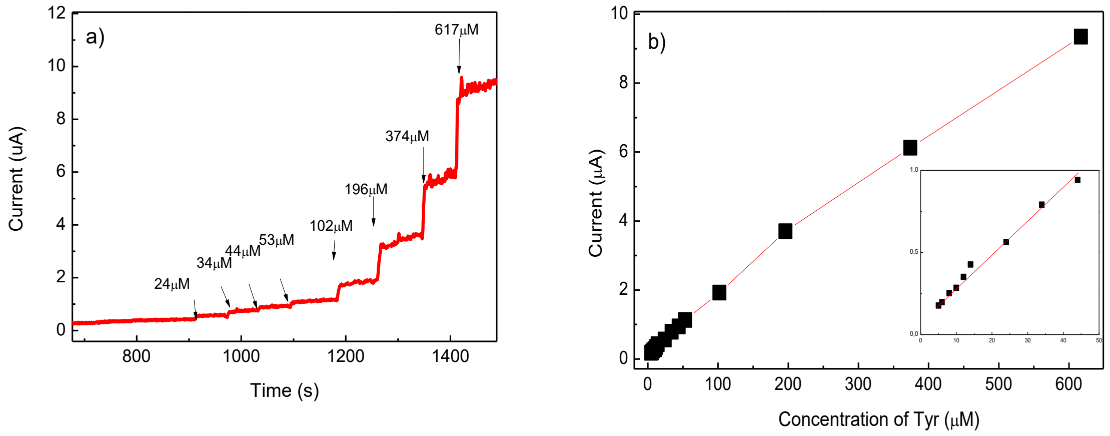

Figure III.18. a) Current–time responses with successive addition of tyrosine at 2D-MoS_2/SPCE electrode in 0.1 M PBS electrolyte at 0.6 V. b) Calibration curve for the determination of tyrosine. The inset displays the calibration curve in the lower concentration range.

The plot in the inset highlights the dynamic linear range of Tyr (0–200 µM), which results wider compared to previous reports and corresponds to the optimal range of Tyr in plasma which is between 38- 100 µM [20]. A linear fit of the current-concentration dependence in the very low concentration range (0–50 µM) yields a sensitivity of 148 µA mM^{-1} cm^{-2}. The modified 2D- MoS_2 carbon electrode can therefore be used for determination of Tyr also exploiting the amperometric method.

II.4. Determination of Tyrosine in a commercial food integrator

To demonstrate a practical application of the developed 2D-MoS_2 based sensors, a quantitative determination of Tyr in a commercial food integrator (Natural Point srl, 500 mg) was performed. A tablet was dissolved in water and further diluted with PBS. Both modified carbon and gold electrodes were tested, performing the CV tests and evaluating the peak current. Recovery values were evaluated as:

$$\text{Recovery (\%)} = (\text{mg Tyr found/mg Tyr expected}) \times 100$$

The results obtained in three different measurements were averaged and the relative standard deviation (RSD) was calculated (Table III.3). A good agreement is obtained between the Tyr quantity reported by the manufacturer and the one quantified by the sensors. Recovery values found were 98.2% (RSD = 4.3%) for the modified gold 2D-MoS_2/SPAuE (400µL) sensor and 104.4% (RSD = 3.0%) for the modified carbon 2D-MoS_2/SPCE (400µL) one. The gold electrochemical platform provided the best performances. Finally, the stability of the sensor was evaluated, by performing tests after storage of the sensor for 1 month in ambient conditions. The sensor retained 93.6% of the initial response, which indicated a good long term stability.

Sensor	Expected (mg Tyr/tablet)	Found (mg Tyr/tablet)	Recovery (%)	RSD (%)
2D- MoS_2/SPCE	500 mg	522 mg	104.4	4.3 (n=3)
2D- MoS_2/SPAuE	500 mg	491 mg	98.2	3.0 (n=3)

Table III.3. Determination of tyrosine in a real food integrator sample.

III. Conclusion

2D-MoS_2 nanosheets produced via LPE were used to modify gold and carbon screen printed electrodes aimed at developing an enzyme-free electrochemical sensor for the determination of tyrosine. The performances improvement of these sensors in physiological pH conditions are attributed to ultra-small size of MoS_2 as well as to the morphological and textural properties of underlying carbon and gold electrodes facilitating the electron and mass transfer. The electroanalytical determination of tyrosine in real samples can be accomplished with good performances.

Chapter 3

Electrochemical tests of Batch "B"

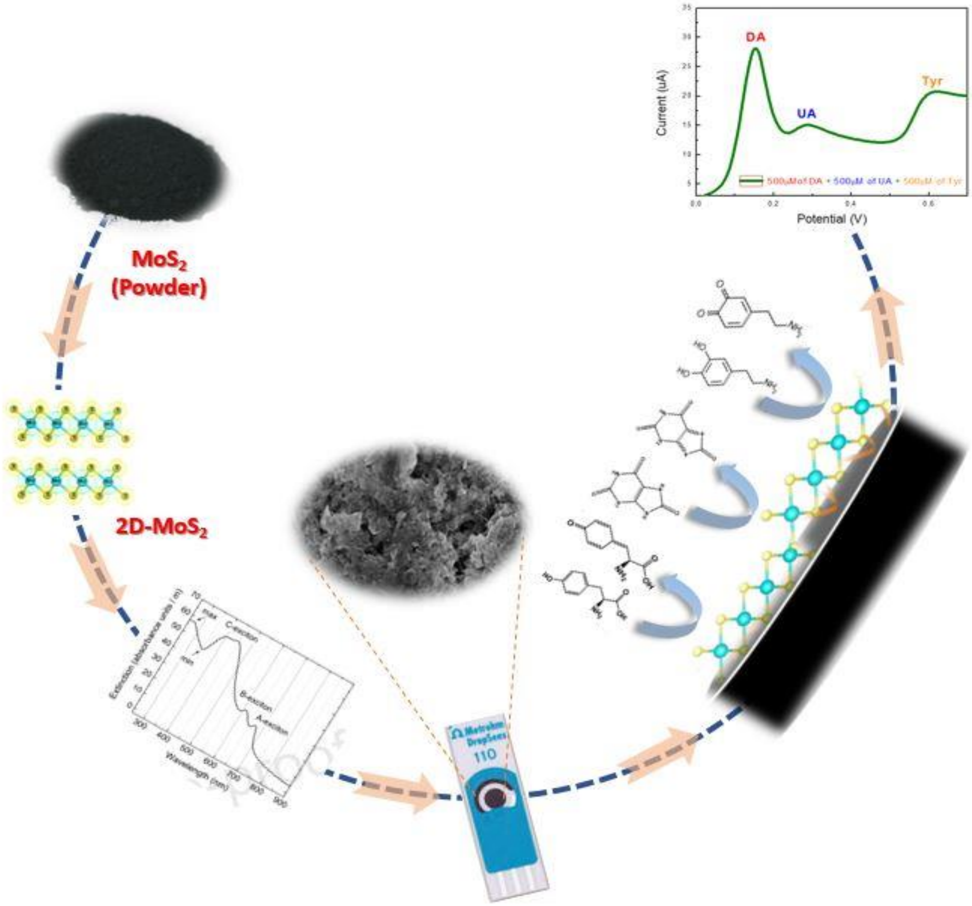

Overview

This chapter will highlight the simultaneous and selective determination of tyrosine and dopamine in the presence of uric acid using the 2D-MoS_2 prepared for the batch “B” previously prepared via liquid phase exfoliation. The following paper was published from the research developed in this chapter [Zribi, R.; et al. FlatChem, 2020, 24, 100187].

I. 2D-Molybdenum disulfide modified carbon electrode for Tyrosine and Dopamine detection

As demonstrated in the previous paragraph in the characterization of the two batches “A” and “B”, the 2D-MoS_2 suspensions obtained for batch “B” were richer in nanosheets compared to batch “A”.

For this reason, further electrochemical sensors were developed for the simultaneous and selective determination of tyrosine and dopamine (DA) in presence of uric acid (UA). The choice of these analytes wasn’t random but, as mentioned in the introduction section, Tyr is a precursor amino acid for DA while UA is a natural waste product and a famous interferent biomolecule in the selective studies.

I.1. Electrochemical behavior in presence of Dopamine and Tyrosine

The electrochemical behaviours of the bare SPCE and 2D-MoS_2/SPCE were evaluated by cyclic voltammetry (CV) in aerated 0.1 M phosphate buffer solution (PBS) in the 0–0.8 V potential window and at a scan rate of 50 mV/s (Fig.III.19.). Previously, it was noted that, compared to bare SPCE electrodes, 2D-MoS_2/SPCE electrodes exhibit a larger CV cycle, likely due to the high surface area of 2D-MoS_2 nanosheets. First, the 2D-MoS_2/SPCE electrodes were cycled 20 times in a PBS solution (0.1 M, pH = 7.4), for stabilization purposes. In this condition, no peak was observed (Fig.III.19.a-b, black dashed lines). Then, electrochemical tests were carried out in presence of DA and Tyr (500 µM in 0.1 M PBS). The CV curve of DA, shown in Fig.III.19.a. (red line), is characterized by the presence of an anodic peak at 0.16 V, related to the oxidation of DA followed by a cathodic peak corresponding to its reduction. Concerning Tyr, the CV is characterized by a peak current at 0.57 V (Fig.III.19.b. red line). The better sensitivity of the modified electrode comparing to the bare one can be associated to the increasing of the effective surface area of the working electrode which leads to an improvement of the electrocatalytic oxidation activity toward DA and Tyr.

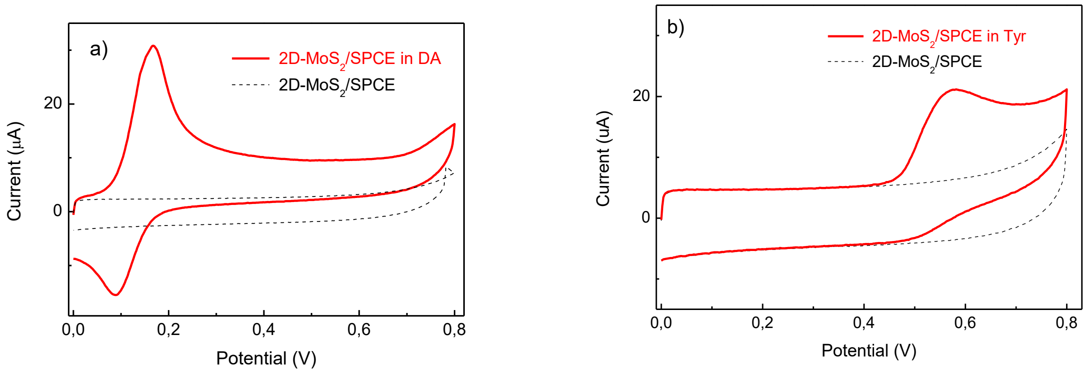

Figure II.19.Electrochemical response of 2D-MoS$_2$/SPCE modified electrode in absence (black dashed lines) and presence (red lines) of 500 µM of: a) DA and b) Tyr. Scan rate 50 mV/s.

I.2. Effect of 2D-MoS$_2$ loading

First, the effect of 2D-MoS$_2$ nanosheets loading on SPCE electrodes was investigated. SPCEs were modified adding various volumes of 2D-MoS$_2$ nanosheets suspension having a concentration about 80 µg/mL. Results of the electrochemical investigation of DA (500 µM) are shown in Fig.III.20. It is clear that there is an optimal 2D-MoS$_2$ loading on the carbon surface leading to maximization of current variation. Indeed, initially the current increases almost linearly with the volume of 2D-MoS$_2$ (up to 100 µL) deposited on the bare electrode, then start to decrease. The same behaviour was also recorded in presence of Tyr. Comparing to the same study done in the chapter 2 of Section III, this finding seems to be so reasonable for the fact that suspensions prepared for batch “B” were richer in 2D-MoS$_2$ nanosheets comparing to batch “A”. That’s why in this case, there is no need to deposit a high volume of 2D-MoS_2 to obtain the maximum response. By considering the result obtained, SPCE electrode with 8 µg which corresponds to 100 µL of 2D-MoS_2 was used in the subsequent experiments.

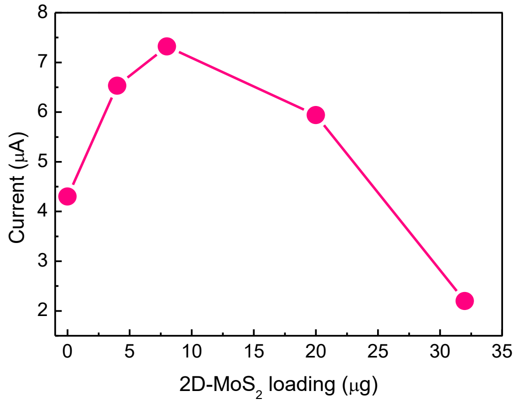

Figure III.20. Current registered in presence of DA (500 µM) vs. 2D-MoS_2 loading deposited on the bare SPCE electrode.

I.3. Effect of scan rate

CV curves were acquired as a function of the scan rate in the range 50 – 400 mV/s on DA and Tyr at a concentration of 500 µM in 0.1 M PBS. Results are displayed in Fig.III.21.a-c. For both analytes, the peak current increased linearly with the scan rate (Fig.III.21.b-d), indicating the occurrence of surface-controlled processes, whereas the positive potential peak shift is typical of irreversible reactions.

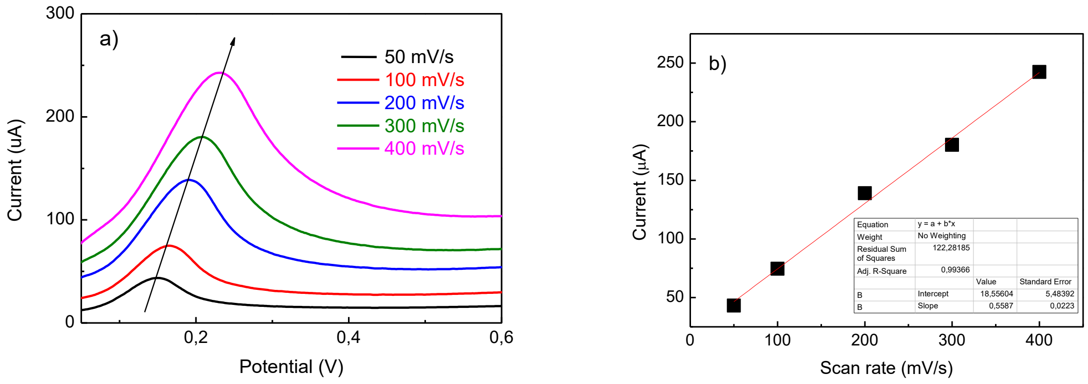

Equation	y = a + b*x		
Weight	No Weighting		
Residual Sum of Squares	122,28185		
Adj. R-Square	0,99366		
		Value	Standard Error
B	Intercept	18,55604	5,48392
B	Slope	0,5587	0,0223

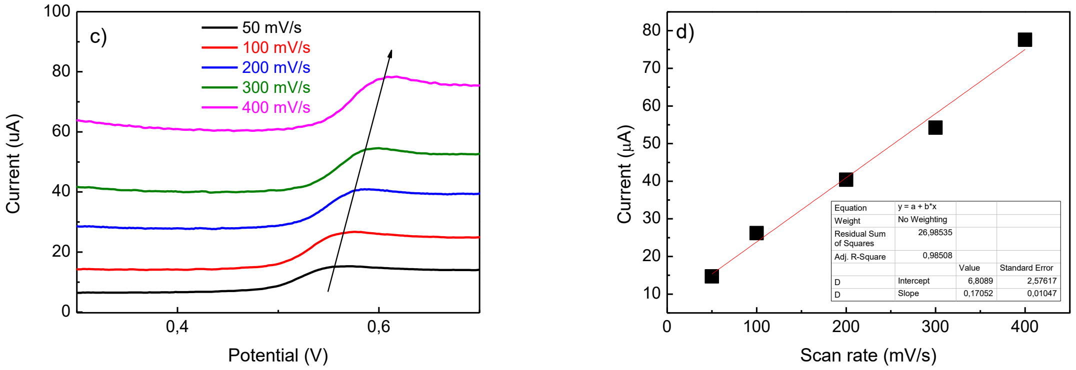

Figure III.21. CV response of DA (a) and Tyr (c) as a function of the scan rate variation. Peak current dependence on the scan rate for DA (b) and Tyr (d). Red lines indicate the linear fits of the data. DA and Tyr concentration is 500 µM.

I.4. Electrochemical sensitivity of the modified electrodes

Based on the good electrochemical response of the 2D-MoS_2/SPCE electrodes, their potentials for quantitative determination of DA and Tyr were investigated (Fig.III.22). In Fig.III.22.a-b is reported the LSV analysis of solutions containing different concentrations of Tyr (0 to 500 µM) and DA (0 to 100 µM). Experimental conditions are the same as applied to obtain the above CV curves. While in the Fig.III.22.c-d is reported the calibration curves for DA and Tyr, in which the peak current as a function of the analyte's concentration is plotted.

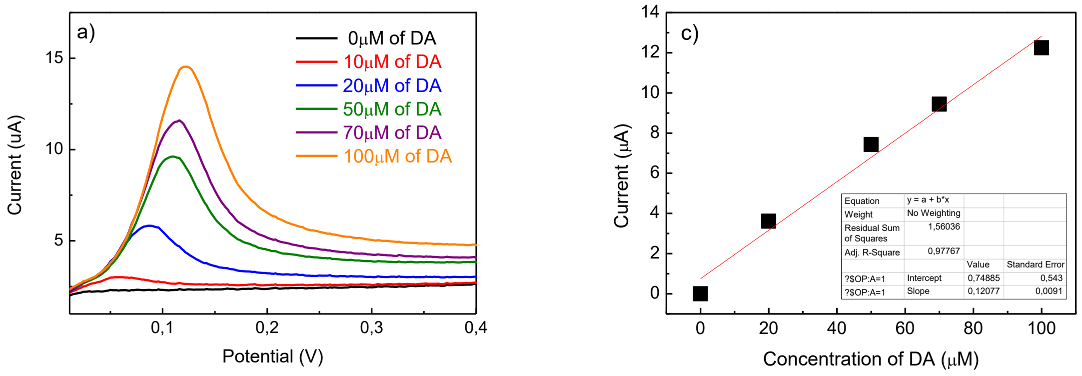

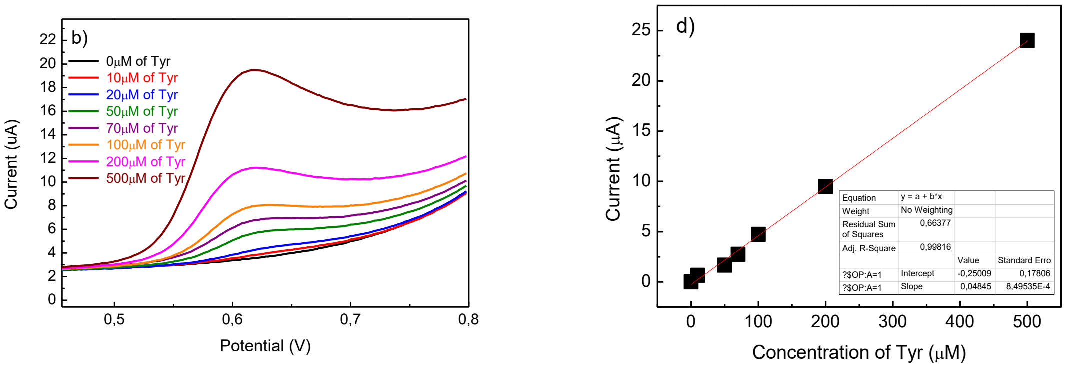

Figure III.22. LSV of 2D-MoS$_2$/SPCE, performed in 0.1 M PBS electrolyte and in the presence of different concentrations of a) DA and b) Tyr, at a scan rate of 50 mV/s. Calibration curve for the determination of c) DA and d) Tyr.

In addition to single determinations, 2D-MoS$_2$/SPCE was also investigated for the possibility to detect DA and Tyr simultaneously. LSV with 2D-MoS$_2$/SPCE sensor highlights the separation between the peaks related to the two analytes (Fig.III.23).

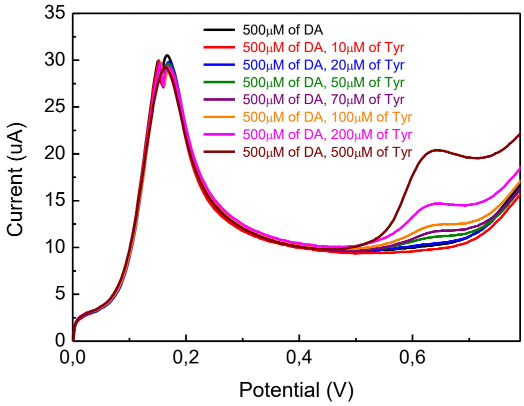

Figure III.23. LSV of 2D-MoS$_2$/SPCE, performed in 0.1 M PBS and in the co-presence of DA and Tyr at different concentrations.

II. Simultaneous electroanalytical determination of tyrosine and dopamine in presence of uric acid

UA coexists with DA and Tyr in human body fluids [21-23]. So, the 2D-MoS$_2$/SPCE was also investigated to detect DA and Tyr simultaneously in the presence of UA. FigIII.24 presents the LSV curve obtained when the three analytes are present simultaneously in the solution, each at the same concentration (500 µM). Three distinct peaks at different potential were observed as shown in Fig.III.24.

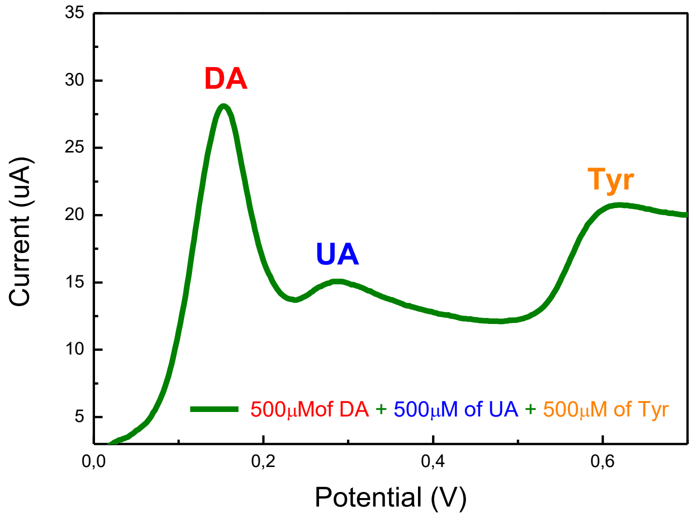

Figure III.24. LSV curve in co-presence of DA, Tyr and UA at concentration of 500 µM , each, in 0.1 M aerated PBS at scan rate 50mV/s.

Fig.III.25.a–c display LSV for DA and Tyr on the modified electrode in presence of uric acid :

a) In the first case (a), UA was kept at 500 µM and DA ranged from 0 to 50 µM,
b) In the second (b), UA concentration was fixed at 50 µM and Tyr concentration was varying from 50 to 100 µM,
c) In the third (c), Tyr at 500 µM was fixed and the concentration of UA was varying from 0 to 200 µM.

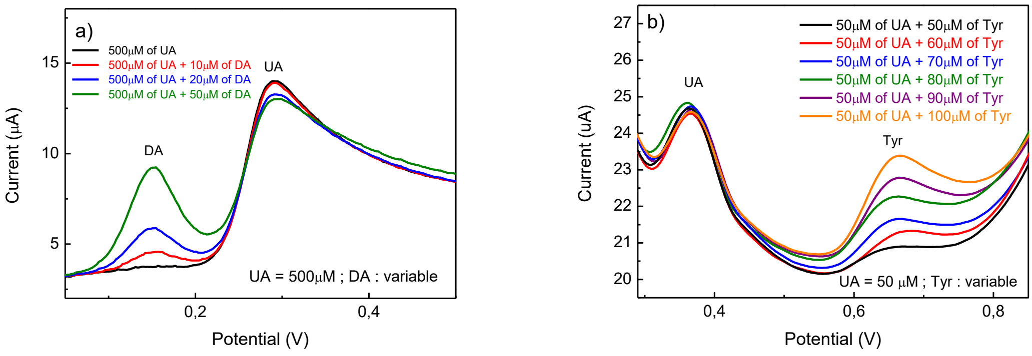

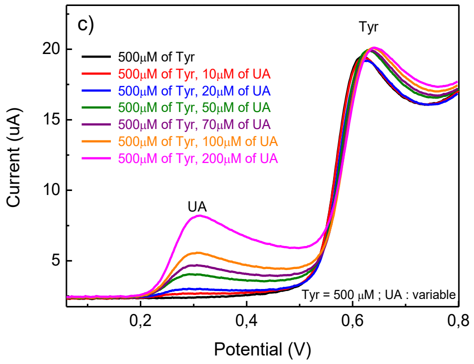

Figure III.25. LSV curves acquired in solutions with the co-presence of a) Dopamine at variable concentration and Uric Acid at constant concentration; b) Tyrosine at variable concentration and Uric Acid at constant concentration; c) Tyrosine at constant concentration and Uric Acid at variable concentration. All tests were performed in aerated 0.1 M PBS as electrolyte.

Square wave voltammetry was also used to detect simultaneously Tyr and DA in presence of UA. Comparing the two analytical methods together, we assume that LSV provides higher sensitivity, lower LOD and less interference phenomena.

It appears clear that the presence of UA at concentrations of 500 μM and 50 μM has no significant effect on the detection of DA and Tyr, respectively. In both cases, it is confirmed that the sensitivity of the electrode in detecting the DA and Tyr is almost independent on the presence or not of uric acid, as reported in the Table III.4. (sensitivity is in terms of (μA μM^{-1} cm^{-2})**)**

Analytes	**Sensitivity in absence of UA**	**LOD (μM)**	**Sensitivity in presence of UA**
Dopamine	1044	0.085	1016
Tyrosine	321	0.5	316

Table III.4. Comparison of the sensor's sensitivity towards dopamine and tyrosine in absence and presence of uric acid.

A comparison with previous sensors proposed in the literature for the simultaneous detection of dopamine and tyrosine has been also made. The presented sensor exhibits a large linear range for both analytes with limit of detection (LOD) comparable to previous sensors. Dopamine is known to poison hardly the surface of electrodes, through the formation of polydopamine, leading to a rapid deterioration of the electrode performances. Therefore, the stability of the developed electrode has been investigated. LSV measurements in presence of 500 µM dopamine were repeated for many cycles, showing no remarkable variation of the anodic peak current and potential (see Fig.III.26).

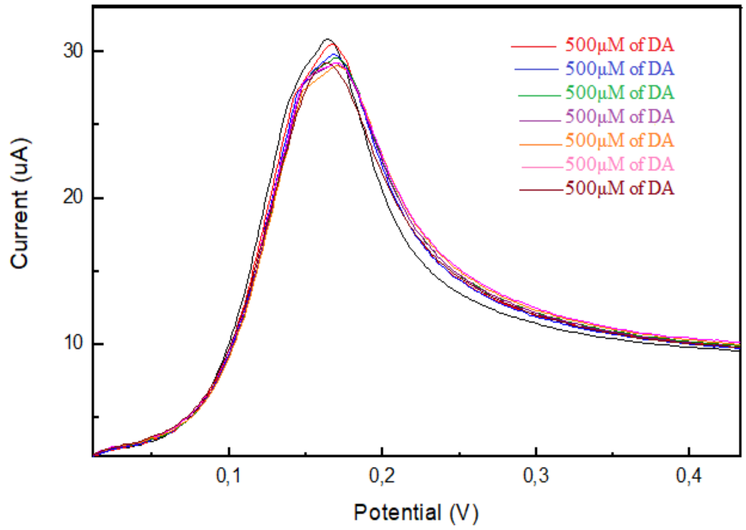

Figure III.26. Repeated cycles of LSV measurements in presence of 500 µM dopamine on the 2D-MoS$_2$ nanosheets modified screen-printed carbon electrode.

To check the long term stability of our electrode, measurements on a time span of 4 months have been carried, detecting periodically the anodic peak current of DA at a concentration of 25 µM. Results indicated that after a period of 4 months, 70% of the initial current is still retained, suggesting good stability of the electrode.

III. Conclusion

2D-MoS$_2$ were casted onto the surface of the SPCE, and have been used for the electrochemical detection of dopamine and tyrosine in presence of uric acid. The large surface area and electrocatalytic activity of 2D-MoS$_2$ are responsible of the great increase of the adsorption and redox reaction of DA and Tyr. The efficiency of the modified electrode was evaluated for the simultaneous and quantitative detection of both analytes by using LSV. The sensor shows outstanding performances, excellent stability, good reproducibility and negligible interference from uric acid.

Chapter 4

Electrochemical tests of Molybdenum disulfide/Molybdenum Oxide - Carbon Cloth composite

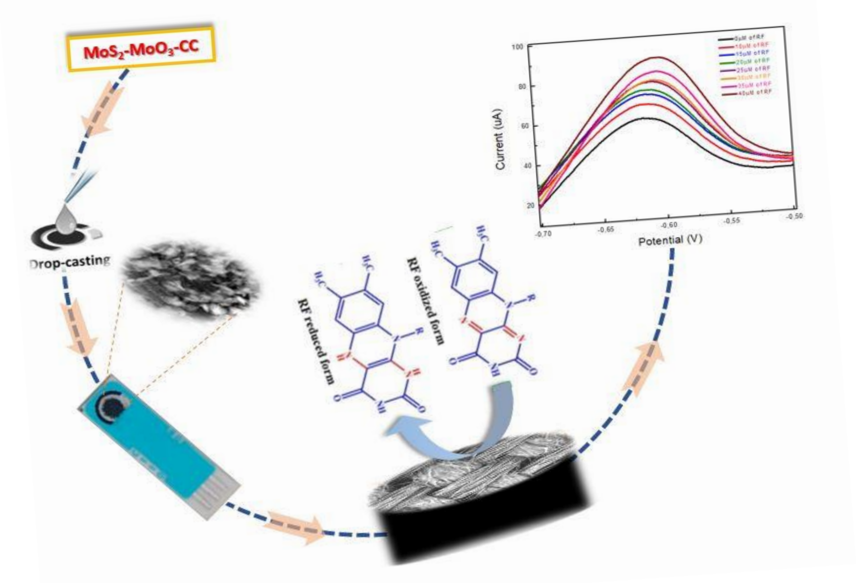

Overview

This chapter will highlight the enhancement produced by the addition of molybdenum disulfide nanosheets, produced for batch “B” via LPE, on a molybdenum oxide-doped carbon cloth in the electrochemical determination of riboflavin. The following paper was published from the research developed in this chapter [Zribi, R.; et al. Sensors, 2021,21,1371].

I. Electrochemical characterization of molybdenum disulfide/ molybdenum oxide-carbon cloth composite

I.1. Scan rate effect in PBS

A series of electrochemical tests has been carried out to characterize the bare screen-printed carbon electrodes and the modified ones. Preliminary CV tests have been conducted in 1 M PBS. Fig.III.27.a compares the CV spectra of the bare SPCE and all modified SPCEs at 50 mV/s. The strong enhancement of the background current of the modified SPCEs, is due to its large electrochemical double-layer capacitance (EDLC). Cyclic voltammograms of the fabricated electrodes at different scan rates have been also collected. As expected, the scan rate amplifies the capacitive current. This is well evident for the modified electrodes, due to the exposure of more active sites on the working electrode’s surface. Plotting the scanning rate versus the current for all electrodes (Fig.III.27.b), a series of straight lines were obtained, allowing us to estimate the EDLC for these electrodes from the slope and the geometrical area.

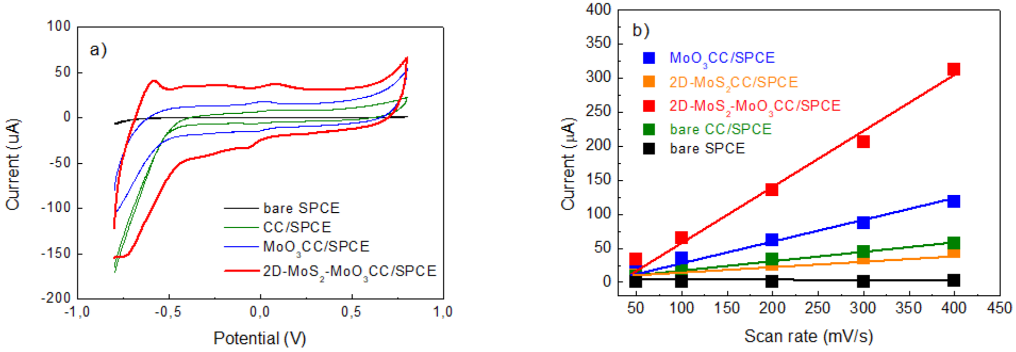

Figure III.27. a) CV of bare and all modified electrodes in 1 M PBS; b) plot of the capacitive current of the different modified electrodes vs scan rate in 1 M PBS.

These data show that the EDLC of the CC/SPCE (green line) has largely grown compared to the bare SPCE (black line). The EDLC is higher by nearly a factor 2 when the MoO_3 layer is grown on CC/SPCE (blue line) and undergoes a further strong enhancement when the 2D-MoS_2 nanosheets are deposited (red line). The 2D-MoS_2-MoO_3CC/SPCE composite electrode shows the highest EDLC (red line). This suggests that the network structure of CC is able to provide a larger surface area compared to bare SPCE, which is further increased in the presence of the layered MoO_3 and hybrid 2D-MoS_2-MoO_3 structure.

I.2. Scan rate effect in redox probe $[Fe(CN)_6]^{3-/4-}$

The electron transfer capability of the various electrodes has been tested with $[Fe(CN)_6]^{3-/4-}$ as redox probe (10 mM in 1 M PBS) by varying the scan rate from 50 to 400 mV/s. In order to provide a quick comparison among the fabricated electrodes, Fig.III.28. displays the cyclic voltammograms obtained at a scan rate of 50 mV/s.

As can be noted, both the current peak intensity (Ip) and the peak-to-peak separation (ΔEp) depend on the investigated electrodes. ΔEp and Ip are helpful parameters as they can provide a qualitative estimation of the electron transfer rate due to the redox process at the electrode's surface. In Table III.5. it is reported the values of the anodic (Ipa) and cathodic (Ipc) current peaks, together with the value of ΔEp for the bare SPCE, the modified CC/SPCE, the MoO_3CC/SPCE, and 2D-MoS_2-MoO_3CC/SPCE measured with 10 mM $[Fe(CN)_6]^{3-/4-}$ at a scan rate of 50 mV/s.

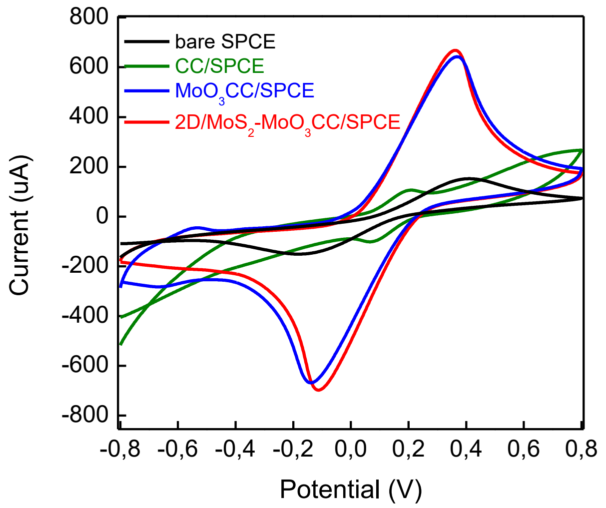

Figure III.28. Cyclic voltammograms performed in 10 mM [Fe(CN)$_6$]$^{3-/4-}$ at a scan rate of 50 mV/s with bare SPCE (black line), CC/SPCE (green line),MoO$_3$CC/SPCE (blue line), and 2D-MoS$_2$-MoO$_3$CC/SPCE (red line).

Electrode	**I$_{pa}$ (µA)**	**I$_{pc}$ (µA)**	**ΔEp (V)**
SPCE	150	-150	0,57
CC/SPCE	110	-107	0.13
MoO$_3$-CC/SPCE	642	-664	0.46
2D-MoS$_2$-MoO$_3$/SPCE	671	-693	0.495

Table III.5. CV data of anodic (Ipa) and cathodic (Ipc) current peaks and ΔEp for the bare SPCE and the modified CC/SPCE, MoO$_3$CC/SPCE, and 2D-MoS$_2$-MoO$_3$CC/SPCE in 10 mM [Fe(CN)$_6$]$^{3-/4-}$ at a scan rate of 50 mV/s.

Lower ΔEp values and higher Ipa and Ipc are measured using the modified electrodes. These values suggest a faster electron transfer in the carbon cloth composite electrodes compared to bare SPCE likely resulting from a larger reaction surface area. Furthermore, the ΔEp values as well as the current peaks increase linearly with the square root of the scan rate (see Fig.III.29.for the anodic peak), indicating a diffusion-controlled process.

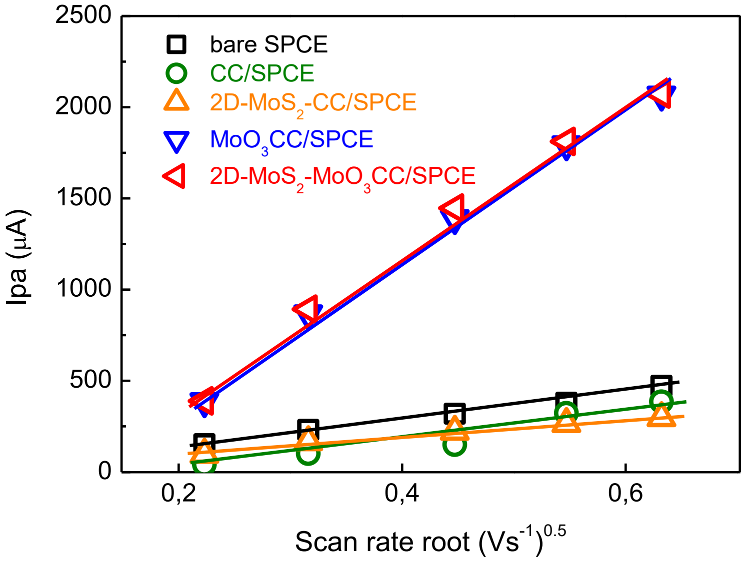

Figure III.29. Plot of the anodic peak current (Ipa) vs. scan rate root. Ipa values were derived by CVs performed with the different bare and modified SPCE in 10 mM $[Fe(CN)_6]^{3-/4-}$ at different scan rate.

These studies suggest that the electrochemical behavior of the bare electrode is improved after modification with CC-based 2D-MoS_2 and MoO_3 layer. Further, it is evidenced that MoO_3CC/SPCE and 2D-MoS_2-MoO_3CC/SPCE present almost similar electrochemical properties for the $[Fe(CN)_6]^{3-/4-}$ redox process, indicating that they have comparable EDLC and electron transfer capability.

II. Electrochemical detection of riboflavin

II.1. Comparative study of bare and modified electrodes in presence of riboflavin

The enhanced electrochemical performances of the 2D-MoS_2-MoO_3 layer on CC have been exploited to develop an electrochemical sensor for riboflavin detection. Here, the new electrode was tested on riboflavin (RF) at a concentration of 100 µM. Figure III.30.a shows the remarkable enhancement of the CV signal measured with the modified 2D-MoS_2-MoO_3CC/SPCE (red lines) compared to the bare SPCE (black lines) and MoO_3CC/SPCE (blue line). This behavior highlights the strong effect of the MoS_2 layer on RF electrocatalysis.

As regarding the CV of the 2D-MoS$_2$-MoO$_3$CC/SPCE (Fig.III.30.a, red line) in presence of riboflavin, at the starting potential -0.8 V, RF exists in its reduced form. At -0.55 V it undergoes an oxidation followed by a reduction at -0.72 V. In this redox reaction of RF, two protons and two electrons are involved.

Figure III.30.b. compares the current response of the different electrodes in the determination of RF. The sensor employing the modified 2D-MoS$_2$-MoO$_3$CC electrode has the highest sensitivity towards riboflavin, dwarfing the performances of other electrodes. The better sensitivity of the composite electrode can be associated to the increase of the effective surface area of the working electrode and the formation of new electroactive sites, formed at the interface between the MoO$_3$ and 2D-MoS$_2$ layers and this fact is improved by optimising the quantity of the 2D-MoS$_2$ deposited on the sensor.

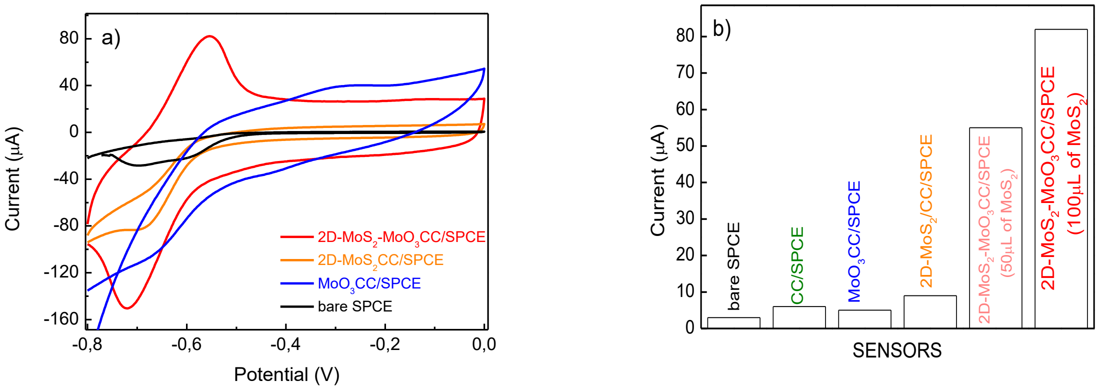

Figure III.30. a) CV of the bare and modified SPCEs in presence of 100 μM RF; b) comparison of the peak current obtained with the different electrodes in presence of 100 μM riboflavin (RF).

II.2. Electrochemical quantification of riboflavin

Based on the results discussed above, the 2D-MoS$_2$-MoO$_3$CC- based sensor have been used for the detection of riboflavin in solution at different concentrations. In Figure III.31.a, is reported the LSV analysis of solutions containing increasing concentrations of RF, from 0 to 40 μM, evidencing the associated increasing to the peak current value. In Figure III.31.b (black dots), is shown the calibration curves for RF, where the peak current is plotted as a function of the analyte concentration. The sensitivity of this composite based sensor is about 0.67 μA μM^{-1}, while LOD is 1.5 μM.

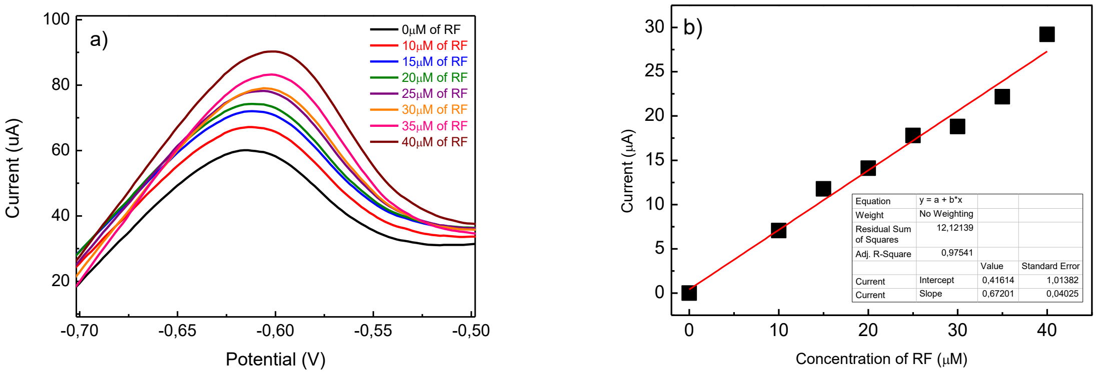

Figure III.31. a) Linear sweep voltammetry (LSV) of 2D-MoS_2-MoO_3CC/SPCE, performed in 1 M PBS electrolyte and in the presence of different concentrations of RF; b) Calibration curve for the determination of RF.

The performances of the proposed 2D-MoS_2-MoO_3CC/SPCE based sensor (linear range, sensitivity and limit of detection) have been compared to some reported riboflavin electrochemical sensors in table III.6. From this comparison, it can be deduced that this sensor platform displays a wide linear range and a high sensitivity comparing to the other sensors. (*sensitivity is in terms of μA μM^{-1}).

Electrode Modifier	Method	Linear Range	Sensitivity*	LOD	Ref.
Cr-SnO_2	DPV	0.2 nM–0.1 mM	0.047	0.11 nM	[24]
ssDNA-MoS_2-Gr	DPV	25 nM–2.25 mM	0.83	20 nM	[25]
Carbon cloth	AMP	5 nM–100 nM	-	2.2 nM	[26]
MnO_2	DPV	20 nM–9 μM	NA	15 nM	[27]
Co^{2+} -Y zeolite	CV	1.7–3.4 μM	NA	0.71 μM	[28]
MnO_2	DPV	2 μM–0.11 mM	NA	15 nM	[29]
2DMoS_2-MoO_3CC	LSV	2 μM–40 μM	0.67	1.5 μM	This work

Table III.6. Comparison of 2D-MoS_2-MoO_3CC/SPCE sensor's performance with other reported riboflavin electrochemical sensors.

II.3. Repeatability test

This test was repeated after about one year using a new prepared 2D-MoS_2 nanosheets suspension for replicating the fabrication of a new 2D-MoS_2-MoO_3CC/SPCE sensor in the same conditions of the first one. The calibration curves obtained by these tests are compared in Figure III.32. It can be clearly observed that the two set of data points can be both fitted well enough with the same linear relationship. The reported findings suggest that the electrochemical properties of the 2D-MoS_2-MoO_3CC network structure as well as the fabrication procedure of 2D-MoS_2-MoO_3CC/SPCE platform can be replicated very well, leading to different sensor devices with reproducible response.

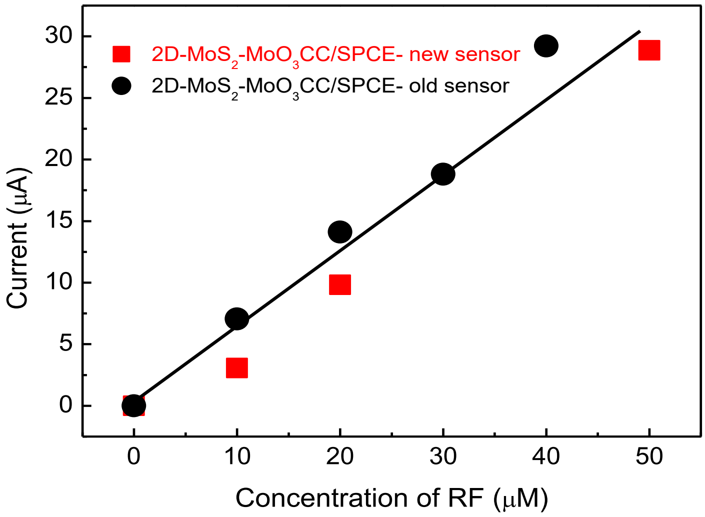

Figure III.32. Current responses versus riboflavin concentrations with two different 2D-MoS_2-MoO_3CC/SPCE sensors. The new sensor was fabricated about one year after the first sensor, using newly prepared 2D-MoS_2 nanosheets.

II.4. Interference test

The effect of some interferent biomolecules has been also investigated. Folic acid (FA), which is another vitamin of B group, and ascorbic acid (AA), a vitamin of C group, are considered as the main interferent analytes in the determination of RF. These two biomolecules are present in human body so it’s mandatory to verify if their presence affect the RF detection. Preliminary tests have shown that these compounds, in absence of RF, show no redox peak in the potential range where the RF peak is present. This is an expected result because, similarly to redox processes of most organic compounds, they take place in the positive potential range. The effect of FA and AA on the detection of riboflavin has been investigated with our 2D-MoS_2-MoO_3CC/SPCE sensor. The test has been carried out at different concentrations of RF in presence of the two analytes. The test confirm that the presence of the two interferent analytes decreases the RF current peak. This behavior can be explained assuming that FA and AA compete with RF for the interaction with a significant fraction of the active site on the sensing layer. The results indicate that the effects of interferents substances on the RF sensor response needs to be checked. Thus, it is planned to investigate in detail this aspect aiming to apply the developed sensor in real applications.

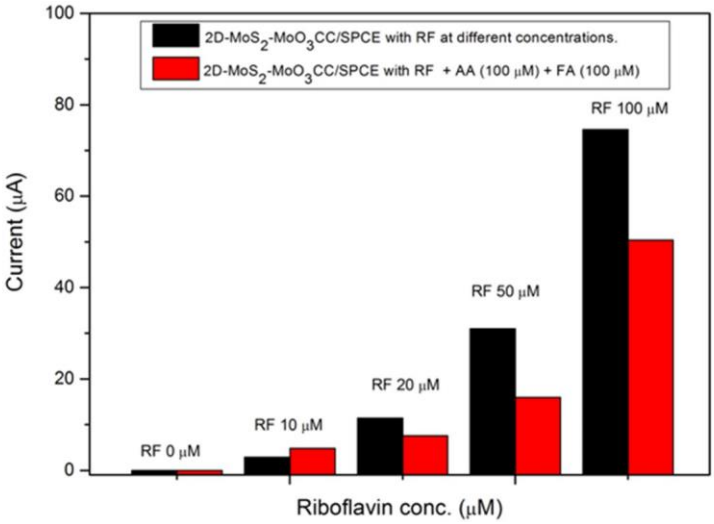

Figure III.33. Ipa current values registered by the 2D-MoS_2-MoO_3CC/SPCE sensor in presence of RF at different concentrations (black bars) and in co-presence (red bars) of FA and AA at 100 μM in 1 M PBS.

III. Conclusion

A 2D-MoS_2-MoO_3CC nanocomposite electrode was prepared and tested for the electrochemical detection of riboflavin in PBS. The modified platform was fabricated by layers of MoO_3 and 2D-MoS_2 nanosheets on the fiber of CC network structure. The structure was used for fabricating a novel electrochemical platform with enhanced properties with respect to the conventional commercial devices and those prepared with the single constituents. Interference from folic and ascorbic acid has been observed to decrease the sensitivity of the sensor for riboflavin, although not dramatically. As it is well known, the electrochemical characteristics of the biomolecules here investigated are largely dependent on pH. This implies that it is possible to optimize the conditions at which riboflavin has the larger interaction with the electrode surface, which means that the sensor response will be probably less influenced by the presence of these interferent analytes.

Part 2:

Electrochemical sensors based on 2-D Materials produced via Liquid Cascade Centrifugation

Chapter 1

Characterization of samples produced via Liquid Cascade Centrifugation

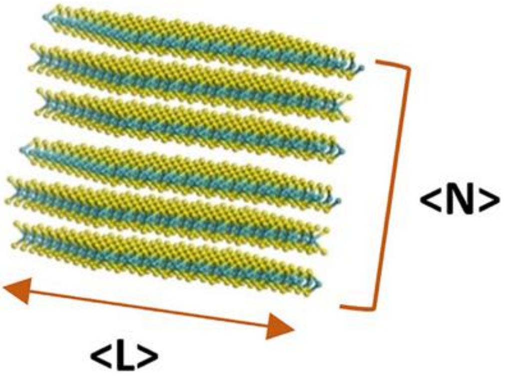

Overview

In this chapter, the fundamental characterizations performed on the samples and sensing substrates prepared via Liquid cascade centrifugation will be illustrated. The following paper was published from the research developed in this chapter [Zribi, R.; et al. Electrochimica Acta, 2022, 436, 141433].

I. Spectroscopic characterization of 2D molybdenum disulfide nanosheets

I.1 UV-Vis spectroscopy

Similar to the samples produced via LPE, UV-Vis measurements were performed on solutions diluted 1:10 v/v. In Fig.III.34, the UV-Vis spectra of the different samples (the inset is a zoom of the 5 krpm sample signal) is presented. In all spectra, the A- (~ 675 nm) and B- (~ 610 nm) excitonic peaks together with the C-excitonic band at 400 – 460 nm are present, superposed to a continuum scattering background, consistent to what expected for the 2H polytype of MoS_2.

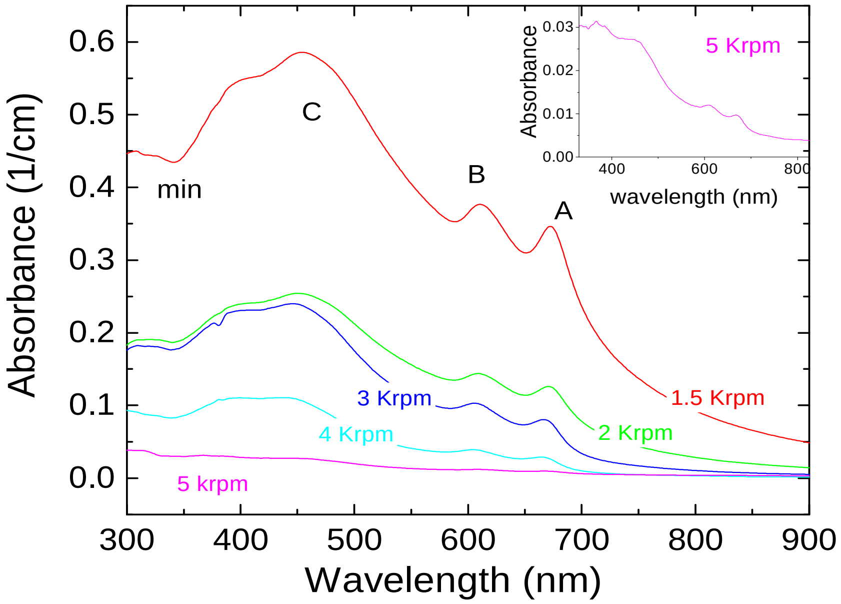

Figure III. 34. Extinction spectra of the different 2D-MoS_2 dispersions (diluted 1:10 v/v) as a function of the centrifugation speed. Inset: spectrum of the 2D-MoS_2 sample produced at 5 krpm.

In order to precisely determine the position of the A and B excitonic peaks and get rid of the background influence, the second derivative of the extinction spectra is calculated and the position of the local minima is measured.

However, as explained in the previous paragraph, other useful information, in addition to the 2D-MoS_2 polytype structure, such as size, thickness and nanosheets concentrations can be extracted from the UV-Vis extinction spectra of MoS_2 using the empirical formulas developped by Varrla *et al.* [5].

First, the average nanosheets size ⟨L⟩ was calculated from the ratio between the local minimum extinction intensity at 350nm and B-exciton extinction value (ExtB) following equation III.1.

In addition to that, the average number of layers ⟨N⟩ per nanosheet, which corresponds to the nanosheets thickness, can be estimated following equation III.2.

One more information can also be extrapolated from the extinction spectrum is the concentration, c, of the MoS_2 nanosheets. Applying Beer's law, the nanosheets concentration can be estimated (eq.III.3).

From the previous presented formulas, the size, the thickness, and the concentration of each solution were computed leading to the plots showed in Fig.III.35, in which these quantities display linear relationship as a function of both the centrifugation speed (top axis) and the central centrifugal acceleration (bottom axis). This latter parameter, expressed in g, is given by equation (III.4):

$$a_c = 4\pi^2/3600 \cdot rpm^2 \cdot r/g \qquad \text{(III.4)}$$

where :

- $g = 9.81\ m/s^2$ is the gravitation acceleration,
- $r = 7$ cm is the radial distance of center of the cuvette holding the solution,
- rpm is the rotation speed in revolutions per minute,

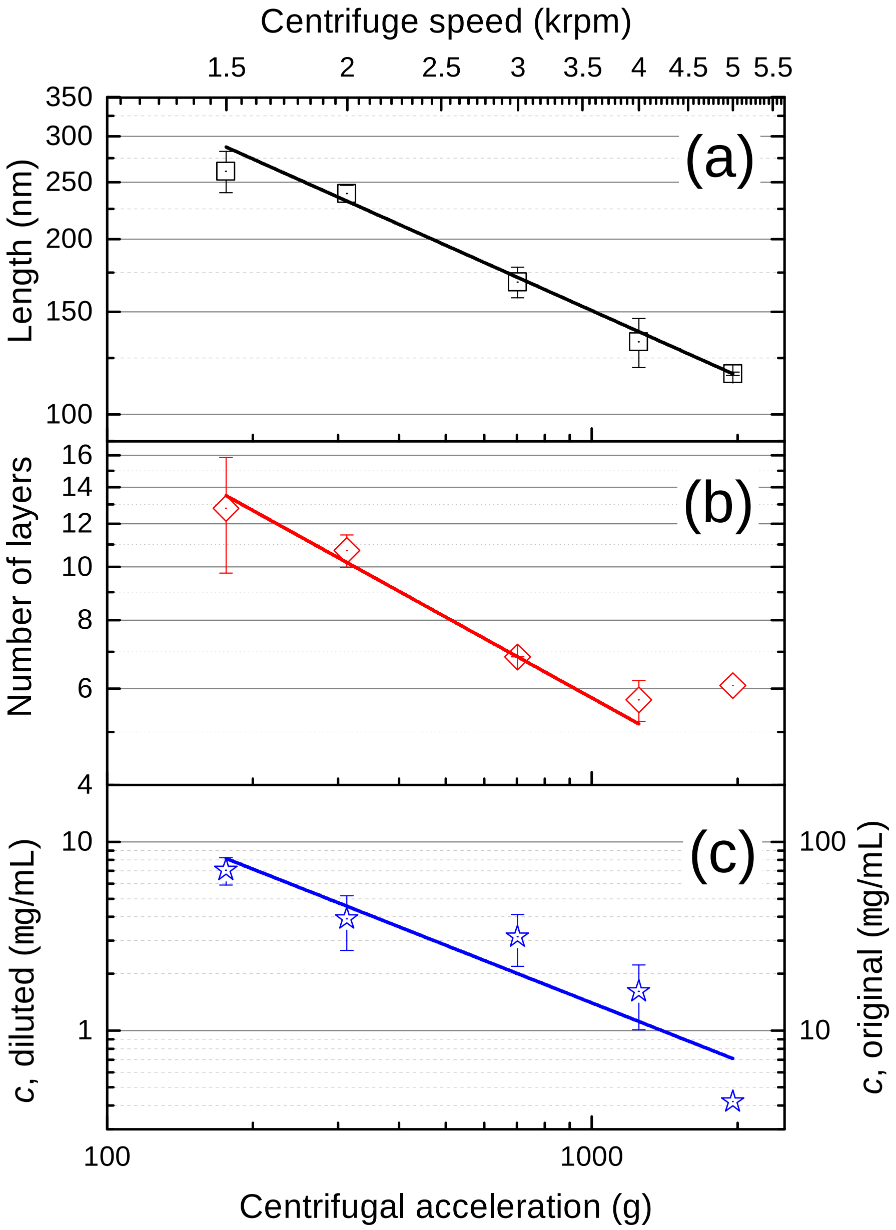

Figure III.35. a) Average lateral size ⟨L⟩ of the MoS_2 nanosheets produced by LCC at increasing centrifugation speed, b) Mean number of layers per nanosheet ⟨N⟩ of the different MoS_2 nanosheets produced by LCC, c) Concentration of the different MoS_2 nanosheets measured on the diluted samples (left axis) and rescaled to the original density (right axis). These values are reported as a function of the centrifugal accelerations (bottom axis), in units of g (the acceleration of gravity), and as a function of the centrifugation speed (top axis). The solid lines represent the power-law best fits to the experimental data (hollow symbols).

As illustrated in Fig.III.35, increasing the centrifugation speed from 1.5 to 5 krpm, the average size of the flakes decreased from 260 to 115 nm. As regarding the thickness, the number of layers decreased from larger than 10 to about 6 going from 1.5 to 4 krpm.

The 5 krpm sample contains flakes with the same average number of layers of the 4 krpm one, but with a size ~ 12% smaller. The concentration decreases from 80 µg/mL at 1.5 rpm to 4 µg/mL at 5 krpm.

I.2. Raman spectroscopy

Raman measurements were carried out exciting at λ_{ex} = 561nm. At this wavelength, the Raman signal between 350 and 430 cm^{-1} (see Fig.III.36) is characterized by two sharp peaks, the E^1_{2g} and the A_{1g} vibrational modes, that in bulk MoS_2 occur at 383 and 408.2 cm^{-1}. Interferences due to Raman resonance effects, inducing overtones and combination modes, as observed when exciting at 638 or 785 nm, are avoided at 561 nm. The frequency shift between the E^1_{2g} and the A_{1g} modes, $\Delta\omega\left(E^1_{2g} - A_{1g}\right)$ varies with the number of flakes, going from 25.2 cm^{-1}, in bulk, to 17.5 cm^{-1} in single layer MoS_2 [30].

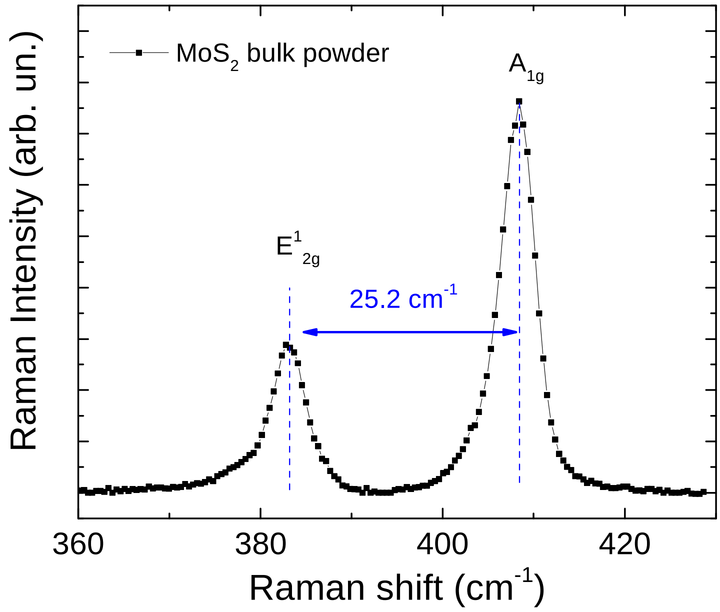

Figure III.36. Raman spectrum of bulk MoS_2 powder acquired at 561 nm. The frequency difference between the E^1_{2g} and A_{1g} Raman vibrational modes is about 25.2 cm^{-1}.

Raman spectra carried out on the 2D-MoS_2 solutions (FigureIII.37.a) and on the 2D-MoS_2 flakes casted on the SPCE (FigureIII.37.b) show a very similar behaviour. The position of the E^1_{2g} mode remains the same measured on the bulk MoS_2 at 383 cm^{-1} in all samples. The A_{1g} mode is unchanged at 408.2 cm^{-1} for the lower speeds (1.5, 2 and 3 krpm), and red-shifts to 407.7 cm^{-1} when we run up the centrifugation speed to 4 and 5 krpm. Figures.III.37.c-d display the , $\Delta\omega\left(E_{2g}^{1}-A_{1g}\right)$ frequency shift Vs the centrifugation speed for both the liquid solutions and the 2D-MoS_2 samples drop casted on the SPCE.

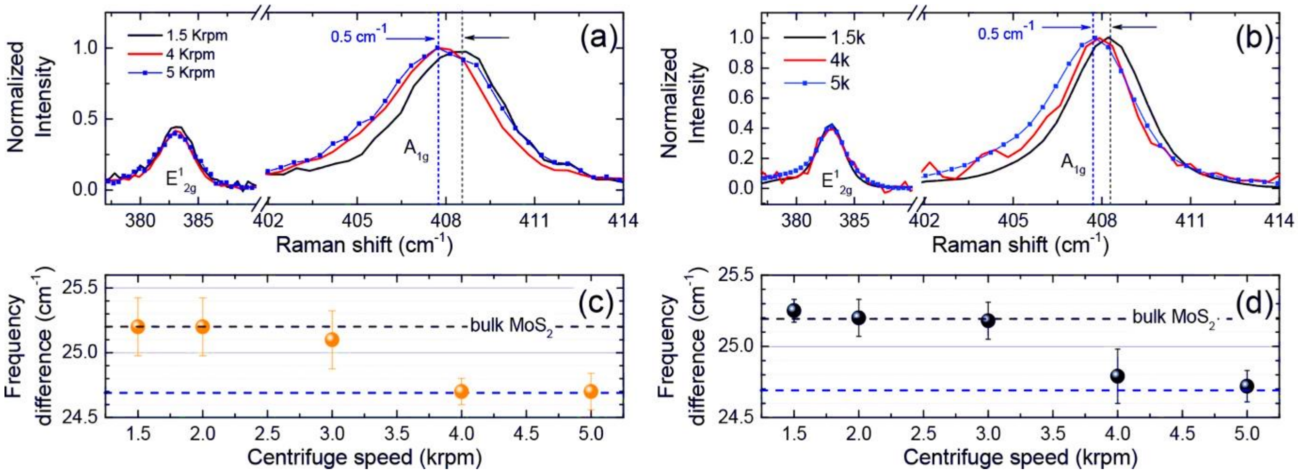

Figure III.37. Raman spectra of : a) 2D-MoS_2 flakes in solution and b) after deposition on the SPCE, produced after centrifugation at 1.5 krpm (black lines), 4 krpm (red lines) and 5 krpm (blue symbols). Plot of the frequency shift $\Delta\omega\left(E_{2g}^{1}-A_{1g}\right)$ as a function of the centrifugation speed for the flakes: c) in solution and d) deposited on the SPCE. The black dashed lines indicate the shift measured on the bulk MoS_2 powder. The blue dashed line is a guide to the eye to highlight the smaller $\Delta\omega$ found on the 4 and 5 krpm samples.

It is noted that $\Delta\omega$ varies from 25.2 to 24.7 cm^{-1} at 4 and 5 krpm suggesting that, in the samples centrifuged at the highest speeds, the nanosheets have a smaller number of layers. Based on other work done before [30] and using the empirical equation III.5:

$$\Delta\omega\ (\mathrm{cm}^{-1}) = 25.8 - 8.4/N \qquad \text{(III.5)}$$

we can estimate $\langle N\rangle \sim 6-7$, confirming the UV-Vis metrology indications, with no significative differences among the two samples. We are not sensitive enough to observe the very small spectral shifts (< 0.5 cm^{-1}) expected for nanosheets with N > 7 with respect to the bulk MoS_2, expected to be present in the solutions centrifuged at the lowest speeds. Finally, the similarity of the data collected in the liquid dispersions and on the SPCEs, tells us that even when the samples are dried in a form of film, as on the SPCEs after water evaporation, the surfactant layer still protects the MoS_2 flakes, conserving the number of layers of each nanosheet.

I.3. Dynamic light scattering

Dynamic light scattering was performed on the sample centrifuged at 1.5 krpm diluted 1:10 v (Fig.III.38). According to this test, the size distribution of the 2D-MoS_2 nanosheets is about 230 nm which is in accordance with the average size found before with the UV-Vis analysis using the empirical formulas. Also, this test reveals the presence of nanosheets having the size arround 100 nm that were seperated from bigger nanosheets by increasing the centrifugation speed.

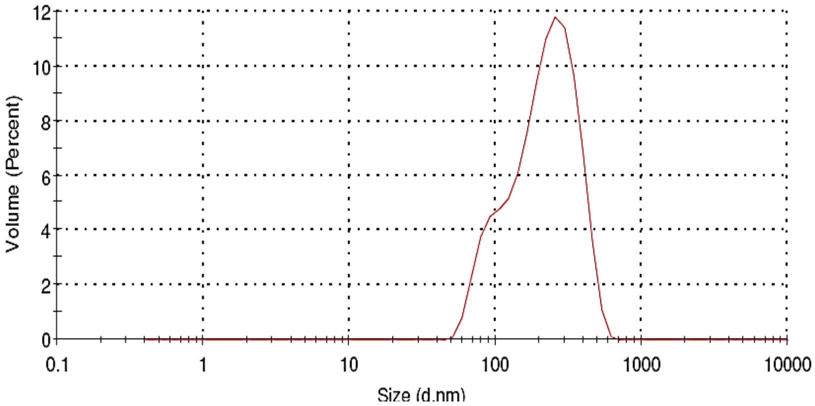

Figure III.38. Dynamic light scattering (DLS) pattern for 2D-MoS_2 (1.5 krpm) nanosheets.

II. Microscopic characterization of 2D molybdenum disulfide nanosheets

I.1. Scanning electron microscopy

SEM measurements were made on the dried solutions. Two 2D-MoS_2 samples are compared, at 1.5 krpm and 4 krpm, respectively. The SEM images at different magnification presented in Fig.III.39 evidence the difference in size of the as prepared 2D-MoS_2 nanosheets deposited on the surface of the working electrodes of the SPCE. Also, this confirms that the obtained material conserves its 2D properties even after drying on the surface of the SPCE.

Using free access image J software, an estimation of the nanosheets size distribution (Fig.III.39.e) can be directly obtained from the obtained SEM images which confirms the results obtained by UV-Vis spectroscopy and DLS.

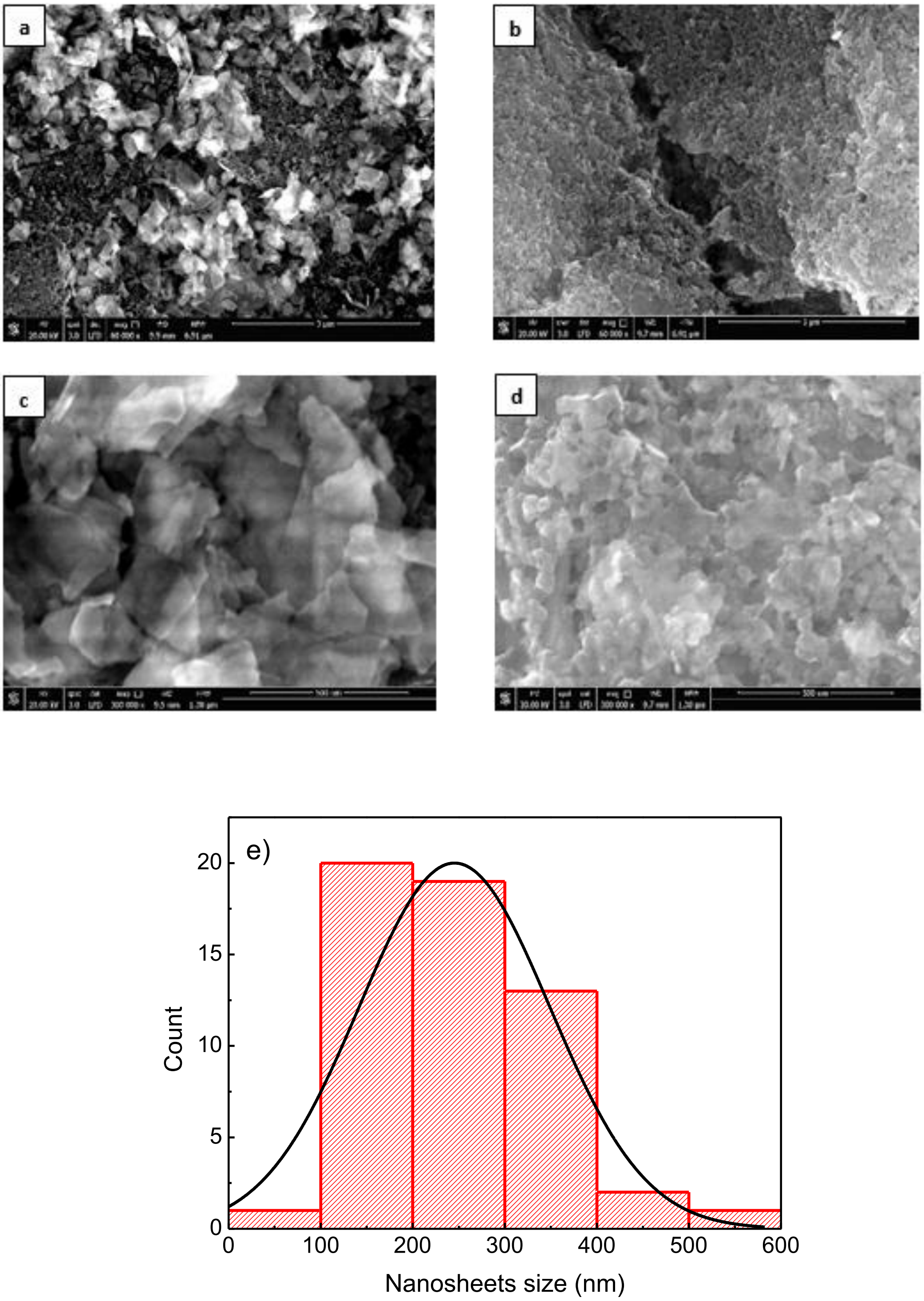

Figure III.39. SEM images showing the surface of: a, b) 1.5 krpm and 4 krpm respectively at magnification of 60k; c, d) 1.5 krpm and 4 krpm respectively at magnification of 300k, e) nanosheets size distribution obtained from image J software.

I.2. Atomic force microscopy

MoS_2 nanoflakes were characterized by atomic force microscopy (AFM) and results are shown in Fig.III.40. The sample (MoS_2 centrifuged at 1.5 krpm) was deposited on a flat silicon wafer as a substrate and left to dry at room temperature. AFM images were carried out using AIST/NT microscope mounting Si cantilevers (HQ: NSC14/Al BS, μmash, Germany) working in tapping mode. Measurements were made under natural ambient conditions. The open source program Gwyddion was used to process the raw data from the microscope. Fig.III.40.a displays the AFM measurement done on the 2D-MoS_2 on a wide portion of the sample in which some flakes are clearly observed. Fig.III.40.b. represents a zoom (yellow rectangle in panel "a") in which the step-like structure of the 2D-MoS_2 is well noted. In fact, the flake crossed by the line "1" presents steps of 4 nm (≈ 6 layers), 8 nm (≈ 12 layers) and 13.5 nm (≈ 20 layers), like highlighted by the line profile in panel "c". However, the flake crossed by the line "2" is smaller and have a more constant thickness of about 4 nm (see panel "e" in Fig.III.40). This findings therefore confirms the "1.5 krpm" 2D-MoS_2 is actually rich on both big and small nanoflakes, which can be isolated by increasing the centrifugation up to 5 krpm. In fact with UV-Vis analysis the flakes present typically feature 6-7 layers. The structure crossed by line "3" in panel "b" corresponds to a big particle (see panel "d") that do not have the shape of a nanoflakes like the one characterized in panel "c". Very likely can be related to the residues of SC which was used as exfoholiating and stabilizing agent for the 2D solution. Panel "f" that is a second zoom in panel "a" (pink rectangle in panel "a") from which the height "profile 4" (panel "g") was recorded. "Profile 4" is compatible with a nanoflake similar to the one of profile "1" with an SC nanoparticle stuck on the top of the flakes which pull the final thickness to more than 25 nm. In panel "h" it is showed the line profile of a sample region where it is evident an accumulation of nanoparticles compatible with aggregated SC nanoparticles of 15 nm height ("Profile 5").

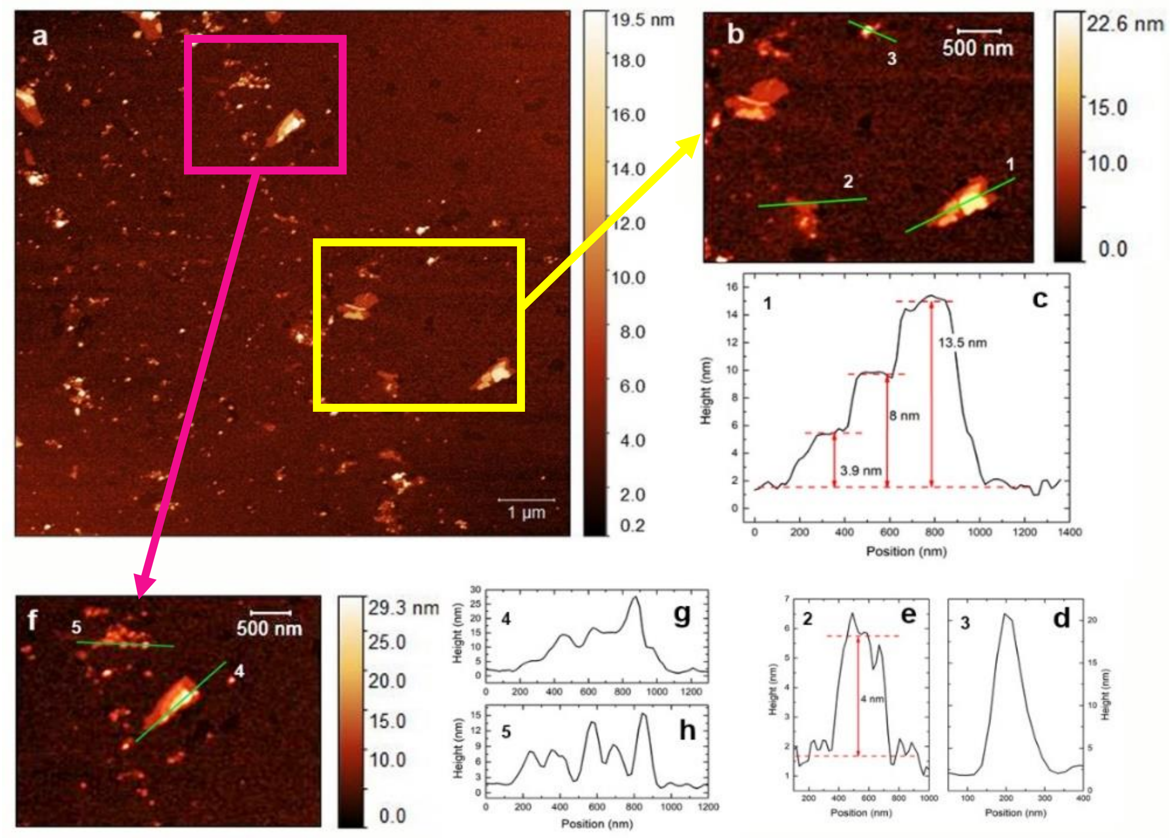

Figure III.40. AFM measurement of the 2D-MoS_2 deposited on a flat silicon wafer on a wide area (10x10 μm^2), b,f) zoom of the AFM image in (a), c,d,e,g,h) line profiles corresponding to green lines drawn in panels (b) and (f).

III. Electrochemical characterization of 2D molybdenum disulfide nanosheets

To study the electrical properties of the obtained nanosheets, electrochemical impedance spectroscopy was carried out for this aim.

Nyquist diagrams allow us to visualize the EIS spectra by plotting the negative of the imaginary part of the complex impedance $-Z''(\omega)$ vs the real part $Z'(\omega)$, in a parametric plot as a function of the frequency ω. The frequency range investigated was 0.1 to 105 Hz. The Nyquist plots are very sensitive to the electron exchange mechanisms, between the electrode surface and the electrolytes in solution.

Nyquist diagrams of different electrodes modified with different 2D-MoS_2 dispersion, produced via LCC, were obtained in 10 mM $[Fe(CN)_6]^{3-/4-}$ in PBS solution, allowing us to compare their dielectric features (see Fig.III.41).

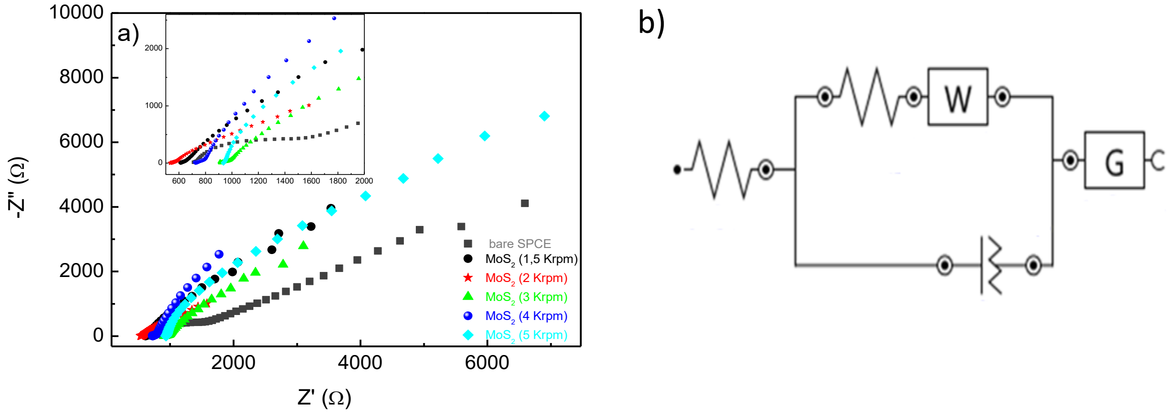

Figure III.41. a) EIS of bare SPCE and modified SPCE with different 2D- MoS_2 dispersions. EIS has been performed in 1 M PBS solution containing 10 mM of $[Fe(CN)_6]^{3-/4-}$, b) the general equivalent circuit used to model the EIS data for the modified-MoS_2 electrodes.

As shown in Fig.III.41.a, the bare SPCE exhibited a semi-circle pattern with small diameter at high frequencies (the inset displays a zoom in the high frequency region) and linear part at low frequencies. The high frequency semicircle represents the electron transfer resistance, and for the bare SPCE (black dots) the results of EIS measurement indicate a low electron transfer resistance to redox probe $[Fe(CN)_6]^{3-/4-}$. After deposition of 2D-MoS_2 nanosheets onto the SPCE, the EIS curves change significantly, suggesting an increased electron transfer resistance. This behavior, likely due to lower conductivity of the deposited layer, is in agreement with the reports of other authors [31]. The general equivalent circuit model that was used to fit Nyquist plots is presented in Fig.III.41.b. This circuit is composed of resistor that represents electron transfer across an interface, capacitor that represents non-faradaic charging at an interface, Warburg Element (W) that represents the diffusion of the electrons, and Gerischer Element (G) that represents an electrochemical reaction coupled with a chemical reaction.

Chapter 2

Electrochemical Study of Batch "C"

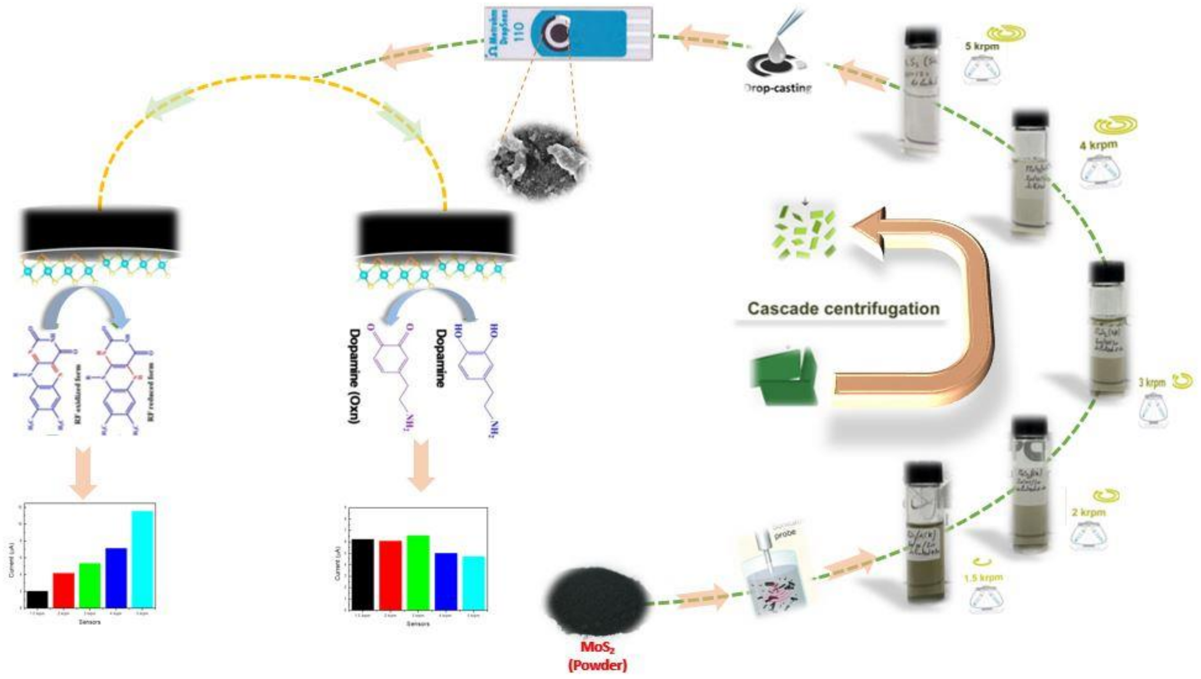

Overview

This chapter will present a study of the effect of size and thickness of the 2D molybdenum disulfide nanosheets, prepared for batch “C” via liquid cascade centrifugation, on the electrochemical behaviour and sensing properties towards dopamine and riboflavin

I. Redox probe tests and scan rate effect

I.1 Cyclic voltammetry in $[Fe(CN)_6]^{3-/4-}$ redox probe

In order to characterize and compare the charge transfer characteristics of the bare screen-printed carbon electrodes and the modified ones, cyclic voltammetry was carried out in $[Fe(CN)_6]^{3-/4-}$ redox probe.

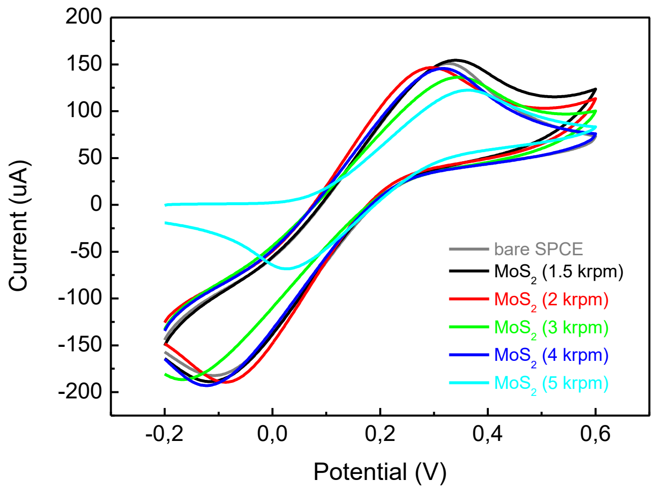

Figure III.42. CV of bare SPCE and modified SPCE with different 2D- MoS_2 dispersions performed in 1 M PBS solution containing 10 mM of $[Fe(CN)_6]^{3-/4-}$.

Fig.III.42. compares the CV curves of the bare SPCE and modified 2D- MoS_2/SPCE at different centrifugation rates in 10 mM of $[Fe(CN)_6]^{3-/4-}$ at 50 mV/s scan rate. A pair of well-defined redox peaks were observed in the bare SPCE curve, due to the characteristic reversible one-electron redox behavior of $[Fe(CN)_6]^{3-/4-}$ system.

The anodic peak current of the modified electrodes decreases with increasing the centrifugation speed, going from 155 µA for 1.5 krpm to 122 µA for 5 krpm, suggesting that the 2D-MoS_2 nanosheets layer acted as a blocking layer and inhibit the charge transfer, with the smaller opposing the higher resistance to charge transfer.

The electrochemical active surface area (ECSA) of the modified electrode was determined using the $[Fe(CN)_6]^{3-/4-}$ as redox probe based on the Randlese–Sevcik equation III.6 :

$$Ip = \pm 0.4463\, n \cdot F \cdot A \cdot C \sqrt{\frac{n \cdot F \cdot \upsilon \cdot D}{R \cdot T}} \qquad \text{III.6}$$

where:

- Ip is the anodic peak current (A),
- n = 1 is the number of electrons transferred in the electrochemical reaction,
- F = 96485.3365 C/mol is the Faraday constant,
- A is the electrode surface area (cm^2),
- C = 10^{-5} Mol/cm^3 is the concentration of redox probe,
- υ = 0.05 V/s is the applied scan rate,
- D = 7.6 × 10^{-6} cm^2/s is the diffusion coefficient,
- R = 8.314 J/mol is the universal gas constant,
- T = 298.15 K is the temperature.

In Table III.7 , anodic peak current (i_p), ΔE_p, as well as ECAS are reported.

Sensors	peak current i_a (µA)	ΔE_p (V)	ECAS (cm^2)
Bare SPCE	150	0.217	0.091
MoS_2 (1.5 krpm)	155.72	0.445	0.094
MoS_2 (2 krpm)	147.96	0.374	0.089
MoS_2 (3 krpm)	143.31	0.434	0.087
MoS_2 (4 krpm)	135.55	0.508	0.082
MoS_2 (5 krpm)	122	0.331	0.074

Table III.7. Anodic peak current, ΔEp, and ECAS for each sensor in presence of 10 mM of the redox probe $[Fe(CN)_6]^{3-/4-}$.

Figure III.43. shows in details the trend of the anodic peak current of the redox probe $[Fe(CN)_6]^{3-/4-}$ as a function of the geometrical features <L> and <N> of the 2D-MoS_2 nanosheets. The current is clearly seen to increase as both <L> and <N> increase.

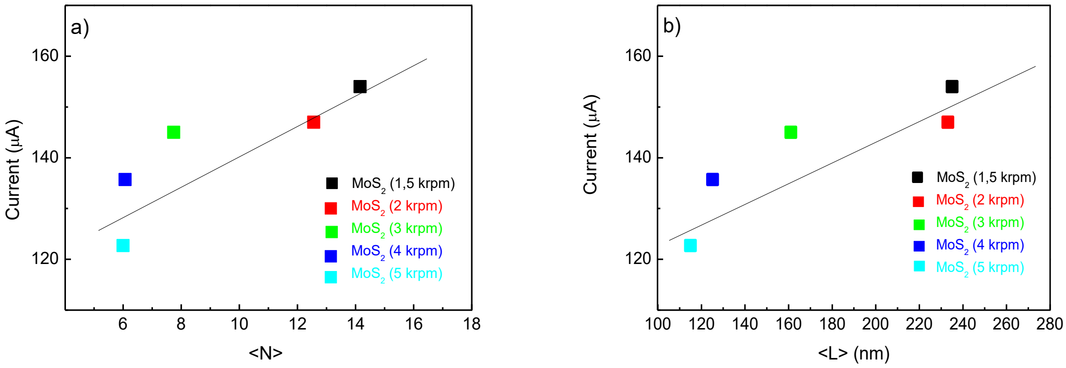

Figure III.43. Anodic peak current vs. the geometrical features a) <N> and b) <L> of the 2D-MoS_2 nanosheets.

I.2. Scan rate effect in presence of $[Fe(CN)_6]^{3-/4-}$ redox probe

Further information has been collected by carrying out CV cycles at different scan rates (υ), from 50 to 400 mV/s (Fig.III.44). The peak current increases linearly with the square root of the scan rate, indicating the occurrence of diffusion processes, independently of the geometrical features <L> and <N> of the 2D-MoS_2 nanosheets.

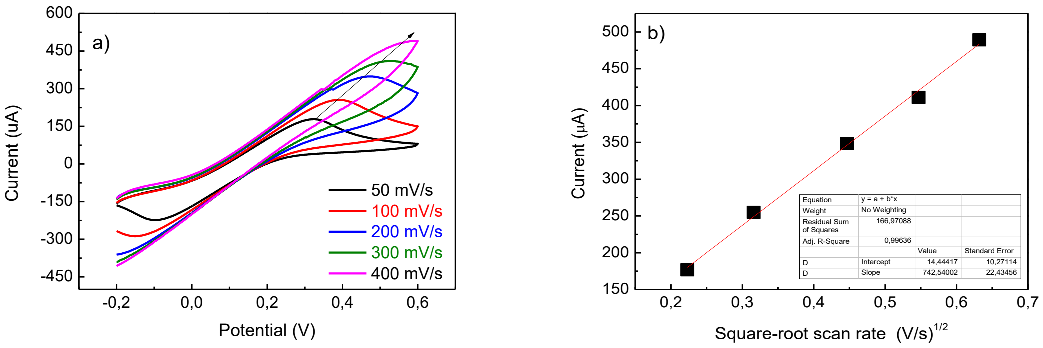

Equation	y = a + b*x		
Weight	No Weighting		
Residual Sum of Squares	166,97088		
Adj. R-Square	0,99636		
		Value	Standard Error
D	Intercept	14,44417	10,27114
D	Slope	742,54002	22,43456

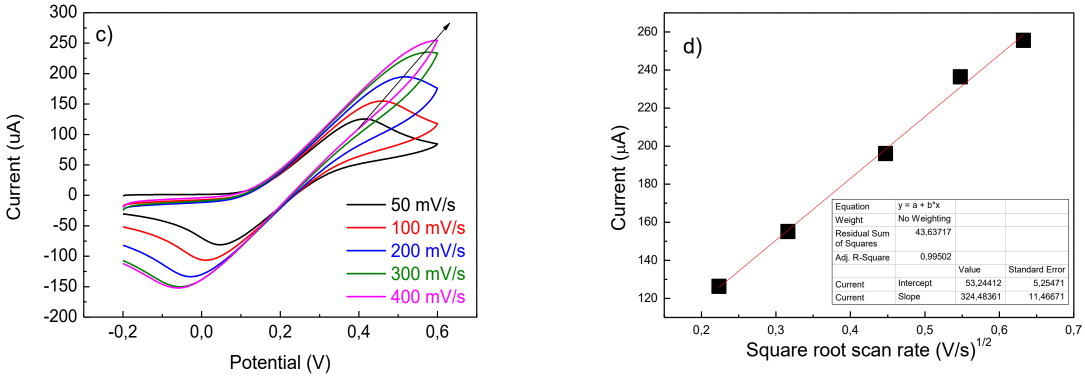

Equation	y = a + b*x		
Weight	No Weighting		
Residual Sum of Squares	43,63717		
Adj. R-Square	0,99502		
		Value	Standard Error
Current	Intercept	53,24412	5,25471
Current	Slope	324,48361	11,46671

Figure III.44. a-c) 2D-MoS$_2$ (1.5 krpm) and (5 krpm) respectively in presence of [Fe(CN)$_6$]$^{3-/4-}$ in 1 M PBS, at different scan rates (υ), from 50 to 400 mV/s; b-d) Peak current dependence on the scan rate Red lines indicate the linear fits of the data.

II. Electrochemical study of the correlation between nanosheets metrology and sensing properties

II.1. Sensing behaviour of different centrifuged 2D molydenum disulfide in presence of dopamine

II.1.a Cyclic voltammogram in presence of dopamine

Different screen-printed carbon electrodes have been modified using the different centrifuged solutions containing 2D-MoS$_2$ nanosheets for the study of their electrochemical properties in presence of dopamine. As demonstrated in part 1 chapter 3 of this section, 2D-MoS$_2$ based SPCE displayed a good response towards DA. More CVs were carried out using SPCE modified with 2D-MoS$_2$ solutions from batch ”C” prepared via LCC. The redox reaction of DA occurring on the surface of the working electrode is at the origin of the characteristic waves observed on all samples. As an exemple, the effect of DA concentration on CV cycles is shown in Fig.III.45.a. for the 2D-MoS$_2$ (4 krpm) electrode. It was obvious that increasing the DA concentrations present in solution, an enhancement in the current peak is observed. Plotting the corresponding calibration curve, a linear increase of the anodic peak current with the DA concentration (Fig.III.45.b) from the 0 to 100 μM range is well evident.

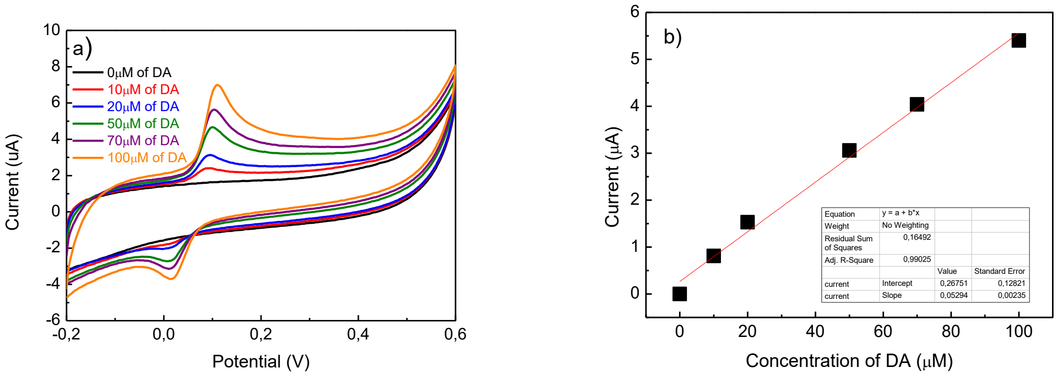

Figure III.45. a) CVs at different DA concentrations. Scan rate 50 mV/s in 1 M PBS solution, b) Calibration curve of modified 2D-MoS₂ (4 krpm) at different DA concentrations. Red line corresponds to the linear fit.

Data were acquired for all the modified electrodes are presented in Fig.III.46.a-b. No significant variations in the electrochemical parameters for DA sensing occurs as a function of the different morphological parameters of the 2D-MoS_2 nanosheets demonstrating that there is no effect of the 2D-MoS_2 size and thinckness on the sensitivity of the sensors towards DA.

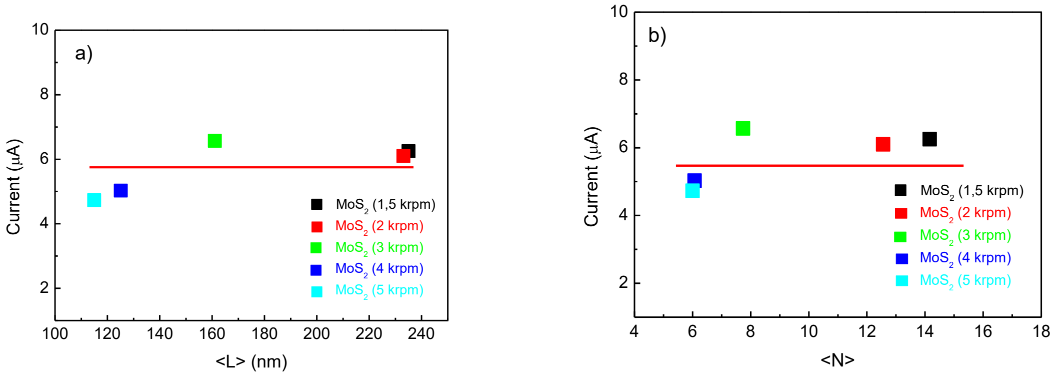

Figure III.46. Effect of the geometrical characteristics of the modified electrode layer on the sensing performances for DA. Anodic peak current vs. a) lateral size and b) number of sheets.

II.1.b Scan rate effect in presence of dopamine

Further information has been collected by carrying out CV cycles of the 2D-MoS_2 (4 krpm) modified SPCE at different scan rates (υ), from 50 to 400 mV/s CV in presence of 100 μM DA, which are reported in Fig.III.47.a. The oxidation peak currents increase linearly with the scan rate (Fig.III.47.b). This behavior is known to be typical of surface adsorption-controlled processes [32].

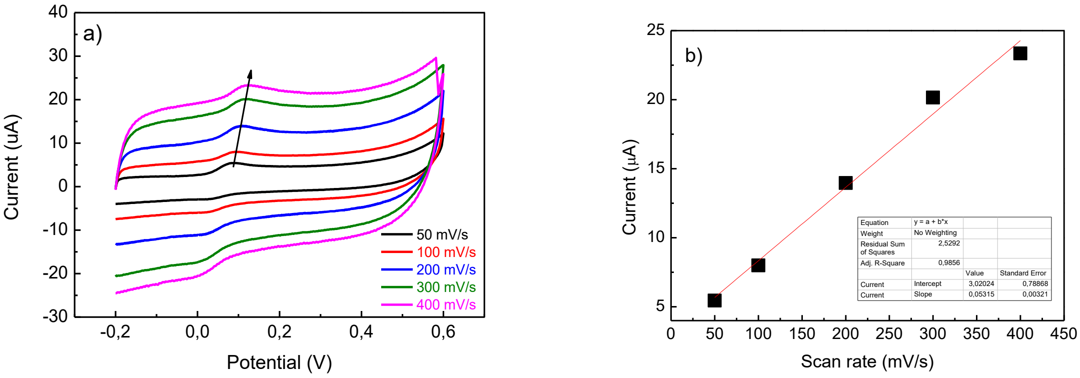

Equation	y = a + b*x		
Weight	No Weighting		
Residual Sum of Squares	2,5292		
Adj. R-Square	0,9856		
		Value	Standard Error
Current	Intercept	3,02024	0,78868
Current	Slope	0,05315	0,00321

Figure III.47. a) CV cycles of 2D-MoS₂ (4 krpm) in 100 µM DA in 1 M PBS, at different scan rates (υ), from 50 to 400 mV/s. b) Plot of the peak current vs scan rate (black symbols) and linear fit (red line) of the data.

II.2. Sensing behaviour of different centrifuged 2D molydenum disulfide in presence of riboflavine

II.2.a Comparaison of different modified electrodes in presence of riboflavin

Tests carried out in presence of riboflavin on the bare and the 2D-MoS_2 modified electrodes are reported in Fig.III.48. The large difference noted in the LSV patterns is a clear proof of the effect that 2D-MoS_2 nanosheets of different geometrical features have on the sensing performances towards this biomolecule.

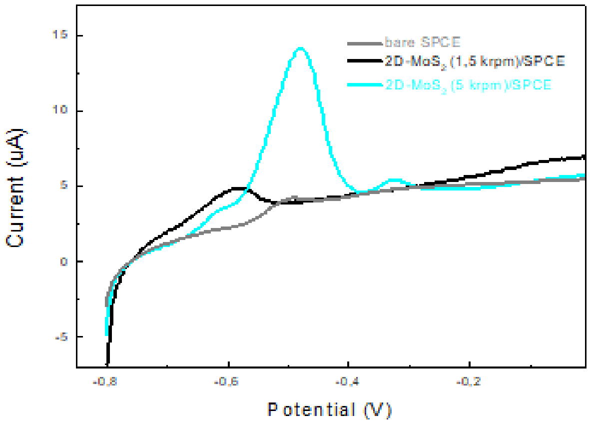

Figure III.48. Comparison of LSVs collected on different sensors at scan rate 50 mV/s in 1 M PBS solution of RF (100 µM).

Figure III.49 compares the peak current of the LSV curves of the bare SPCE with the modified 2D-MoS_2/SPCE at different centrifugation rates in RF at 100 µM. It can be clearly seen that the sensing performances toward RF improved strongly increasing the centrifugation rate. The electrochemical reaction involved in the oxidation/reduction of RF is easier when using electrodes having smaller and thinner 2D-MoS_2 nanosheets. The anodic peak current of the modified electrodes increases with increasing the centrifugation rate going from 2.04 µA for 2D-MoS_2 (1.5 krpm) to 11.57 µA for 2D-MoS_2 (5 krpm).

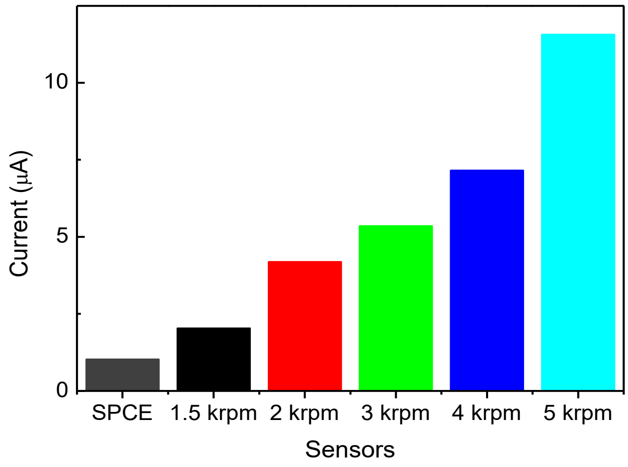

Figure III.49. Peak current registered on the bare SPCE and modified 2D-MoS_2/SPCE at different centrifugation rate in 100 µM of RF.

Figure III.50 shows in more details the increase of the peak current for a) thinner and b) smaller 2D-MoS_2 flakes, following the linear regression equations here described: current (µA) = -0.62 $<N>$ + 9.72 and current (µA) = -0.042 $<L>$ + 11.2 , for $<N>$ and $<L>$, respectively. This finding can be explained assuming that, by reducing the dimensions along both the in-plane $<L>$ and the out of plane $<N>$, there is an increase of active sites available for the electrocatalytic reaction of RF to occur, contributing to the observed current enhancement. Notably, an increased current is observed for 2D-MoS_2 flakes of equal number of average layers but smaller size (blue and cyan symbols in Fig.III.49), as for the substrates fabricated from the 4 krpm ($< N > \sim 6$, $< L > \sim 130$ nm) and 5 krpm ($< N > \sim 6$, $< L > \sim 115$ nm) 2D-MoS_2 solutions.

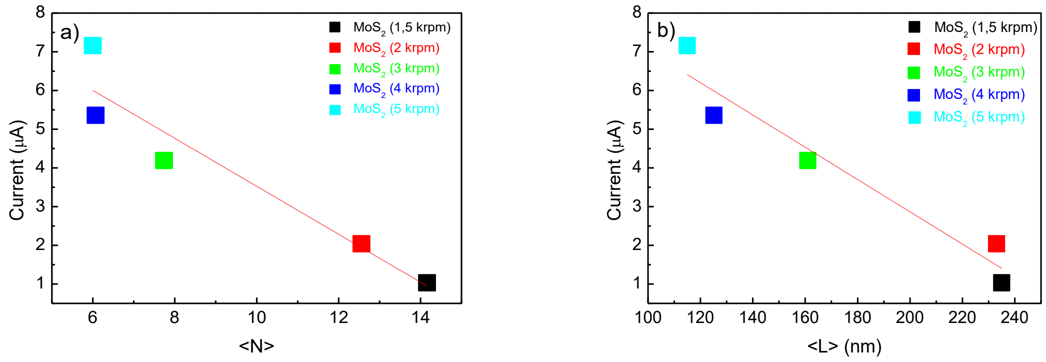

Figure III.50. Effect of the geometrical characteristics of the modified electrode layer on the sensing performances for RF. Anodic peak current vs. a) number of sheets and b) lateral size.

Accordingly, previous papers report that, using TMD nanosheets of different sizes during the hydrogen evolution reaction, improvements in both exchange current density and Tafel slope were observed as the nanosheet size was reduced [31, 32]. Generally, having smaller nanosheets deposited on the working electrode also gives the possibility to offer a larger relative surface area which enhances the electron transfer between the 2D-MoS_2 nanosheets and the analyte. However, calculation of the electrochemical surface area of our modified electrodes, using data reported in Fig.III.42. and table III.7 indicate that this is not exactly true. Indeed, higher value of ECAS were calculated on the nanosheets prepared at low centrifugation rate (see Fig.III.51). Then, the observed current enhancement in the presence of RF on the nanosheets prepared at high centrifugation rate can be explained assuming that there is an increase of the number of active sites available for the electrocatalytic reaction of RF.

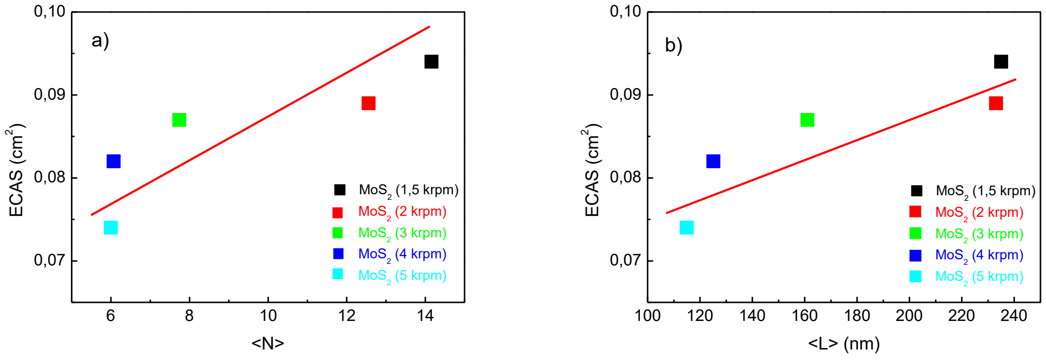

Figure III.51. Electrochemical active surface area vs. a) number of sheets and b) lateral size.

The effect of RF concentration on the linear sweep voltammogram is shown in Fig.III.51.a for the 2D-MoS$_2$ (5 krpm) electrode. The anodic peak current increases linearly with the RF concentration (Fig.III.52.b, black squares) in the 0 to 100 µM range. Results in Fig.III.52.b (pink circles) show the performances of the modified 2D-MoS$_2$ (5 krpm)/SPCE electrode on different days, in presence of riboflavin. The response of the sensor after 4 months is almost the same indicating the good stability of the fabricated electrode sensor excluding any hypothesis of 2D-MoS$_2$ nanosheets aglomeration even at small size and thickness.

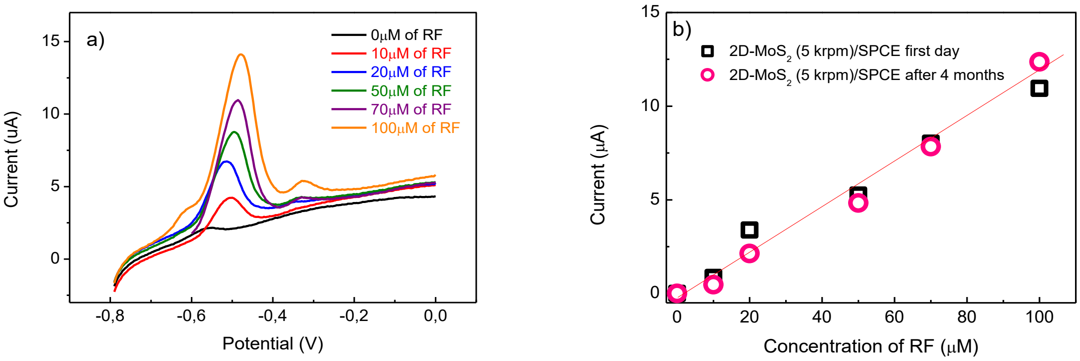

Figure III.52. a) LSV at different RF concentrations. Scan rate 50 mV/s in 1 M PBS solution. b) Calibration curves of 2D-MoS$_2$ (5 krpm)/SPCE in presence of riboflavin (black squares). Results from a test carried out after four months in the same conditions and using the same sensor are also shown (pink circles).

II.2.b. Scan rate effect in presence of riboflavin

Measurements carried out on RF by changing the scan rate in the range 50-400 mV/s, at a concentration of 100 µM (Fig.III.53), evidence that the current is linear with the scan rate. This behavior is similar to that found for DA (Fig.III.47), and indicates that the electroactive species are confined to the electrode surface, typical of surface adsorption-controlled processes [32].

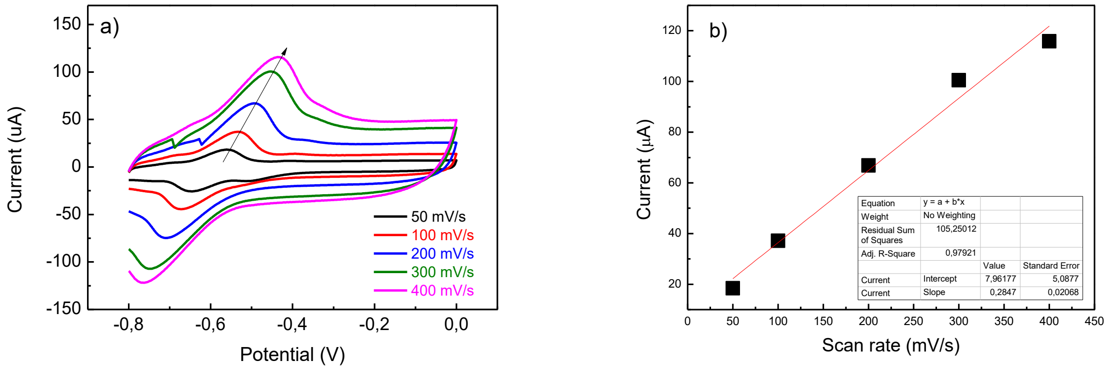

Equation	y = a + b*x		
Weight	No Weighting		
Residual Sum of Squares	105,25012		
Adj. R-Square	0,97921		
		Value	Standard Error
Current	Intercept	7,96177	5,0877
Current	Slope	0,2847	0,02068

Figure III.53. a) Effect of scan rate from 50 to 400 mV/s on CVs of 2D-MoS₂ (5 krpm)/SPCE in 100 µM RF; b) scan rate vs peak current.

II.3. Further comparaison of the sensing behaviour in presence of riboflavin and dopamine

The relative responses obtained for DA and RF sensing, calculated as the ratio of the anodic peak current obtained from CV analysis performed in 100 µM DA and RF, respectively, and the background current measured at the same potentials in 1 M PBS solution, were directly compared into the graphs reported in Fig.III.54.a-c in order to better highlight the differences in the electric response of the electrodes integrated with 2D-MoS_2 nanosheets produced at different centrifugation rate. Data clearly indicates that there is a different behavior for DA and RF sensing on changing the centrifugation rate of the LCC process, and therefore the flakes dimensions. As no direct comparison can be made with previous works on 2D-MoS_2 nanostructures featuring different layers number, some considerations could be made using literature data reported for graphene, the most used 2D-nanomaterial. Pumera's group compared the electroanalytical performances of single, few, and multilayer graphene electrodes in terms of sensitivity and showed that in the case of ascorbic acid, the sensitivity of the single graphene electrode is about 30% larger than that of the multilayer one. On the contrary, in the case of dopamine and uric acid, the sensitivity was practically the same for all electrodes [33, 34]. The size variations between the two electrode systems under consideration, in addition to their chemical peculiarities, must be taken into account when comparing these findings to this work. In fact, the 2D-graphene samples were created by exfoliating a graphitic raw material, which only affects the <N> parameter while leaving the <L> parameter essentially unchanged. Contrary, in this case, increasing the centrifugation rate, a clear in a drop in both <N> and <L> is observed. It's also interesting to note that these data show a strict analogy. In the case of dopamine, both graphene and 2D-MoS_2 electrodes display the same behavior, i.e. no differences occurred whatever are the size values. Conversely, RF behavior displayed on 2D-MoS_2 electrodes, is similar to that reported for ascorbic acid on graphene-based electrodes, with the best performances occurring for the 2D nanosheets with lower <L> or <N> values. It is also worthy to note that, while graphene samples show a sensitivity improvement for ascorbic acid of only about 30%, 2D-MoS_2 electrodes have been proved to provide a better relative improvement with an impressive value of more than 500% in the case of riboflavin sensing. Additional insight can be provided by making a comparison with 2D- MoS_2 electrodes used in the electrochemistry of small molecules. Coleman's groups first reported an inverse dependence of electrocatalytic activity for hydrogen evolution reaction HER with ⟨L⟩, as would be expected if the catalytic sites reside on the nanosheet edge [35]. Small sized 2D-MoS_2 nanosheets provide indeed more surface and edge sites compared to larger 2D-MoS_2 nanosheets. Edge sites are highly catalytically active and are, thus, preferred at the catalyst surface over 2D-MoS_2 basal planes, which are inert [36]. The same results were reported by other groups for the HER and oxygen evolution reaction OER [37]. On these bases, the large activity observed for RF can be reasonably attributed to a larger number of active edge sites present over the smaller and thinner 2D-MoS_2 nanosheets. At equal number of layers, <N>~ 6, smaller flakes appear to be more reactive (see Fig.III.50). These preferentially exposed active edges facilitate specific and enhanced interactions between the sensor material and target analyte and promote the application of 2D-TDMs in high-performance biochemical sensors [38, 39]. On the other hand, the reason behind the independent electrocatalytic activity regarding DA, is still unclear. Lou et al. noted a substantial independence of the electrocatalytic activity for DA from <N> of 2D-MoS_2 nanosheets mixed with Au quantum dots, while noticeable differences are reported operating at higher temperature, suggesting that kinetics effects can influence the behavior observed [30].

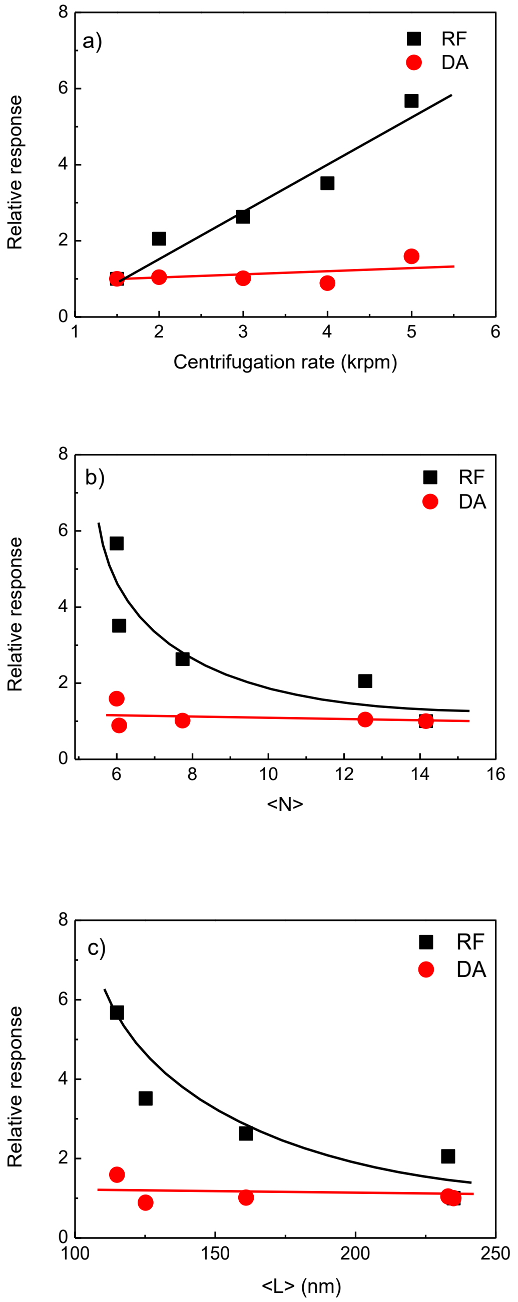

Figure III.54. Relative response to DA and RF as a function of: a) the centrifugation rate; b) the layer number <N>; and c) the lateral sheet size <L>.

III. Conclusion

2D-MoS_2 were produced via liquid cascade centrifugation by varying the centrifugation speed leading at the end to dispersions containing nanosheets with different size and thickness. These dispersions were then used to modify the surface of SPCE and to study the effect of the morphological and structural properties on the sensing behaviour towards dopamine and riboflavin. The data obtained showed two different detection behaviors. In the case of DA, the sensitivity of the sensor remains unchanged when the nanosheets are smaller and thinner. Unlike RF, a great improvement in electrocatalytic oxidation of RF for sensors modified with small and thin nanosheets.

References

1. Paton, K.R. and J.N. Coleman, *Relating the optical absorption coefficient of nanosheet dispersions to the intrinsic monolayer absorption.* Carbon, 2016. **107**: p. 733-738.
2. Quirantes, A., F. Arroyo, and J. Quirantes-Ros, *Multiple Light Scattering by Spherical Particle Systems and Its Dependence on Concentration: A T-Matrix Study.* Journal of Colloid and Interface Science, 2001. **240**(1): p. 78-82.
3. Backes, C., et al., *Edge and confinement effects allow in situ measurement of size and thickness of liquid-exfoliated nanosheets.* Nature Communications, 2014. **5**(1): p. 4576.
4. Backes, C., et al., *Guidelines for Exfoliation, Characterization and Processing of Layered Materials Produced by Liquid Exfoliation.* Chemistry of Materials, 2017. **29**(1): p. 243-255.
5. Varrla, E., et al., *Large-scale production of size-controlled MoS2 nanosheets by shear exfoliation.* Chemistry of Materials, 2015. **27**(3): p. 1129-1139.
6. Windom, B.C., W. Sawyer, and D.W. Hahn, *A Raman spectroscopic study of MoS 2 and MoO 3: applications to tribological systems.* Tribology Letters, 2011. **42**: p. 301-310.
7. Sahoo, S., et al., *Temperature-Dependent Raman Studies and Thermal Conductivity of Few-Layer MoS2.* The Journal of Physical Chemistry C, 2013. **117**(17): p. 9042-9047.
8. Placidi, M., et al., *Multiwavelength excitation Raman scattering analysis of bulk and two-dimensional MoS2: vibrational properties of atomically thin MoS2 layers.* 2D Materials, 2015. **2**(3): p. 035006.
9. Li, H., et al., *From bulk to monolayer MoS2: evolution of Raman scattering.* Advanced Functional Materials, 2012. **22**(7): p. 1385-1390.
10. Benavente, E., et al., *Intercalation chemistry of molybdenum disulfide.* Coordination chemistry reviews, 2002. **224**(1-2): p. 87-109.

11. Smith, R.J., et al., *Large-scale exfoliation of inorganic layered compounds in aqueous surfactant solutions.* Advanced materials, 2011. **23**(34): p. 3944-3948.
12. Saito, R., et al., *Raman spectroscopy of transition metal dichalcogenides.* Journal of Physics: Condensed Matter, 2016. **28**(35): p. 353002.
13. Ferrari, A.C., et al., *Raman spectrum of graphene and graphene layers.* Physical review letters, 2006. **97**(18): p. 187401.
14. de Castro Silva, I., et al., *Raman spectroscopy-in situ characterization of reversibly intercalated oxygen vacancies in α-MoO3.* RSC Advances, 2020. **10**(31): p. 18512-18518.
15. Carvalho, B.R., et al., *Symmetry-dependent exciton-phonon coupling in 2D and bulk MoS 2 observed by resonance Raman scattering.* Physical review letters, 2015. **114**(13): p. 136403.
16. Chakraborty, B., et al., *Layer-dependent resonant Raman scattering of a few layer MoS2.* Journal of Raman Spectroscopy, 2013. **44**(1): p. 92-96.
17. Rowley-Neale, S.J., et al., *2D nanosheet molybdenum disulphide (MoS 2) modified electrodes explored towards the hydrogen evolution reaction.* Nanoscale, 2015. **7**(43): p. 18152-18168.
18. Neri, G., *Thin 2D: The new dimensionality in gas sensing.* Chemosensors, 2017. **5**(3): p. 21.
19. Chia, X., et al., *Electrochemistry of nanostructured layered transition-metal dichalcogenides.* Chemical reviews, 2015. **115**(21): p. 11941-11966.
20. *Health matters*. Available from: https://healthmatters.io/understand-blood-test-results/tyrosine-plasma.
21. Yang, Y., et al., *A laser-engraved wearable sensor for sensitive detection of uric acid and tyrosine in sweat.* Nature biotechnology, 2020. **38**(2): p. 217-224.
22. Xiao, L., et al., *Solvent-free synthesis of sheet-like carbon coated MnO with three-dimensional porous structure for simultaneous detection of dopamine and uric acid.* Journal of Electroanalytical Chemistry, 2020. **858**: p. 113823.
23. Tian, F., et al., *A tantalum electrode coated with graphene nanowalls for simultaneous voltammetric determination of dopamine, uric acid, L-tyrosine, and hydrochlorothiazide.* Microchimica Acta, 2017. **184**: p. 1611-1619.

24. Lavanya, N., et al., *Fabrication of Cr doped SnO2 nanoparticles based biosensor for the selective determination of riboflavin in pharmaceuticals.* Analyst, 2013. **138**(7): p. 2061-2067.
25. Wang, Y., Q. Zhuang, and Y. Ni, *Fabrication of riboflavin electrochemical sensor based on homoadenine single-stranded DNA/molybdenum disulfide–graphene nanocomposite modified gold electrode.* Journal of Electroanalytical Chemistry, 2015. **736**: p. 47-54.
26. Si, R.-W., et al., *Wiring Bacterial Electron Flow for Sensitive Whole-Cell Amperometric Detection of Riboflavin.* Analytical Chemistry, 2016. **88**(22): p. 11222-11228.
27. Mehmeti, E., et al., *Manganese dioxide-modified carbon paste electrode for voltammetric determination of riboflavin.* Microchimica Acta, 2016. **183**(5): p. 1619-1624.
28. Nezamzadeh-Ejhieh, A. and P. Pouladsaz, *Voltammetric determination of riboflavin based on electrocatalytic oxidation at zeolite-modified carbon paste electrodes.* Journal of Industrial and Engineering Chemistry, 2014. **20**(4): p. 2146-2152.
29. Huang, D.-Q., et al., *The determination of Riboflavin (Vitamin B2) using manganese dioxide modified glassy carbon electrode by differential pulse voltammetry.* Int. J. Electrochem. Sci, 2018. **13**: p. 8303-8312.
30. Lou, X., et al., *Nano-sensor Based on MoS2 Nanosheet mixed with Au quantum dot: Role of Layer Number and Temperature.* Electroanalysis, 2019. **31**(3): p. 422-427.
31. Parra-Alfambra, A.M., et al., *MoS2 nanosheets for improving analytical performance of lactate biosensors.* Sensors and Actuators B: Chemical, 2018. **274**: p. 310-317.
32. Su, S., et al., *Highly sensitive and selective determination of dopamine in the presence of ascorbic acid using gold nanoparticles-decorated MoS2 nanosheets modified electrode.* Electroanalysis, 2013. **25**(11): p. 2523-2529.

33. Goh, M.S. and M. Pumera, *Single-, Few-, and Multilayer Graphene Not Exhibiting Significant Advantages over Graphite Microparticles in Electroanalysis.* Analytical Chemistry, 2010. **82**(19): p. 8367-8370.
34. Goh, M.S. and M. Pumera, *The electrochemical response of graphene sheets is independent of the number of layers from a single graphene sheet to multilayer stacked graphene platelets.* Chemistry-An Asian Journal, 2010. **5**(11): p. 2355-2357.
35. Gholamvand, Z., et al., *Electrochemical applications of two-dimensional nanosheets: the effect of nanosheet length and thickness.* Chemistry of Materials, 2016. **28**(8): p. 2641-2651.
36. Kibsgaard, J., et al., *Engineering the surface structure of MoS2 to preferentially expose active edge sites for electrocatalysis.* Nature Materials, 2012. **11**(11): p. 963-969.
37. Ghanashyam, G. and H.K. Jeong, *Size Effects of MoS 2 on Hydrogen and Oxygen Evolution Reaction.* Journal of Electrochemical Science and Technology, 2021. **13**(1): p. 120-127.
38. Liu, L., et al., *Ultrasensitive biochemical sensors based on controllably grown films of high-density edge-rich multilayer WS2 islands.* Sensors and Actuators B: Chemical, 2022. **353**: p. 131081.
39. Anichini, C., et al., *Chemical sensing with 2D materials.* Chemical Society Reviews, 2018. **47**(13): p. 4860-4908.

Section IV

Side Works

Overview

This part of the thesis will highlight the side works done during the Ph.D. course different than the ones discussed in the previous sections but always dealing with the same class of materials :

- The first is a US patent underwriting dealing with 2D transition metal dichalcogenides.
- The second work focuses on developing a sensor based on carbon nanotubes decorated with tungsten disulfide nanosheets (CNTs/WS_2) core-shell heterostructure for riboflavin determination.
- The third work presents a sensor based on 2D molybdenum disulfide prepared via liquid phase exfoliation following the same steps as batch “B” decorated with gold nanoparticles for folic acid determination.

US patent

2D-based transition metals dichalcogenides-based electrochemical sensors

This work was done during the 6-month internship in the USA in collaboration with Iowa State University. In general, 2D materials were used to develop an electrochemical sensor for a specific analyte.

Electrochemical Properties of CNT/WS_2 core-shell Heterostructures for riboflavin detection

Rayhane Zribi, Simona Crispi, Daniele Giusi, Medet Zhukush, Claudio Ampelli, Chengxu Shen, Muhammad Hamid Raza, Nicola Pinna, Giovanni Neri.

Under revision

Abstract

Tungsten disulfide (WS_2) layers with different thicknesses and morphology were deposited on carbon nanotubes (CNTs) by atomic layer deposition (ALD), forming CNTs/WS_2 core-shell heterostructures. WS_2 conformally grows like small platelets-flakes on the CNTs initially at low ALD cycles; with increasing the number of ALD cycles, WS_2 platelets grow to form a continuous film. Indeed, CNTs with deposited WS_2 have greater coverage and density as the number of ALD cycles increases. The as-synthesized CNTs/WS_2 hierarchical heterostructures were tested as effective electrochemical probes for the detection of riboflavin (vitamin B_2) by drop-casting the dispersions onto the surface of the working electrodes of the screen-printed carbon electrode. Cyclic voltammetry (CV) and Differential Pulse Voltammetry (DPV) experiments demonstrated that the modified CNTs-WS_2/SPCE sensors exhibit superior electrochemical performances compared to the bare SPCE. The distribution of WS_2 in flakes of different sizes and thicknesses affects the electrochemical performances that have been discussed thoroughly. The best sensing and electrochemical properties are found at a shell thickness of 100 ALD cycles which have been exploited, for the first time, in the electroanalytical determination of riboflavin (RF). The sensitivity to RF, equal to 2.06 $\mu A \mu M^{-1} cm^{-2}$ in the linear range from 0 μM to 45μM, and a limit of detection (LOD) of 0.9 μM demonstrate the promising characteristics of the proposed

CNTs-WS_2 (100ALD) /SPCE electrochemical sensor for the detection and quantification of riboflavin.

I. Introduction

Owing to their discovery two decades ago, carbon nanotubes (CNTs) have emerged as an amazing class of nanomaterials due to their unique physical, chemical, optical, electrical, electrochemical, and magnetic properties [1]. In many applications, they are also used to support the active phase(s), usually dispersed/coated on them, forming a shell layer [2-5]. It is well known that the functional properties of the shell layer significantly depend on the shape and morphology of the active phase, as well as the thickness and distribution of the substrate assume a fundamental role [6]. These latter characteristics depend on the coating method used for the deposition, so the search for optimal methods is an important step in their preparation. Atomic layer deposition (ALD) allows the conformal and homogenous coatings of CNTs with high control over the thickness of the deposited layers [7, 8]. This fine-tuning of the thickness of the active shell layer provided the possibility to demonstrate a clear structure-property relationship [3, 7]. In this study, we employed ALD to synthesize CNT/WS_2 core-shell hierarchical heterostructures with different thicknesses and morphology of WS_2 shell. Tungsten disulfide (WS_2) is a member of the 2D transition metal dichalcogenides nanomaterial family, characterized by a large surface-to-volume ratio, confined atomic thickness, and peculiar electronic properties [9]. Functionalizing/coating the surface of CNTs with active layers of WS_2 has proven to be a promising way to improve the performance of the electrode's electroanalysis and electrocatalysis [10].

The CNT/WS_2 core-shell nanocomposites were evaluated to detect the riboflavin (RF) using the screen-printing electrode (SPCE) [11]. Riboflavin is an important vitamin not produced in the body, so it should be introduced by food intake, and its deficiency is associated with some health disorders [12].

As far as we know, this is the first time CNT/WS_2 core-shell nanocomposites with different thicknesses of WS_2 layer prepared by ALD have been applied to investigate its electrochemical characteristics. By tuning the WS_2 sensing layer's thickness, the applications' performances have been optimized, shedding light on the effect of WS_2 shell thickness on the electrochemical properties of the CNT/WS_2 core-shell nanocomposite.

II. Experimental section

II.1. Materials and reagents

Carbon nanotubes were purchased from Applied Science Inc. All gases (purity, 99.99%) used in the ALD process were supplied by Air Liquide. Bis(t-butylimido)bis(dimethylamino)tungsten(VI) (BTBMW, >97%) was supplied by Strem and H_2S (> 99.5%) was purchased from Air Liquide. A phosphate buffer solution, PBS 0.1 M and pH 7. 4, Riboflavin were purchased from signma Aldrich. All chemicals and reagents were of analytical grades and used without further purification unless otherwise stated.

II.2. Synthesis of CNT/WS_2 nanostructures by ALD

Carbon nanotubes (CNTs) were functionalized as described in the previous report [7]. 10 mg of dried powder (80 ºC overnight) was dispersed in 2 mL ethanol by ultrasonication (30 minutes) and drop-cast on an Al foil for ALD-WS_2 deposition. WS_2 films were deposited in our homemade ALD system at 300 ºC with the established process. BTBMW (maintained at 80 ºC) and H_2S were precursors [13]. The thickness of the WS_2 layer was controlled by changing the number of ALD cycles and samples were named CNT/WS_2(X), where X represents the number of ALD cycles.

II.3. Physical characterization

High-resolution transmission electron microscopy (HRTEM) was carried out at an operation voltage of 200 kV on a FEI Talos F200S. X-ray diffraction (XRD) patterns were recorded on a STOE Stadi MP Diffractometer with Mo Kα1 radiation source (λ= 0.7093).

II.4. Preparation of modified electrodes and electrochemical tests

Electrochemical tests were performed using a commercial SPCE (mod. C110, DropSens, Spain), comprising a planar substrate equipped with a 4 mm carbon working-electrode (geometric area, 0.125 cm^2), a silver pseudo-reference electrode and a carbon auxiliary electrode. Cyclic voltammetry (CV) and Differential pulse voltammetry (DPV) techniques were performed using DropSens µStat 400 Potentiostat empowered by Dropview 8400 software for data acquisition.

For the fabrication of modified electrochemical sensors, SPCEs were modified as follows; 1mg of each of the CNT/WS$_2$(X) nanocomposite samples was ultrasonically dispersed in distilled water (1 mL). Thereafter, 10 µL of each suspension was directly dropped onto the surface of the carbon working electrode and allowed to dry at room temperature until further use.

III. Results and discussion

III.1. Morphological and structural characterization of CNTs/WS$_2$ (X)

III.1.a. X-ray diffraction (XRD)

The formation of the CNTs/WS$_2$ composites were first investigated by X-ray diffraction (XRD). As shown in Figure IV.1, the peaks at 6.50°, 15.28°, 17.92°, 22.09°, and 26.24° are attributed to (002), (101), (013), (015), (008) planes of the hexagonal phase of WS$_2$ based on the reference card of COD 96-900-9146. The peak at 12° is attributed to the diffraction of (002) plane of graphite carbon in CNTs (COD 96-101-1061). Moreover, the diffraction peaks become sharper and more intense with the increase of ALD cycle number, indicating an increased mass loading of crystalline WS$_2$ deposited onto the CNTs substrates [13].

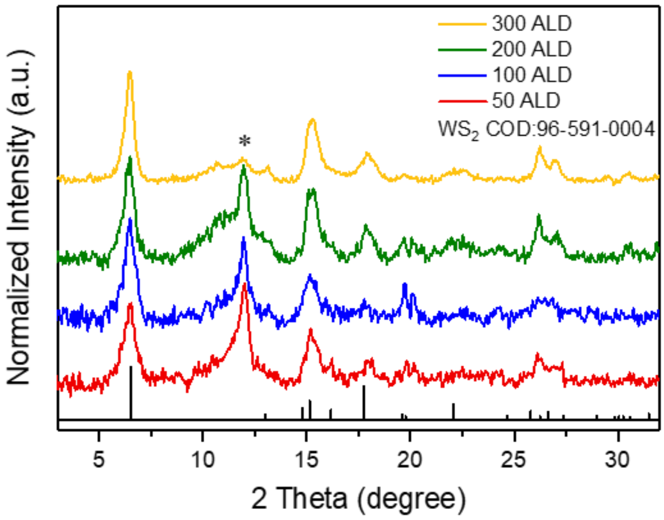

Figure IV.1. X-ray diffraction (XRD) patterns of CNTs/WS$_2$(X) composites with varying WS$_2$ ALD cycles from 50 to 300. Asterisks reflect the diffraction of the graphite carbon from the CNTs substrates.

III.1.b. High-resolution transmission electron microscopy (HR-TEM)

The prepared CNTs/WS$_2$(X) were further characterized by high-resolution transmission electron microscopy (HR-TEM), as shwon in Figure IV.2. There are only few flakes with ~30 nm length and ~6 nm thickness grown on the CNTs in the CNTs/WS$_2$(50) sample (Fig.IV.2.a). However, these flakes are individual and disconnected with each other, exposuring some uncompletely covered surfaces as well. When the ALD cycles number increases to 100, the size of the flakes also increase, indicating ~50 nm length and 10 nm thickness (Fig.IV.2.a-b). A portion of the flakes became bigger after connecting with neighboring ones. The composites with more than 200 ALD cycles deposition depict continuous WS$_2$ layer on the CNTs, showing a film thickness of ~10 nm for CNTs/WS$_2$(200) and ~15 nm for CNTs/WS$_2$(300), (Fig.IV.2.c-d). The clear lattice fringes in HRTEM with d-spacing of 0.7 nm are ascribed to the (002) lattice plane of WS$_2$ (Fig.IV.2.e). The selected area electron diffraction (SAED) pattern is recorded for CNTs/WS2(200), suggesting the deposited WS$_2$ is polycrystalline (Fig.IV.2.f).

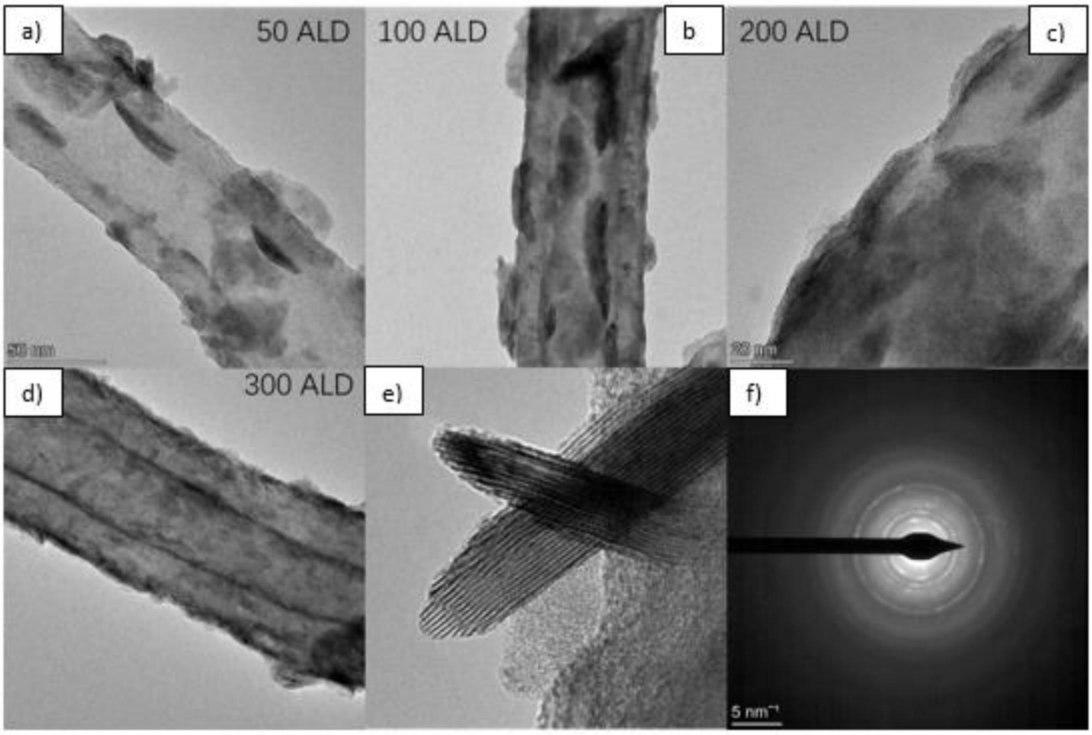

Figure IV.2. TEM images of CNTs/WS$_2$(X) composites with: a) 50, b) 100, c) 200 and d) 300 ALD cycles of WS2. e) HR-TEM image of the grown WS$_2$ flakes and f) SAED pattern of the prepared CNTs/WS$_2$(X) sample.

III.2. Electrochemical characterization

The prepared CNT/WS$_2$(X) nanocomposite samples were then evaluated for assessing their electrochemical characteristics (Fig.IV.3).

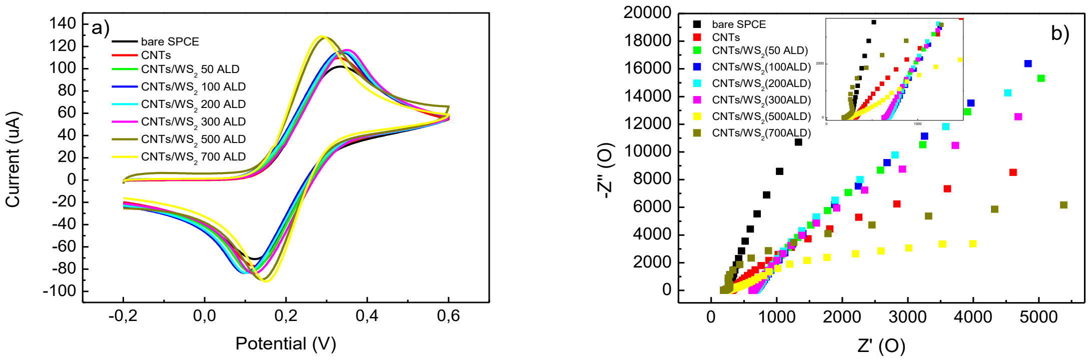

Figure IV.3. a) CV in 10 mM of [Fe(CN)$_6$]$^{3-/4-}$ and b) EIS tests of bare SPCE and CNT/WS$_2$ (X) nanostructures modified-SPCE in PBS.

As regarding the electrochemical properties, the electron transfer rate at the interface between the analyte and the electrode surface, is one of the most important characteristics to evaluate. Thus, to study the electrochemical behavior of the CNT/WS_2(X) nanostructures, CV in the presence of a redox probe $[Fe(CN)_6]^{3-/4-}$ and EIS measurements were performed. CV curves (Fig.IV.3.a) show that modified electrodes behave better in promoting the electro-oxidation/reduction of the redox probe. This can be attributed to the larger surface area of the modified electrodes. In Fig.IV.3.b, EIS was carried out to further study the modified electrode interface. Compared to bare electrode, a remarkable shift of the RS value was observed (see inset in Fig.IV.3.b) on the modified electrodes; further, the decrease in the semicircle diameter indicates that the charge transfer is favored, mainly because of the presence of the highly conductive CNT.

III.3. Electrochemical tests

III.3.a. Electrochemical behavior of different modified electrodes in presence of riboflavin

A preliminary test was done using Cyclic Voltammetry and placing bare SPCE and modified electrodes in the solution containing 45 µM of RF dissolved in 0.1 M PBS with pH= 7.4 at scan rate of 50 mV/s. The figure IV.4. shows a plot demonstrating the response of the different modified sensors toward the RF.

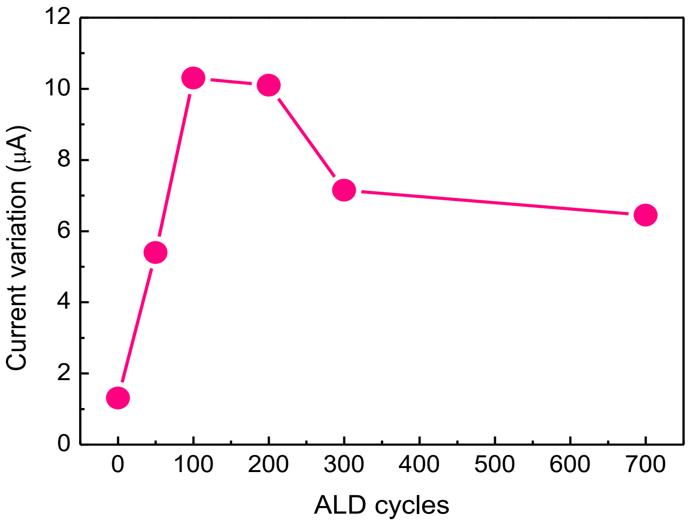

Figure IV.4. a) Peak current registered on the bare SPCE and modified CNTs/WS_2(X) in 50µM of RF.

As demonstrated in the figure IV.4, compared to the bare SPCE, all CNT/WS$_2$(X)@SPCE samples depicts improved anodic peak current (Ipa). Moreover, the I$_{pa}$ promotes with the shell thickness increase (50-100 ALD) because of the increased WS$_2$ active sites on CNT/WS$_2$(X) surface. However, the I$_{pa}$ significantly decreases when the WS$_2$ shell excesses an optimal thickness (100-200 ALD cycles). This result indicates that WS$_2$ shell with an optimal thickness provides the best combination of low interfacial resistance to charge transport and the presence of WS$_2$ as oxidation reactive sites, making the sensor more sensitive to RF.

As result, the CNTs/WS$_2$ (100ALD) sensor has been selected to be the best sensor and used for further studies.

In Fig.IV.5.a, CV curves of the bare SPCE highlight the presence of a cathodic peak at around −0.6 V characteristic of VB$_2$ reduction. However, a much smaller oxidation peak was also observed at −0.5 V. This implies that on the bare electrode, reduction of the riboflavin is the preferred reaction process. Results reported below in the Fig.IV.5.b for the modified CNTs/WS$_2$(100ALD)-SPCE, showed a pair of obvious redox peaks on the modified electrode, where anodic and cathodic current peaks appeared at – 0.5 and -0.4 V, respectively correlated with quasi-reversible oxidation and reduction of VB$_2$. The higher response of CNT/WS$_2$(100)-SPCE toward RF oxidation indicated that modified electrodes have more oxidation reactive sites than the bare one, which might be assigned to the presence of CNTs/WS$_2$ composite.

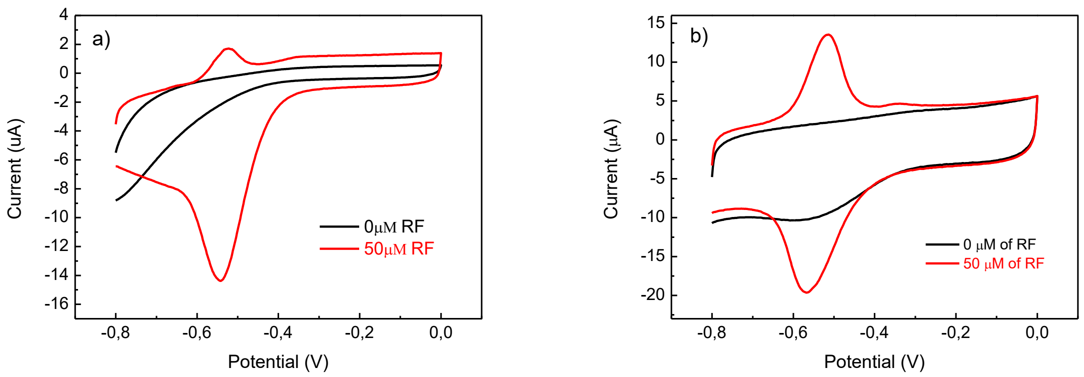

Figure IV.5. a) CVs of bare SPCE in absence and in presence of 50 µM of RF. b) CVs of WS$_2$-CNTs/SPCE (100ALD) in absence and in presence of 50 µM of RF. All tests are done in room temperature in 0.1M PBS at pH = 7.4 and at scan rate of 50mV/s.

The effect of RF on all the synthesized samples was investigated and the relevant electrochemical parameters were evaluated. As shown in Fig.IV.6 below, the capacitive current increase linearly increasing the ALD cycles. We can ascribe this improvement in the electrochemical performance of the sensor to the numerous adsorption sites provided by WS_2 which can potentially modify the reaction pathway.

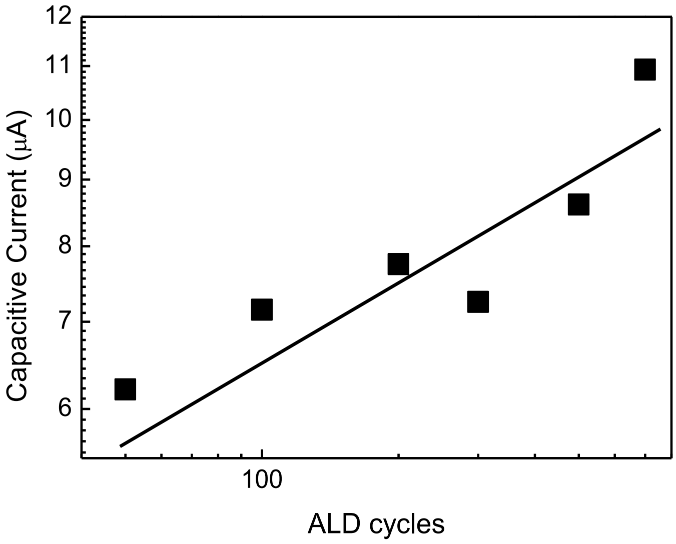

Figure IV.6. Plot of the capacitive current as a function of the ALD cycles.

III.3.b. Scan rate effect

In addition to that, studies were also performed while monitoring the current peak as a function of the scan rate (υ) in the range of 50 − 400 mV/s in 0.1 M PBS containing 50 μM of RF. The anodic and cathodic peak currents increased linearly with the scan rate (Fig.IV.7), indicating the occurrence of a redox process involving surface-confined species. It was noted that, by increasing the scan rate, the anodic and cathodic peak potentials shifted toward positive and negative directions, indicating charge-transfer kinetics limitations.

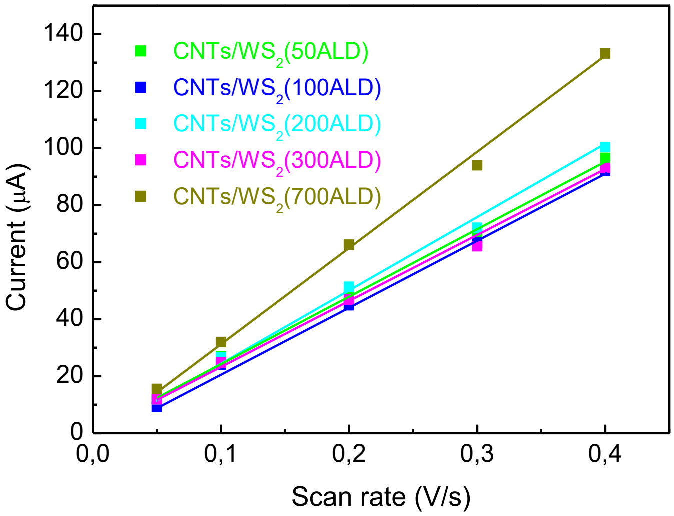

Figure IV.7. Plot of the anodic peak current (I_{pa}) vs. scan rate.

III.4. Sensing mechanism on different modified electrodes

The effect of the WS_2 layer thickness on the oxidation of riboflavin was investigated. Compared to bare CNTs, the sensitivity of the bare SPCE towards riboflavin detection first decreases in the lowest thickness of WS_2 (50 cycles). Adding more layers of WS_2, the sensitivity was more and more promoted going from 0.35 $\mu A \mu M^{-1} cm^{-2}$ to 2.06 $\mu A \mu M^{-1} cm^{-2}$. On bare SPCE and bare CNTs, oxidation sites are less and/or little active. Also, at the low number of ALD cycles (50 cycles) seems to be less effective in providing enough active sites to maximize the oxidation peak currents. With increasing the number of ALD cycles, and up to 100-200 ALD layers, the sensor film became more effective. However, with further increasing of the number of ALD cycles, the film becomes denser and acts as a blocking layer to the electron transfer between the CNTs/WS_2(X) and the analyte.

Therefore, the highest electrochemical performance for this electrochemical sensor was achieved for a layer that is, from one side, enough thick to provide maximum active adsorption sites for analytes and, from the other side, is enough thin to allow electron transfer between adsorbed species and electrode.

III.5. Quantitative determination of riboflavin

CNT/WS_2(100) nanocomposite was selected as the optimum sensing material for the quantitative determination of RF since it showed the highest peak currents and consequently the highest sensitivity. Based on that, the response of the CNT/WS_2(100)-SPCE modified sensor at different RF concentrations has been evaluated. In Fig. IV.8.a, is reported the differential pulse voltammetry (DPV) analysis of solution containing different concentrations of RF, from 0 to 45 µM, evidencing the associated augmentation of the peak current value. In Fig.IV.8.b (black dots), is shown the calibration curves for RF, plotting the peak current as a function of the analyte's concentration. The sensitivity is computed from a linear fit of the data (red line), and is 2.06 µAµ$M^{-1}$$cm^{-2}$ and LOD was 0.9 µM.

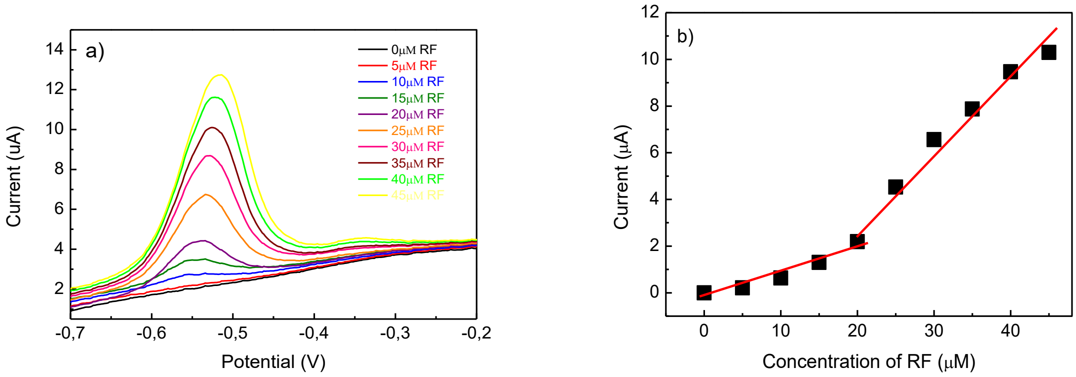

Figure IV.8. a) DPV of CNT/WS_2(100)-SPCE in 0.1 M PBS in presence of different RF concentrations at a scan rate of 50 mV/s, b) Calibration curve for the determination of RF.

The electroanalytical performance of the proposed sensor, for RF detection, was summarized and compared to other electrochemical sensors, Table IV.1.

Sensing material	Linear Range (µM)	LOD (µM)	Method	Ref.
2D-MoS_2-MoO_3CC	0 - 40	1.5	LSV	[16]
AuNPs-SPCE	0 - 70	1.3	LSV	[17]
Co^{2+}-Y zeolite	1.7 - 34	0.71	CV	[18]
CNT/WS_2 (100)	0 – 20	0.9	DPV	This work

Table IV.1. Performance of the proposed sensor in comparison to previously reported electrochemical sensors for riboflavin measurements.

III.6. Repeatability, long-term stability, reproducibility and interferences test of the modified electrode

III.6.a. Repeatability and long-term stability of the modified electrode

The repeatability and long-term stability of the developed modified sensor have been investigated. This assumes high importance since it’s one of the most important properties of electrochemical sensors. The repeatability and long-term stability of the selected sensor was investigated by performing the test using the same sensor one more time after one year under the same conditions as the first time and as presented in Fig.IV.9. It’s well evident that the sensor shows very good stability especially at low concentrations.

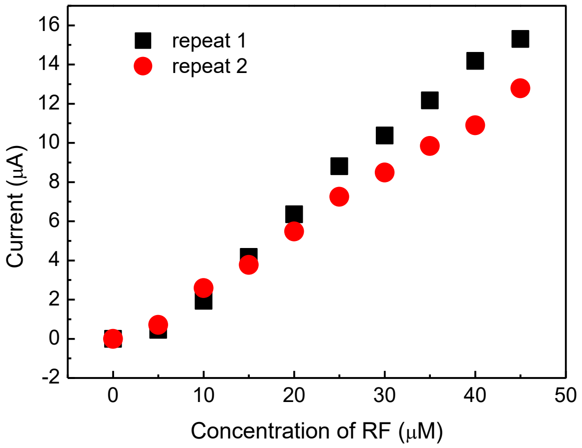

Figure IV.9. Calibration curves for RF using the same CNTs/WS_2(100ALD) sensor tested in 12 months apart.

III.6.b. Reproducibility of the modified electrode

To study the reproducibility, a new CNTs/WS_2 (100ALD)/SPCE was fabricated after one year using the same material used to prepare the first sensor and tested under identical conditions. Table IV.2 presents the sensitivity and LOD of both sensors indicating that the new sensor displays almost identical parameters as the old sensor confirming that obtained results are reproducible.

Sensors	**Sensitivity ($\mu A \mu M^{-1} cm^{-2}$)**	**LOD (µM)**
Old sensor	2.06	0.9
New sensor	2.27	1.08

Table IV.2. Comparison of two sensors modified with the same material.

III.6.c. Selectivity and interference test

Interference test was done adding folic acid (FA, vitamin B_9) and Ascorbic Acid (AA, vitamin C). As presented in Fig.IV.10, in presence of FA (50 µM), with the same concentration as for RF, a small increase of the current peak related to RF was observed of about 1 µA compared to the DPV curve in presence of only RF (50 µM). This behaviour can be explained by the fact that RF and FA, both B-group vitamins, have a lot of common functional groups that can similarly interact with the surface of the working electrode. While adding 50 µM of AA to the solution, no variation is observed on the DPV cycle confirming that the presented sensor is particularly selective for our target vitamin.

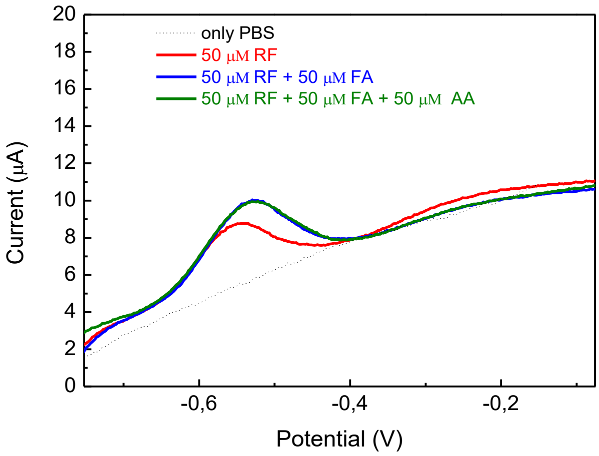

Figure IV.10. DPV curves in co-presence of RF, FA, and AA at a concentration of 50 µM in 0.1 M PBS.

IV. Conclusion

In summary, WS_2 layers with different thicknesses were deposited onto carbon nanotubes (CNTs) by atomic layer deposition (ALD) forming CNTs/WS_2 core-shell nanocomposites. The obtained material was characterized by X-Ray diffraction and high-resolution transmission electron microscopy. The core-shell nanocomposites were used to fabricate a novel electrochemical platform with enhanced properties by modifying commercial screen-printed carbon electrodes for the detection of riboflavin.

V. References

1. Raza, M.H., et al., *Role of Heterojunctions of Core–Shell Heterostructures in Gas Sensing*. ACS Applied Materials & Interfaces, 2022. **14**(19): p. 22041-22052.
2. Moulaee, K., et al., *CNT/Al2O3 core–shell nanostructures for the electrochemical detection of dihydroxybenzene isomers*. Physical Chemistry Chemical Physics, 2021. **23**(25): p. 14064-14074.
3. Raza, M.H., et al., *Gas sensing of NiO-SCCNT core–shell heterostructures: optimization by radial modulation of the hole-accumulation layer*. Advanced Functional Materials, 2020. **30**(6): p. 1906874.

4. Raza, M.H., et al., *Tuning the NiO thin film morphology on carbon nanotubes by atomic layer deposition for enzyme-free glucose sensing.* ChemElectroChem, 2019. **6**(2): p. 383-392.
5. Fan, Y., et al., *Optimization of the activity of Ni-based nanostructures for the oxygen evolution reaction.* ACS Applied Energy Materials, 2018. **1**(9): p. 4554-4563.
6. Staerz, A., et al., *Dominant role of heterojunctions in gas sensing with composite materials.* ACS applied materials & interfaces, 2020. **12**(18): p. 21127-21132.
7. Dasgupta, N.P., L. Li, and X. Sun, *Atomic layer deposition for energy and environmental applications.* 2016.
8. Pinna, N. and M. Knez, *Atomic layer deposition of nanostructured materials*. 2012: John Wiley & Sons.
9. Kim, H.-C., et al., *Engineering optical and electronic properties of WS2 by varying the number of layers.* ACS nano, 2015. **9**(7): p. 6854-6860.
10. Saleh Ahammad, A., J.-J. Lee, and M.A. Rahman, *Electrochemical sensors based on carbon nanotubes.* sensors, 2009. **9**(4): p. 2289-2319.
11. Cioates, C.N., *Electrochemical sensors used in the determination of riboflavin.* Journal of The Electrochemical Society, 2020. **167**(3): p. 037558.
12. Tigari, G. and J. Manjunatha, *A surfactant enhanced novel pencil graphite and carbon nanotube composite paste material as an effective electrochemical sensor for determination of riboflavin.* Journal of Science: Advanced Materials and Devices, 2020. **5**(1): p. 56-64.
13. Wu, Y., et al., *A Self-Limited Atomic Layer Deposition of WS2 Based on the Chemisorption and Reduction of Bis (t-butylimino) bis (dimethylamino) Complexes.* Chemistry of Materials, 2019. **31**(6): p. 1881-1890.
14. Poon, J., et al., *Altered electrochemistry at graphene-or alumina-modified electrodes: Catalysis vs electrocatalysis in multistep electrode processes.* Journal of Physical Chemistry C, 2015. **119**(24): p. 13777-13784.
15. Lin, Q., et al., *Two-Electron, Two-Proton Oxidation of Catechol: Kinetics and Apparent Catalysis.* The Journal of Physical Chemistry C, 2015. **119**(3): p. 1489-1495.

16. Zribi, R., et al., *Fabrication of a novel electrochemical sensor based on carbon cloth matrix functionalized with MoO3 and 2D-MoS2 layers for riboflavin determination.* Sensors, 2021. **21**(4): p. 1371.
17. Chelly, M., et al., *Synthesis of silver and gold nanoparticles from rumex roseus plant extract and their application in electrochemical sensors.* Nanomaterials, 2021. **11**(3): p. 739.
18. Nezamzadeh-Ejhieh, A. and P. Pouladsaz, *Voltammetric determination of riboflavin based on electrocatalytic oxidation at zeolite-modified carbon paste electrodes.* Journal of Industrial and Engineering Chemistry, 2014. **20**(4): p. 2146-2152.

FlatChem 36 (2022) 100433

Contents lists available at ScienceDirect

FlatChem

journal homepage: www.sciencedirect.com/journal/flatchem

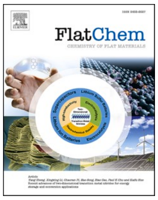

Electrochemical and sensing properties of AuNps-2D-MoS_2/SPCE for folic acid determination

Khouloud Abid [a,b], Rayhane Zribi [a,c], Ramzi Maalej [b], Antonino Foti [c], Amani Khaskhoussi [a], Pietro Giuseppe Gucciardi [c], Giovanni Neri [a,*]

[a] Department of Engineering, University of Messina, C.da Di Dio, I-98166 Messina, Italy
[b] Laboratory of Dielectric and Photonic Materials, Faculty of Sciences of Sfax, Sfax University, Sfax 3018, Tunisia
[c] CNR IPCF Istituto per i Processi Chimico-Fisici, viale F. Stagno D'Alcontres 37, I-98156 Messina, Italy

ARTICLE INFO

Keywords:
Molybdenum disulphide nanosheets (MoS_2 NS)
Gold nanoparticles (AuNPs)
Electrochemical sensor
Folic acid (FA)

ABSTRACT

A simple and sensitive electrochemical sensor was developed for the detection of folic acid (FA) based on gold nanoparticles (AuNPs) dispersed on exfoliated MoS_2 (2D-MoS_2) nanosheets by a simple impregnation method. The prepared 2D-MoS_2 and AuNPs-MoS_2 samples were characterized by scanning electron microscopy (SEM-EDX), UV–vis, and Raman spectroscopy. Screen-printed carbon electrodes (SPCE) were modified by the 2D-MoS_2 and AuNPs-MoS_2 nanosheets and their electrochemical characteristics were investigated by means of electrochemical impedance spectroscopy (EIS) and cyclic voltammetry (CV) techniques and tested in the electroanalytical determination of folic acid (FA). The modified 2D-MoS_2/SPCE was found to promote the FA electrooxidation process compared to bare SPCE. Instead, with the AuNPs-MoS_2/SPCE sensor a different sensing mechanism, based on the inhibition of the Au NPs redox peaks current, has been found to be more effective. This behavior was due to the strong binding of FA on AuNPs, as probed by in situ ATR-FTIR and SERS measurements. The decrease of the anodic peak current of Au NPs with the concentration of FA provided an indirect signal which has been used here for detecting FA.

Introduction

Over recent years, thin two-dimensional materials have received great attention in the field of energy storage, catalysis, sensors, drug carriers, solar cells, and among others [1–4]. They displayed a fast-growing interest due to their peculiar properties that would play a significant role in future technology. Among these 2D materials, the transition metal disulphide (TMDS) materials show interesting features citing high-carrier mobility, large surface-to-volume ratio, and indirect-to-direct crossover when decreasing the thickness. These features are of outmost importance especially for their use in the biosensing field [5]. Indeed, compared with conventional analytical techniques, electrochemical methods display many advantages for example ease of operation and low cost.

Folic acid, known as vitamin B9, is a water-soluble vitamin that can be found in fruits, green vegetables, animal products [6]. However, this vitamin is unstable, and it possesses an ease of degradation by pH, oxygen, UV light, and temperature. The deficiency of B9 can affect adversely human beings and pregnant women increasing the possibilities of diseases such as anemia, psychosis, and neural tube defects [7,8]. Various techniques can be used for the detection of FA but they are generally time consuming, high-cost, and requiring an expert for the use. Folic acid (see Scheme 1a,b showing the 3D conformer and the molecular structure) is an electroactive molecule, so its electrochemical determination, mainly based on the oxidation reaction as described in Scheme 1c, is feasible on many electrode surfaces [9,10]. Further, electrochemical methods are low-cost, simple to use, and time-saving, then their use for the determination of FA is highly promising.

$$C_{19}H_{19}N_7O_6 \xrightarrow{oxidation} C_{19}H_{17}N_7O_6 + H^{2+} + 2e$$

In a previous paper an electrochemical sensor based on MoS_2-AuNPs dispersed on graphene nanosheets (GNS), with gold particle sizes of about 10–50 nm, and deposited onto the surface of a screen-printed electrode was reported. Due to the good synergic effect between GNS, MoS_2, and AuNPs, the composite shows excellent electrocatalytic ability for the electrooxidation of FA [11].

---

* Corresponding author.
E-mail address: gneri@unime.it (G. Neri).

https://doi.org/10.1016/j.flatc.2022.100433
Received 5 June 2022; Received in revised form 25 September 2022; Accepted 5 October 2022

Apart from the classical electrochemical scheme above illustrated, other electrochemical pathways have been explored for FA detection. For example, based on the strong ability of FA to bind many metal surfaces, adsorptive stripping techniques using a mercury electrode have been previously proposed [12,6]. In the same manner, a lead electrode was also used [13]. As both mercury and lead electrodes have the drawback of a certain degree of environmental toxicity, here we introduce more friendly electrodes.

In this work, we propose an electrochemical sensor for the detection of folic acid (FA), based on 2-D MoS2 nanosheets. The nanosheets were synthesized through the liquid-phase exfoliation (LPE) technique which is a low-cost and easy method to produce few-layers 2D materials. Further, the 2-D MoS2 nanosheets were coated with gold nanoparticles (AuNPs), deposited on the surface of the nanosheet by the simple impregnation method. A commercial screen-printed carbon electrode (SPCE) platform was then used to fabricate Au NPs-MoS2/SPCE sensors for the detection of FA. We attempted the electrochemical detection of FA exploiting the well-known strong interaction between FA and gold [14]. Briefly, AuNPs nanoparticles on 2-D MoS_2 nanosheets can serve as attachment sites for FA. The steric/electronic hindrance induced by the formation of the FA-Au complex prevents electrons from reaching the surface of the electrode and consequently decreases the current, which is thus exploited for the development of an electroanalytical sensor. A similar procedure, where AuNPs have been used as electrochemical and plasmonic substrates for the detection of FA, has been reported in previous papers [15–18]. Rather than using the expensive procedure and precursors previously reported in the cited papers, we used low-cost, accurate, real-time method, but, to our knowledge, this represents the first attempt for detecting FA by the described sensing mechanism with disposable screen-printed electrodes.

Experimental

Synthesis of 2D-MoS_2 nanosheets

2D-MoS_2 nanosheets were prepared by surfactant-assisted liquid-phase exfoliation of MoS_2 powder in a watery solution of sodium cholate (SC – 1.5 mg/mL), whose stabilizing action prevents the MoS_2 nanosheets aggregation [19–21]. MoS_2 powder was dispersed in the SC solution at the final concentration of 5 mg/mL. Afterwards the dispersion was sonicated with Branson 250 sonifier mounting a flat tip (3/16″ diameter), and operating at 50 % of amplitude for 30 min with an ultrasonics time-on/time-off ratio of 1:1 for every second. Samples were kept in an ice bath to reduce detrimental heating effects during sonication. After the sonication process, the dispersions were left to decant in a flask overnight. After the rest period the surnatant was separated from the sediment and centrifuged at 1500 rpm for 90 min (ALC 4235, swinging rotor). The top part of the centrifuged sample (rich in few-layer nanosheets) was extracted and used in our experiments.

The hybrid sample combining AuNPs and MoS_2 nanosheets (2D-MoS_2) was fabricated through the impregnation method [22]. In particular we mixed, at room temperature, 0.2 ml of a HAuCl4 solution (5 mM) with 0.2 ml of a 2D-MoS2 suspension, keeping the final sample under stirring for 1 min. In these conditions, spontaneous electron transfer from MoS2 to gold ions occurs leading to the formation of Au nanoparticles [22].

Characterization

SEM images were acquired with a Zeiss CrossBeam 540, while UV–vis spectra were recorded in the 250–900 nm wavelength range with a Perkin Elmer Lambda 25 UV–vis setup using 1 cm length sample cell. Micro-Raman spectroscopy experiments were carried out on MoS2 flakes at room temperature with a Horiba Labram HR800 confocal spectrometer (Horiba JobinYvon) coupled with an Argon ion laser emitting at 514.5 nm (Spectra Physics). The laser beam is focused on the sample surface using a 100X objective (NA 0.9, WD 0.2 mm) and the scattered light is collected through the same objective in a backscattering configuration. The Raman signal is then dispersed by a 1800 l/mm grating and detected by a Peltier-cooled silicon CCD (Synapse, Horiba Jobin-Yvon). Spectra of the MoS_2 drop on glass were acquired using a laser power of 9mW, integration time of 20 s, with up to 10 accumulations. SERS characterizations was performed using an Horiba Xplora coupled with a 785 nm diode laser with a power at the sample of 2 mW, integration times of 20 s and 3 accumulation. The Raman signal is then dispersed by a 1200 l/mm grating and detected by a Peltier-cooled silicon CCD (Syncerity, Horiba Jobin-Yvon). Fourier transform infrared spectroscopy (FT-IR) spectra were collected by a Perkin Elmer Spectrum 100 spectrometer equipped with a universal ATR sampling accessory.

Fabrication of Au-MoS_2/SPCE sensor

Screen-printed carbon electrodes (SPCEs) were purchased from DropSens, Spain. The platform used was: DRP-100 (named SPCE), constituted of a 4-mm diameter carbon working electrode, a silver pseudo reference electrode, and a carbon auxiliary electrode. To modify the bare SPCE with 2D-MoS_2 or Au NPs-MoS_2 nanosheets, 50 µl of an aqueous dispersion containing these nanosheets, were deposited on the carbon working electrode and allowed to dry at room temperature until further use. These sensors are named MoS_2/SPCE and Au NPs-MoS_2/SPCE, respectively.

Electrochemical measurements

Electrochemical analyses were performed by using a DropSens µStat 400 Potentiostat empowered by Dropview 8400 software for data acquisition. Electrochemical impedance spectroscopy (EIS) tests were performed by using an Autolab PGSTAT204 system in ferrocyanide solution ($[Fe(CN)6]^{4-/3-}$) at frequency range 10^5–10^{-2} Hz. The sensors were characterized by cyclic voltammetry (CV) tests in aerated 1 M PBS as electrolyte. CV tests were carried out at a scan rate of 50 mV/s. All experiments were performed at room temperature.

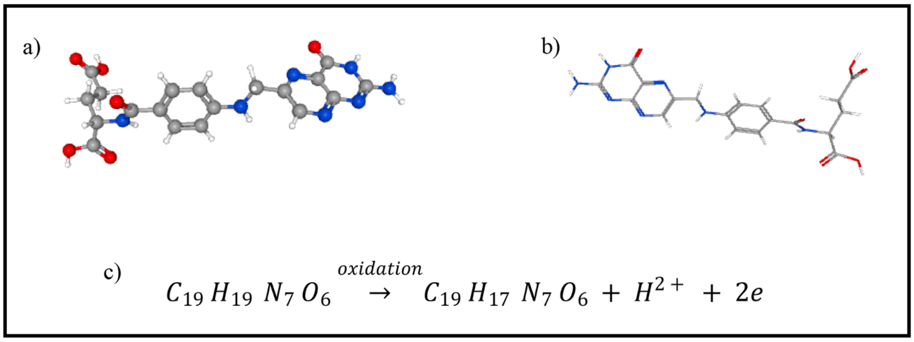

$$C_{19}H_{19}\,N_7\,O_6 \xrightarrow{oxidation} C_{19}H_{17}\,N_7\,O_6 + H^{2+} + 2e$$

Scheme 1. a) 3D conformer and b) molecular structure of folic acid; c) oxidation reaction of FA.

Results and discussions

Morphological, microstructural, and electrical measurements

The prepared 2D-MoS_2 sample was first investigated for evaluating its morphological and microstructural characteristics. UV–vis measurements were performed on solutions diluted at 1:10 v/v to minimize the influence of multiple scattering. Under these conditions information on the samples' concentrations can be obtained by applying Beer's law. Fig. 1 reports the UV–vis spectrum, showing the A- and B- excitonic peaks, respectively at ~676 nm and ~613 nm, together with the C-excitonic band at 467 nm, superposed to a scattering background, and consistent with what was expected for the 2H polytype of MoS_2. Moreover, the direct transition of excitons from VB to CB results in peaks located at 382 nm, named D excitonic band.

The average nanosheets size $\langle L\rangle$, concentration, and average number of layers $\langle N\rangle$, are parameters characterizing the 2D- exfoliated nanomaterials that can be extracted from empirical formulas [23]. From the ratio between the local minimum extinction intensity at 350 nm (Ext350) and the extinction value at the B-exciton peak wavelength (ExtB), we can calculate $\langle L\rangle$:

$$L\ (\mu m) = \frac{3.5 * Ext_B/Ext_{350}\ - 0.14}{11.5 - Ext_B/Ext_{350}} \qquad (1)$$

Based on the extinction on the empirical absorption coefficient $\varepsilon_{350} = 69\,L\,g^{-1}cm^{-1}$, the concentration of these dispersions is computed as [23]:

$$C = \frac{1}{l} Ext350/\varepsilon_{350} = -\frac{1}{\varepsilon_{350}\ l} Log_{10}T(\lambda = 350\ nm) \qquad (2)$$

where l is the length of cuvette containing the solution (1 cm in our case) and $T(\lambda = 350\,\mathrm{nm})$ the transmittance at the local minimum at 350 nm. From the position of the A-exciton λ_A (in nm), $\langle N\rangle$ can be estimated as follows:

$$\langle N\rangle = 2.3 * 10^{36}\ e^{-54888/\lambda_A} \qquad (3)$$

From the data in Fig. 1, the average number of layers $\langle N\rangle \sim 12$, with an average length <L> ~ 200 nm and concentration in the order of 32 μg/mL.

Raman spectroscopy

Fig. 2 shows the Raman fingerprint of MoS_2 nanosheets which is dominated by two sharp peaks, the E^1_{2g} (385 cm^{-1}) and the A_{1g} (410 cm^{-1}). The first mode is related to the in-plane vibration of S with M atom in-plane while the second mode represents the out of plane S vibration (inset Fig. 2) [24]. The number of layers of MoS_2 is sensitive to the in-plane and out of plane modes wavelength, then, the difference between these modes, Δω (E^1_{2g} - A_{1g}), can be an indicator for the number of layers contained in the nanosheets [25]. For instance, passing from bulk to single layer the Δω changes from 26 cm^{-1} to 17.5 cm^{-1} [26]. The difference between the two modes in our case is equal to 25 cm^{-1}, corresponding to more than 6 layers, which is in agreement with previous investigations [27]. Using the relationship Δω (A_{1g} − E^1_{2g}) = 25.8–8.4/N, we can also determine number of layers, that in our case is equal to 10 [28,29]. The average number of layers estimated by Raman spectroscopy (N ~ 10) is slightly lower than that retrieved by UV–vis (N ~ 12). However, some small discrepancy can be acceptable since these two calculations are based on different techniques.

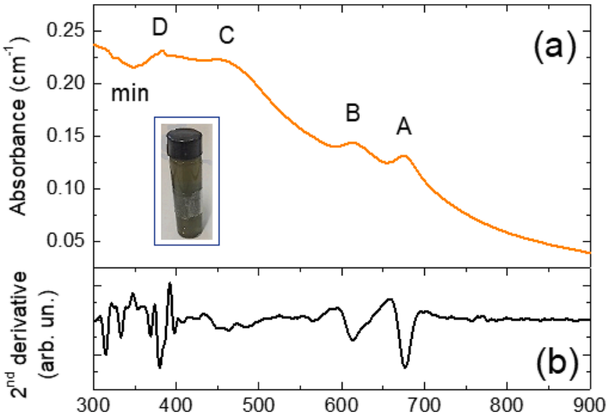

Fig. 1. (a) Extinction spectrum of the 2D-MoS2 dispersion (diluted 1:10 v/v). (b) Second derivative of the extinction signal. Inset: Picture of the MoS2 nanosheets suspension (non-diluted solution).

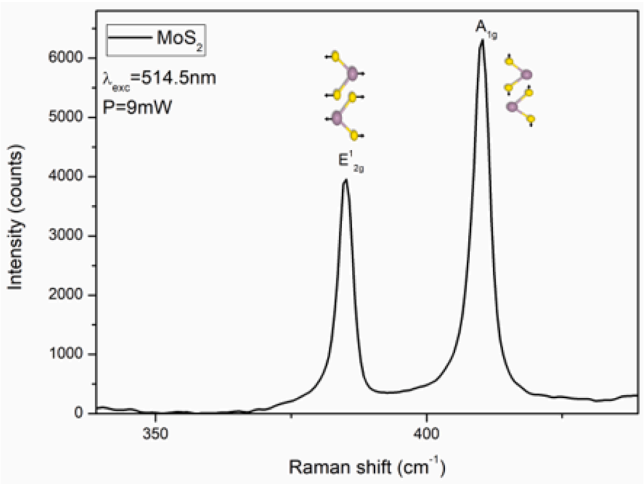

Fig. 2. Raman spectrum of MoS_2 at room temperature under 514.5 nm laser line. Inset: atomic displacement of active (E^1_{2g}, A_{1g}).

SEM characterization

SEM image reported in Fig. 3a,b shows the morphology of the bare SPCE and the as prepared 2D-MoS_2 nanosheets dispersed on the SPCE surface, respectively.

SEM images from the Au modified-MoS_2 deposited layer on the SPCE electrochemical platform, are shown in Fig. 4. At low magnification (Fig. 4a), AuNPs are seen dispersed on the surface of the MoS_2/SPCE, forming aggregates. Gold nanoparticles with size ranging from 80 to 200 nm, can be clearly seen at higher magnification (Fig. 4b). This confirms previous data in ref. [22], where is reported that a redox reaction occurs between MoS_2 and gold ions, allowing spontaneous electron transfer from MoS_2 to gold ions and leading to the formation of Au nanoparticles on the surface of chemically exfoliated TMDC sheets. The density and size of the gold nanoparticles decorating the MoS_2 sheets can be easily tuned by controlling the concentration of $HAuCl_4$. Further, the size distribution has been demonstrated to be maintained relatively narrow, without the use of any stabilizer.

The presence of the expected elements is confirmed from the EDX spectrum in Fig. 4c: Au (wt%=71), C (wt%=24), Mo (wt%=4), and S (wt %=0.3). The presence of chlorine (Cl) element may be due to the contamination of this ion by HAuCl4 used as precursor material for Au during the preparation of Au-MoS_2 nanosheets.

Electrochemical characterization of AuNPs-MoS_2/SPCE

The redox probe $[Fe(CN)_6]^{3-/4-}$ has been used for the study of the electrochemical characteristics of SPCE, MoS_2/SPCE and AuNPs MoS_2/SPCE, respectively, under the following conditions: scan rate 0.05 V/s and the potential window between −0.2 V and −0.6 V.

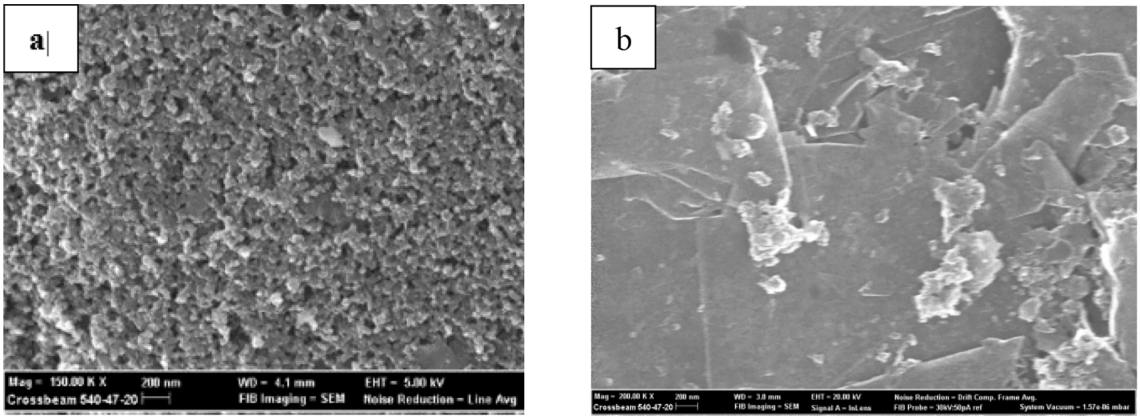

Fig. 3. SEM images showing the morphology of: a) bare SPCE; b) 2D-MoS_2 nanosheets over SPCE surface.

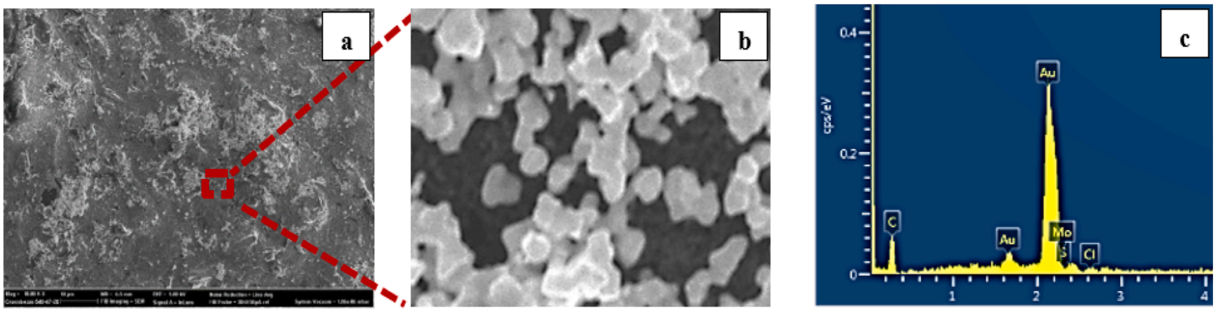

Fig. 4. a, b) SEM image at different magnification of the AuNPs-MoS_2/SPCE surface; c) EDX spectrum.

As noted in Fig. 5, MoS_2/SPCE shows only a minimal improvement in the current response with respect to bare SPCE. Instead, using Au NPs-MoS_2/SPCE revealed an enhancement in anodic and cathodic currents (I_{pa} and I_{pc}) compared with bare and modified MoS_2/SPCE. This finding appears to be due to the higher surface area of the modified electrode.

Based on the equation of Randles-Sevcik, the active surface area (SA) of unmodified and modified electrodes were calculated [30]:

$$I_{pa} = 2.69 \times 10^5 SAD^{1/2} n^{3/2} \nu^{1/2} C$$

where I_{pa} is the anodic peak current in μA, D is the diffusion coefficient in $cm^2\ s^{-1}$ ($7.6 \times 10^{-6}\ cm^2\ s^{-1}$), C is the concentration of the analyte in mol cm^{-3}. The number of electrons involved in the oxidation reaction is n and the scan rate is ν. Calculation indicated that the active surface area of AuNPs-MoS_2/SPCE is increased by 12 % compared to that of the unmodified SPCE, confirming the expected results. We have further characterized the electrochemical response of the various electrodes employing electrochemical impedance spectroscopy (EIS). The Nyquist plot collected in $[Fe(CN)^6]^{3-/4-}$ solution is reported in Fig. 6a. In the case of bare SPCE, we observed a semicircle in high-frequencies and a linear segment in low-frequencies. Through the analysis of the equivalent circuit of the electrochemical cell (Fig. 6.b), we can calculate R_s, R_{CT}, C_{dl}, and Z_w standing for electrolyte resistance, charge transfer resistance, double-layer capacitance, and Warburg impedance, respectively (see Table 1). For the bare SPCE, R_{CT} was equal to ~3707 Ω. The significant change in R_{CT} value is attributed to the modification of the charge-transfer rate across the modified interface. This value becomes 19.6KΩ and 19.3 K Ω for MoS_2/SPCE and Au-MoS_2/SPCE, respectively.

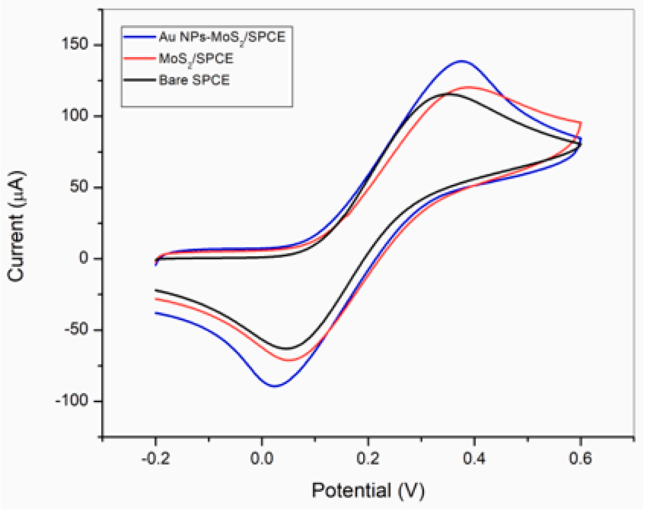

Fig. 5. CV in $[Fe(CN)_6]^{3-/4-}$solution for the SPCE, MoS_2/SPCE and AuNPs MoS_2/SPCE.

In summary, the electrochemical characterization above reported indicate that improvement of the electrochemical properties of the Au NPs-MOS2 composite, is not only due to a different surface area but the presence of Au NPs as the electroactive sites should be considered as prominent.

Electroanalytical determination of FA on AuNPs-MoS2/SPCE

Preliminary tests in 0.01 M phosphate buffer solution (PBS, pH = 7.4) with bare SPCE, modified MoS_2/SPCE, and both Au NPs MoS_2/SPCE were first performed in the potential range 0.0 V to 1.0 V and at 0.05 V/s scan rate (Fig. 7). Test on bare SPCE and MoS_2/SPCE in PBS showed a smooth cycle without any faradaic peak in the potential window investigated. However, on the MoS_2/SPCE the CV cycle is much larger, due to the occurrence of higher capacitive effects. This finding is intuitively linked to the expected higher surface area of this modified SPCE

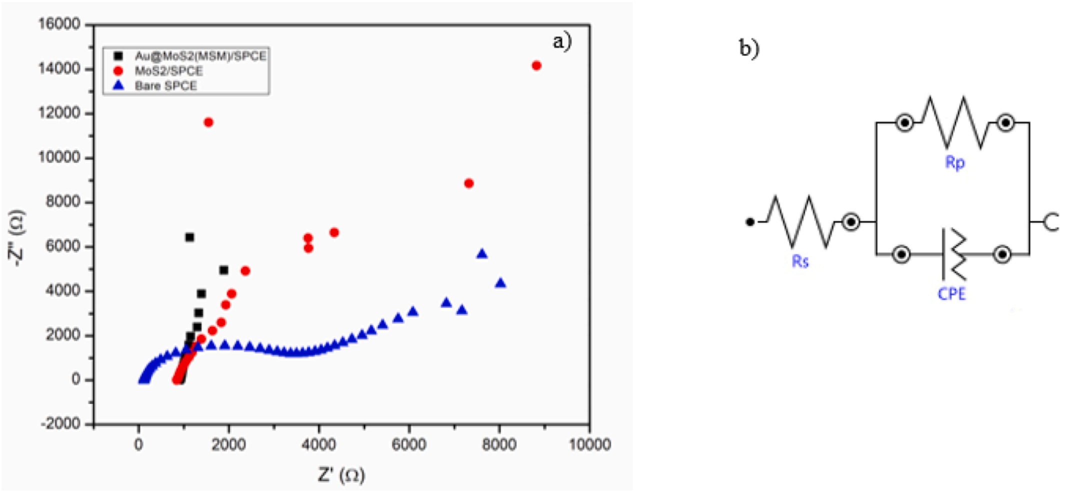

Fig. 6. (a) Nyquist plot of bare SPCE, MoS2/SPCE and Au NPs-MoS2/SPCE. (b) equivalent circuit.

Table 1
Randles equivalent circuit parameters; R_s and $R_{CT.}$

Electrode nature	R_S (Ω)	R_{CT}(KΩ)
Bare SPCE	92.855	3707.1
MoS_2/SPCE	909.08	19,693
Au@MoS_2(MSM)/SPCE	1015.5	19,333

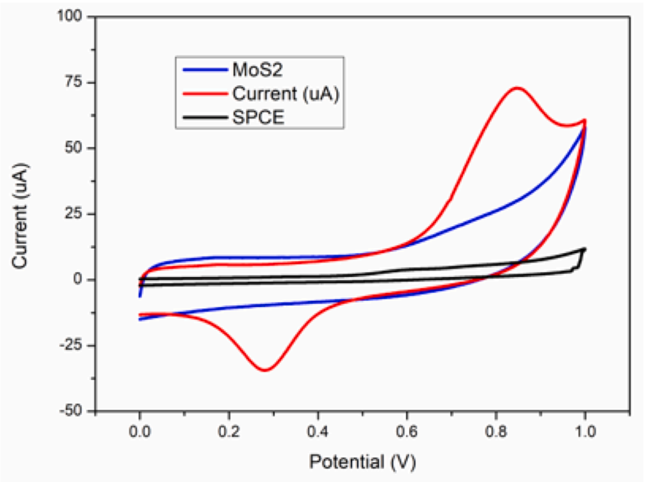

Fig. 7. CV of bare SPCE, MoS_2/SPCE, and Au NPs MoS_2/SPCE in PBS solution at 50 mVs^{-1}.

with respect to the bare one. Vice versa, the Au NPs-MoS2/SPCE sensor exhibits a pair of peaks, at +0.27 V and +0.85 V, attributed to redox cycle Au_{ox}/Au_{red} which dominates the CV cycle, confirming the successful AuNPs formation.

With the objective to develop a method for the electroanalytical determination of FA based on the described sensors, they were then investigated by Linear Sweep Voltammetry (LSV) in the presence of different folic acid concentrations (Fig. 8a). On the bare SPCE a weak anodic peak was observed to appear in the presence of FA at ~0.60 V. Compared with bare SPCE, the MoS_2/SPCE (reported in the inset of Fig. 8a) showed an anodic peak at ~0.52 V. The shift to lower potential, along an increase of the anodic peak current (Fig. 8b), was an indication of the good electrocatalytic ability of MoS_2 nanosheets for folic acid electrooxidation.

Tests with different FA concentrations were then performed on the AuNPs-MoS_2/SPCE sensor. We noted that by using this sensor the anodic peak at around 0.5 V is almost negligible. On the other hand, we observed a strong decrease of the intensity of the gold redox peaks with increasing the concentration of FA (Fig. 9a). Further, after each addition of FA results in a systematic decrease of redox current of both anodic and cathodic gold peaks. What occurred at the anodic peak on the addition of folic acid is much clearer, subtracting the baseline in absence of FA and reporting the variation associated (see Fig. 9b). The change of anodic peak current observed on AuNPs-MoS_2/SPCE with FA concentration is shown in Fig. 9c and compared with the variation of the current of the electroxidation peak of FA observed on the bare and MoS_2/SPCE sensors. The AuNPs-MoS_2/SPCE sensor clearly exhibits a larger variation than the signals showed by the other investigated sensors. Based on the above reported graphs, two linear regimes were noted. The sensitivity, computed in the concentration range 0 to 20 μM is equal to 20.636 $\mu A \mu M^{-1} cm^{-2}$ with a limit of detection (LoD) calculated using the formula: 3σ/S, where σ is the slope and S is the standard deviation, of 1.04 μM, while in the higher concentration range between 20 and 100 μM the sensitivity is comparatively lower and is equal to 3.949 $\mu A \mu M^{-1} cm^{-2}$.

Sensing mechanism

The different mechanisms we observed on the SPCE and MoS_2/SPCE from one hand, and the Au NPs-MoS_2/SPCE on the other hand, can be explained based on the different interaction of the folic acid analyte with the sensing layer electrode and specifically if Au is present or not.

In the case of the SPCE and MoS_2/SPCE, i.e. when Au is not present, the carbon surface of the first sensor and the MoS_2 terminated surface of the modified sensor, behave as the activated surfaces for the electrooxidation of FA, following the reaction pathway shown in Scheme 1a. MoS_2/SPCE has a larger surface area than the bare SPCE and this makes it more sensitive for FA sensing.

The results reported with the Au NPs-MoS_2/SPCE, suggests that this mechanism is not operative. We explain the observed finding on the assumption that the surface of the Au NPs-MoS_2/SPCE is covered by the folic acid molecules strongly adsorbed on the Au NPs (see Scheme 2b). The adsorbed FA molecules act as a poisoning layer which does not permit the electrooxidation of FA as noted for the SPCE and MoS_2/SPCE and, even at very low concentration where the full surface coverage could not be reached, this limits the oxidation/reduction redox pathway of Au NPs.

The high binding affinity of FA for the Au surface was well described in previous papers. Castillo et al. [31] demonstrated by SERS, Raman analysis, and DFT calculations, that FA interacts with gold nanopillars mainly through the nitrogen in the pterin moiety (see red circle in

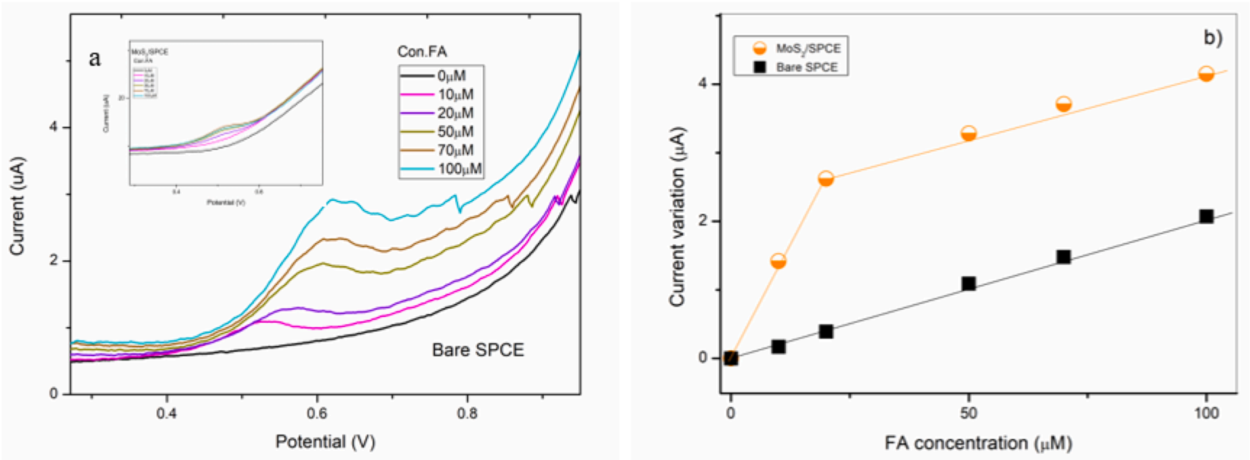

Fig. 8. a) LSV measurement and (b) calibration curve of FA on the bare SPCE and MoS_2/SPCE.

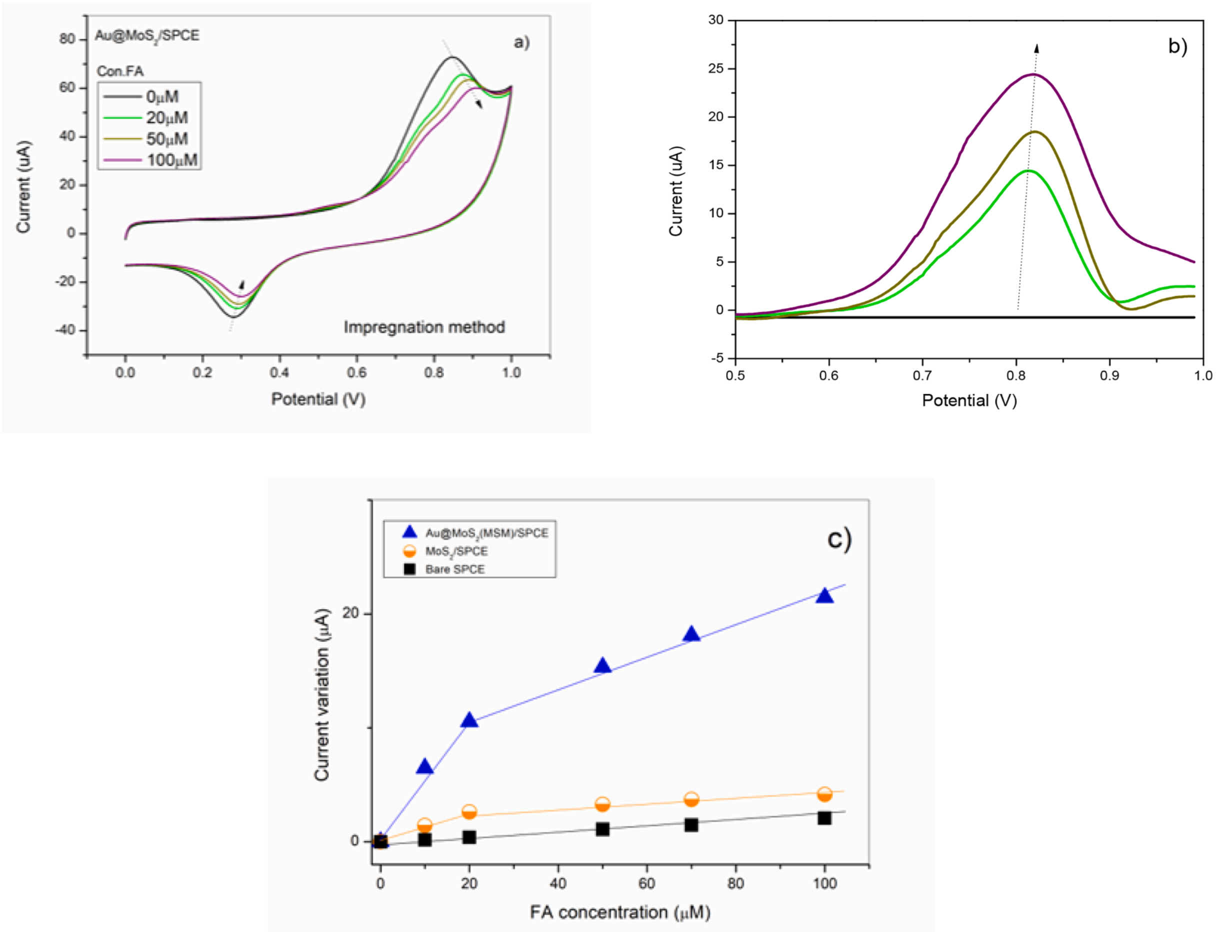

Fig. 9. (a) CV measurement at different concentration of FA on AuNPs-MoS_2/SPCE; (b) LSV measurement at different concentration of FA on AuNPs-MoS_2/SPCE with subtraction of the baseline (c) Calibration curve of AuNPs-MoS_2/SPCE. Calibration curve of FA on SPCE and MoS_2/SPCE are also shown for comparison.

Scheme 2b). However, it cannot be excluded that FA molecules are joined mainly by the carboxylic groups to the metal surface of the Au, leaving out the pterin ring. As probed by FT-IR, Majidi et al., proposed that FA can interact with the surface of the AuNP through the carboxylate groups of glutamic acid portion and the amine group of pterin moiety [32].

Anyway, when FA binds to Au NPs, the number of gold surface sites which remains free decrease. Thus, during LSV, the FA adsorbed layer prevents the stripping of Au, resulting in the observed reduction of current. A similar mechanism has been reported for the detection of glutathione (GSH) on Au NPS on TiO_2 nanotubes [33]. On adding GSH, the redox current is decreased due to the binding of GSH to Au NPs. However, compared to our sensors, the redox current due to Au NPs on TiO_2 nanotubes decreased only after incremental addition of GSH starting from 1 mM GSH, whereas we can detect FA in the micromolar or less range.

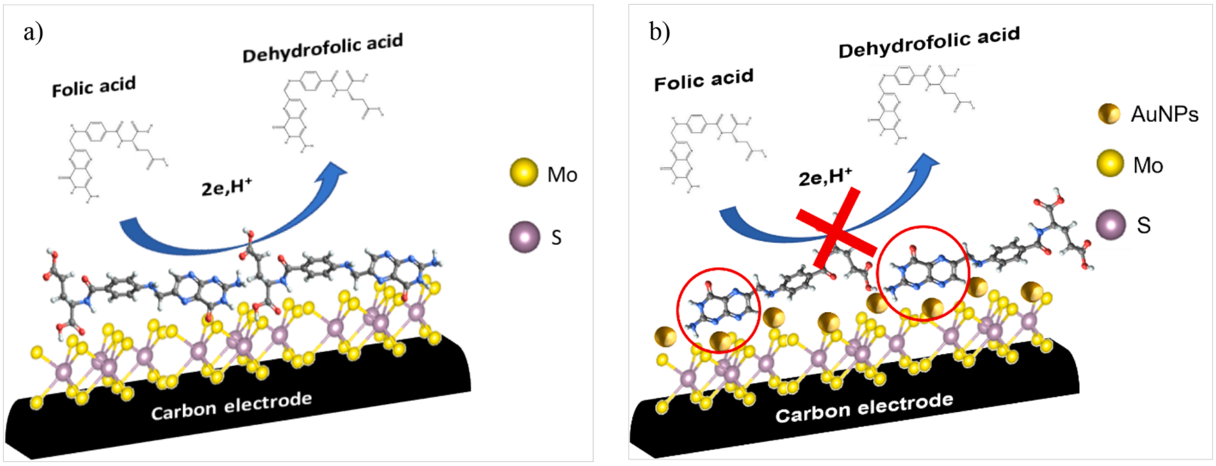

Scheme 2. Schematic representation of adsorption/reaction processes occurring in the presence of FA on the surface of: a) MoS_2/SPCE and b) Au NPs-MoS_2/SPCE. The red circle marks the petrin portion of FA.

To highlight the strong interaction between the FA with the surface of AuNPs, the AuNPs-MoS_2/SPCE was investigated through ATR-FTIR and SERS spectroscopies. It is well known that in the presence of an interaction between the probe molecules and gold nanoparticles, a strong enhancement of the signal is detected [34]. In Fig. 10 are shown the ATR-FTIR spectra of free FA and ones collected on bare SPCE, MoS_2/SPCE, and AuNPs-MoS_2/SPCE. The ATR-FTIR spectrum of pure folic acid revealed the characteristic absorption peak at 1692 cm^{-1}, which corresponds to CO stretching from –COOH, and 1607 cm^{-1}, 1475 cm^{-1}, which correspond to the phenyl and pterin rings.

On bare SPCE and MoS_2/SPCE, the folic acid signature is barely discernible from the background. Instead, with AuNPs-MoS_2/SPCE, the folic acid spectrum is well evidentiated. This suggests that folic acid interaction occurs with AuNPs presents on the surface of AuNPs-MoS_2/SPCE. Additionally, the absence of the peak due to skeletal vibration of the pterin ring at 1508 cm^{-1} in the spectrum of this latter sample could indicate that AuNPs perhaps interact strongly with the pterin portion of FA.

Raman analysis performed on FA adsorbed on the bare SPCE didn't reveal the characteristic vibrational modes of the target molecule (Fig. 11 – black line), while for MoS_2/SPCE, some characteristic peaks of FA were observed in the low-frequency region together with the ones of MoS_2 (Fig. 11 – blue line). On the other side SERS analysis on AuNPs MoS_2/SPCE, highlights strong vibrational peaks that can be related to the FA, which indeed is characterized by a strong chemisorption on Au NPs, in agreement with the results of Kokaislová and Matějka [35].

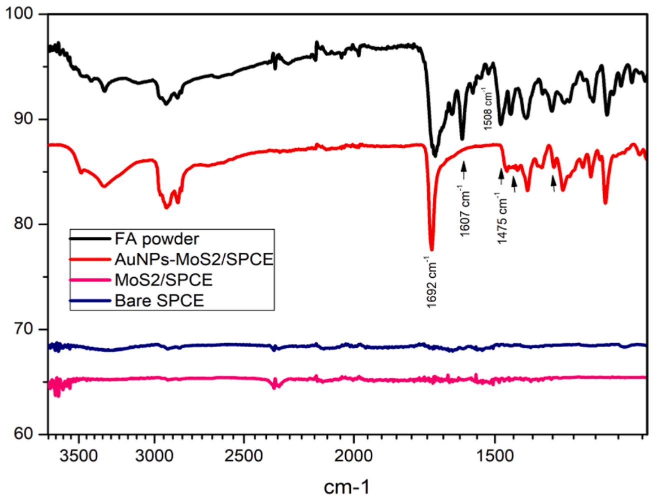

Fig. 10. FT-IR spectra acquired from FA deposited from a solution 10^{-4} M on the investigated electrodes.

In particular, the SERS signal on this sample presents two vibrational modes belonging to MoS_2 NS at 237 cm^{-1} (LA(M)) and 468 cm^{-1} (2LA) and others peaks in the fingerprint region that can assigned to FA [29]. Indeed, three prominent vibrational modes of FA were observed at 690 cm^{-1}, 1238 cm^{-1}, and 1574 cm^{-1}. The first one assigned to either ν_s(C═N) pteridine(pt) group or ν_{as}(C═C) p-aminobenzoic acid (paba) [33]. The second and the third vibrational modes are assigned to two different couplings: ρ(NH)(OH) + ω(CH2) of glutamic acid (Glu) and ν(CN-NH2) + ν(CC-CN)pt [35]. The vibrational mode at 1574 cm^{-1} can assigned either toS(NH2) + V_{as}(c = n)p t or to Vs(c-c) + p(CH)(Paba) [35].

In the low-frequency region, the peak at 615 cm^{-1} can be due either to the NH_2 out of plane stretching or to the in-plane OH stretching of the pteridine group [18]. As far as we know, the vibrational mode at 761 cm^{-1} is not assigned yet while the vibrational mode observed at 817 cm^{-1} can be assigned either to the stretching of C—N deformation of the paba group or to the CNO bending and the (OH)(CH_2) stretching modes of glutamic acid coupling [18]. The rocking mode of CH_2 in the p-aminobenzoic acid is observed at 959 cm^{-1} while OH rocking deformation of the pteridine group is at 996 cm^{-1} [18,35]. A coupling between rocking of (NH)(OH) mode and CH_2 wagging mode of glutamic acid is observed at 1024 cm^{-1} [35]. The peak at 1052 cm^{-1} is due to three different modes: C—N deformation stretching of p-aminobenzoic acid group, (NH_2)(CH)(OH) deformation bending of pteridine group, and C—C stretching deformation of glutamic acid [18].

In the high-frequency region, the peak at 1195 cm^{-1} is due to the bending mode of OH in the pteridine group coupled with CH_2 in the glutamic acid group [36]. All the observed vibrational modes are listed in Table 2. Castillo et *al* suggest that the absence of vibrational modes located at 661 cm^{-1} and 1489 cm^{-1} reveals significant information. Indeed, the absence of the first peak indicates the strong interaction between the benzene ring of paba and AuNPs while the second suggests the indirect contact between AuNPs and glutamic acid [36]. The huge differences in SERS spectra of FA compared to FA signal detected on MoS_2/SPCE is due to the strong interaction occurring between FA molecules and the gold surface, which foster the creation of a surface complex [37]. In fact, the pteridine can be considered as an anchor site since vibrational mode located at 1574 cm^{-1} is shifted and enhanced, suggesting this group is very close to the gold surface.

Conclusion

An easy electrochemical method for the detection of the FA was

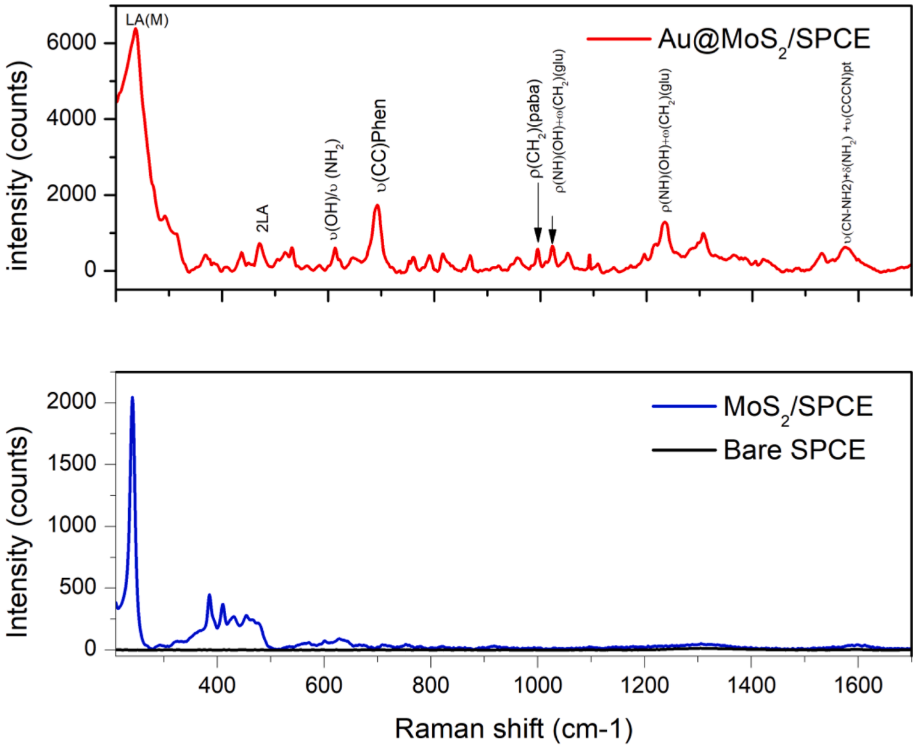

Fig. 11. SERS spectra acquired from FA deposited from a solution 10^{-4} M on the investigated electrodes.

Table 2
Assignment of SERS vibrational mode.

Wavelength (cm^{-1})	Assignment	Ref.
237	LA(M); MoS_2	[29]
468	2LA; MoS_2	[29]
615	$\rho(OH)(pt)$ IP DEF; $\rho(NH_2)(pt)$ OOP	[18]
761	**	[18]
817	δ (CNO)$\rho(OH)(CH_2)(Glu)$;$\nu(C-N)(paba)def$	[18]
959	ρ (CH_2)(paba)	[35]
996	ν(C—C) ρ(CH)(paba)def; ρ(OH)(pt)def;	[18]
1024	$\omega(CH_2)$(Glu) + ρ (NH)(OH)	[35]
1052	ν(C—C)(paba); $\rho(NH_2)$(CH)(OH)(pt) def;$\nu(C-C)(glu)def$	[18]
1195	(CH_2)(Glu) + δ(OH)(pt)	[36]
1238	ρ(NH)(OH) + $\omega(CH_2)$(Glu); $\nu(CN\text{-}NH_2)$ + ν(CC-CN)pt	[35]
1574	$s(NH_2)+\nu_{as}\ (C=N)(pt)$ or $\nu_s(C-C)+\rho(CH)(paba)$	[35]

developed based on the inhibition of the electrochemical activity of Au NPs deposited on exfoliated 2D-MoS_2 nanosheets when the gold surface is interacting with FA molecules. Indeed, differently from the 2D-MoS_2/SPCE, which was found to promote the FA electro-oxidation process, on the AuNPs-MoS_2/SPCE the surface is self-inactivated by FA due to binding between FA and AuNPs and consequently the FA electro-oxidation process is hindered. The FA-AuNPs binding was probed on the different electrodes by in situ ATR-FTIR and SERS measurements. This binding lead also to a remarkable decrease of the redox activity of AuNPs, which is reflected in the diminution of the intensity of anodic/cathodic Au couple, providing thus an indirect signal which has been used here for detecting FA.

CRediT authorship contribution statement

Khouloud Abid: Conceptualization, Investigation, Methodology, Data curation, Writing – original draft. **Rayhane Zribi:** Investigation, Methodology. **Ramzi Maalej:** Supervision. **Antonino Foti:** Supervision, Data curation. **Amani Khaskhoussi:** Investigation. **Pietro Giuseppe Gucciardi:** Supervision, Data curation. **Giovanni Neri:** Supervision, Data curation, Writing – review & editing.

Declaration of Competing Interest

The authors declare that they have no known competing financial interests or personal relationships that could have appeared to influence the work reported in this paper.

Data availability

The data that has been used is confidential.

References

[1] R. Turki, G. Ghimire, K. Damak, H.Y. Song, S. Boandoh, J. Kim, C. Rüssel, R. Aad, J. Kim, R. Maalej, Luminescent Sm-doped aluminosilicate glass as a substrate for enhanced photoresponsivity of MoS2 based photodetector, Appl. Surf. Sci. 565 (2021), 150342, https://doi.org/10.1016/j.apsusc.2021.150342.

[2] S. Suresh, G.E. Unni, M. Satyanarayana, A.S. Nair, V.P.M. Pillai, Plasmonic Ag@Nb2O5 surface passivation layer on quantum confined SnO2 films for high current dye-sensitized solar cell applications, Electrochim. Acta 289 (2018) 1–12.

[3] W. He, Y. Huang, J. Wu, Enzyme-free glucose biosensors based on MoS2 nanocomposites, Nanoscale Res. Lett. 15 (2020) 60, https://doi.org/10.1186/s11671-020-3285-3.

[4] K. Abid, N.H. Belkhir, S.B. Jaber, R. Zribi, M.G. Donato, G. Di Marco, P. G. Gucciardi, G. Neri, R. Maâlej, Photoinduced enhanced Raman spectroscopy with hybrid Au@WS2 nanosheets, J. Phys. Chem. C. 124 (2020) 20350–20358, https://doi.org/10.1021/acs.jpcc.0c04664.

[5] R. Khan, A. Radoi, S. Rashid, A. Hayat, A. Vasilescu, S. Andreescu, Two-dimensional nanostructures for electrochemical biosensor, Sensors 21 (2021) 3369, https://doi.org/10.3390/s21103369.

[6] V.D. Vaze, A.K. Srivastava, Electrochemical behavior of folic acid at calixarene based chemically modified electrodes and its determination by adsorptive stripping voltammetry, Electrochim. Acta 53 (4) (2007) 1713–1721.

[7] J.A. Greenberg, S.J. Bell, Y. Guan, Y. Yu, Folic acid supplementation and pregnancy: more than just neural tube defect prevention, Rev Obstet Gynecol. 4 (2011) 52–59.

[8] K.K. Sukla, R. Nagar, R. Raman, Vitamin-B12 and folate deficiency, major contributing factors for anemia: a population based study, E-SPEN J. 9 (2014) e45–e48. https://doi.org/10.1016/j.clnme.2013.11.003.

[9] A. Di Tinno, R. Cancelliere, L. Micheli, Determination of folic acid using biosensors—a short review of recent progress, Sensors 21 (2021) 3360, https://doi.org/10.3390/s21103360.

[10] N. Lavanya, E. Fazio, F. Neri, A. Bonavita, S.G. Leonardi, G. Neri, C. Sekar, Electrochemical sensor for simultaneous determination of ascorbic acid, uric acid and folic acid based on Mn-SnO2 nanoparticles modified glassy carbon electrode, J. Electroanal. Chem. 770 (2016) 23–32.

[11] V. Mani, Determination of folic acid using graphene/molybdenum disulfide nanosheets/gold nanoparticles ternary composite, Int. J. Electrochem. Sci. (2017) 258–267, https://doi.org/10.20964/2017.01.35.

[12] J. Han, H. Chen, H. Gao, Alternating current adsorptive stripping voltammetry in a flow system for the determination of ultratrace amounts of folic acid, Anal. Chim. Acta 252 (1991) 47–52, https://doi.org/10.1016/0003-2670(91)87195-D.

[13] M. Korolczuk, K. Tyszczuk, Determination of folic acid by adsorptive stripping voltammetry at a lead film electrode, Electroanalysis 19 (2007) 1959–1962, https://doi.org/10.1002/elan.200703969.

[14] K. Prechtel, Breast neoplasms. Importance of histology and prognosis for the treatment planning, MMW Munch Med. Wochenschr. 121 (1979) 1203–1207.

[15] L. Mirmoghtadaie, A.A. Ensafi, M. Kadivar, M. Shahedi, M.R. Ganjali, Highly selective, sensitive and fast determination of folic acid in food samples using new electrodeposited gold nanoparticles by differential pulse voltammetry, Int. J. Electrochem. Sci. 8 (2013) 13.

[16] S.-W. Tsai, J.-W. Liaw, F.-Y. Hsu, Y.-Y. Chen, M.-J. Lyu, M.-H. Yeh, Surface-modified gold nanoparticles with folic acid as optical probes for cellular imaging, Sensors. 8 (2008) 6660–6673, https://doi.org/10.3390/s8106660.

[17] Z. Zhang, J. Jia, Y. Ma, J. Weng, Y. Sun, L. Sun, Microwave-assisted one-step rapid synthesis of folic acid modified gold nanoparticles for cancer cell targeting and detection, Med. Chem. Commun. 2 (2011) 1079, https://doi.org/10.1039/c0md00274g.

[18] E.V. Solovyeva, E. Borisov, Demonstration of physical and analytical features of surface-enhanced raman scattering by analysis of folic acid in commercial tablets, J. Chem. Educ. 97 (2020) 2249–2253, https://doi.org/10.1021/acs.jchemed.0c00103.

[19] C. Backes, T.M. Higgins, A. Kelly, C. Boland, A. Harvey, D. Hanlon, J.N. Coleman, Guidelines for exfoliation, characterization and processing of layered materials produced by liquid exfoliation, Chem. Mater. 29 (2017) 243–255, https://doi.org/10.1021/acs.chemmater.6b03335.

[20] R. Zribi, A. Foti, M. Donato, P. Gucciardi, G. Neri, Fabrication of a novel electrochemical sensor based on carbon cloth matrix functionalized with MoO3 and 2D-MoS2 layers for riboflavin determination, Sensors. 21 (2021) 1371, https://doi.org/10.3390/s21041371.

[21] M.G. Donato, E. Messina, A. Foti, T.J. Smart, P.H. Jones, M.A. Iatì, R. Saija, P. G. Gucciardi, O.M. Maragò, Optical trapping and optical force positioning of two-dimensional materials, Nanoscale. 10 (2018) 1245–1255, https://doi.org/10.1039/C7NR06465A.

[22] J. Kim, S. Byun, A.J. Smith, J. Yu, J. Huang, Enhanced electrocatalytic properties of transition-metal dichalcogenides sheets by spontaneous gold nanoparticle decoration, J. Phys. Chem. Lett. 4 (2013) 1227–1232, https://doi.org/10.1021/jz400507t.

[23] Z. Gholamvand, D. McAteer, A. Harvey, C. Backes, J.N. Coleman, Electrochemical applications of two-dimensional nanosheets: the effect of nanosheet length and thickness, Chem. Mater. 28 (2016) 2641–2651, https://doi.org/10.1021/acs.chemmater.6b00009.

[24] L. Ottaviano, S. Palleschi, F. Perrozzi, G. D'Olimpio, F. Priante, M. Donarelli, P. Benassi, M. Nardone, M. Gonchigsuren, M. Gombosuren, A. Lucia, G. Moccia, O. A. Cacioppo, Mechanical exfoliation and layer number identification of MoS $_2$ revisited, 2D Mater. 4 (2017), 045013, https://doi.org/10.1088/2053-1583/aa8764.

[25] S. Ghayeb Zamharir, R. Karimzadeh, S.H. Aboutalebi, Laser-assisted tunable optical nonlinearity in liquid-phase exfoliated MoS2 dispersion, Appl. Phys. A Mater. Sci. Process. 124 (2018) 692, https://doi.org/10.1007/s00339-018-2115-2.

[26] D. Sahoo, B. Kumar, J. Sinha, S. Ghosh, S.S. Roy, B. Kaviraj, Cost effective liquid phase exfoliation of MoS2 nanosheets and photocatalytic activity for wastewater treatment enforced by visible light, Sci. Rep. 10 (2020) 10759, https://doi.org/10.1038/s41598-020-67683-2.

[27] C. Lee, H. Yan, L.E. Brus, T.F. Heinz, J. Hone, S. Ryu, Anomalous lattice vibrations of single- and few-layer MoS $_2$, ACS Nano 4 (2010) 2695–2700, https://doi.org/10.1021/nn1003937.

[28] Z.-Y. Cao, X.-J. Chen, Phonon scattering processes in molybdenum disulfide, Appl. Phys. Lett. 114 (2019) 052102. https://doi.org/10.1063/1.5082932.

[29] X. Zhang, X.-F. Qiao, W. Shi, J.-B. Wu, D.-S. Jiang, P.-H. Tan, Phonon and Raman scattering of two-dimensional transition metal dichalcogenides from monolayer, multilayer to bulk material, Chem. Soc. Rev. 44 (2015) 2757–2785, https://doi.org/10.1039/C4CS00282B.

[30] O. Parlak, A. İncel, L. Uzun, A.P.F. Turner, A. Tiwari, Structuring Au nanoparticles on two-dimensional MoS2 nanosheets for electrochemical glucose biosensors, Biosens. Bioelectron. 89 (2017) 545–550, https://doi.org/10.1016/j.bios.2016.03.024.

[31] J.J. Castillo, T. Rindzevicius, K. Wu, M.S. Schmidt, K.A. Janik, A. Boisen, W. Svendsen, N. Rozlosnik, J. Castillo-León, Synthesis and characterization of covalent diphenylalanine nanotube-folic acid conjugates, J Nanopart Res. 16 (2014) 2525, https://doi.org/10.1007/s11051-014-2525-9.

[32] F.S. Majidi, E. Mohammadi, B. Mehravi, S. Nouri, K. Ashtari, A. Neshasteh-Riz, Investigating the effect of near infrared photo thermal therapy folic acid conjugated gold nano shell on melanoma cancer cell line A375, Artif. Cells Nanomed. Biotechnol. 47 (2019) 2161–2170, https://doi.org/10.1080/21691401.2019.1593188.

[33] S.S. Mers, E.T.D. Kumar, V. Ganesh, Gold nanoparticles-immobilized, hierarchically ordered, porous TiO2 nanotubes for biosensing of glutathione, Int. J. Nanomed. 10 (Suppl 1) (2015) 171–182, https://doi.org/10.2147/IJN.S80054.

[34] C. D'Andrea, J. Bochterle, A. Toma, C. Huck, F. Neubrech, E. Messina, B. Fazio, O. M. Maragò, E. Di Fabrizio, M.L. de La Chapelle, P.G. Gucciardi, A. Pucci, Optical nanoantennas for multiband surface-enhanced infrared and Raman spectroscopy, ACS Nano 7 (4) (2013) 3522–3531, https://doi.org/10.1021/nn4004764.

[35] A. Kokaislová, P. Matějka, Surface-enhanced vibrational spectroscopy of B vitamins: what is the effect of SERS-active metals used? Anal Bioanal Chem. 403 (2012) 985–993, https://doi.org/10.1007/s00216-011-5704-x.

[36] J.J. Castillo, T. Rindzevicius, C.E. Rozo, A. Boisen, Adsorption and vibrational study of folic acid on gold nanopillar structures using surface-enhanced raman scattering spectroscopy, Nanomater. Nanotechnol. 5 (2015) 29, https://doi.org/10.5772/61606.

[37] R.A.R. Teixeira, F.R.A. Lima, P.C. Silva, L.A.S. Costa, A.C. Sant'Ana, Tracking chemical interactions of folic acid on gold surface by SERS spectroscopy, Spectrochim. Acta Part A. 223 (2019) 117305. https://doi.org/10.1016/j.saa.2019.117305.

Section V

General Conclusions

The development of electrochemical sensors based on two-dimensional molybdenum disulfide nanosheets for the detection of different biomolecules was the subject of this Ph.D. thesis. Detecting and monitoring biomolecules have become increasingly relevant in many contexts, from industrial demands for faster and large-scale production of cheap materials and sensor production to medical applications looking for a reliable substitution for the available expensive detection techniques. These materials have attracted the attention of scientists from different research fields due to their outstanding properties. Hence, various applications based on 2D materials or 2D-material composites have lately been observed, in which the field of sensing has been one of the most interesting in this class of materials since the discovery of graphene. *(Section I)*

The main objective of this Ph.D. thesis was to develop a reliable sensor from synthesizing 2D materials using low-cost and scalable methods to apply this sensor to real samples. So to quickly summarize this thesis, first of all, 2D-MoS_2 nanosheets have been successfully synthesized via liquid phase exfoliation technique starting from bulk molybdenum disulfide powder purchased from Aldrich. The first obtained solution, having a concentration of about 0.45 μg/mL, contained nanoflakes with lateral sizes around 450 nm and thicknesses ranging between 15 and 20 layers for each nanoflake. This suspension was used to detect tyrosine, an essential amino acid, using commercial screen-printed electrodes and analyzing the electrochemical properties of each electrode. *(Section III. Part 1. Chapters 1&2)*

After that, optimizing the synthesis process to obtain better sensitive and selective sensors was the following goal to achieve. Here, the resulting suspension was richer in nanoflakes, having a concentration of around 80 μg/mL, a lateral size of about 170 nm, and a thickness of about 9 layers in each nanosheet. Firstly, this solution was used to modify screen-printed carbon electrodes for the simultaneous and selective determination of tyrosine and dopamine in the presence of uric acid. *(Section III. Part 1. Chapter 3)*

In addition, the same solution was used to functionalize the carbon cloth matrix doped with molybdenum oxide nanoparticles leading to the obtention of Mo-sulfide/Mo-oxide nanocomposite. This new nanohybrid material was successfully used to determine riboflavin alone and in the presence of folic acid and ascorbic acid. The selectivity of the sensor obtained was not optimal. In such cases, and when dealing with biomolecules, many parameters can significantly improve the properties of the sensor, such as pH. Varying the pH of the electrolyte can be a perfect solution to eliminate the interference problem. The optimization of the electrochemical selectivity of this nanocomposite will be considered as future work. *(Section III. Part 1. Chapter 4)*

Furthermore, deepening more in the literature and analyzing what was missing, the idea of studying the electrochemical and sensing properties of 2D molybdenum disulfide with different geometrical characteristics was raised. For this reason, 2D-MoS_2 nanosheets were produced via liquid cascade centrifugation leading to the obtention of suspensions having different concentrations that goes from 80 µg/mL to 4 µg/mL when increasing the centrifugation speed from 1.5 krpm up to 5 krpm. Moreover, a decrease in the lateral size of the nanosheets, going from 260 nm to 115 nm, and the thickness, which decreases from 14 to 6 layers, was observed when increasing the centrifugation speed. The obtained suspensions were used to modify commercial screen-printed carbon electrodes. These modified electrodes were first electrochemically characterized in the presence of $[Fe(CN)_6]^{3-/4-}$ redox probe to better understand these materials' electrochemical kinetics and electron transfer. After that, their efficiencies for the electrochemical detection of biomolecular analytes such as dopamine and riboflavin were tested and here, different behaviors were noticed. Using dopamine as an analyte, results indicated no significant variations in the electrochemical parameters among electrodes modified with 2D-MoS_2 nanosheets of different sizes and thicknesses. Conversely, the oxidation of riboflavin was observed to be largely promoted on electrodes modified with nanosheets of smaller lateral size and a reduced number of layers. The peak current was observed to increase more than 5 times. This result can be explained by the higher amount of active edge sites in 2D-MoS_2 crystallites with fewer layers and smaller lateral sizes, which enhances the catalytic activity. The results reported here are interesting for producing nano-engineered 2D-MoS_2 sheets suitable as the core of more sensitive electrochemical devices for biomolecule detection. *(Section III. Part 2. Chapters 1&2)*

Another part of the Ph.D. course was dedicated to developing new electrochemical sensors, always dealing with 2D transition metals dichalcogenides. The most successful part is currently a patent underwriting in which details can’t be provided. The other part was the development of an electrochemical sensor based on CNT/WS_2 core-shell heterostructures via atomic layer deposition for riboflavin detection. Also, an electrochemical sensor using the sample produced via LPE decorated with gold nanoparticles was developed for folic acid determination. *(Section IV)*

Overall, although the work presented for this doctoral thesis has succeeded in its primary goal of developing and optimizing electrochemical sensors based on 2D materials to detect biomolecules, other more advanced work is planned shortly, such as improving the synthesis method and why not applying it to other 2D materials, enhancing the selectivity of certain sensors and lowering their limits of detections, and also extending the range of the tested analyte to other interesting biomolecules or even changing the application to other important fields like food analysis or environmental safety... This work is only the beginning of others hoping to achieve, together with all the other researchers, the main goals of this vast and interesting research field which try to provide a better life.

Appendix A: List of Figures & Schema

Section I: Chemical sensors & 2D Materials: State of the Art

Section II: Materials & Methods

Section III: Results & Discussions

List of Schema

Appendix B: List of Tables

Appendix C: List of publications and conferences

Scientific publications

[1]: **Zribi, R.**; Maalej, R.; Messina, E.; Gillibert, R.; Donato, M.G.;Marag`o, O.M.; Gucciardi, P.G.; Leonardi, S.G.; Neri, G. Sens. Actuators B Chem. 2020, 303, 127229. *(IF: 7.071).*

[2]: **Zribi, R.**; Maalej,R.; Gillibert, R.; Donato, M.G; Gucciardi, P.G; Leonardi, S.L; Neri, G. FlatChem. 2020, 100187. *(IF: 4.85).*

[3]: **Zribi, R.**; Neri,G. Sensors. 2020, 20(18), 5404. *(IF: 3.576).*

[4]: **Zribi, R.**; Foti, A.; Donato, M.G.; Gucciardi, P.G.; Neri, G. Sensors. 2021, 21(4), 1371. *(IF: 3.847).*

[5]: **Zribi, R.**; Foti, A.; Donato, M.G.; Gucciardi, P.G.; Neri, G. Electrochimica Acta. 2022, 141433. *(IF: 7.336).*

[6]: **Zribi, R.**; Ferlazzo A.; Fazio, E.; Condorelli, M.; D'Urso, L.; Neri, G.;Corsaro, C.; Neri, F.; Compagnini, G.; Neri, G. IEEE Transactions on Instrumentation and Measurement. 2023, 72, 1-8, 6002708. *(IF: 5.332).*

[7]: Abid, K.; **Zribi, R.**; Maalej, R.; Foti, A.; Khaskhoussi, A.; Gucciardi, P.G.; Neri, G. FlatChem. 2022, 100433. *(IF: 5.829).*

[8]: Chelly, M.*; Chelly, S.*; **Zribi, R.**; Bouaziz-Ketata, H.; Gdoura, R.; Nehru, L.; Veerapandi, G.; Sekar, C.; Neri, G. Nanomaterials. 2021, 11, 739. *(IF: 5.719).*

[9]: S. Chelly, S.; Chelly, M.*; **Zribi, R.**; Gdoura, R.; Bouaziz- Ketata, H.; Neri, G. ACS Omega. 2021, 6, 37, 23666–23675. *(IF: 4.132).*

[10]: Abid, K.; Belkhir, N.H.; Jaber, S B.; **Zribi, R.**; Donato, M.G.;Di Marco,G.; Gucciardi, P.G.; Neri, G.; Maâlej, R. J. Phys. Chem.C. 2020, 124, 20350−20358. *(IF: 4.126).*

Conferences

1. Associazione Italiana di Chimica per Ingegneria. **(2019) Poster presentation.**
2. New times-new trends in Materials science and Engineering. **(2021) Oral presentation.**
3. Congresso Nazionale della Società Chimica Italiana, SCI. **(2021) Oral presentation.**
4. Medical Measurement and Applications. **(2022) Oral presentation and paper submission.**